Matériaux architecturés pour refroidissement par transpiration : application aux chambres de combustion

Sébastien Pinson

Communauté
UNIVERSITÉ Grenoble Alpes

THÈSE

Pour obtenir le grade de

DOCTEUR DE LA COMMUNAUTÉ UNIVERSITÉ GRENOBLE ALPES

Spécialité : **Ingénierie-Matériaux, Mécanique, Génie civil, Electrochimie**

Arrêté ministériel : 25 mai 2016

Présentée par

Sébastien PINSON

Thèse dirigée par **Rémy Dendievel**

préparée au sein du **Laboratoire SIMaP**
dans **l'École Doctorale IMEP2**

Architectured materials for transpiration cooling : application to combustion chambers

Matériaux architecturés pour le refroidissement par transpiration : application aux chambres de combustion

Thèse soutenue publiquement le **09 décembre 2016**
devant le jury composé de :

M., Frédéric FEYEL
Directeur de recherche, SAFRAN CRT, Président
M., Jérôme BELLETTRE
Professeur, Université de Nantes, Rapporteur
M., Frédéric TOPIN
Maître de conférences, Aix-Marseille Université, Rapporteur
Mme, Cécile DAVOINE
Ingénieur de recherche, ONERA, Examinateur
M., Daniel GAFFIE
Ingénieur de recherche, ONERA, Examinateur
M., Rémy DENDIEVEL
Professeur, Grenoble INP, Directeur de thèse

Remerciements

La thèse, ça ressemble à une voie d'escalade un peu longue et un peu dure. On commence par hésiter. Doit-on se lancer ? Pourquoi ne pas choisir une autre voie ? Celle-ci a l'air plus facile, au moins on aperçoit son arrivée. Celle-là... plein de gens l'ont déjà essayée. Mais finalement, on décide de relever le défi. La première année, on analyse minutieusement le rocher et on choisit le matériel adapté. Waouh, la route promet d'être longue ! On s'entoure des bonnes personnes, celles qui sauront nous conseiller tout au long de l'ascension,. On ne s'engage réellement que lors de la deuxième année. On passe les premières dégaines, on sécurise les premiers résultats, on accumule de l'expérience et on gagne en confiance en soi. Arrive alors le premier véritable obstacle. On chute, on s'écrase contre la paroi, puis on hésite à se relancer, on n'avance plus. Mauvaise lecture de la voie ? Manque de compétences ? La seule solution : écouter les gens qui nous assurent, nous soutiennent et nous encouragent. On finit alors par ajuster ses mouvements, par changer d'approche ou simplement par donner tout ce qu'on a. Ça finit par passer ! Après de nombreuses péripéties, arrive finalement la dernière longueur : la troisième année. La rédaction est son épreuve finale. C'est un peu comme un bon dernier surplomb qui achève. De plus, on sait que la fin est proche, mais on ne la voit pas encore. Comme les bras ne suivent plus, on doit prendre sur soi. Après avoir mobilisé ses dernières forces, le sommet tant rêvé finit par arriver. On se redresse et on regarde en bas. Le chemin parcouru nous donnerait presque le vertige. Cependant, le plus impressionnant reste peut être le moment où on lève les yeux et où on se rend compte des possibilités futures qui s'ouvrent à nous. Une seule chose nous vient alors à l'esprit : What's next ?

Il est évident que je n'aurais jamais pu arriver au bout de ce projet sans l'aide précieuse de mon coach/directeur de thèse Rémy Dendievel. Tout au long de ces trois années, tu as été à mon écoute, tu as su me guider et me réorienter dans mes démarches. J'ai apprécié l'autonomie que tu m'as laissée pour réaliser cette thèse, elle a été le témoin de la confiance que tu avais dans mes recherches. Travailler avec toi a été à la fois une expérience riche en enseignements et un réel plaisir. Pour toutes ces raisons, je tiens à te remercier très sincèrement.

Je remercie également tout particulièrement Cécile Davoine. Tu as fait preuve de disponibilité et tu as su m'intégrer efficacement au sein du projet MOTRICE. Malgré la distance entre nos bureaux, nous avons rapidement noué un lien qui a, je pense, réelle-

ment participé à l'aboutissement de cette thèse. Je remercie aussi Daniel Gaffié et Marc Thomas pour leur implication dans mes travaux. Au cours de ces trois années, leurs remarques ont toujours été très constructives et ont permis à cette thèse d'avancer. Je tiens aussi à remercier Océane Lambert. Je suis persuadé que nos travaux ont été très complémentaires et je te souhaite donc tout le meilleur pour la fin de ta thèse. Enfin, je souhaiterais également remercier Pierre Beauchêne qui m'a apporté l'aide nécessaire pour réaliser les mesures de conductivités thermiques.

Je suis également très reconnaissant envers Audrey Guyon qui a été mon principal contact industriel à Sintertech. Je te remercie pour tous les échantillons que tu m'as livrés et pour toutes les informations techniques que tu m'as données.

Je tiens également à montrer beaucoup de gratitude envers les rapporteurs Jerôme Bellettre et Frédéric Topin pour avoir pris le temps lire en détail ce manuscrit. Un grand merci également à Frédéric Feyel pour avoir accepté de présider mon jury de thèse. Je les remercie tous pour la qualité et l'utilité des remarques qu'ils ont pu faire lors de leur participation au jury de thèse.

Contrairement à certaines idées reçues, une thèse est un travail d'équipe. Le laboratoire SIMaP, et plus particulièrement le groupe GPM2, a été un véritable acteur dans la réussite de ce projet. Tous les chercheurs, ingénieurs et techniciens ont su faire preuve d'une grande disponibilité et j'en suis très reconnaissant. Je tiens à remercier tout particulièrement Luc Salvo, Pierre Lhuissier, Christophe Martin, David Jauffres, Didier Bouvard, Fabien Volpi, Xavier Bataillon et Franck Pelloux pour leur aide apportée sur différents plans techniques. Un laboratoire, c'est aussi des doctorants et des stagiaires. Je les remercie également pour tous les bons moments passés ensemble ! Les randos, les via-ferratas, les séances d'escalade, les sorties ski, les séances de courses à pied, les grand débats pendant les pauses sur la différence entre un fruit et un légume, les soirées jeux et les soirées tout court. Merci notamment à Jérémy, Anthony, Xavier, Charles, Camila, Robin, Paul, Edouard et les Alexis.

Mes amis tiennent également une place importante dans l'accomplissement de cette thèse. Pendant les phases les plus difficiles, ils m'ont donné le soutien moral nécessaire pour franchir les différents obstacles. Un grand merci à la promo 10 avec qui je passe de véritables moments de bonheur depuis plus de 6 ans à présent. Merci Jerem, Lothaire,

Valou, Theo, Simon, Jérome, Iannis, Xav, Guigui et encore bien d'autres qui se reconnaitront ! Je remercie également les supers colocs qui ont su me supporter tous les jours après le travail. Un merci tout spécial à Camilo et à Anne Cha.

Il est évident que je dois également beaucoup à ma famille et notamment à mes parents. Les études longues n'ont jamais été une habitude dans la famille. Pourtant, ils ont toujours encouragé mes choix et n'ont jamais hésité à m'aider durant toutes ces longues années. Pour votre soutien, je vous adresse, Maman et Papa, tout mon respect et ma plus grande gratitude.

Enfin, j'adresse mes derniers remerciements à mon assureuse préférée, Elise. Tu tiens une place très spéciale dans ma vie depuis un petit moment à présent. Je sais que ces trois années ont été longues pour toi, alors merci pour avoir attendu et merci pour m'avoir soutenu. Nous allons finalement pouvoir organiser notre futur tous les deux.

Contents

List of Figures

List of Tables

Nomenclature

Latin Symbols

Symbol	Units	Description
A	m^2	Cross-sectional area
A_{sf}	m^2	Interfacial surface area
A_{sp}	m^2/m^3	Specific surface area
c_p	$J/(kg.K)$	Fluid calorific capacity
d	m	Equivalent particle diameter
d_c	m	Channel hydraulic diameter of the annulus
d_p	m	Particle size
d_{pores}	m	Pore size
d_h	m	Hydraulic diameter
f	-	Friction factor
geo	-	Geometrical family
Gr	-	Grashof number
h	$W/(m^2.K)$	Heat transfer coefficient
h_b	-	Burke-Plummer parameter
h_k	-	Kozeny parameter
h_{sf}	$W/(m^2.K)$	Interfacial heat transfer coefficient
h_v	$W/(m^3.K)$	Volumetric heat transfer coefficient
I	A	Current intensity
K	m^2	Permeability coefficient
L	m	Thickness
Nu	-	Nusselt number
p	Pa	Pressure
Pr	-	Prandtl number
q_{rad}	W/m^2	Radiative heat flux
R	Ω	Electrical resistance
Re	-	Reynolds number
r_{cc}	-	Pressure loss
St	-	Stanton number
T	K	Temperature
V	m^3	Volume
V_{el}	V	Voltage difference
u	m/s	Fluid velocity
v_i	m/s	Intersitial velocity
v_s	m/s	Superficial velocity

Greek Symbols

Symbol	Units	Description
α_g	-	Gas absorptivity
β	m^{-1}	Forchheimer coefficient
η	$Pa.s$	Fluid dynamic viscosity
ε	-	Porosity
ε_g	-	Gas emissivity
ε_w	-	Inner wall emissivity
γ	-	Luminosity factor
λ	$W/(m.K)$	Thermal conductivity
$\lambda_{s,eff}$	$W/(m.K)$	Effective thermal conductivity of the solid phase
λ^*	$W/(m.K)$	Relative thermal conductivity
ρ	kg/m^2	Density
ρ_{el}	$\Omega.m$	Electrical resistivity
φ	$W/(m^2.K)$	Heat flux
σ	$W/(m^2/k^4)$	Stephan's radiation constant
σ_{el}	S/m	Electrical conductivity
τ	-	Tortuosity

Subscripts

Symbol	Description
$_0$	$x = 0$
$_L$	$x = L$
$_g$	Hot gases
$_c$	Coolant
$_{bulk}$	Bulk material
$_f$	Fluid phase
$_s$	Solid phase
$_{eff}$	Effective
$_{cs}$	Conduction through the solid phase
$_{cf}$	Conduction through the fluid phase
$_{cv}$	Convection within the fluid phase
$_r$	Radiation across a pore
$_{in}$	Inlet
$_{wc}$	Without cooling
$_{MPW}$	Multi-perforated wall

Part I

French Summary - Résumé en français

Cette partie est un résumé étendu de la thèse en français. Elle présente le contexte, les principaux résultats ainsi que les perspectives qui en découlent. Ce résumé est une vulgarisation des résultats obtenus. Par conséquent, le lecteur pourra se référer au manuscrit en anglais pour avoir un accès à un développement plus détaillé

Chapter 1

Introduction et revue bibliographique

Dans une turbine à gaz, la combustion a lieu dans la chambre de combustion, et plus particulièrement dans le tube à flamme, repéré en rouge sur la figure 1.1.

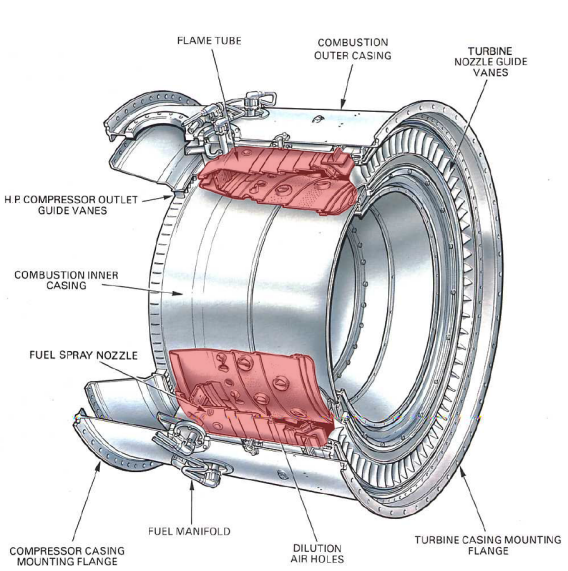

Figure 1.1: Chambre de combustion annulaire du RB211 (Rolls-Royce Plc, 1996).

La température des gaz générés par la combustion est extrêmement élevée (> 2000 K) et menace l'intégrité de la paroi du tube à flamme (température maximale de 1100 K pour les super-alliages à base de nickel ou de cobalt). Afin d'être refroidie, la paroi est multi-perforée. Elle utilise ainsi une partie de l'air sortant du compresseur, qui est détournée pour venir s'écouler au travers des multi-perforations.

Face aux nouvelles contraintes environnementales imposées au secteur aéronautique, les constructeurs cherchent à s'orienter vers des technologies de chambres de combustions étagées à mélange pauvre, turbulent et pré-mélangé. Bien que cette technologie permettrait de diminuer la température de flamme (1700-1900 K) et d'ainsi réduire les émissions de NO_x, elle restreindrait la quantité d'air jusqu'alors réservée au refroidissement. Il est alors **indispensable de développer une technologie de refroidissement plus efficace.** Cette thèse de doctorat vise à étudier **une technologie de refroidissement potentielle : le refroidissement par transpiration.**

1.1 Evolution des technologies de refroidissement de la chambre de combustion

La manière la plus simple de refroidir la paroi du tube à flamme est le refroidissement par film. C'est le nom générique donné à toutes les technologies qui font passer de l'air de refroidissement à travers une fente annulaire et dans la direction axiale afin de former une couche limite protectrice le long de la paroi. Les différents systèmes de film cooling sont légers et mécaniquement robustes mais mènent à des refroidissements non homogènes et à une grande consommation d'air.

Pour améliorer les échanges convectifs, les parois multi-perforées sont actuellement utilisées (figure 1.2a). La paroi est perforée par laser de milliers de trous ayant un diamètre d'environ 0.5 mm. Les trous sont légèrement inclinés dans le sens du flux principal et sont placés en quinconce. Lorsque le fluide de refroidissement est éjecté des trous d'une rangée, il forme une couche limite protectrice qui est rapidement renouvelée par les trous de la rangée suivante. Grâce à des échanges convectifs à l'intérieur des trous, la quantité d'air utilisée pour le refroidissement est ainsi réduite.

Le refroidissement par transpiration (figure 1.2b) est théoriquement la technique la plus efficace. La paroi multi-perforée est remplacée par une paroi poreuse. Grâce à une multitude de pores uniformément distribués à la surface du matériau, une couche protectrice limite homogène peut être générée. Cette couche limite limiterait alors les problèmes de points chauds existants avec la paroi multi-perforée. De plus, grâce à l'énorme surface spécifique du matériau, l'énergie emmagasinée par radiation pourrait être retirée de manière efficace par convection interne.

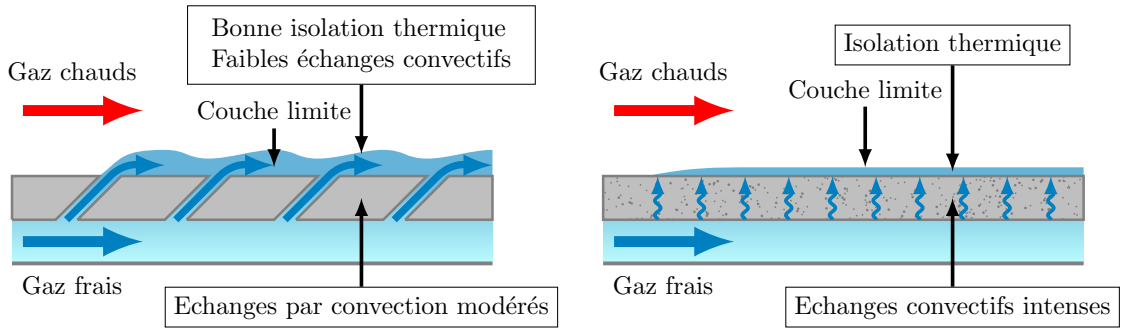

(a) Refroidissement au travers d'une paroi multiperforée.

(b) Refroidissement par transpiration au travers d'une paroi poreuse.

Figure 1.2: Technologies de refroidissement améliorées.

1.2 Le refroidissement par transpiration dans la littérature

Les travaux portant sur le refroidissement par transpiration ont longtemps été séparées en deux études distinctes :

- L'étude de la couche limite et du rôle du taux de soufflage (Rannie, 1947; Eckert and Livingood, 1954; Rubesin, 1954; Mickley et al., 1953; Moffat and Kays, 1968; L'Ecuyer and Colladay, 1972; Colladay and Stepku, 1971) ;
- L'étude des échanges internes (Koh and Fortini, 1973; Kar, 1981; Yamamoto, 1990; Andoh and Lips, 2003).

Ces études tentent de montrer que dans le cas du refroidissement par transpiration, la phase solide et la phase fluide peuvent être à des températures locales différentes. Un modèle de non-équilibre thermique local est souvent utilisé pour décrire les échanges internes (Wakao and Kagei, 1982; Quintard et al., 1997; Kuwahara et al., 2001; Amiri and Vafai, 1994; Von Wolfersdorf, 2005; Reutter et al., 2008; Amatachaya et al., 2011).

Conservation de l'énergie dans la phase solide :

$$\underbrace{\frac{\partial}{\partial x_i}\left(\boldsymbol{\lambda}_{\mathbf{s,eff}}\frac{\partial T_s}{\partial x_i}\right)}_{\text{Conduction dans la phase solide}} - \underbrace{\mathbf{h_v}(T_s - T_f)}_{\text{Convection entre les phases}} = 0 \tag{1.1}$$

Conservation de l'énergie dans la phase fluide :

$$\underbrace{\frac{\partial}{\partial x_i}\left(\rho_f c_p v_{s,i} T_f\right)}_{\text{Advection}} - \underbrace{\frac{\partial}{\partial x_i}\left(\varepsilon\lambda_f\frac{\partial T_f}{\partial x_i}\right)}_{\text{Conduction dans la phase fluide}} - \underbrace{\mathbf{h_v}(T_s - T_f)}_{\text{Convection entre les phases}} = 0 \tag{1.2}$$

Conservation de la masse :

$$\frac{\partial}{\partial x_i}(\varepsilon\rho_f v_i) = 0 \tag{1.3}$$

Conservation de la quantité de mouvement :

$$\underbrace{\frac{1}{\varepsilon^2}\frac{\partial}{\partial x_j}(\rho_f v_{s,i} v_{s,j})}_{\text{Terme inertiel}} = \underbrace{-\frac{\partial p}{\partial x_i}}_{\text{Terme de pression}} + \underbrace{\frac{1}{\varepsilon}\frac{\partial}{\partial x_j}\left[\eta\left(\frac{\partial v_{s,i}}{\partial x_j} + \frac{\partial v_{s,j}}{\partial x_i}\right)\right] - \frac{1}{\varepsilon}\frac{2}{3}\frac{\partial}{\partial x_i}\left(\eta\frac{\partial v_{s,j}}{\partial x_j}\right)}_{\text{Terme visceux}}$$
$$\underbrace{-\frac{\eta}{\mathbf{K}}v_{s,i} - \rho_f\boldsymbol{\beta}|v_s|v_{s,i}}_{\text{Darcy-Forchheimer}} \tag{1.4}$$

Ce modèle fait apparaitre quatre propriétés matériaux effectives qui gouvernent les transferts de chaleur lors d'un écoulement fluide dans un milieu poreux :

- **La conduction thermique effective de la phase solide** ($\boldsymbol{\lambda}_{s,eff}$);
- **Les coefficients de perméabilité et de Forchheimer** ($\mathbf{K}$ & $\boldsymbol{\beta}$);
- **Le coefficient de transfert thermique volumique** ($\mathbf{h_v}$).

Ces propriétés sont **directement liées à l'architecture poreuse**.

1.3 Matériaux poreux pour le refroidissement par transpiration

Cette thèse s'est focalisée sur l'étude de **matériaux poreux issus du frittage partiel de poudres métalliques**. Ces structures assurent des architectures poreuses complètement interconnectées pour des porosités comprises entre 20 et 40%. Des poudres de super-alliage peuvent être utilisées afin de conserver la diffusivité thermique et les bonnes propriétés mécaniques à haute température du matériau.

1.4 Objectif et approche de la thèse

L'objectif de la thèse est de trouver l'architecture partiellement frittée qui permet d'optimiser le refroidissement par transpiration d'une chambre de combustion aéronautique. Le travail est divisé en deux parties :

- La première partie de la thèse consiste à déterminer les relations reliant les propriétés effectives des matériaux à leurs propriétés architecturales. La méthodologie décrite sur la figure 1.3 a été adoptée pour mener à bien cette étude.
- La seconde partie se focalise sur l'optimisation multi-objectifs de l'architecture pour laquelle un modèle de transfert de chaleur a été développé.

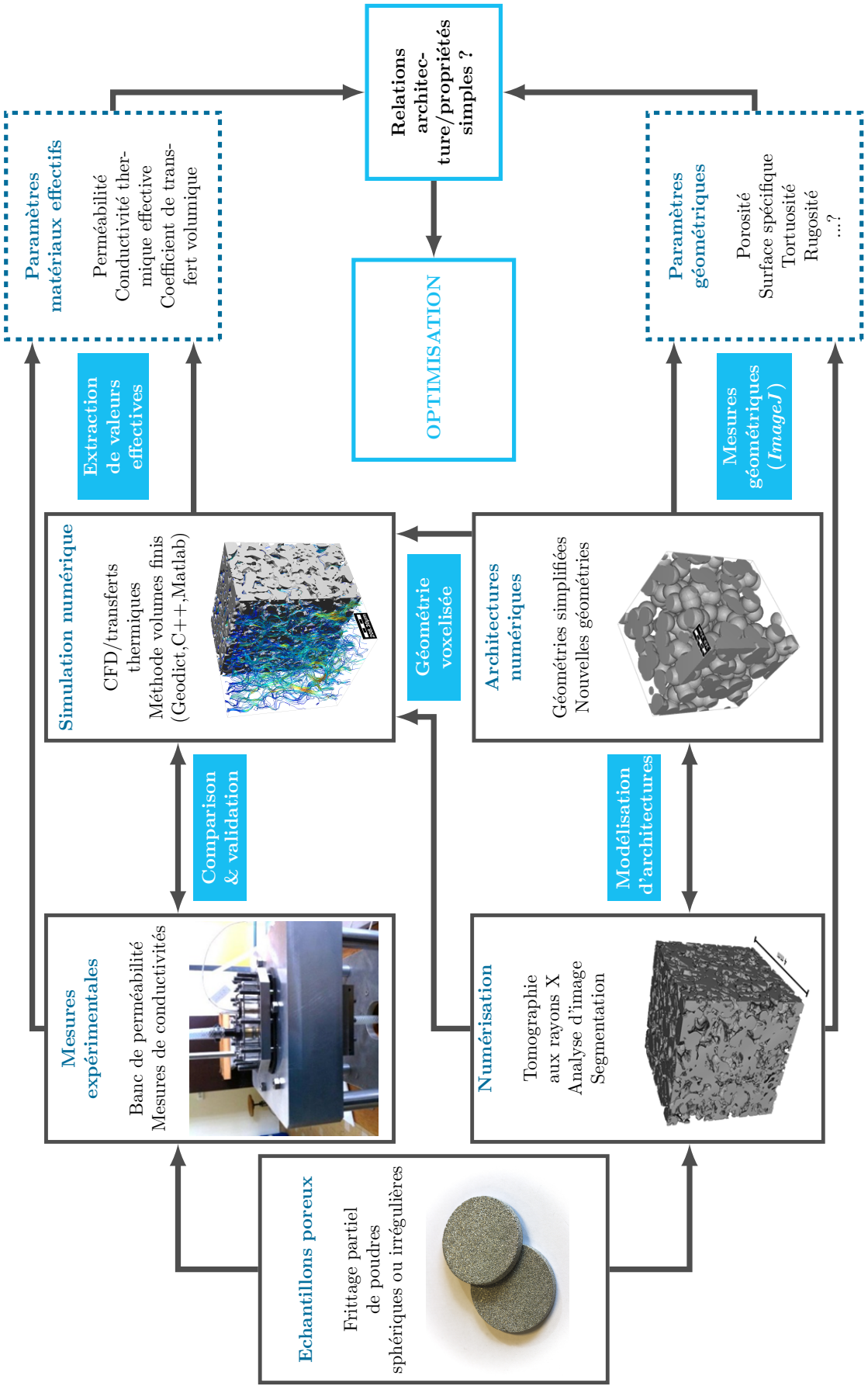

Figure 1.3: Méthodologie appliquée pendant la thèse

Chapter 2

Matériaux partiellement frittés et caractérisation géométrique

Au cours de cette thèse, deux catégories de matériaux ont été étudiées : des matériaux partiellement frittés réels et des matériaux modèles numériques.

2.1 Les matériaux partiellement frittés réels

La thèse s'est focalisée sur l'étude de deux familles d'échantillons de matériaux partiellement frittés formés à partir :

- de poudres métalliques sphériques (matériaux référencés SP);
- de poudres métalliques irrégulières (matériaux référencés IP);

Les échantillons ont été produits par l'entreprise Sintertech (Pont-de-Claix, France) à partir de poudres monodispersées ayant un grade compris entre 50 et 600 μm. Au cours de leur procédé, le frittage partiel conduit à une réduction de la porosité d'environ 6%. Des matériaux ayant différentes porosités sont obtenus avec différents niveaux de compression de la poudre avant frittage. Pour pouvoir être étudiés numériquement, des échantillons ont été numérisés par tomographie aux rayons X au laboratoire *Matéis* (Lyon, France) et au laboratoire *SIMaP* (Grenoble, France). Les figures 2.1a et 2.1b représentent les deux types d'architectures étudiées.

2.2 Génération de matériaux numériques

Comme la numérisation par tomographie est chronophage, des architectures modèles ont été générées numériquement. Le logiciel *dp3D* (Martin and Bordia, 2008), développé au laboratoire *SIMaP* et basé sur la méthode des éléments discrets, a permis de générer facilement des empilements de sphères (Packed bed) ainsi que des images tri-dimensionelles mimant l'architecture des poudres sphériques partiellement frittées (SPnum). Les figures 2.1c et 2.1d représentent les deux types d'architectures pouvant ainsi être générées.

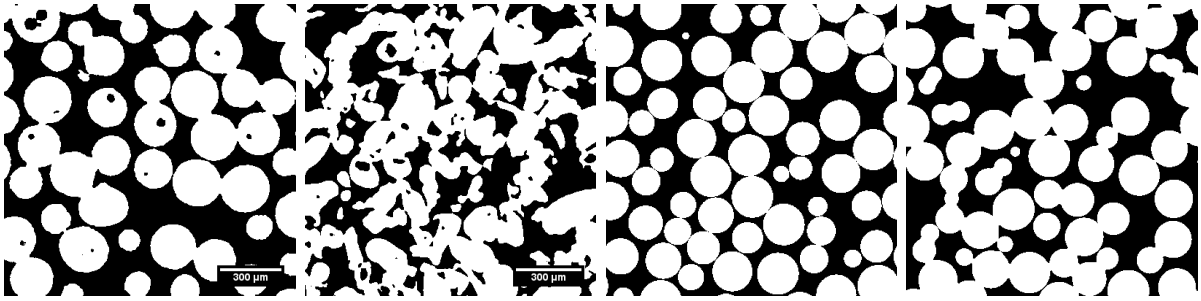

(a) SP **(b)** IP **(c)** Packed bed **(d)** SPnum

Figure 2.1: Coupes 2D des architectures étudiées: a) SP (taille des particules 200 μm), b) IP (taille des particules 200 μm), c) Packed bed, d) SPnum, (Toutes les images ont une porosité d'environ 38%)

2.3 Caractérisation des matériaux poreux

La porosité : D'un point de vue expérimental, la porosité totale des échantillons a simplement été estimée à partir de leur masse et de leurs dimensions géométriques. Les images numériques ont également permis d'estimer la porosité des échantillons étudiés en calculant le rapport entre le nombre de voxels appartenant à la phase vide et le nombre total de voxels. Les mesures ont révélé que la porosité fermée était généralement très faible (<1%) et qu'elle était due à des pores formés lors de l'étape d'atomisation des poudres.

La surface spécifique : La surface spécifique a été uniquement mesurée de manière numérique à l'aide d'un algorithme "marching cubes". Pour minimiser l'erreur due à la voxélisation de la géométrie, il a été décidé qu'une particule devait être représentée avec au moins 40 voxels le long de son diamètre.

La taille des pores : La distribution de taille des pores a été mesurée à l'aide d'une méthode numérique d'intrusion de sphères proposée par le logiciel *Geodict*.

Volumes représentatifs : Lorsque des paramètres sont mesurés dans un volume ayant une taille finie, il est important de vérifier que les dimensions de ce volume sont suffisamment grandes pour considérer les valeurs extraites comme représentatives. En utilisant le critère de voxélisation donné dans le paragraphe sur la surface spécifique, il a été montré qu'un volume de 300^3 voxels^3 permettait d'extraire des valeurs de porosités et de surfaces spécifiques représentatives pour les familles géométriques SP et IP.

Chapter 3

Conductivité thermique effective des matériaux partiellement frittés

La conductivité thermique joue un rôle important dans le refroidissement par transpiration. Elle transporte une partie de la chaleur vers la face extérieure de la paroi permettant ainsi à l'air de refroidissement de capter l'énergie de manière efficace sur toute l'épaisseur de la paroi.

3.1 Généralités

Lorsqu'on s'intéresse aux phénomènes de conduction en milieu poreux, le flux thermique $\vec{\varphi}$ peut être lié au gradient thermique $\vec{\nabla}T$ via la loi de Fourier en faisant intervenir un coefficient de conductivité thermique effectif λ_{eff} :

$$\vec{\varphi} = -\lambda_{eff}.\vec{\nabla}T \tag{3.1}$$

Dans le cas de poudres métalliques partiellement frittées, la conduction dans la phase solide participe à la quasi-totalité de la conductivité thermique effective (phase métallique bien percolante et cous de frittages relativement larges). **La conductivité thermique effective est alors essentiellement fonction du matériau constitutif et de l'architecture du matériau poreux. La conductivité effective de la phase solide $\lambda_{s,eff}$ apparaissant dans l'équation 1.1 peut être identifiée à λ_{eff}.** On introduira la conductivité thermique effective λ^*:

$$\boxed{\lambda^* = \frac{\lambda_{eff}}{\lambda_{s,bulk}}} \tag{3.2}$$

où $\lambda_{s,bulk}$ représente la conductivité du matériau dense.

3.2 Modèles de conductivité thermique effective

Plusieurs modèles théoriques de conductivité thermique effective sont présentés dans la littérature. Les plus connus considèrent un matériau poreux comme un matériau composite

et sont présentés dans le tableau 3.1 dans le cas limite où la conduction de la phase poreuse est négligée. Comme ces modèles ne tiennent pas spécialement compte de l'architecture particulière des matériaux partiellement frittés, d'autres travaux ont préféré considérer des modèles empiriques. Plusieurs de ces modèles sont introduits dans le tableau 3.1. Toutes ces lois sont comparées dans la figure 3.1 et tendent à ne prédire la conductivité thermique effective d'un matériau métallique partiellement fritté qu'à l'aide de la porosité. Au cours de cette thèse, des mesures expérimentales ont été effectuées afin de vérifier si une de ces lois était adaptée à la prédiction de la conductivité thermique des matériaux partiellement frittés.

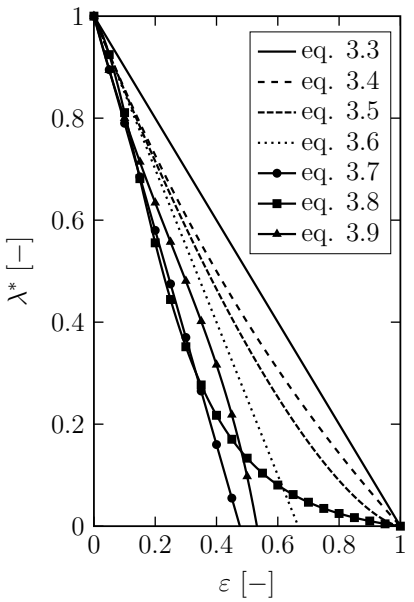

Figure 3.1: Comparaison des modèles théoriques et empiriques de conductivité thermique effective.

	Models	λ^*	
Modèles théoriques	Wiener (1912) Limite haute	$1-\varepsilon$	(3.3)
	Maxwell (1873) Limite haute	$1-\frac{3\varepsilon}{2+\varepsilon}$	(3.4)
	Bruggeman (1935) assymétrique	$(1-\varepsilon)^{\frac{3}{2}}$	(3.5)
	Bruggeman (1935) symétrique	$1-\frac{3}{2}\varepsilon$	(3.6)
Modèles empiriques	Grootenhuis et al. (1952)	$1-2.1\varepsilon$	(3.7)
	Aivazov and Domashnev (1968)	$\frac{1-\varepsilon}{1+n\varepsilon^2}$	(3.8)
	Agapiou and DeVries (1989)	$\frac{1-1.88\varepsilon}{1+0.38\varepsilon+2.3\varepsilon^2}$	(3.9)

Table 3.1: Modèles théoriques et empiriques de conductivité thermique effective.

3.3 Détermination expérimentale de la conductivité thermique effective.

La diffusivité thermique d'échantillons partiellement frittés a été mesurée à l'aide de la méthode flash à l'ONERA Châtillon. Différents échantillons composés de poudres sphériques de bronze (SP) et de poudres irrégulières d'acier inoxydable (IP) partiellement frittées ont été étudiés. Après avoir mesuré la porosité des différents échantillons, la conductivité thermique effective a été calculée à partir de la relation suivante :

$$\lambda_{eff} = a(1-\varepsilon)\rho_{s,bulk}c_p \tag{3.10}$$

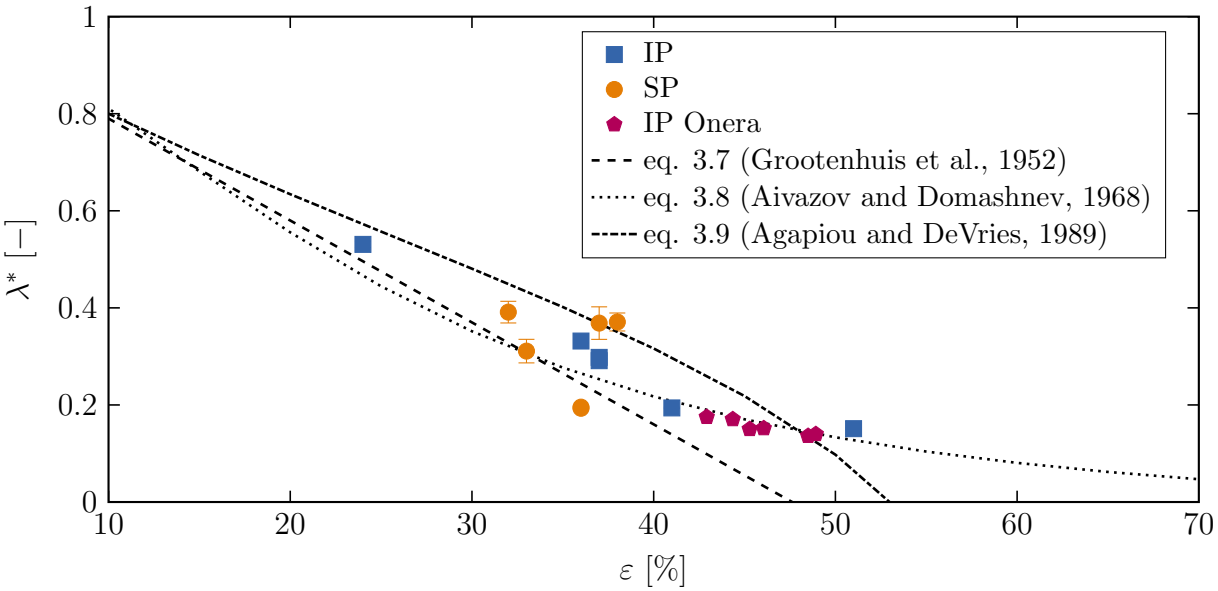

Figure 3.2: Conductivités thermiques relatives d'échantillons SP et IP mesurées à l'aide de la méthode flash. Les données sont comparées aux lois empiriques de la littérature.

où a, $\rho_{s,bulk}$ et c_p sont la diffusivité thermique, la densité et la capacité calorifique du matériau dense. L'étude des thermogrammes a tout d'abord montré que les mesures effectuées sur les matériaux IP étaient de bonnes qualités. Les mesures réalisées sur les matériaux composés de sphères de bronze ont conduit à des thermogrammes très bruités. Ce phénomène est certainement dû à la pénétration de l'impulsion lumineuse dans le matériau. Ce phénomène est d'autant plus important que la taille des particules est grande.

La figure 3.2 montre que les mesures effectuées sur les matériaux IP sont en très bon accord avec la loi empirique de Aivazov and Domashnev (1968). Malgré la divergence des mesures faites sur les matériaux SP, les résultats restent tout de même relativement proches des lois empiriques. Les lois théoriques surestiment la conductivité relative des matériaux et ne sont pas adaptées au problème. Des mesures additionnelles ont été réalisées sur des échantillons IP en faisant varier la température du matériau. Il en a été conclu que **la conductivité relative d'un matériau métallique partiellement fritté variait peu avec la température**. Afin d'obtenir des résultats plus concluants pour les matériaux frittés faits à partir de particules sphériques, une autre approche expérimentale basée sur la mesure de la conductivité électrique a été adoptée.

3.4 Détermination expérimentale de la conductivité thermique effective

Dans les matériaux métalliques, la conductivité thermique est essentiellement due à la participation de la conduction électronique. Grootenhuis et al. (1952), Aivazov and Domashnev (1968) et Koh et al. (1973) ont montré que la conductivité thermique relative λ^* était sensiblement égale à la conductivité électrique relative σ^*_{el}. Des mesures électriques ont été réalisées sur des barreaux de matériaux poreux (SP et IP) à température ambiante via la méthode quatre points. La figure 3.3 montre que la loi de Aivazov and Domashnev (1968) permet de prédire la conductivité électrique relative uniquement à l'aide de la porosité.

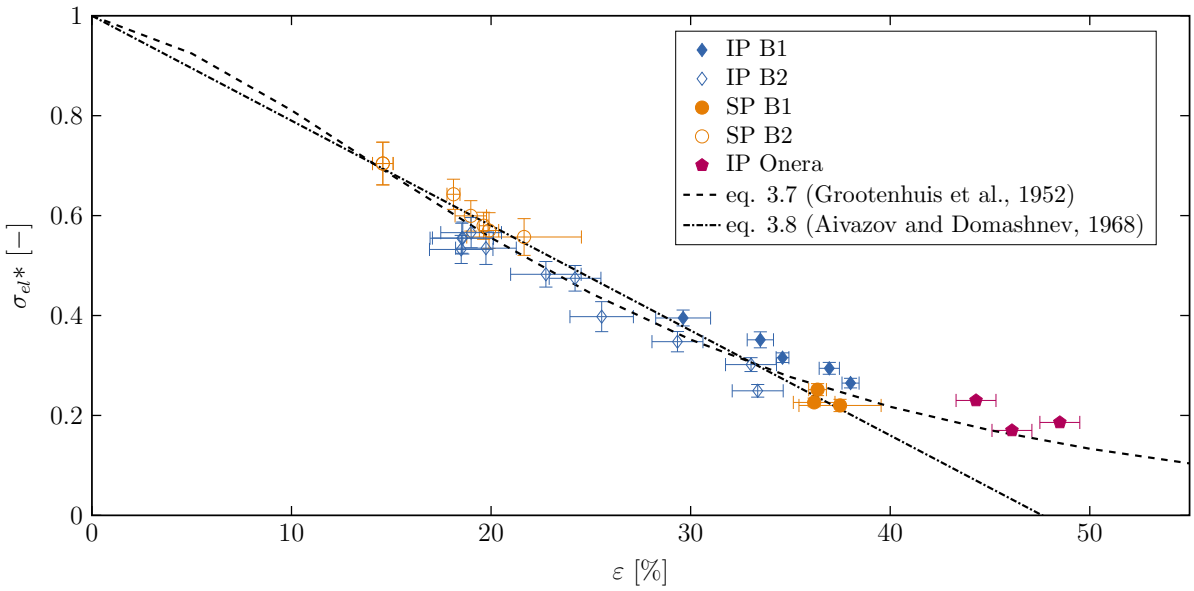

Figure 3.3: Conductivités électriques relatives d'échantillons SP et IP mesurées à l'aide de la méthode quatre pointes. Les données sont comparées aux lois empiriques de la littérature.

.

3.5 Résumé

La conductivité relative λ^* de matériaux métalliques partiellement frittés est indépendante de la température et peut être prédite à l'aide de la loi de Aivazov and Domashnev (1968) ne faisant intervenir que la porosité. La conductivité thermique effective du matériau $\lambda_{s,eff}$ à la température souhaitée T_s est déduite de λ^* à l'aide de la conductivité du matériau dense à la température T_s.

Chapter 4

Perméabilité des matériaux partiellement frittés

La perméabilité représente la faculté qu'un matériau poreux a à laisser un fluide s'écouler à travers lui. Elle joue un grand rôle dans le refroidissement par transpiration car elle détermine le débit d'air qui va traverser la paroi.

4.1 Ecoulement à travers un matériau poreux

Pour décrire un écoulement au sein d'un matériau poreux, il est largement accepté dans la litterature de lier le gradient de pression ∇p à la vitesse de filtration de l'écoulement v_s, via la loi de Darcy-Forchheimer :

$$-\frac{\Delta p}{L} = \frac{\eta}{K} v_s + \beta \rho v_s^2 \tag{4.1}$$

où ρ_f et η sont respectivement la masse volumique du fluide et sa viscosité dynamique. **Les deux coefficients K et β, appelés respectivement le coefficient de perméabilité et le coefficient de Forchheimer, sont uniquement fonctions de l'architecture de la phase poreuse**.

4.2 Modèles pour prédire les coefficients K et β

La loi d'Ergun (1952), qui utilise les travaux successifs de Kozeny (1927), Carman (1937) et Burke-Plummer, est généralement utilisée pour prédire le comportement macroscopique d'un écoulement dans un lit de sphères. Nous pouvons citer la forme suivante de la loi :

$$\boxed{\frac{\Delta p}{L} = h_k \frac{A_{sp}^2}{\varepsilon^3} \eta v_s + h_b \frac{A_{sp}}{\varepsilon^3} \rho_f v_s^2} \tag{4.2}$$

qui prédit la valeur des coefficients K et β à partir de la porosité ε et de la surface spécifique A_{sp} du lit de sphères. L'équation fait également intervenir la constante de Kozeny h_k et celle de Burke-Plummer h_b, généralement fixées à 5 et 0.3 pour des empilements de sphères. La simplicité de cette équation a encouragé certains auteurs à l'adapter à des géométries

plus complexes (Macdonald et al., 1979; Meyer and Smith, 1985; Papathanasiou et al., 2001; Nemec and Levec, 2005). **La question est alors de savoir si une équation semblable à celle d'Ergun peut être appliquée dans le cas d'architectures partiellement frittées ou si de nouveaux paramètres géométriques doivent être introduits pour prédire convenablement les coefficients K et β.**

Pour répondre à ces questions, des écoulements ont été simulés dans les architectures poreuses digitalisées afin d'estimer les coefficients K et β de ces architectures.

4.3 Simulation des écoulements avec *Geodict*

Les simulations d'écoulements ont été réalisées directement sur les images voxelisées d'architectures poreuses à l'aide du module *FlowDict* de *Geodict* utilisant une méthode *FFT-SIMPLE*. La vitesse de filtration est calculée pour différents gradients de pression afin d'obtenir un profil vitesse/gradient de pression. Les coefficients K et β sont ensuite déduits de ce profil à l'aide de l'équation 4.1.

L'étude a montré que des calculs réalisés sur des volumes composés de 400^3 voxels, en utilisant la règle de voxélisation donnée dans la sous-partie 2.3, donnaient des résultats représentatifs. Les propriétés de perméabilité des échantillons étaient relativement isotropiques. En calculant les coefficients dans les trois directions de l'espace, des coefficients moyens peuvent alors être obtenus.

La précision des calculs numériques a été montrée en comparant quelques résultats avec des résultats expérimentaux fournis par Sintertech (figure 4.1).

4.4 Analyse des données

Les coefficients K et β calculés ont été confrontés aux données géométriques des différents matériaux. Les figures 4.2 et 4.3 présentent l'ensemble des points (K, ε^3/A_{sp}^2) et (β, A_{sp}/ε^3) pour chacune des architectures étudiées.

L'analyse montre que les coefficients K et β croissent en effet avec les rapports géométriques ε^3/A_{sp}^2 et A_{sp}/ε^3 présents dans l'équation d'Ergun. Pour autant, les relations linéaires entre les différents paramètres de l'équation d'Ergun ne semblent pas être adaptées pour des matériaux partiellement frittés. Une étude plus approfondie de l'évolution des coefficients h_k et h_b a donc été menée:

$$\bar{h}_k = \frac{\varepsilon^3}{A_{sp}^2 \bar{K}} \;\&\; \bar{h}_b = \frac{\varepsilon^3}{A_{sp}} \bar{\beta} \tag{4.3}$$

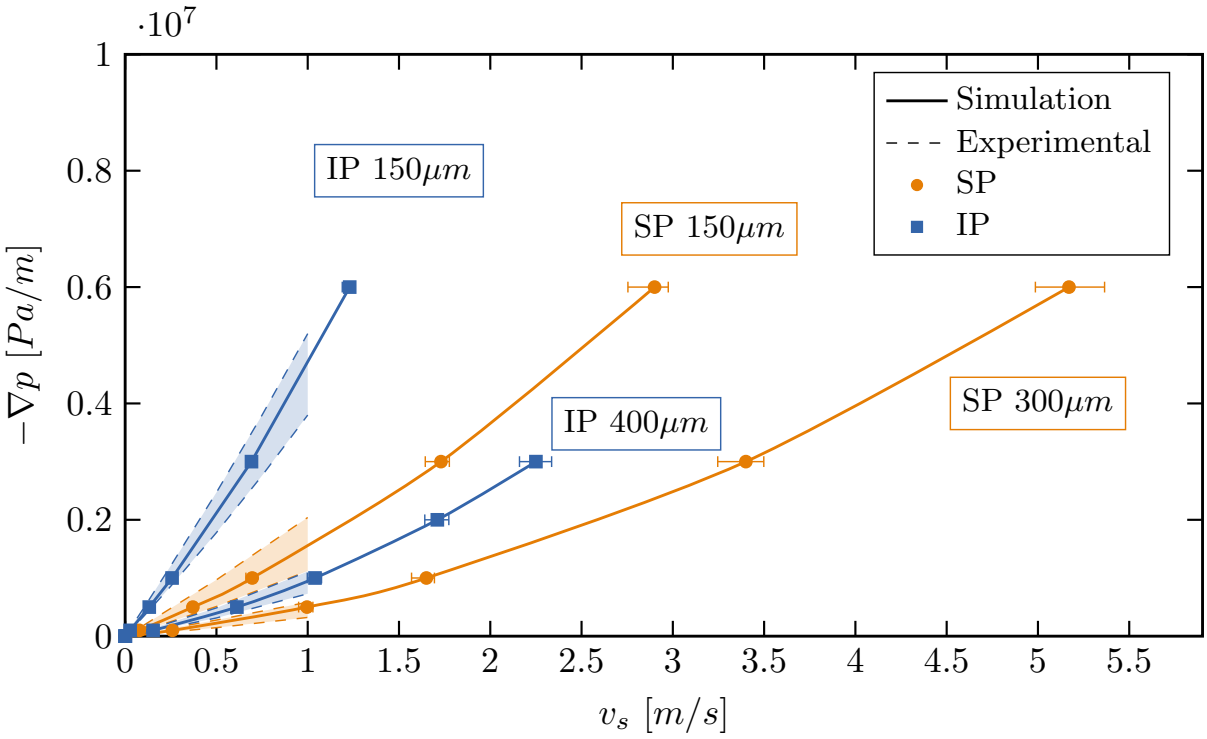

Figure 4.1: Comparaison des profils numériques vitesse/gradient de pression d'architectures SP (d_p = 150 et 300 μm) et IP (d_p = 150 et 400 μm) avec les données expérimentales de *Sintertech*.

D'après les travaux de Kozeny, le coefficient h_k d'un lit de sphère est lié à sa tortuosité hydraulique, qui est un paramètre difficilement mesurable. Avec le développement de la tomographie par rayons X, certaines études ont tenté d'estimer une tortuosité géométrique basée sur le chemin le plus court reliant les deux côtés opposés d'un matériau (Lindquist et al., 1996; Gommes et al., 2009; Sun et al., 2011). Cependant cette définition n'est pas équivalente à la tortuosité hydraulique puisqu'elle ne tient pas compte de la taille des canaux. D'autres auteurs ont tenté de mesurer une tortuosité hydraulique en utilisant la longueur moyenne des lignes de courant calculée par la simulation numérique (Koponen et al., 1996; Matyka et al., 2008; Ghassemi and Pak, 2011; Duda et al., 2011). Toutefois, aucun auteur n'a tenté de relier ces tortuosités au coefficient h_k. De plus, cette méthode est lourde et ne permet pas de prédire le coefficient h_k à partir de données géométriques.

Concernant le coefficient h_b, peu de tentatives de corrélations ont été trouvées dans la littérature.

Les coefficient $\bar{h}_k$ et $\bar{h}_b$ d'architectures partiellement frittées numériques (SPnum) ont également été étudiés grâce au procédé de génération expliqué dans le chapitre 2. Des corps à vert numériques ayant des porosités variant de 38.5 à 51% sont tout d'abord créés. Un

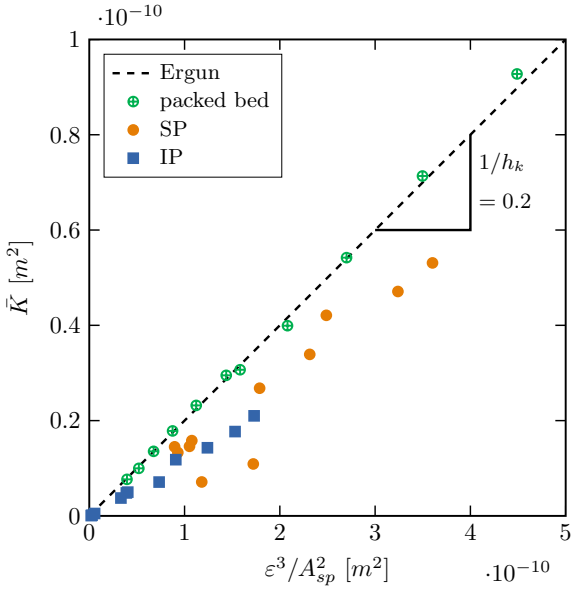

Figure 4.2: Coefficients de perméabilité $\bar{K}$ calculés numériquement en fonction du ratio ε^3/A_{sp}^2.

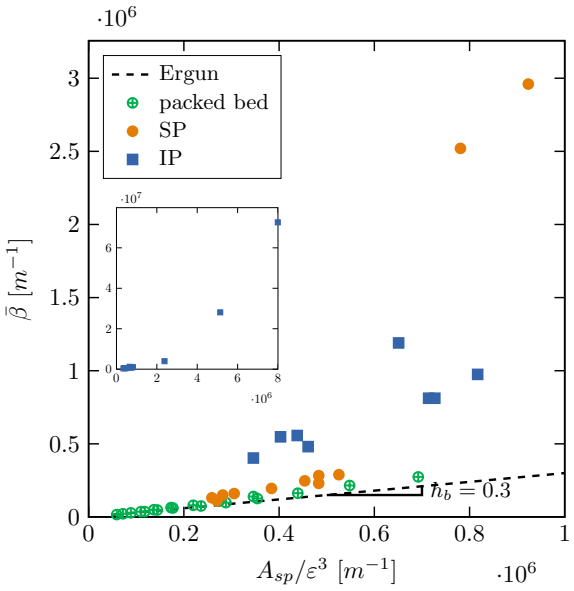

Figure 4.3: Coefficients de Forchheimer $\bar{beta}$ calculés numériquement en fonction du ratio A_{sp}/ε^3.

frittage "numérique" vient ensuite réduire leur porosité de 6% et les géométries voxélisées sont générées avec leurs cous de frittage. Les figures 4.4 et 4.5 donnent l'évolution des coefficients $\bar{h}_k$ et $\bar{h}_b$ en fonction de la porosité. On remarque que :

- $\bar{h}_k(IP) > \bar{h}_k(SP)$ et $\bar{h}_b(IP) > \bar{h}_b(SP)$;
- les coefficients s'éloignent des valeurs théoriques $h_k = 5$ et $h_b = 0.3$ d'un empilement de sphère lorsque la porosité décroit ;
- $\bar{h}_k(SPnum) \simeq \bar{h}_k(SP)$ et $\bar{h}_b(SPnum) \simeq \bar{h}_b(SP)$.

Les relations suivantes ont été proposées pour prédire l'évolution des coefficients :

geo	$\bar{h}_k$		$\bar{h}_b$	
SP	$5.45 + 0.8\dfrac{0.45-\varepsilon}{\varepsilon^{2.6}}$	(4.4)	$0.35 + 0.034\dfrac{(0.45-\varepsilon)}{\varepsilon^{3.8}}$	(4.5)
IP	$6.5 + 1.4\dfrac{0.45-\varepsilon}{\varepsilon^{2.6}}$	(4.6)	$0.8 + 0.073\dfrac{(0.45-\varepsilon)}{\varepsilon^{3.8}}$	(4.7)

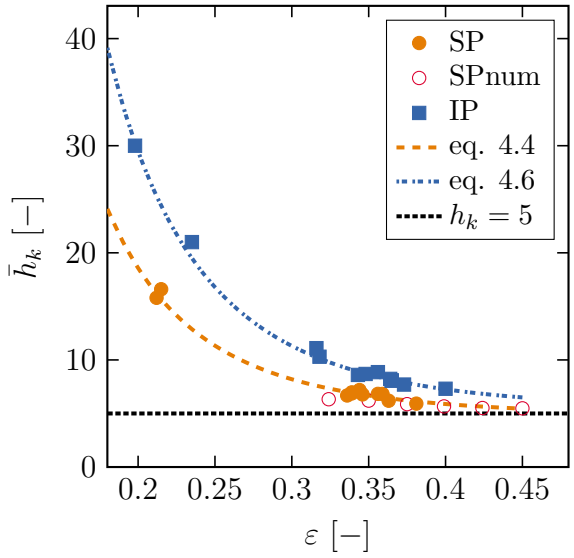

Figure 4.4: Evolution du coefficient h_k des différentes architectures (SP, SPnum and IP) avec la porosité.

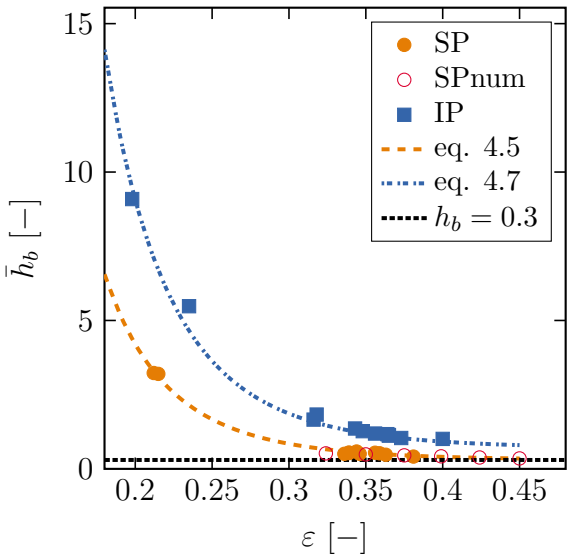

Figure 4.5: Evolution du coefficient h_b des différentes architectures (SP, SPnum and IP) avec la porosité.

4.5 Résumé

Les coefficients de perméabilité et de Forchheimer des architectures partiellement frittées peuvent être calculés avec **une relation similaire à celle d'Ergun**. Cependant, les coefficients $\mathbf{h_k}$ **et** $\mathbf{h_b}$ **sont fonctions de la famille géométrique (SP ou IP) et de la porosité**.

Chapter 5

Le coefficient de transfert volumique des matériaux partiellement frittés

Les échanges de chaleur par convection entre la phase solide et le fluide réfrigérant sont au cœur du concept de refroidissement par transpiration. Grâce à la grande surface spécifique des matériaux poreux, une grande quantité de chaleur pourrait être échangée dans de petits volumes.

5.1 Généralités

Quel que soit le régime d'écoulement, le flux échangé φ par convection au travers d'une surface S est généralement modélisé par:

$$\varphi = hS\Delta T \tag{5.1}$$

où h $[W/(m^2.K)]$ et ΔT représentent respectivement le coefficient de transfert convectif et la différence de température entre le fluide et la paroi solide. La forme de cette expression est simple mais le coefficient de transfert est généralement difficile à déterminer car celui-ci est directement lié au profil de l'écoulement. Il est généralement calculé à partir de corrélations expérimentales du type :

$$Nu = f(Re,Pr) \tag{5.2}$$

où $Nu = hl/\lambda_f$, $Re = \rho_f lv/\eta$ et $Pr = c_p\eta/\lambda_f$ représentent respectivement le nombre de Nusselt, le nombre de Reynolds et le nombre de Prandtl. l, v, λ_f, ρ_f, η et c_p sont respectivement la longueur caractéristique de l'écoulement, sa vitesse, la conductivité thermique du fluide, sa masse volumique, sa viscosité dynamique et sa capacité calorifique.

Le modèle de non-équilibre thermique locale (NETL) (section 1.2) fait apparaitre un terme source q représentant les échanges de chaleurs convectifs internes :

$$q = h_v(T_s - T_f) \tag{5.3}$$

Ce terme source fait intervenir le coefficient de transfert volumique h_v $[W/(m^3.K)]$ qui peut être exprimé en fonction d'un coefficient de transfert h et de la surface spécifique du

matériau A_{sp}.

$$h_v = hA_{sp} \tag{5.4}$$

La température de la phase solide qui apparait dans le modèle NETL est une température moyenne et non la température à l'interface de la phase solide. Selon Dixon and Cresswell (1979), le coefficient de transfert h est alors fonction du coefficient de transfert à l'interface h_{sf} et de la conductivité de la particule λ_s :

$$\frac{1}{h} = \frac{1}{h_{sf}} + \frac{d_p/\gamma}{\lambda_s} \tag{5.5}$$

où d_p et γ sont respectivement le diamètre de la particule et un facteur géométrique (10 pour des sphères). Cependant, dans le cas de matériaux métalliques ayant des particules assez petites, la conductivité de la particule ne limite pas les échanges avec la phase fluide. Il a donc été supposé dans la suite que :

$$h_v = hA_{sp} = h_{sf}A_{sp} \tag{5.6}$$

A cause de la complexité de l'écoulement, la détermination expérimentale du coefficient de transfert dans la littérature a généralement été préférée à l'approche théorique.

5.2 Calcul du coefficient de transfert volumique par une approche numérique

Une méthode numérique a été proposée pour calculer les coefficients de transferts volumiques sur des images 3D de matériaux poreux métalliques. Le principe de la méthode est donné sur la figure 5.1. Elle consiste à résoudre la champ de température dans la phase fluide en utilisant le champ de vitesse précédemment calculé avec Géodict. Le matériau est maintenu à une température uniforme et le fluide est supposé entré dans celui-ci à une température légèrement inférieure. Un profil de température moyen 1D est ensuite extrait du champ 3D. Finalement, h_v est déduit du profil par comparaison avec un modèle de transfert de chaleur 1D.

La précision de la méthode a été évaluée sur des images d'empilements de sphères. Les résultats numériques sont proches des valeurs données par les lois empiriques de Whitaker (1972), Wakao and Kagei (1978) et Achenbach (1995) trouvées dans la littérature.

Les calculs ont finalement été réalisés sur des images numérisées de matériaux partiellement frittés. La figure 5.2 donne l'évolution du nombre de Nusselt en fonction du nombre de Reynolds (les deux nombres adimensionnels utilisent le diamètre hydraulique $d_h = 4\varepsilon/A_{sp}$ comme longueur caractéristique).

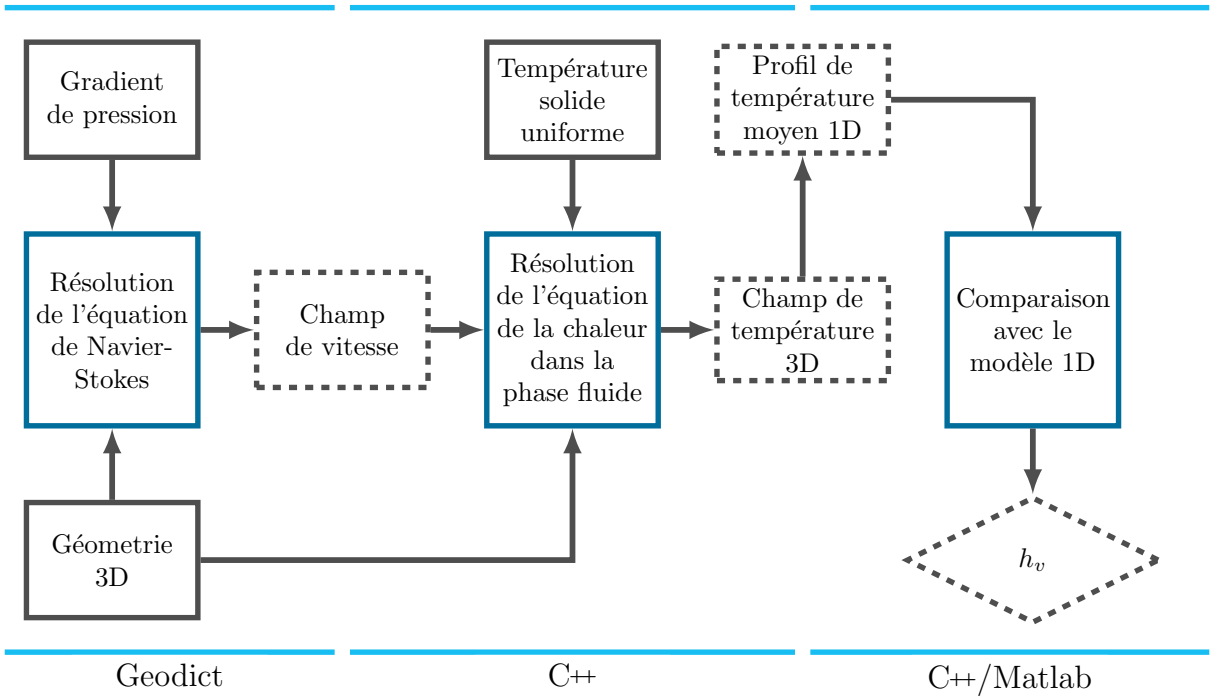

Figure 5.1: Principe de la méthode numérique permettant le calcul du coefficient de transfert volumique.

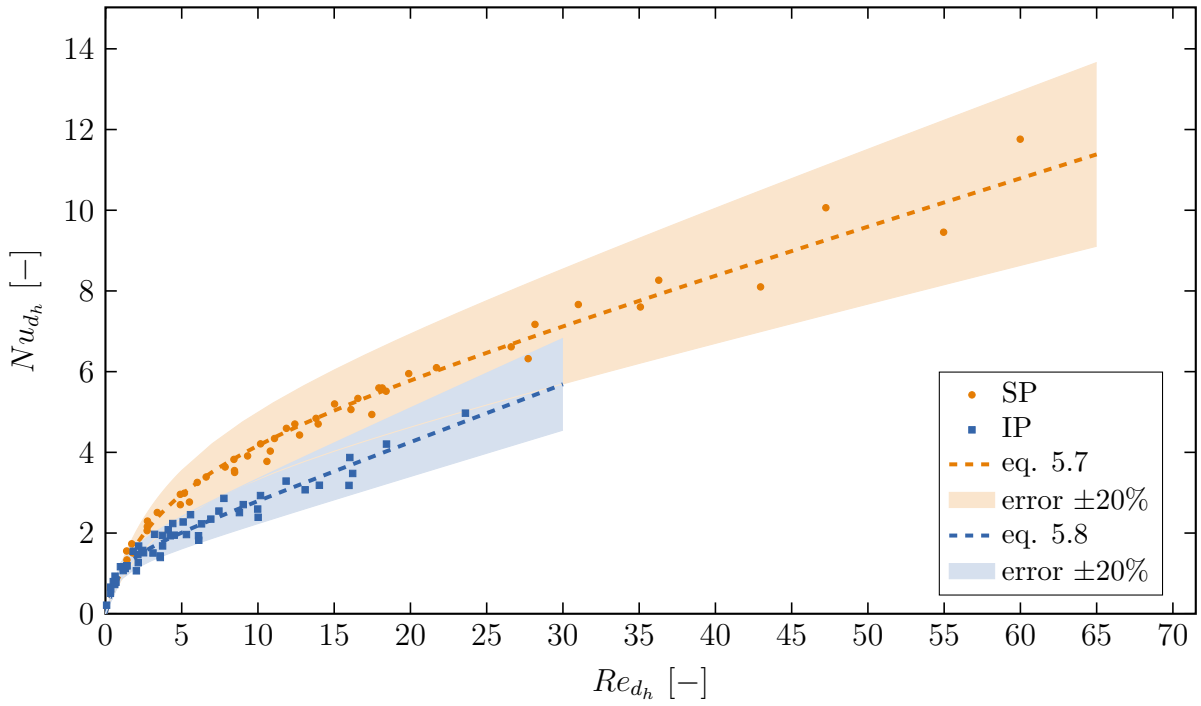

Figure 5.2: Nombre de Nusselt des poudres sphériques et irrégulières partiellement frittées en fonction du nombre de Reynolds.

Les relations suivantes sont proposées pour prédire h_v dans les matériaux partiellement frittés. Pour les poudres sphériques :

$$\boxed{Nu_{d_h} = \left(\frac{0.13Re_{d_h}^2 + 5.08Re_{d_h}}{Re_{d_h} + 3.6}\right) Pr^{1/3}} \tag{5.7}$$

Pour les poudres irrégulières :

$$\boxed{Nu_{d_h} = \left(\frac{0.16Re_{d_h}^2 + 1.73Re_{d_h}}{Re_{d_h} + 0.59}\right) Pr^{1/3}} \tag{5.8}$$

5.3 Résumé

Une **nouvelle méthode numérique** a été mise en place pour estimer les coefficients de transfert volumique au sein de matériaux métalliques partiellement frittés. Ces **coefficients de transfert** peuvent être estimés à l'aide de relations adimensionnelles fonctions de la **vitesse de l'écoulement, de la porosité, de la surface spécifique et de la famille géométrique (SP ou IP) des particules.**

Chapter 6

Optimisation de l'architecture partiellement frittée pour le refroidissement par transpiration

Comme les performances d'une architecture poreuse dépendent notamment de la manière dont l'énergie est retirée de la paroi, un modèle de transfert de chaleur est tout d'abord introduit. La méthode d'optimisation et l'analyse des résultats sont ensuite présentées.

6.1 Modélisation des transferts de chaleur lors du refroidissement par transpiration

Un modèle unidimensionnel, représenté sur la figure 6.1 et tenant compte des effets de compressibilité, a été considéré dans cette étude. Les échanges de masse et de chaleur internes à la paroi ont été modélisés à l'aide du modèle de non équilibre thermique introduit au chapitre 1. Les quatre propriétés effectives sont calculées à l'aide des expressions développées dans les précédents chapitres. La paroi est supposée être composée d'un alliage d'Hastelloy X.

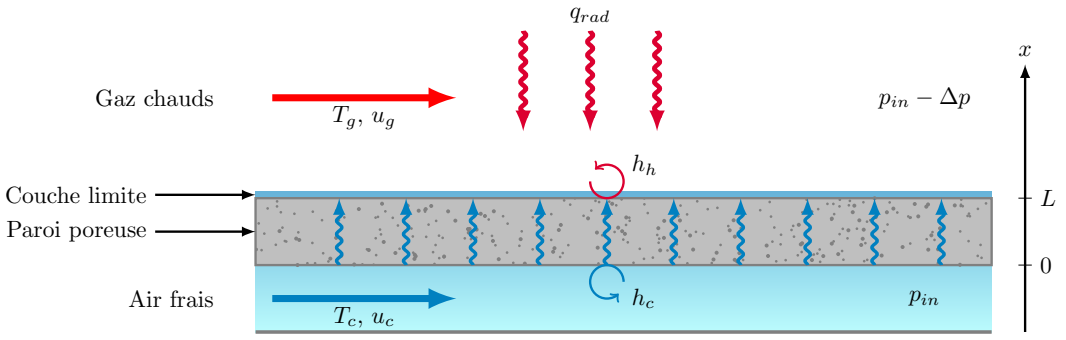

Figure 6.1: Représentation des transferts de masse et de chaleur au cours du refroidissement par transpiration.

Des conditions limites spécifiques ont été appliquées de chaque côté de la paroi. Du

côté froid, le fluide pénètre dans la paroi avec la température de sortie du compresseur $T_c = 800K$. Des échanges convectifs avec la paroi sont également pris en compte en utilisant un coefficient de transfert h_f, calculé d'après l'approche utilisée par Lefebvre and Ballal (2010) et Glass et al. (2001). Du côté chaud, des échanges radiatifs avec les gaz chauds en condition de combustion pauvre ($T_g = 1900K$) sont considérés. Ils résultent de la participation d'une radiation non-lumineuse émise par les gaz hétéropolaires et d'une radiation lumineuse émise par les suies, comme décrit par Lefebvre and Ballal (2010). Les échanges convectifs avec les gaz chauds sont modélisés à l'aide d'un coefficient de transfert h_h qui tient compte de la protection offerte par la couche limite transpirée. La réduction des transferts de chaleurs par rapport au cas de non-transpiration est fonction du taux de soufflage et de la température de fluide éjecté suivant le modèle développé par L'Ecuyer and Colladay (1972) et Colladay and Stepku (1971). Enfin, la différence de pression entre chaque côté de la paroi est estimée comme représentant 2% de la pression en sortie de la partie compresseur ($p_{in} = 30 \times 10^5\ Pa$).

Les équations sont résolues avec une méthode de volumes finis et un processus itératif est mis en place jusqu'à convergence des profils de température.

6.2 Définition de problème d'optimisation

Quatre critères de performance sont pris en considération au cours de cette optimisation de l'architecture:

- Minimisation du débit d'air de refroidissement : le but premier du refroidissement par transpiration est de réaliser une économie en air de refroidissement.

- Minimisation de la densité surfacique de la paroi : la masse est un critère important dans toute application aéronautique.

- Maximisation de la taille des pores : pour limiter les problèmes liés à l'encrassement, il est essentiel d'avoir des pores aussi larges que possible. Après une étude numérique de porosimétrie par intrusion, la dimension caractéristique des pores est prise comme le taille médiane. Celle-ci peut être calculée à partir du diamètre hydraulique de l'architecture.

- Maximisation de la température d'éjection des gaz : les faibles températures favorisent l'émission de monoxyde de carbone en bloquant la combustion.

Pour assurer l'intégrité de la paroi, tous les designs menant à une température de paroi supérieure à 1100 K sont rejetés.

Les variables utilisées lors de l'optimisation sont présentées dans le tableau 6.1.

Variable	Min	Max	step size
L $[mm]$	1	4	0.5
ε [%]	20	40	1
A_{sp} $[m^2/m^3]$	6000	50000	2000
geo		SP or IP	

Table 6.1: Les quatre variables et leur domaine de variation.

Comme le temps de simulation est relativement court, les performances de tous les designs ont été évaluées. **713 designs optimaux ont alors été sélectionnés**.

6.3 Analyse des designs optimaux

L'analyse des designs optimaux a été menée à l'aide des coordonnées parallèles, une méthode de visualisation multidimensionnelle interactive. L'application de contraintes supplémentaires, permettant d'obtenir des designs potentiellement intéressants par rapport à la solution multi-perforée a encore restreint le nombre de designs optimaux. L'analyse a révélé que des architectures partiellement frittées faites de larges particules irrégulières ($> 150\mu m$) étaient les plus adaptées pour le refroidissement par transpiration en condition de chambre de combustion. Afin d'obtenir un débit d'air de refroidissement suffisamment faible, les faibles porosités (20-22%) semblent être les plus adaptées. Il a également été montré que l'utilisation d'un système de filtration est nécessaire pour éviter un encrassement trop rapide des solutions retenues. C'est alors le niveau de filtration qui impose le débit minimum atteignable. Enfin, il s'est avéré que les solutions retenues pour l'application avaient une masse supérieure à la paroi multiperforée actuelle.

Conclusions

6.4 But et stratégie

Le but de la thèse était de développer une méthodologie permettant l'optimisation de l'architecture de matériaux partiellement frittés pour une application de refroidissement par transpiration dans des chambres de combustion aéronautiques. Deux types de matériaux ont été étudiés : des matériaux faits à partir de poudres sphériques et des matériaux faits à partir de poudres irrégulières. L'étude a alors été divisée en deux parties :

- La première partie de ce travail s'est focalisée sur la détermination des relations liant l'architecture des matériaux poreux à leurs propriétés effectives. La conductivité thermique effective a été étudiée expérimentalement. Les propriétés de perméabilités et le coefficient de transfert volumique ont été étudiés numériquement. Pour cela, des échantillons ont été numérisés grâce à la tomographie par rayons X et des matériaux faits de particules sphériques ont été générés numériquement.
- La seconde partie s'est concentrée sur l'optimisation "multi-objectifs" de l'architecture. Un modèle de transfert de masse et de chaleur a été créé afin d'estimer les performances de plusieurs designs.

6.5 Principaux résultats

Conductivité thermique effective :

- La conductivité thermique effective a été analysée expérimentalement grâce à la méthode flash et la méthode quatre-points.
- Des mesures menées à différentes températures ont montré que la conductivité relative pouvait être considérée comme étant indépendante de la température jusqu'à 1300 K.
- La porosité suffit pour prédire la conductivité relative des matériaux étudiés.

Perméabilité :

- La perméabilité de matériaux poreux peut être déterminée avec précision à l'aide du calcul sur image.
- Les pertes de charges au sein de matériaux partiellement frittés peuvent être prédites à l'aide d'une équation similaire à l'équation d'Ergun faisant intervenir la porosité et la surface spécifique.
- Cependant, les coefficients h_k et h_b de l'équation d'Ergun doivent à présent être fonctions de la porosité et de la forme de la poudre.

Coefficient de transfert volumique :

- Une méthode numérique a été suggérée pour prédire le coefficient de transfert volumique dans des matériaux partiellement frittés. La précision de la méthode a été démontrée par comparaison avec des lois empiriques trouvées dans la littérature.
- Les simulations réalisées sur les images de matériaux partiellement frittés ont permis le développement de nouvelles lois adimensionnelles permettant la prédiction du coefficient de tranfert.

Optimisation "multi-objectifs" :

- Les besoins de réduire les quantités nécessaires en air de refroidissement, de minimiser la masse de la paroi, d'éviter un encrassement trop rapide et de limiter les émissions en monoxyde de carbone tout en assurant une température de paroi inférieure à une température limite, ont été pris en considération dans une optimisation multi-objectifs.
- Les performances thermiques de différents designs de parois poreuses partiellement frittées ont été évaluées à l'aide d'un modèle de transfert de chaleur de non équilibre thermique local. Les propriétés effectives sont estimées à l'aide des relations développées lors des précédentes parties.
- L'étude des designs optimaux a mis en évidence la nécessité d'avoir recours à un système de filtration en amont pour utiliser des solutions transpirantes intéressantes. Les matériaux faits de larges particules irrégulières ($> 150\mu m$) semblent être les plus adaptés. De plus des porosités de l'ordre de 20-22% doivent être visées. Les designs mis en avant ont néanmoins une masse supérieure à la solution multi-perforée.

Part II

English thesis manuscript

Preface

This thesis is linked to a project called *Projet de Recherche Fédérateur MOTRICE*[1] developed at *ONERA, the French Aerospace Lab.* This project aims to assess the viability of the concept of **transpiration cooling**, a potential new liner cooling technology for aero-engine combustion chambers. The *PRF MOTRICE* plans to assess the quality and the risks associated to the choice of several transpirating materials with the help of experimental tests as well as by the development and validation of numerical behavior models. Several scientific aspects are covered by the project. They include the elaboration of new transpirating materials, their aero-thermal and aero-acoustic characterization and modeling as well as the study of their mechanical resistance in realistic situations.

This thesis was carried out at the laboratory *SIMaP* (Sciences et Ingénierie des Matériaux et des Procédés). It was funded by the Labex CEMAM (Center of Excellence of Mulitfunctional Architectured Materials) thanks to the creation, one year later, of a twin thesis co-funded by *ONERA* and the *DGA*[2]. This twin thesis is undertaken by Océane Lambert and focused on the elaboration of new porous architectures. The present PhD thesis is complementary to the twin one since it first aims to understand the existing relationships between the porous architecture and the thermal performance of a porous material. In a second step, an optimization of the architecture is carried out in order to develop simple design rules for the transpiration cooling application.

After a brief **general introduction** of the current aeronautic context which justifies the need for the development of a new combustion chamber cooling technology, the manuscript is structured as followed:

Chapter 1 - Transpiration cooling: This chapter gives some basic knowledge about combustion chamber cooling and introduces the theoretical benefits of transpiration cooling. A literature review emphasizes both experimental and theoretical works related to this technology. The way to model transpiration cooling is then introduced. It highlights the main material properties impacting the performance of a design (permeability, effective thermal conductivity of the solid phase and volumetric heat transfer coefficient). After justifying the particular interest in partially-sintered materials, the methodology of the present study is presented.

[1] Mise en Oeuvre de Traitements Refroidis Innovants pour Chambres de combustion Endurantes (Implementation of innovative cooling treatments for resistant combustion chambers)

[2] Direction Générale de l'armement/French defense procurement agency

Chapter 2 - Partially-sintered materials and geometrical characterization: This chapter aims to give more details about the partially-sintered materials investigated in the present work. The manufacturing process of the materials made of spherical or irregular powders and their digitization by X-ray tomography are first detailed. The numerical generation of partially-sintered spherical powders is then explained. To close the chapter, the numerical tools, which enable the three-dimensional characterization of the porous architecture, are introduced.

Chapter 3 - Effective thermal conductivity of partially-sintered materials: This chapter deals with the relationships between the architecture of partially-sintered metallic materials and their effective solid thermal conductivity. Experimental measurements carried out with the flash method are analyzed and compared with literature results. By using the physical similarity between thermal and electrical conduction in metals, additional measurements obtained with the four-point probes method complete the discussion.

Chapter 4 - Permeability of partially-sintered materials: This chapter is focused on the prediction of the permeability of partially-sintered materials. After a review of flow in porous materials, the numerical method which permits the flow field to be solved for three-dimensional images is introduced. The accuracy of the simulations is assessed by comparing numerical results with literature and experimental data. All the numerical results obtained for partially-sintered materials are then analyzed. New behavior laws based on the material geometrical characteristics are finally suggested.

Chapter 5 - Volumetric heat transfer coefficients of partially-sintered materials: In this chapter, the volumetric heat transfer coefficient of partially-sintered metallic materials is studied. After a brief literature review related to the volumetric heat transfer coefficient, a numerical method is suggested to predict the desired coefficient from three-dimensional images of porous metallic materials. The accuracy of the method is tested by comparing the simulation performed on packed beds of spherical particles with literature data. The results obtained on digitized images of partially-sintered materials are then analyzed and discussed. They permitted new behavior laws, predicting volumetric heat transfer coefficients in this kind of material, to be established .

Chapter 6 - Optimization of the partially-sintered architecture for transpiration cooling: This chapter deals with the optimization of the partially-sintered architecture for a transpiration cooling application. The simplified heat transfer model used to assess the performance of a design is first described. The objectives and the constraints of the multi-objective optimization are then explained. The chapter finally ends with an analysis of optimal architectures which leads to the selection of some interesting designs.

General Introduction

Thanks to their high efficiency in producing thrust, most commercial aircraft engines are gas turbines. The gas turbine can be divided into five main parts (figure 2):

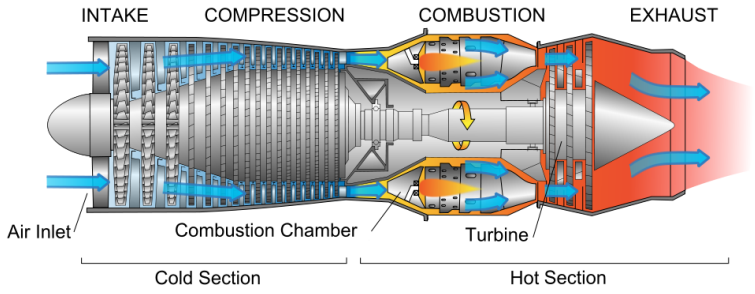

Figure 2: Scheme of a gas turbine jet engine (Engine, 2016).

- the inlet delivers the air at an acceptable speed for the compressor;
- the compressor increases the pressure of the air through different stages;
- the combustor adds fuel to the air and then burns the mixture;
- the turbine recovers a part of the energy of the hot gases during their expansion to drive the compressor;
- the exhaust transforms the surplus of energy into a high velocity jet in the nozzle, thus generating the thrust.

The combustion takes place in the flame tube. This last aircraft component is highlighted in red in the figure 3 showing the current aspect of a civil aircraft combustion chamber. This process generates extremely high temperature gases ($> 2000\ K$) which threaten the integrity of the combustor liner. Since the maximum operating temperature of the nickel- or cobalt- superalloys (Nimonic 75, Hastelloy X and HS188) which composed current combustors should not go over 1100 K, a cooling technology is required to remove heat from the liner. The combustion chamber cooling consists in using a part of the compressed air delivered by the compressor (at a temperature of $600 - 900\ K$ depending on the engine regime) to create a by-pass flow around the flame tube before making it pass through the wall liner. As it is shown in figure 4, about 40% of the air entering the combustion chamber is reserved for the cooling. The rest is used for the combustion and the dilution of the hot gases. Over the years, the technology has experienced a constant development while keeping the principle of cooling unchanged. Nowadays, the environmental context forces the technology to evolve once again.

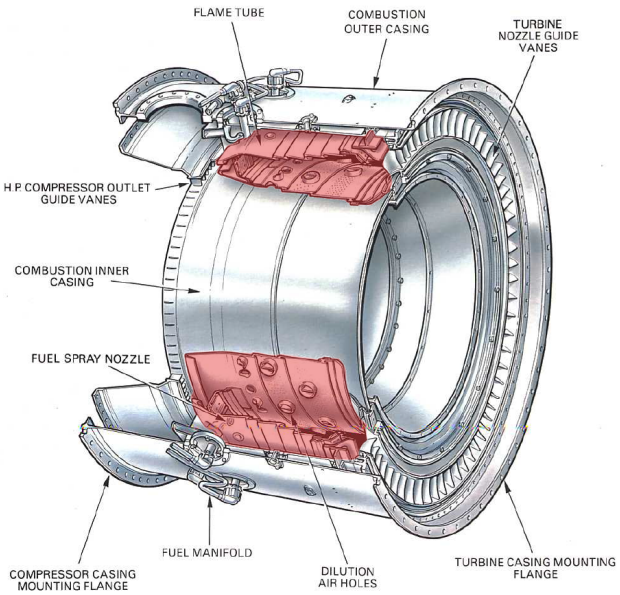

Figure 3: Annular combustion chamber of the RB211 (Rolls-Royce Plc, 1996).

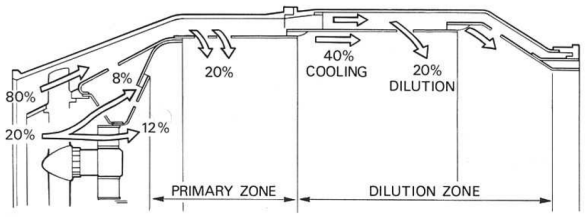

Figure 4: Air partitioning in the combustion chamber (Rolls-Royce Plc, 1996).

Indeed, due to the growth of air traffic volume, the International Civil Aviation Organization (ICAO) has adopted several resolutions to reduce the environmental impact of the civil aviation. These measures deal not only with the emission of CO_2, the main responsible for global warming, but also with NO_x and soot. The solutions suggested to reduce the polluting emissions are focused on several key areas (Direction Générale de l'Aviation civile, 2013):

- an improvement of the air traffic management;
- a better control of the engine cycle with a potential new legislation including not only the LTO cycle (Landing/Take-off) in the airport space but also the cruise regime (Angrand, 2015);
- the use of alternative fuels, with notably synthetic fuels which do not have any aromatic particles, precursors of soot;
- improvement of the aircraft design and technologies.

Since the pollutant particles are produced by the engine, and more particularly in the combustion chamber, a major part of the technological efforts to reduce emissions are turned toward this latter aircraft component. In order to properly control the pollutant emissions, the combustion chamber has to be designed to ensure an optimal combustion at every engine working point. If the emissions of CO_2 are simply the result of the combustion of hydrocarbons, a major part of the other pollutant emissions can be controlled by the flame temperature. Figure 5 shows that a narrow temperature range of 1700-1900K is acceptable to generate low CO and NO_x emissions. As the flame temperature depends on the stoichiometry of the air/fuel mixture, engine manufacturers are trying to move the combustion chamber technology toward a lean pre-mixed turbulent combustion which allows a better control of the mixture richness (v.d. Bank et al., 2006). However, the lean combustion will have for impact to increase the amount of air involved in the combustion at the expense of that used for cooling. Despite the fact that the flame temperature will decrease, **the important reduction in the amount of available cooling air forces the development of a more efficient air cooling technology**. Transpiration cooling is a high potential candidate and will be the main topic of this PhD thesis. Further explanation about this cooling technology are introduced in chapter 1.

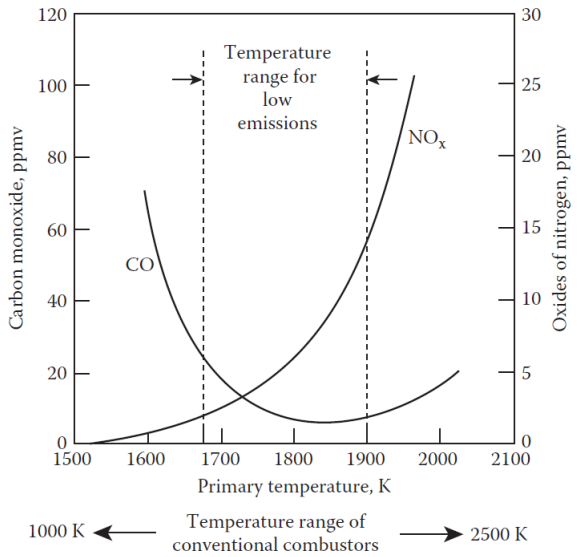

Figure 5: Emission characteristics of gas turbine (Lefebvre and Ballal, 2010).

Chapter 1

Transpiration cooling

Contents

1.1 Evolution of the combustion chamber cooling

This section aims to introduce the different technologies which were used over the years to protect and cool the combustion liner. It is shown how their evolution leads to the concept of transpiration cooling.

1.1.1 Film cooling

The simplest way to cool the liner is the film cooling. This name is given to all the cooling techniques which inject air through annular slots (highlighted with red marks in

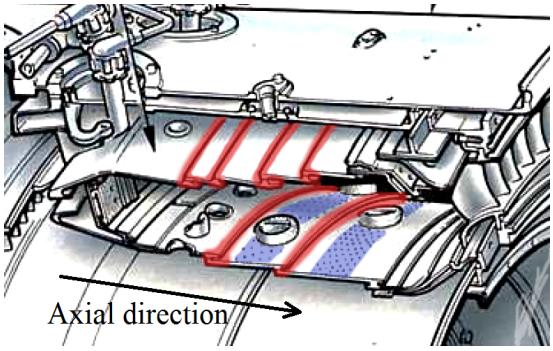

Figure 1.1: Zoom on a flame tube. The annular slots for film cooling are highlighted with red marks, the multi-perforated walls with blue ones. (Rolls-Royce Plc, 1996)

figure 1.1) in the axial direction and along the inner combustor wall to form a protective boundary layer. As the film is gradually destroyed by turbulent mixing, slots are regularly placed along the axial direction. Corrugated strips, machined rings and splash-cooling rings are examples of film-cooling devices (figure 1.2). Such designs lead to light liners with sufficient mechanical robustness to withstand high pressure and thermal constraints. However, the non-uniform temperature, with cooler spots near the slots, proves that there is a waste of cooling air. Moreover, even though the film can insulate the liner, convective heat transfers between the cooling air and the wall are not high enough to remove efficiently the energy which is emitted by hot gas radiation.

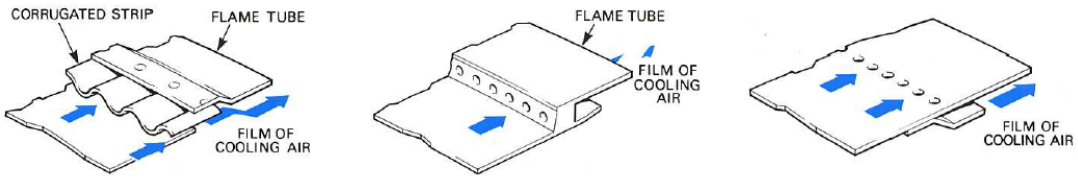

(a) Corrugated cooling strip **(b)** Machined cooling ring **(c)** Splash cooling strip

Figure 1.2: Various film cooling devices (Rolls-Royce Plc, 1996).

1.1.2 Cooling with a multi-perforated wall

Cooling with a multi-perforated wall improves convective heat transfers in the wall. The liner is perforated with thousands of holes having a diameter of about 0.5 mm (highlighted in blue in figure 1.1). The holes are generally drilled in staggered rows and inclined in the direction of the flow as shown in figures 1.3 and 1.4a. As the fluid emerges from a raw, the air jets coalesce and form a protective film which is quickly renewed with fresh fluid from the following row. Thanks to convective heat transfers in the small holes, the

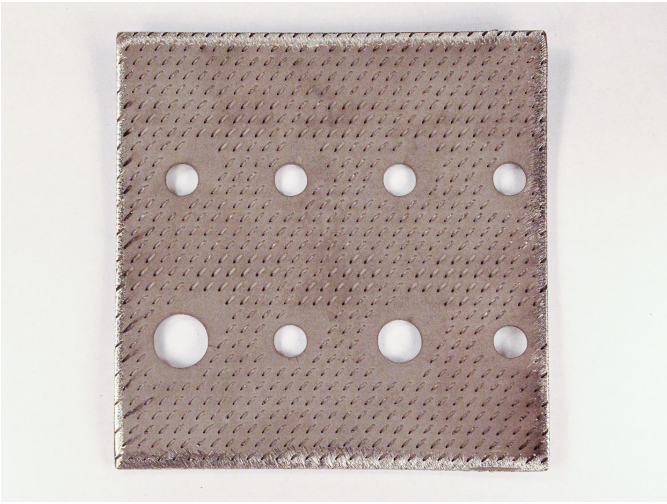

Figure 1.3: A typical multi-perforated wall (the biggest holes are dilution holes) (courtesy of *CRMA*).

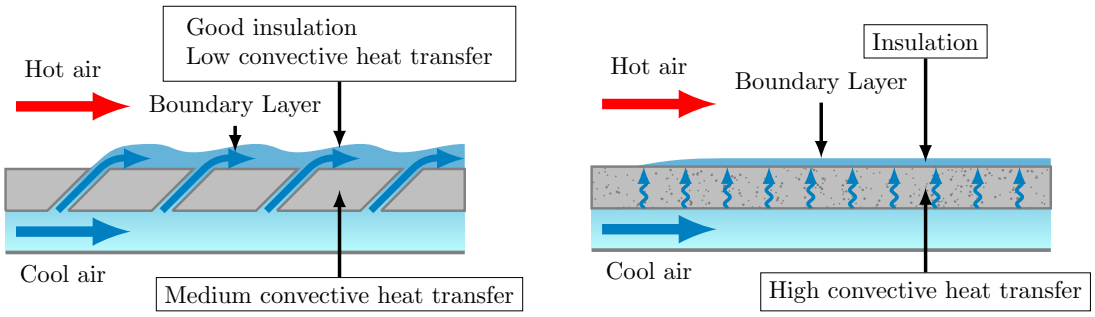

(a) Effusion cooling through a multi-perforated wall.

(b) Transpiration cooling through a porous wall.

Figure 1.4: Enhanced heat transfer cooling technologies.

liner can be internally cooled and the need in film cooling is reduced. Due to its ease of implementation, the low drilling costs and its acceptable efficiency, the multi-perforated wall is the most used cooling technique in current combustion chambers. However, as the maximal efficiency of this cooling is reached after some rows, film cooling is still required upstream the multi-perforated walls and near the more exposed areas.

In order to improve the liner life, a thermal barrier coating is added on the inner part of the wall by plasma spraying. The coating is composed of a metallic base coat and of one or two ceramic layers. It provides an additional thermal insulation and reduces the oxidation of the liner. An overall coating thickness of about $400 - 500\ \mu m$ can lead to a metal temperature decrease of about $40 - 70\ K$ (Lefebvre and Ballal, 2010).

1.1.3 Toward transpiration cooling

Transpiration cooling is theoretically close to the ideal cooling technique in which the entire liner is maintained at the maximum acceptable temperature. The idea is to extend the concept of the multi-perforated wall by using a porous material (figure 1.4b). Thanks to a multitude of pores uniformly distributed over the surface, the boundary layer could be regularly renewed and uniform on the entire inner surface. The high number of pores could thus limit the problem of hot spots caused by the discretization of the multi-perforated wall holes. Moreover, thanks to a very large specific surface area, the radiation heat would be removed by tremendous internal convective heat transfers. Transpiration cooling would therefore provide a more efficient and uniform internal cooling and could therefore reduce the required amount of cooling air.

1.2 Previous studies about transpiration cooling

The concept of transpiration cooling is very old since H. Oberth suggested to cool a porous surface with a liquid as early as 1929. The first experiments were carried out by Goddard in 1930 (Asere, 1986). Duwez and Wheeler (1948) were the first to experimentally prove the high cooling potential of air for gas turbine components by forcing air through copper, nickel and stainless steel porous materials exposed to combustion gases.

1.2.1 The transpirated boudary layer

The first studies related to transpiration cooling were essentially focused on the study of the transpirated boundary layer and its role in the overall cooling effectiveness. Rannie (1947) suggested an analytical model of a laminar transpirated boundary layer and correlated the porous wall temperature to the coolant mass flow. However, his theory only agreed with experiments carried out on low thermal conductivity porous materials. Eckert and Livingood (1954) analytically showed the superiority of the transpiration cooling on flat plates for Reynolds number (with respects to the length of the flat plate) ranging from 10^5 to 10^9 and for blowing ratios (ratio of the coolant mass flux to the mainstream mass flux) up to 0.012. In this analysis, it was assumed that the coolant is ejected at the same temperature as the wall. It was shown that the reduction in convective heat transfer with the hot gases could be predicted with the blowing ratio. In the early 1950s, additional theoretical works done by Rubesin (1954) and experimental ones carried out by Mickley

et al. (1953) or Moffat and Kays (1968) also investigated the relationships between hot convective heat transfers and blowing ratios.

Contrary to what Eckert and Livingood (1954) assumed, Colladay and Stepku (1971) and L'Ecuyer and Colladay (1972) explained that with a thin porous wall, the temperature of the coolant leaving the wall could be at a temperature lower than the inner wall temperature. They were the first to investigate the influence of this temperature difference on the protective boundary layer. L'Ecuyer and Colladay (1972) explained that this **thermal non-equilibrium** would increase the protection offered by the boundary layer.

1.2.2 Transpiration cooling for combustion chamber

The first experimental works focused on transpiration cooling systems for combustion chamber appeared only on the early 1970s. Bayley et al. (1973) investigated the cooling performance of a transpiration system applied to a Rolls Royce 'Dart' combustor by using commercial Rigidmesh materials (sintered woven wire porous materials). They showed that the transpired solution required less air than the traditional splash cooling strip design (figure 1.2c). The transpiration process with a Rigidmesh material was also investigated by Andrews and Asere (1984). Their study showed that internal heat transfers were responsible for the major part of the cooling effectiveness.

Two well-known applications using quasi-transpiration cooling, the *Lamilloy* solution (figure 1.5a) from Detroit Diesel Allison (General Motors Corporation)(Nealy and Reider, 1980) and the *Transply* solution (figure 1.5b) from Rolls-Royce (Wassell and Bhangu, 1980), were developed in the early 1980s.

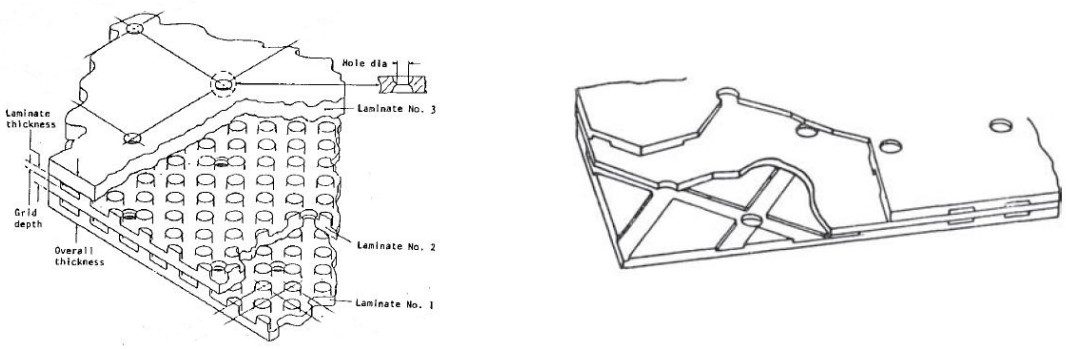

(a) Lamilloy (Nealy and Reider, 1980) **(b)** Transply (Wassell and Bhangu, 1980)

Figure 1.5: Quasi-transpiration cooling systems.

The term "quasi-transpiration" was adopted because even though the systems use many small internal passages, the hole distribution at the liner surface is similar to a

multi-perforated system. Both solutions are multi-laminated porous structures made of high-temperature alloys. The Transply combustor was especially developed for the Rolls-Royce Spey engine. A reduction in cooling air requirement of about 70%, relative to the classical film-cooled combustor, as well as a dramatic reduction of pollutant emissions were recorded (Wassell and Bhangu, 1980). The Lamilloy combustor was designed for operation at 4045 kPa and 2478 K burner outlet temperature. A reduction in cooling air of about 40% compared to the conventional cooling system was noticed (Nealy and Reider, 1980). At that time, the cost of manufacturing and the lack of mechanical strength were the main disadvantages of these solutions. The durability of a Lamilloy combustor was investigated by Essman et al. (1983) using an Allison TF41 turbofan. They showed that after a period of tests equivalent to 1000 hours of field service, thermal stress cracks and erosion had already appeared.

More recently, Bellettre et al. (2000) studied the thermal behavior of partially-sintered stainless steel materials protected by transpiration cooling. They highlighted the effects of the injection rate and of the specific surface areas. Liu et al. (2013) studied the local wall temperature and the cooling effectiveness of $32-37\%$ porous plates made by partial sintering of bronze or stainless steel particles. Even though they were aware that these alloys are not adapted for aerospace application, they wanted to investigate the impacts of the injection rate and of the solid conductivity. They showed that the cooling effectiveness rises with the increasing coolant injection rate and with the decreasing particle size.

1.2.3 Internal heat transfer

All the previous studies were mainly focused on the hot gas side boundary layer and were essentially related to the effect of the injection rate on hot side convection heat transfers. All the aspects related to heat transfers in a porous structure appeared quite late in the literature, after the works of L'Ecuyer and Colladay (1972) and Colladay and Stepku (1971). However, most of them admitted that the solid phase and the fluid could have different local temperatures. The first internal heat transfer studies related to aerospace applications are probably the works of Koh et al. (1973). They measured pressure drops, related to the **permeability** of the porous material, and heat transfers in stainless steel Rigidmesh as well as in stainless steel and copper sintered powders. They claimed that there is no simple relation between the internal heat transfer and the porosity. Kar (1981) suggested friction factor and Nusselt number correlations after investigating Darcian flow in sintered porous materials. He also highlighted the key roles played by the **effective thermal conductivity** of the solid matrix and by the **volumetric heat**

transfer coefficient. Yamamoto (1990) measured surface and internal temperatures of porous material cooled with gaseous CO_2 and H_2. He showed that only the internal temperature was affected by the porosity of the material. Thanks to a numerical model based on thermal balance, Andoh and Lips (2003) studied the impact of the governing material parameters on the temperature profile. They showed once again the importance of the internal heat transfer.

Situations such as transpiration cooling, where the coolant and the porous material can have different temperatures, are referred as **Local Thermal Non-Equilibriums** (LTNE). Heat transfers in homogeneous porous media and at LTNE are generally modeled with macroscopic energy and momentum equations obtained thanks to several approaches:

- empirical modelings (Wakao and Kagei, 1982)
- use of a volume averaging method on both the fluid and the solid phases then length-scale considerations to close the system and determine the effective transfer coefficients (Quintard et al., 1997)
- use of a volume averaging method then closure of the system with heuristic macroscopic equations (Kuwahara et al., 2001)

Each approach leads to a two-temperature model which can be simplified in the case of a steady compressible flow as:

Energy equation in the solid phase:

$$\underbrace{\frac{\partial}{\partial x_i}\left(\boldsymbol{\lambda}_{\mathbf{s,eff}}\frac{\partial T_s}{\partial x_i}\right)}_{\text{Conduction in the solid phase}} - \underbrace{\mathbf{h_v}(T_s - T_f)}_{\text{Convection between both phases}} = 0 \tag{1.1}$$

Energy equation in the fluid phase:

$$\underbrace{\frac{\partial}{\partial x_i}\left(\rho_f c_p v_{s,i} T_f\right)}_{\text{Convection term}} - \underbrace{\frac{\partial}{\partial x_i}\left(\varepsilon\lambda_f\frac{\partial T_f}{\partial x_i}\right)}_{\text{Conduction in the fluid phase}} - \underbrace{\mathbf{h_v}(T_s - T_f)}_{\text{Convection between both phases}} = 0 \tag{1.2}$$

Conservation of mass:

$$\frac{\partial}{\partial x_i}(\varepsilon\rho_f v_i) = 0 \tag{1.3}$$

Fluid momentum equations:

$$\underbrace{\frac{1}{\varepsilon^2}\frac{\partial}{\partial x_j}(\rho_f v_{s,i} v_{s,j})}_{\text{Inertial term}} = \underbrace{-\frac{\partial p}{\partial x_i}}_{\text{Pressure term}} + \underbrace{\frac{1}{\varepsilon}\frac{\partial}{\partial x_j}\left[\eta\left(\frac{\partial v_{s,i}}{\partial x_j} + \frac{\partial v_{s,j}}{\partial x_i}\right)\right] - \frac{1}{\varepsilon}\frac{2}{3}\frac{\partial}{\partial x_i}\left(\eta\frac{\partial v_{s,j}}{\partial x_j}\right)}_{\text{Viscous terms}}$$
$$\underbrace{-\frac{\eta}{\mathbf{K}}v_{s,i} - \rho_f\boldsymbol{\beta}|v_s|v_{s,i}}_{\text{Darcy-Forchheimer}} \tag{1.4}$$

T_f, T_s,ε, ρ_f, c_p, η, p and v_s are the fluid temperature, the solid temperature, the fluid density, the fluid calorific capacity, the fluid dynamic viscosity, the pressure and the superficial velocity respectively. This set of equations also involves several **effective material parameters**:

- the **effective thermal conductivity** of the solid phase $\boldsymbol{\lambda_{s,eff}}$ which characterizes the ease to diffuse heat by conduction through the solid matrix;
- the **volumetric heat transfer coefficient** $\mathbf{h_v}$ which gives the ability of both the solid and the fluid phases to exchange heat by convection when they have different local temperatures;
- the **permeability coefficient K** and the **Forchheimer coefficient** $\boldsymbol{\beta}$ which measure additional viscous and inertial pressure losses due to the flow in a porous material.

Many works from the literature use the LTNE model. Amiri and Vafai (1994) studied heat transfer due to incompressible forced convective fluid flow in packed beds. Von Wolfersdorf (2005) investigated the effect of the backside cooling on the overall cooling effectiveness. Thanks to experiments and a one-dimensional LTNE model, Reutter et al. (2008) assessed the temperature profile of transpiration cooled metal foams produced by Slip-Reaction Foam Sintering. Amatachaya et al. (2011) studied transpiration cooling through Ni-Cr open-cellular porous plate having a porosity of 0.93.

More information about the four effective properties ($\lambda_{s,eff}$, h_v, K and β) are given in the next chapters. Nevertheless, at this point, it is primordial to understand that the performance of a transpirating system depends on each of these effective parameters values.

1.3 Porous materials for transpiration cooling

The present work focuses on the study of porous materials. This section therefore aims to give more information about this particular type of material.

1.3.1 What is a porous material ?

A porous material is a material containing pores. Many natural materials are considered as porous (rocks, soil, wood, bones,etc.). A porous material can also be seen as **an architectured material**: it is possible to combine mechanical, acoustical, thermal, chemical or even electromagnetic properties by wisely choosing the porous geometry. For

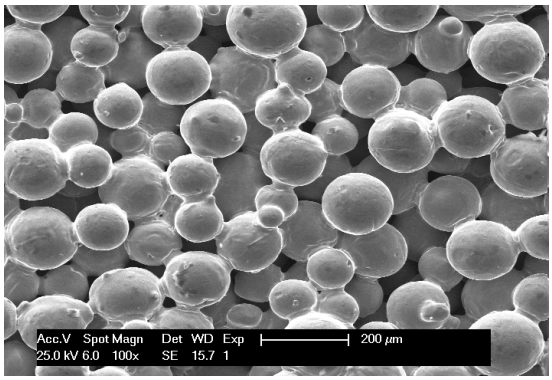

(a) SEM micrograph of sintered bronze spherical powders (courtesy of Sintertech).

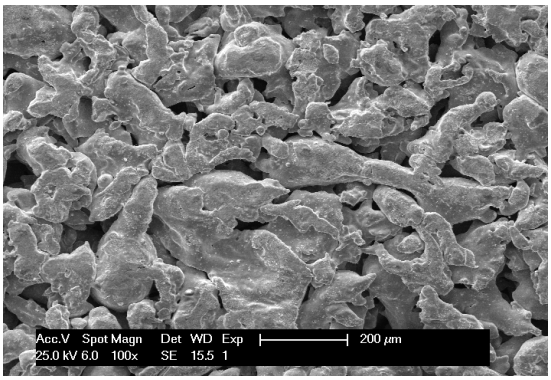

(b) SEM micrograph of sintered stainless steel irregular powders (courtesy of Sintertech).

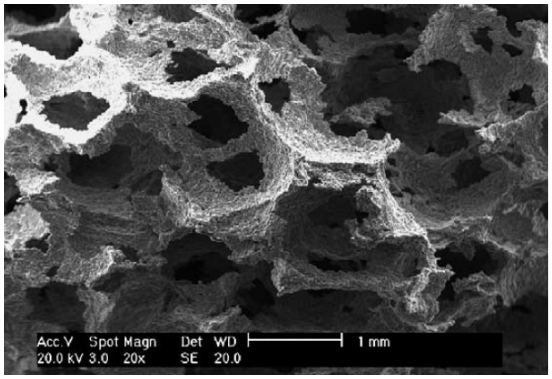

(c) SEM micrograph of an aluminum foam by powder sintering process with space holders(Jiang et al., 2005).

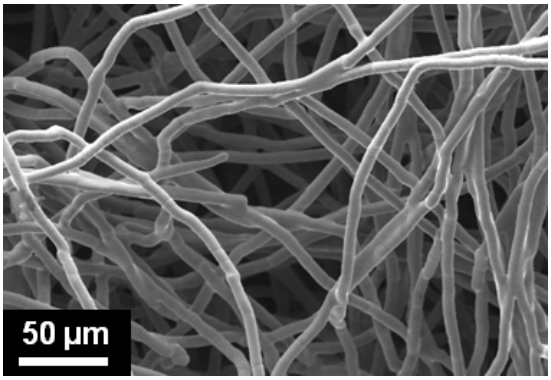

(d) SEM micrograph of sintered stainless steel fibers (courtesy of Sintertech).

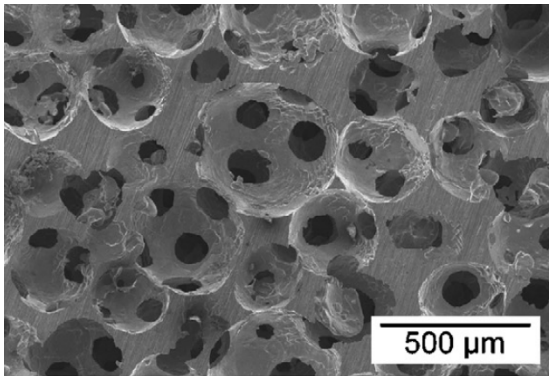

(e) Open-cell aluminum foam obtained by replication process (Goodall et al., 2007).

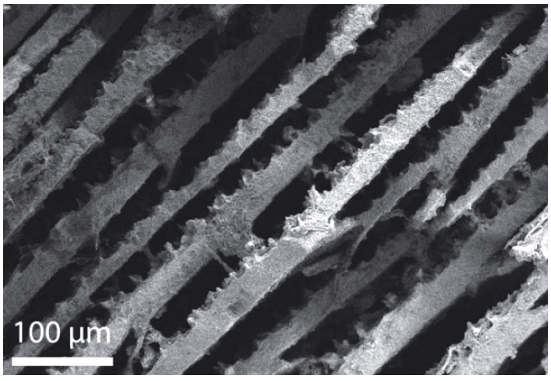

(f) SEM micrograph of ceramic macroporosities created by freeze-casting (Lichtner et al., 2013).

Figure 1.6: Examples of porous materials

this reason, there is an increasing interest in porous materials in many engineering fields: weight saving, energy absorption (Hammetter et al., 2013), filtration, separation, flow equalization, flow restriction, bubbling, aspiration, fluidized bed, noise reduction protection, heat pipes,etc. (German, 1994; Sintertech, 2016). Moreover, as **the properties of a porous material are a combination of the porous geometry and of the constitutive material properties**, various techniques have been developed to produce them from metallic, ceramic or polymer materials. Powder or fiber sintering with or without foaming agent (figures 1.6a-1.6d), casting (figure 1.6e), metal deposition or directional solidification (figure 1.6f) are good examples of manufacturing process which lead to a wide range of porous material geometries.

1.3.2 Characterization of porous materials

Various geometrical parameters can characterize a porous material architecture. The most important ones are introduced in this section.

1.3.2.1 The porosity

The porosity is obviously the main parameter that describes a porous medium. The **overall porosity** takes into account all the pores and is defined as:

$$\varepsilon = \frac{V_p}{V} = \frac{\text{Volume of pores}}{\text{Overall volume}} \tag{1.5}$$

ε varies between 0 (fully dense) and 1 (only void). When a flow through a porous medium is considered, the **open porosity** is more adapted to describe the porous media. It only takes into consideration the pores which take part to the flow:

$$\varepsilon_{open} = \frac{V_{op}}{V} = \frac{\text{Volume of pores which take part to the flow}}{\text{Overall volume}} \tag{1.6}$$

The fraction of pores which cannot participate to the flow is called the **closed porosity**:

$$\varepsilon_{closed} = \frac{V_{cp}}{V} = \varepsilon - \varepsilon_{open} = \frac{\text{Volume of pores which do not take part to the flow}}{\text{Overall volume}} \tag{1.7}$$

1.3.2.2 Specific surface area

The specific surface area A_{sp} of a porous medium is defined as:

$$A_{sp} = \frac{A_{sf}}{V} = \frac{\text{Interfacial solid/pores surface area}}{\text{Overall volume}} \ \left[m^2/m^3\right] \tag{1.8}$$

As with the porosity, it can be useful to distinguish the **open specific surface area** and the **closed specific surface area** from the **overall specific surface area**. In the following, only the open specific surface area will be taken into consideration. It will be simply referenced as A_{sp}.

1.3.2.3 Grain and pore size distributions

In materials science, it is often interesting to characterize the statistical size distribution of the particles or elements (granulometry) or of the pores (porosimetry) composing a material. From these distributions, various quantifiable aspects can then be defined: mean size, median size, variance,etc.

1.3.2.4 The tortuosity

The tortuosity defines the ratio of a characteristic length L_c to the size (thickness) of the porous material L:

$$\tau = \frac{L_c}{L} \tag{1.9}$$

There is not a unique definition of the tortuosity since it depends on what is studied. With hydraulic problems, the characteristic length can be the mean length of the streamlines (Koponen et al., 1996; Matyka et al., 2008; Ghassemi and Pak, 2011; Duda et al., 2011). With geometrical problems, it can be the length of the shortest path which passes through the materials (Lindquist et al., 1996; Gommes et al., 2009; Sun et al., 2011). With diffusion problems, the tortuosity can be defined as the ratio of the diffusivity in the free space to the diffusivity in the porous material (Boudreau, 1996; Garrouch et al., 2001).

1.3.3 The porous materials in this study

This study focuses on porous materials made **by partial sintering of metallic powders**. Various reasons justify this choice. First of all, partial sintering ensures a completely interconnected porous phase in the $20-40\%$ porosity range. In terms of porous material, this kind of material has a relatively good mechanical resistance. Finally, the use of metallic powders offers the possibility to use the superalloys constituting the current multi-perforated walls. Thus, the porous walls should be able to preserve a sufficient thermal diffusivity and good mechanical properties at high temperature.

One of the main interests of the thesis is related to the relationships existing between the architecture and the effective material properties. As the type of metallic alloy has a

low impact on the study of the interesting effective properties, model materials made for example of bronze and stainless steel were studied for practical reasons.

1.4 Present work

1.4.1 Aims of the thesis

The goal of this PhD thesis is to **develop a methodology helping the designer to choose the porous architectures which are the most adapted for transpiration cooling in aero-engine combustion chambers.**

In order to optimize the material, the performance of a specific architecture at given engine operating conditions can be assessed on different criteria (e.g. the air cooling mass flow or the weight) and submitted to various constraints (e.g. the temperature of the liner). As explained in section 1.2, many studies have already identified the effective materials properties permitting the thermal performance to be predicted:

- the permeability of the porous wall ($\mathbf{K}$ & $\boldsymbol{\beta}$);
- the effective thermal conductivity of the solid matrix ($\boldsymbol{\lambda}_{\mathbf{s,eff}}$);
- the volumetric heat transfer coefficient ($\mathbf{h_v}$).

These effective properties are directly dependent on the porous architecture. In the literature, the performance of some solutions were generally numerically predicted after experimental determination of some or all their effective properties. Otherwise, correlations developed for packed beds of spherical particles were used. However, the behavior of a partially-sintered materials can diverge from that of packed beds. Moreover, even though a large range of porous materials have been experimentally investigated in the literature, clear relationships still have to be defined for partially-sintered materials.

The first part of this thesis is therefore focused on **the determination of relationships between the architectural parameters and the effective material properties.** As many architectural parameters (porosity, specific surface area, pore distribution, connectivity and shape, tortuosity, rugosity, etc) can affect the effective properties, it is fundamental to find some relevant geometrical parameters which permit an easy and accurate prediction of the effective material properties.

The framework of this PhD thesis is summarized in the figure 1.7. Before focusing on the optimization procedure in the chapter 6, the specific relationships linking the architecture to the effective material properties are developed from the chapter 3 to 5.

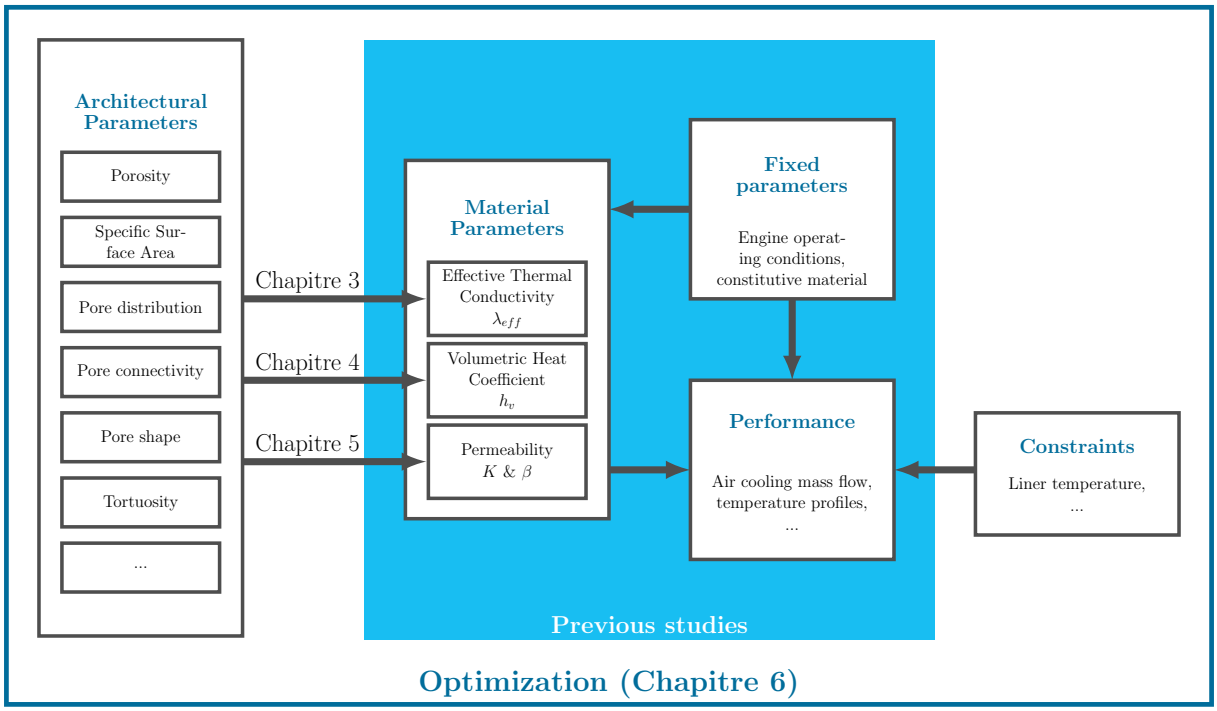

Figure 1.7: Framework of the study

1.4.2 Methodology

A specific methodology was applied during this PhD thesis. It is introduced in the figure 1.8.

First of all, a database of three-dimensional images of porous architectures was created thanks to digitization of porous samples with X-ray tomography or thanks to direct numerical generation. The chapter 2 introduces these architectures as well as the numerical methods allowing their geometrical parameters to be measured.

Numerical simulations performed on the three-dimensional images and experimental measurements permitted the assessment of the effective materials properties. Analysis of all the gathered data aimed to identify the relationships existing between the geometrical parameters and the effective properties. The works performed on the effective thermal conductivity, the permeability and the volumetric heat transfer coefficient are developed in the chapters 3, 4 and 5 respectively.

In order to optimize the architecture, the relationships were finally integrated into a heat transfer model which assesses the thermal performance of a design. Chapter 6 introduces the optimization process and gives more details about the model and the different optimization criteria. It also shows how some interesting designs for transpiration cooling could be highlighted thanks to a multi-dimensional analysis.

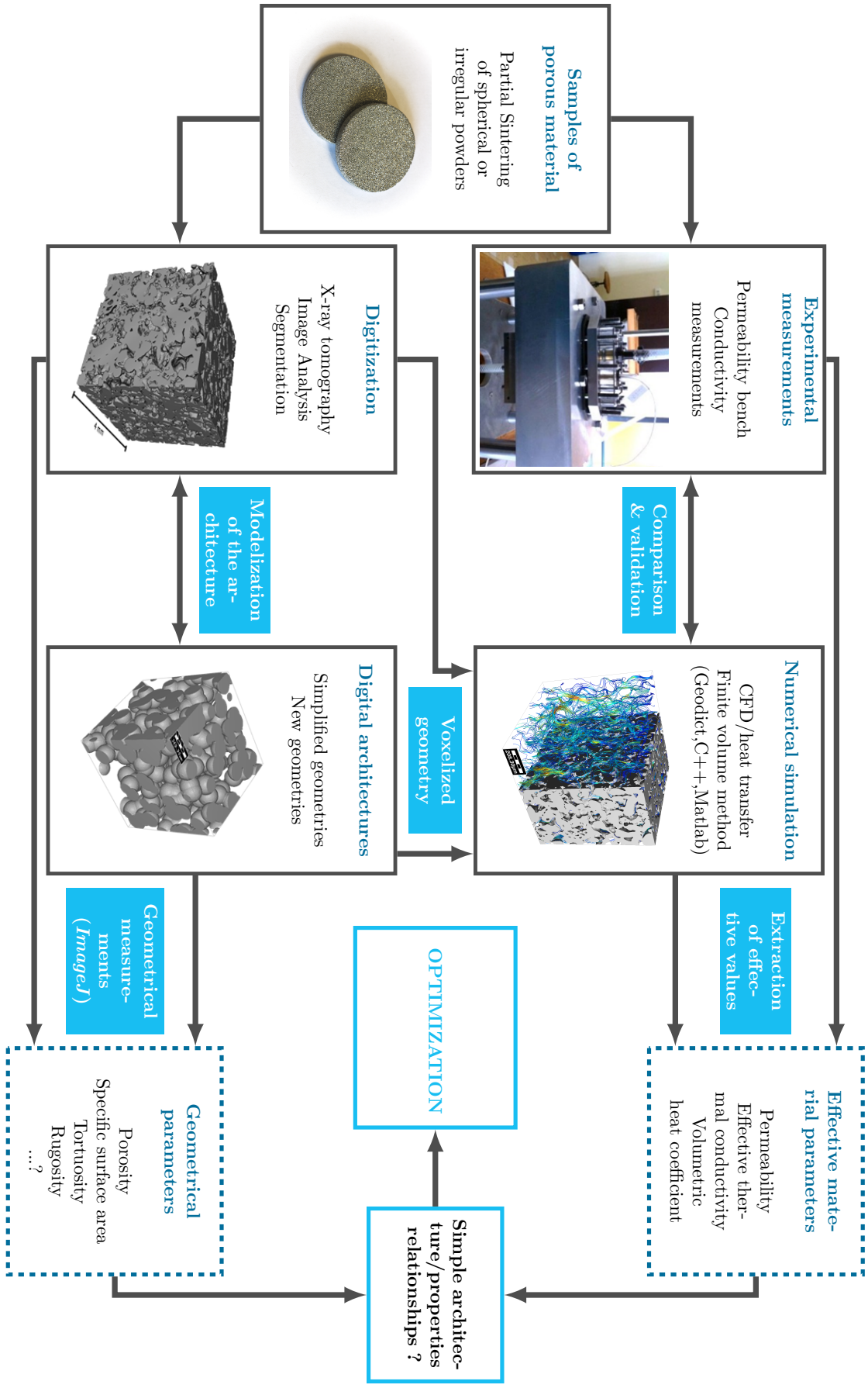

Figure 1.8: Methodology applied during the thesis

Chapter 2

Partially-sintered materials and geometrical characterization

Contents

This PhD thesis focuses on the experimental and numerical investigation of partially-sintered metallic materials in view of a transpiration cooling application. Two categories of materials were studied:

- Partially-sintered samples made of spherical powders (**SP**) or irregular powders (**IP**);
- Numerically generated materials used as model architectures: packed beds of spherical particles (**Packed bed**) and numerically generated partially-sintered spherical powders (**SPnum**).

This chapter introduces these different architectures as well as the different tools and methods which were used to characterize their architectures.

2.1 Real partially-sintered materials

In this section, the manufacturing process of partially-sintered materials is first explained. The architecture digitization process enabling the numerical studies is then introduced.

2.1.1 Two kinds of powders

Partially-sintered materials are manufactured thanks to powder metallurgy. The study was focused on materials made from two kinds of metallic powders:

- **spherical powders** produced by gas atomization (figure 2.1a);
- **irregular powders** produced by water atomization (figure 2.1b).

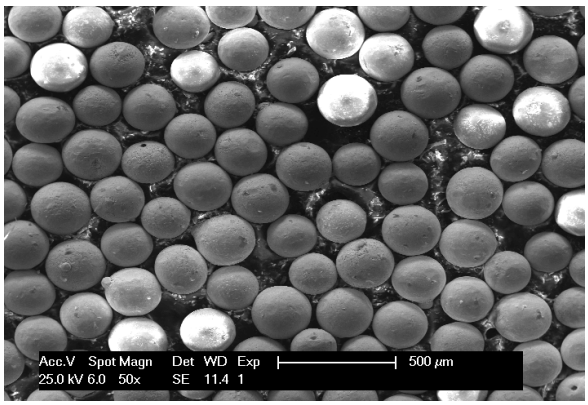

(a) SEM micrograph of a bronze spherical powdera (particle size: $\sim 200\ \mu m$).

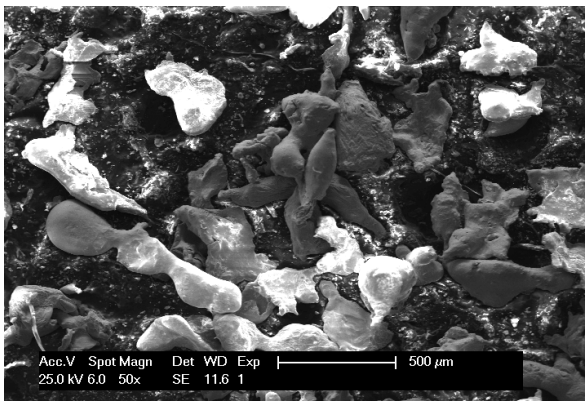

(b) SEM micrograph of a stainless steel irregular powder (particle size: $\sim 200\ \mu m$).

Figure 2.1: SEM micrographs of metallic powder particles used by the company *Sintertech*.

Two distinct families of partially-sintered architectures could therefore be produced:

- materials made of spherical powders (referenced as **SP** for Spherical Powders);
- materials made of irregular powders (referenced as **IP** for Irregular Powders).

The studied samples were manufactured from different grades of quasi-monomodal powders. The mean size of the powder particles varied between 50 μm and 600 μm. Pictures of specimens made of 400 μm particles are introduced in figures 2.2a-b

Due to the atomization process, some internal pores can be present in the powders. These pores are due to gas or water trapped in the particles during atomization (Suri et al., 2005; Gerling et al., 2004). These defects can remain in the final partially-sintered

(a) Picture of partially-sintered bronze spherical powders (particle size: $\sim 400\ \mu m$).

(b) Picture of partially-sintered stainless steel irregular powders (particle size: $\sim 400\ \mu m$).

Figure 2.2: Picture of partially-sintered samples.

architecture. Even though they do not participate directly to the flow properties, these pores can reduce the effective thermal conductivity of the metallic phase.

2.1.2 Partial-sintering

Sintering is a thermal treatment applied to a powder or a powder compact. It occurs at a temperature below the melting point of the main constituent so as to increase its strength by inter-particle bonding. The superficial energy decrease is the driving force of sintering. It results in a microstructural rearrangement where the solid-vapor interfaces are replaced by solid-solid interfaces as shown in the figure 2.3. At a macroscopic scale, sintering leads to densification (and therefore to reduction of porosity).

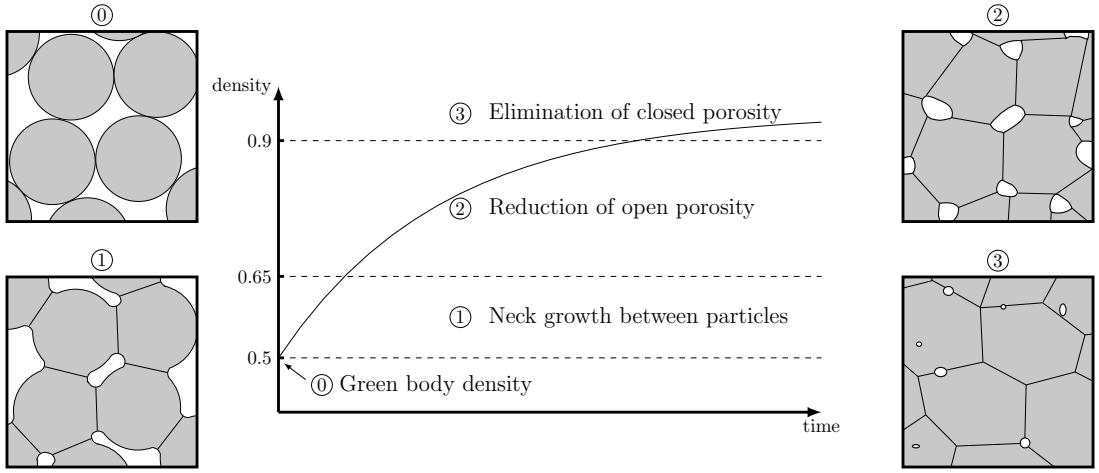

Figure 2.3: Macroscopic and microstructural variations of the powder during the different sintering steps (density values are given for indication).

Initially, a powder compact, also called *green body*, is formed (step 0). Its density depends on the shape of the powder and on the compaction process. Quickly, necks are created between the particles (step 1). The mechanical resistance of the material is thus increased without large variation of density. Above a certain threshold, densification leads first to reduction of the open porosity (step 2) then to the closed porosity (step 3). **Partial sintering** consists in stopping the sintering process just after the creation of the bonds between the particles.

During the first step of sintering, the bonding process can be modeled by the welding of two spherical particles with the formation of a toric bonding neck having two main curvature radius x (positive) and α (negative). The six mechanisms responsible for the interfacial energy reduction are introduced in the figure 2.4 and table 2.1. If the six mechanisms lead to consolidation, only the mechanisms 4,5 and 6 entail a shrinkage.

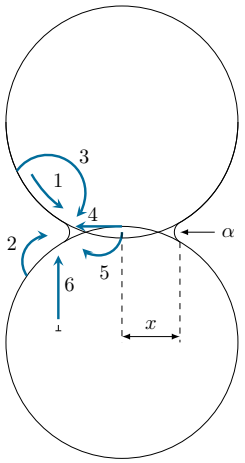

Mechanism	Type of transport	Source
1	Surface diffusion	Particle surface
2	Vapor transport	Particle surface
3	Lattice diffusion	Particle surface
4	Lattice diffusion	Grain boundary
5	Grain boundary diffusion	Grain boundary
6	Plastic deformation	Grain boundary

Figure 2.4 & Table 2.1: The six mass transport mechanisms responsible for particle bonding.

Porous material samples produced by partial sintering were delivered by the French company *Sintertech* (Pont-de-Claix, France). With its manufacturing process, partial-sintering leads to a porosity difference between the green-body and the final material of about 6%. Different levels of final porosity are achieved by modifying the green-body porosity with a more or less important powder compression. Because of confidentiality issues, the detailed manufacturing process cannot be given.

2.1.3 Digitization of the partially-sintered samples

In order to quantitatively characterize the previous porous samples, 3D images of their architectures were obtained thanks to X-ray tomography and image processing.

2.1.3.1 Principle of X-ray tomography

X-ray tomography has generated a great deal of excitement in the material science domain for several years, especially because of its possibility to scan a 3D structure in a non-destructive way.

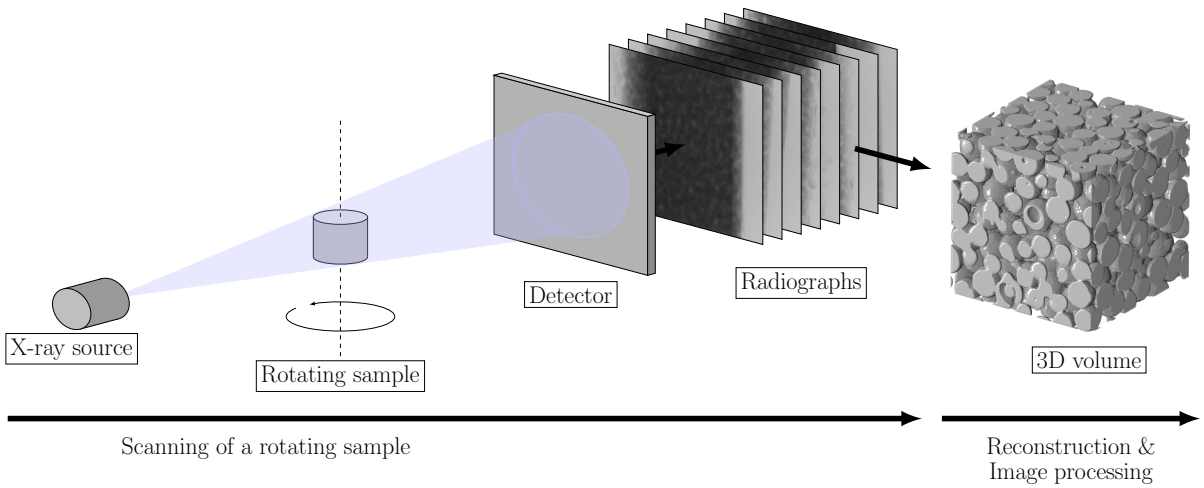

Figure 2.5: Working principle of X-ray tomography.

The working principle of X-ray tomography is given figure 2.5. A sample is placed between an X-ray source and a CCD[1] detector. Depending on the local absorption of the material, the X-ray intensity is more or less reduced. The X-ray signal recorded by the CCD detector leads to the generation of a grey-scale image. In order to obtain a 3D image, 2D X-ray images are recorded at different sample orientation angles. A reconstruction algorithm uses all the 2D scans to generate a reconstructed 3D grey-scale image. More information about X-ray tomography are given for example by Salvo et al. (2003). This imaging technique has already been applied to many porous materials in the literature: sintered powders (Lame et al., 2004), metallic foams (Laschet et al., 2009; Youssef et al., 2005), fibrous materials (Koivu et al., 2009), reticulate porous ceramics (Petrasch et al., 2008), freeze-cast ceramics (Roussel et al., 2016),etc.

[1] Charge-couple device

2.1.3.2 Tomographs and samples

The samples were digitized by X-ray tomography with scanners from two laboratories:

- At the laboratory *MATEIS* (Lyon, France) with a v|tome|x from GE Sensing & Inspection Technologies Phoenix X|ray which allows a voltage up to 160 kV;
- At the laboratory *SIMaP* (Grenoble, France) with an EasyTom XL150-160 from RXSolutions which allows a voltage up to 100 kV.

The operational conditions were $140 - 150$ kV with 1200 projections at *MATEIS* and $80 - 100$ kV with 800-1600 projections at *SIMAP*. In the present study, the choice of the tomograph did not have a major effect on the quality of the digitized images. It was guided by the availability of the machines. Depending on the studied materials, and notably on the constitutive powder size, the voxel[2] size varied between $(1.6\ \mu m)^3$ and $(5\ \mu m)^3$.

2.1.3.3 Thresholding of reconstructed 3D-images

The different phases of a material can be discriminated thanks to the pixel colors of the reconstructed image. To be able to analyze the porous architecture, it is essential to clearly separate the void phase (closed and open porosity) from the solid one. This separation can be carried out thanks to thresholding. Thresholding consists in converting a grey-scale (or a color) image to a binary image (only black and white pixels) by using an optimal threshold. It was performed with the software *ImageJ* (Abràmoff et al., 2004). Despite the fact that it is one of the simplest segmentation technique, it remains a sensitive step of image processing. The threshold value, beyond which a pixel is considered to belong to the solid phase, is the user's choice, even though algorithm may guide him. This choice is more or less easy depending on the image quality, and notably on the contrast between the phases. In the case a 8-bit grey-scale image, the value of the pixel can vary between 0 (black pixel) and 255 (white pixel).

Figure 2.6 illustrates how a ± 5 variation of the chosen threshold value can impact the binarization. The image 2.6b was generated by applying the *Default* threshold algorithm of *ImageJ* on the image 2.6a. As there is a good contrast between both phases, a modification of the threshold value by $\pm 5\%$ only leads to a maximal variation of the porosity of the 2D image by 0.6%. As a result, the quality and the accuracy of the thresholding step was considered as sufficient in the present work.

[2]three-dimensional pixel

(a) Grey-scale image

(b) Binarized image ($\varepsilon = 48.6\%$)

(c) Removed voxels with default threshold value $+5$ ($\varepsilon = 48\%$)

(d) Added voxels with default threshold value -5 ($\varepsilon = 49\%$)

Figure 2.6: Thresholding of a grey-scale image and sensitivity of the threshold value. The removed and added voxels respectively due to an increase or a decrease of the threshold are highlighted in white in 2.6c and 2.6d.

2.1.3.4 Visualization of the digitized partially-sintered materials

Three-dimensional digitized images of partially-sintered materials made of spherical powders (SP) or irrelugar ones (IP) are shown in figures 2.7a-b. One can notice that both kinds of powders clearly lead to two distinct types of porous architectures. On each image face, internal pores can also be observed.

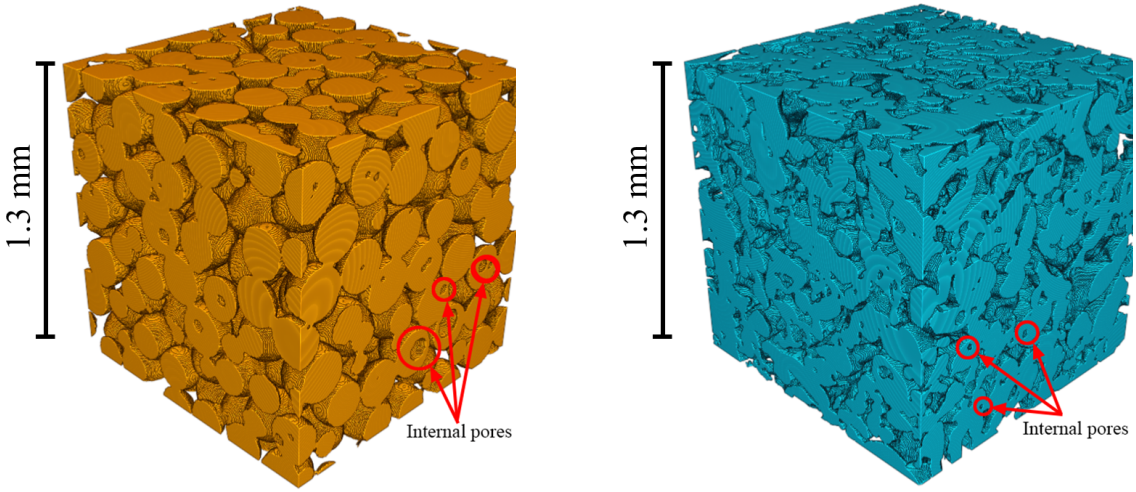

(a) 3D reconstruction of a SP porous material ($\varepsilon = 39\%$).

(b) 3D reconstruction of a IP porous material ($\varepsilon = 38\%$).

Figure 2.7: 3D reconstructed images of a SP and an IP partially-sintered materials having both 200 μm particles and produced by the company *Sintertech*. Both images are composed of 400^3 voxels having a size of 3.3 μm.

2.2 Numerically generated porous materials

As the digitization of porous materials by X-ray tomography is time-consuming (sample preparation + 30-180 min of scanning + image processing), the idea was to be able to generate digital architectures modeling real ones. This section introduces the three-dimensional architectures modeling packed beds of spherical particles and partially-sintered materials made of spherical particles (SP) which were generated thanks to the Discrete Element Method. It has to be noted that the complexity of the materials made of irregular powders (IP) prevents their architectures to be numerically modeled.

2.2.1 Introduction to the software *dp3D*

The software *dp3D*, developed at *SIMaP* by Martin and Bordia (2008), was used to generate digital architectures. *dp3D* is a Discrete Element Method (DEM) computation software. The idea of the method is to simulate mesoscopic scale phenomena by modeling the interactions between discrete objects (spherical particles). Contrary to the the Finite Element Simulation, which is based on continuum mechanics, DEM does not need to mesh the system. The interactions are simulated thanks to different contact laws (elasticity, plasticity, bonded contacts, bonded contacts with interactions as well as sintering) depending on the physics of interest. The use of Newton's second law with a quasi-static equilibrium assumption permits the forces exerted on the particles and the displacements to be computed. For more information, the reader may refer to Cundall and Strack (1979).

2.2.2 Generation process

The porous material generation with DEM followed three steps summarized in figure 2.8:

- Figure 2.8a: The software generates a gas of particles in a simulation box with a density of about 30%. The number of particles included in this box as well as the size distributions can be chosen;
- Figure 2.8b: The particles are then compacted by reducing the size of the simulation box until reaching the requested green body density ($49 - 61\%$);
- Figure 2.8c: Despite the fact that dp3D can simulate sintering thanks to the model of Parhami and McMeeking (1998), this phenomenon was here simply taken into account with homothetic particle displacements towards the volume center. An image file including the spherical particles and their sintering necks is then generated. The necks are represented as inverse torus based on the model of Coble (1958).

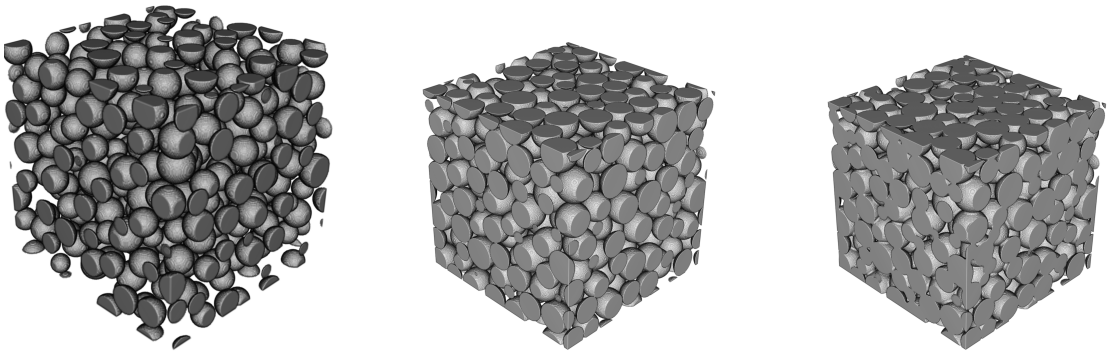

(a) Generation of a gas of particules. **(b)** Green body after compaction **(c)** Sintered body with sintering necks

Figure 2.8: Generation of a porous architecture by DEM

All along the generation, periodic conditions were applied so as to get periodic three-dimensional architectures. The only use of the process defined previously is to reproduce representative sintered porous materials. Indeed, as the physical parameters controlling the sintering kinetics were not known, it was impossible to simulate properly this phenomenon. The numerically generated partially-sintered spherical powders are referenced in the following as **SPnum**. Packed beds of spherical particles can also be generated if the sintering step is removed. These architectures are referenced as **Packed bed**. Examples of generated packed beds and SPnum architectures are represented in figures 2.9a-b.

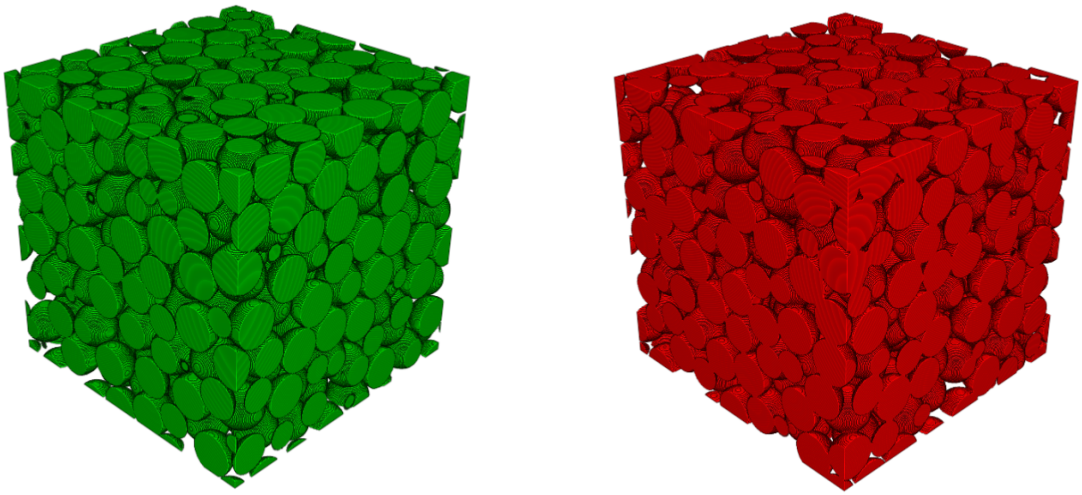

(a) Packed bed ($\varepsilon = 39\%$). **(b)** SPnum ($\varepsilon = 38\%$).

Figure 2.9: Three-dimensional geometries generated with DEM thanks to *dp3D*.

2.3 Characterization of a porous material

A porous material can be characterized by many geometrical parameters. This section introduces the tools enabling the assessment of the porosity, the specific surface area and the pore size, the main geometrical parameters studied in this work.

2.3.1 The porosity

2.3.1.1 Experimental measurement

Many experimental techniques have been developed to measure the porosity. Most of them are based on physical measurements of weight, length or pressures. The most famous one is based on the Archimedes buoyancy principle. During this PhD thesis, a geometrical approach was preferred for the experimental measurements of the overall porosity. Considering the large size of the measured samples as well as their regularities, accurate assessment of their volumes could be obtained. The porosity was simply calculated using:

$$\varepsilon = 1 - \frac{m}{V \rho_{bulk}} \tag{2.1}$$

where m, V and ρ_{bulk} are the mass of the sample, its volume and the density of the bulk material respectively. As this method permits only the overall porosity assessment (it is impossible to differentiate the closed- from open- porosity), it was only used for the analysis of the effective thermal conductivity. By taking into account the accuracy of the balance, most of the errors are made during the measurement of the sample's dimensions. However, the sample geometries were regular and the accuracy of the experimental measurements of the porosity was assessed to be at worst $\pm 2\%$.

2.3.1.2 Numerical measurement

Once a porous material 3D image is binarized, its porosity can be easily assessed. Indeed, the porosity is simply defined as the ratio of the number of voxels corresponding to the void phase to the overall number of voxels. The overall porosity is measured when this process is carried out just after thresholding. If only the interconnected phase properties have an interest, the closed porosity has first to be removed. A problem may then arise with isolated pores at the edge of the image. Due to the finite size of the image, it can be difficult to distinguish them as open or closed pores. However, as they will not participate to the flow in the numerical simulations, they were simply considered as being closed pores. The closed porosity was removed with an algorithm based on region growing

segmentation from the plugin *3D toolkit* of *ImageJ*. It deletes all the isolated pores which are not connected to the main void phase. The algorithm principle is given figure 2.10.

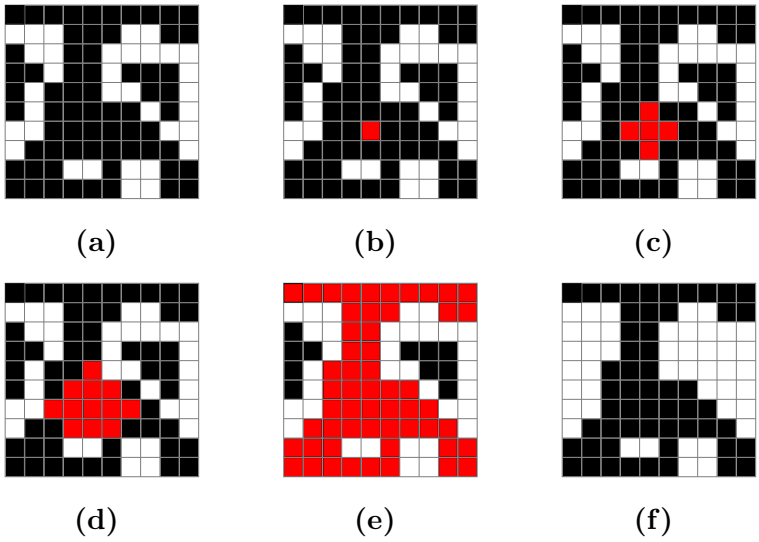

Figure 2.10: Algorithm of region growing segmentation: a) initial image (black voxels=void phase, white voxels=solid phase), b) seed in the main void phase (red pixel), c) first growth of the seed, d) second growth of the seed, e) after last growth, f) all the voxels which do not belong to the grown phase are considered as solid voxels.

Table 2.2 introduces open and closed porosity measurements performed on 400^3 voxels images of partially-sintered architectures. It can be noticed that the closed porosity of each architecture is very low. This emphasizes the high interconnection of the partially-sintered materials. The closed pores are highlighted in the figures 2.11a-b. This closed porosity is composed of pores formed during the atomization of the powders. Despite the low closed porosity of the studied architectures and because of the sensitivity of the investigated phenomena, only the open-porosity was considered in the chapters 4 and 5 related to the permeability and to the volumetric heat transfer coefficient.

Porous samples	ε_{open} [%]	ε_{closed} [%]
SP 150 μm	36.3	0.3
SP 400 μm	35.7	1.1
IP 150 μm	36.5	0.2
IP 400 μm	40.0	0.2

Table 2.2: Numerical measurements of open and closed partially-sintered sample porosities.

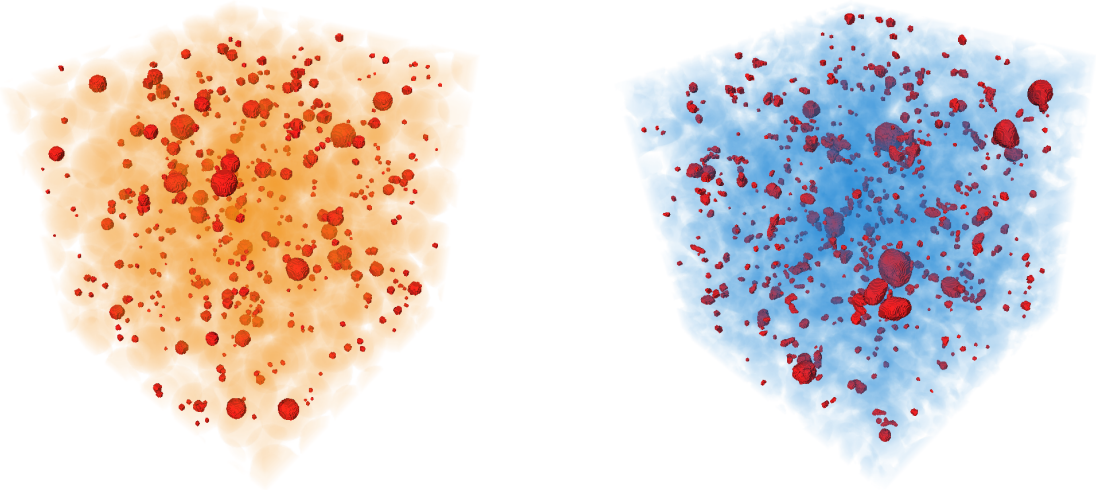

(a) SP porous material with $\sim 200\ \mu m$ particles and $\varepsilon = 39\%$.

(b) IP porous material with $\sim 200\ \mu m$ particles and $\varepsilon = 38\%$

Figure 2.11: Closed pores (in red) entrapped in the partially-sintered materials introduced in figure 2.7.

2.3.2 Specific surface area

As for the porosity, experimental methods were especially developed to assess the specific surface area of porous materials. One of these methods is based on adsorption and allows the surface of very fine and/or deep structures to be measured. However, the results are sensitive to the substance adsorbed. An other technique is based on the gas permeability. Despite its simplicity, it requires to well know the relationship between the specific surface area and the resistance to gas-flow. In this PhD thesis, only a numerical approach was carried out to characterize the specific surface area of the porous samples.

The geometrical parameter was computed with an *Analysis_3D* plugin tool (Boulos et al., 2012) in the software *ImageJ*. The assessment is based on the marching cubes algorithm, proposed by Lorensen and Cline (1987). By taking into consideration eight neighbour voxels forming an imaginary cube, a polygonal isosurface passing through the cube is determined among fourteen existing possibilities (figure 2.12). The accuracy of the numerical method was assessed by computing the surface of voxelized spheres (figure 2.13). Voxelized spheres were generated by varying the number of voxels per diameter d from 2 to 100. The computed surface areas are compared to the theoretical one:

$$error = \frac{A_{theo} - A_{num}}{A_{theo}} \tag{2.2}$$

where A_{theo} is the theoretical sphere surface area (πd^2) and A_{num} is the numerically

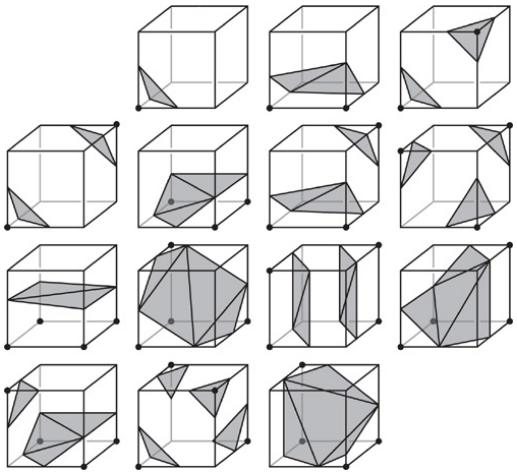

Figure 2.12: The fourteen fundamental cases of the marching cubes algorithm

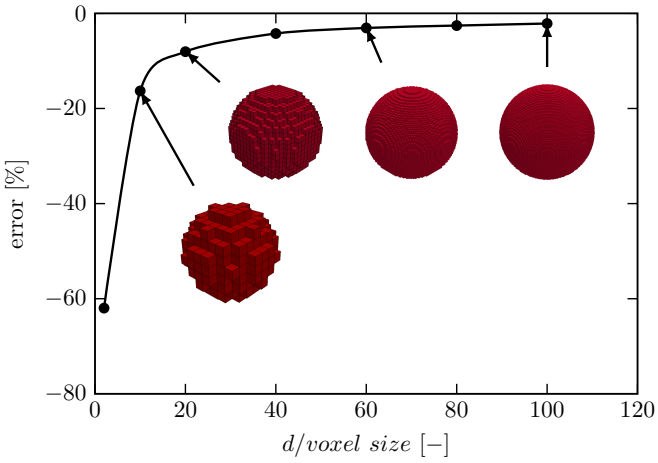

Figure 2.13: Relative error done on the assessment of the surface of a digitized sphere thanks to the marching cube algorithm compared to the theoretical surface of a sphere

assessed surface area. It is shown that as soon as a sphere is represented with 40 voxels along its diameter, the error made on the surface area is less than 5%. As it is highlighted by Dalla et al. (2002), the marching cube algorithm tends to slightly overestimate the surface area. The error entailed by the voxelization could be minimized by refining the mesh. However, as the marching cubes algorithm creates parallel or 45° inclined surfaces, the isosurface estimation always leads to residual errors.

2.3.3 The pore size

Specific measurement techniques associated to statistical analysis methods are used to characterize the pore size distribution (porosimetry). Various quantifiable aspects can also be defined: mean size, median size, variance,etc. The porosimetry can be experimentally determined by the intrusion of a non-wetting liquid at high pressure (Abell et al., 1999). The balance between the external pressure and the opposing force of the liquid's surface tension allows the determination of a pore diameter.

When images are available, image analysis is a good way to characterize the pore distribution (Maire et al., 2003). The common technique is purely geometrical and the pore sizes are determined by fitting spheres into the porous phase. However, this method does not give any information on the size of the particles which can actually go through a porous material. In the present work, a numerical method based on intrusion porosimetry was preferred. It is proposed by the *PoroDict* module of the software Geodict (2014). The

method consists in making spheres go through the porous phase. The size of a pore is then the size of the largest sphere which can reach this pore. The principle of the numerical intrusion porosimetry is explained in the figure 2.14. It is compared to the geometric porosimetry. In this work, the median pore size is considered as a characteristic value. It means that half of the porous phase volume cannot be reachable by larger spherical particles.

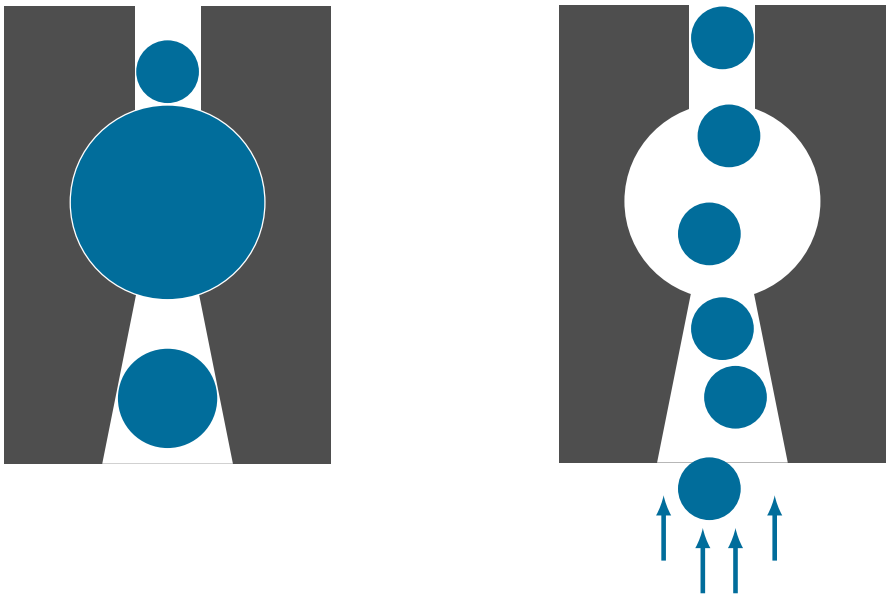

(a) Geometrical approach **(b)** Approach by intrusion

Figure 2.14: Different numericl approaches to measure the pore size distribution.

2.3.4 Representative elementary volume

To extract an effective parameter from a finite size image, one needs to ensure that the measure is carried out on a Representative Elementary Volume (REV). A REV is defined as the smallest volume in which a measurement can be considered as representative. For a same material, the size of the REV can vary depending on the measured property. The sizes of REVs for the porosity and the specific surface area were assessed for different grades of SP and IP materials (for particle sizes ranging from 150 to 400 μm). The geometrical parameters were computed in several size of cubic volume of interest (VOI). The results are introduced figures 2.15a-d. A VOI is here considered as a REV when the variation of the measured parameter stays below 5%. The relative differences are computed by using the property value of the biggest tested VOI (400^3 voxels) as reference. It is shown that the specific surface area of all the tested 3D images rapidly converges.

The relative differences of all the tested images are below the threshold of 5% as soon as the VOI is bigger than 150^3 voxels. The differences are even less than 2% for volumes of 250^3 voxels or larger. The convergence of the porosity is a little bit slower since the relative differences of all the tested 3D images remains below the threshold of 5% as soon as the size of the VOI is larger than 200^3 voxels. For volumes larger than 300^3 voxels, the relative difference of the porosity is then less than 3%. As a conclusion, in the studied porosity and particle size ranges, porosity and specific surface area measurements in VOI larger than 300^3 voxels ensure representative values.

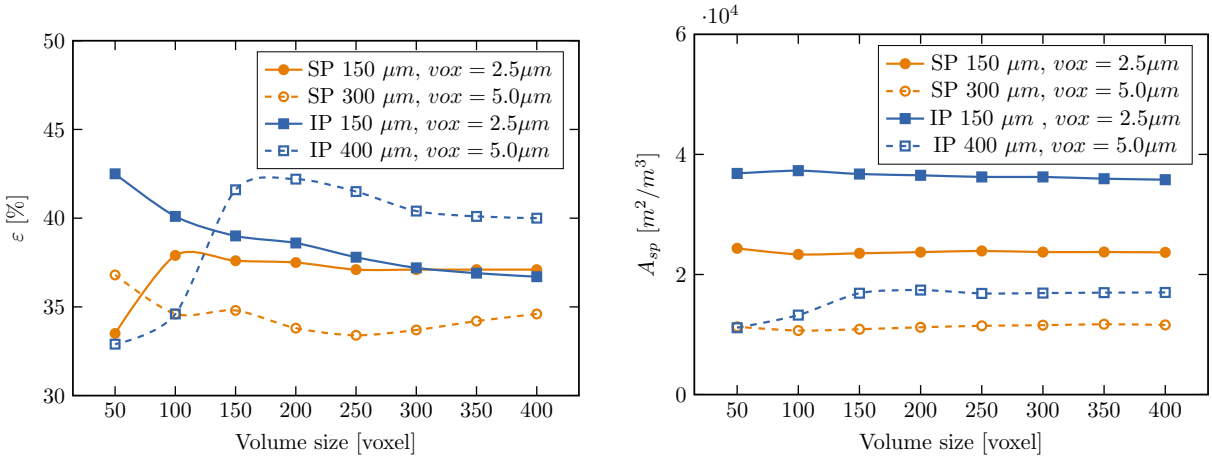

(a) Convergence of the porosity

(b) Convergence of the specific surface area

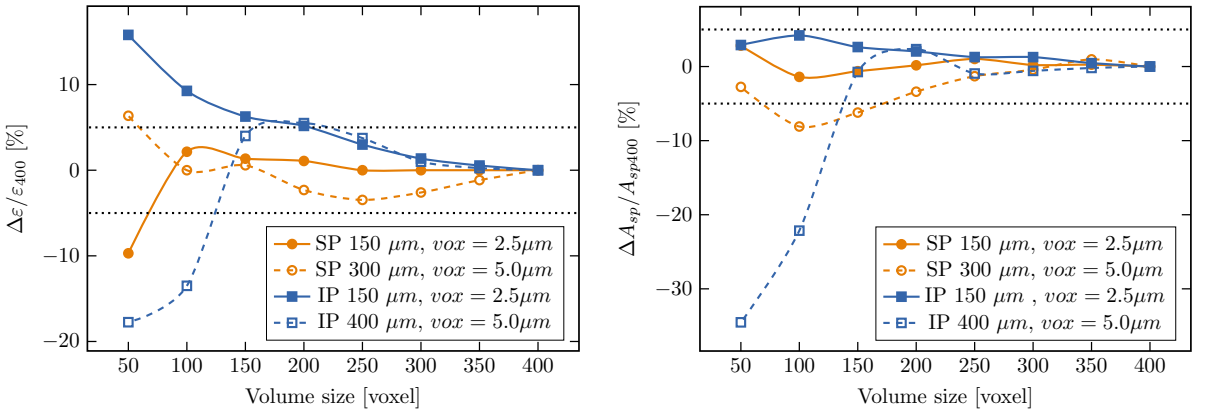

(c) Relative difference of the porosity compared to the porosity of the biggest VOI (400^3 voxels)

(d) Relative difference of the specific compared to the porosity of the biggest VOI (400^3 voxels)

Figure 2.15: Convergence of the porosity and the specific surface area with the size of the cubical volume (expressed as the number of voxels along the cube edge) and for different grades of SP and IP materials (*vox* is the voxel size)

2.4 Summary

The partially-sintered materials studied in this PhD thesis were introduced in this chapter. Two kinds of samples were investigated: samples made of spherical powders (**SP**) and samples made of irregular powders (**IP**). To enable the numerical study of these materials, the architectures were digitized thanks to X-ray tomography and image processing. Moreover, to enrich the data base, packed beds of spherical particles (**Packed bed**) and partially-sintered spherical powder architectures (**SPnum**) were numerically generated thanks to a discrete element method. Two-dimensional images of the different types of studied porous architectures are displayed in figures 2.16a–d. The four represented architectures have a similar porosity of about 38%.

For experimental analysis, the porosity of the samples was geometrically measured. The porosity and the specific surface area of the digital three-dimensional images were measured thanks to image analysis. The pore sizes were also characterized with a numerical method based on sphere intrusion. The voxel size and the volume of each image were chosen as a function of the powder size and gave representative porosity and specific surface area measurements.

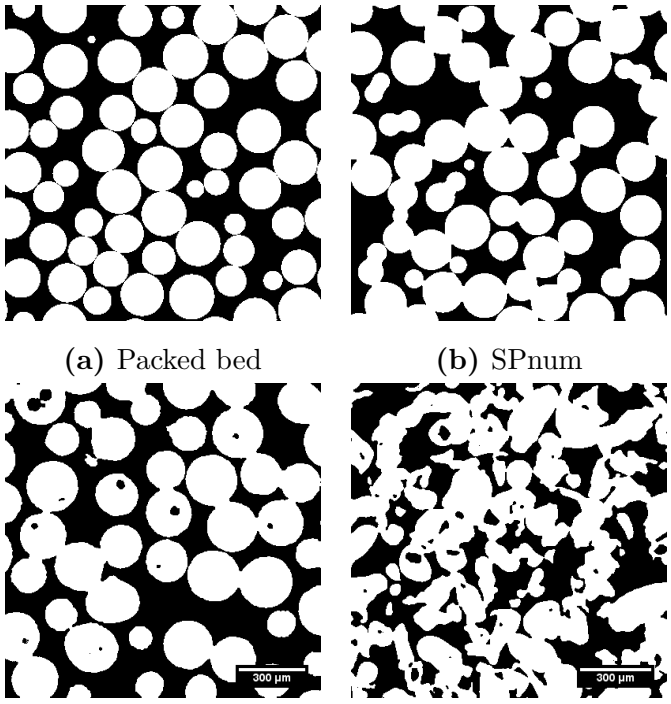

(a) Packed bed **(b)** SPnum

(c) SP **(d)** IP

Figure 2.16: Two dimensional images of: a) Packed bed, b) SPnum, c) SP (particle size 200 μm), d) IP (particle size 200 μm) (All the images have a porosity of about 38%)

Chapter 3

Effective thermal conductivity of partially-sintered materials

Contents

The effective thermal conductivity of the solid phase impacts the thermal performance of a transpirating porous material. Indeed, a high thermal conductivity permits:

- the temperature gradient through the liner to be reduced;
- the heat to be carried away toward the outer side of the liner so as to help the cooling air to extract energy on the entire thickness.

This chapter aims to study and predict how the architecture of partially-sintered materials can impact their solid effective thermal conductivity.

3.1 The thermal conductivity of partially-sintered metallic materials

3.1.1 Generalities

Thermal conduction is a physical phenomenon appearing in a substance in which heat is transported because of a temperature difference and without any transport of matter. The material ability to transport heat by conduction is characterized by the conductivity coefficient λ $(W/(m.K))$. This parameter is involved in the Fourier relationship which relates the heat flux $\vec{\varphi}$ to the temperature gradient $\vec{\nabla}T$:

$$\vec{\varphi} = -\lambda.\vec{\nabla}T \tag{3.1}$$

In equation 1.1, **the conductivity of the solid phase $\boldsymbol{\lambda_{s,eff}}$** has to be considered. This physical quantity takes into account **the effective conductivity of the constitutive material and the material architecture**. In a porous material, occupied by a unique, steady and non reactive fluid phase and submitted to a **uniform temperature gradient**, the **heat flux** can also be represented with the Fourier law:

$$\boxed{\vec{\varphi} = -\lambda_{eff}.\vec{\nabla}T} \tag{3.2}$$

where the thermal conductivity has to be replaced by an effective thermal conductivity λ_{eff}. This effective conductivity includes the four mechanisms of heat propagation which can appear in a porous material (Gibson and Ashby, 1999):

- thermal conduction through the solid phase λ_{cs};
- thermal conduction through the fluid phase λ_{cf};
- convection within the fluid phase λ_{cv};

- radiation across the pores λ_r.

The different mechanisms can be coupled to each other. The solid phase effective conductivity $\boldsymbol{\lambda_{s,eff}}$ **from equation 1.1 can be identified to** $\boldsymbol{\lambda_{cs}}$. **The question is now to know if** $\boldsymbol{\lambda_{s,eff}}$ **can be determined from measurements of** $\boldsymbol{\lambda_{eff}}$.

The relative thermal conductivity λ^* is defined as:

$$\boxed{\lambda^* = \frac{\lambda_{eff}}{\lambda_{s,bulk}}} \tag{3.3}$$

and represents the ratio of the effective thermal conductivity to the conductivity of the constitutive material $\lambda_{s,bulk}$.

3.1.2 Contribution of the heat transport mechanisms in metallic partially-sintered materials

The contributions of each one of the mechanisms highly depend on the constitutive materials and on the porous architecture. They can be assessed in the case of partially-sintered materials. To fix ideas, measurements made by Koh and Fortini (1973) on partially-sintered 304L stainlees steel powders will be taken for reference. The effective conductivity λ_{eff} of a 31% porous material varied between 5.5 and 9.6 $W/(K.m)$ for a temperature range of 373-1173 K.

3.1.2.1 Heat conduction in the fluid phase

The thermal conductivity of air is $\lambda_{air} = 0.0262\ W/(m.K)$. As this value is much lower than λ_{eff} measured by Koh and Fortini (1973), it is clear that the contribution of conduction in the fluid phase can be neglected in partially-sintered metallic materials:

$$\lambda_{cf}/\lambda_{eff} \ll 1 \tag{3.4}$$

3.1.2.2 Convection in the pores

The convection part of the effective thermal conductivity can be considered as important only when the Grashof number (Gr) is higher than 1000 (Gibson and Ashby, 1999):

$$Gr = \frac{g\beta_e \Delta T_c d^3 \rho_f^2}{\eta^2} \tag{3.5}$$

where g, β_e, ΔT_c, d, ρ_f and η are the acceleration of gravity, the volume expansion coefficient of the gas ($\beta = 1/T$ for ideal gas), the temperature difference across a pore,

the pore size, the density of the fluid and the fluid dynamic viscosity respectively. This dimensionless number measures the ratio of the buoyant force driving the convection to the viscous force. By setting a maximal pore size of 400 μm and by taking the properties of air at atmospheric conditions, the effects of convection would appear for a temperature difference in the pore higher than 1×10^5 K. As a result, it is relevant to assume that the contribution of convection in the pores is in the present case negligible:

$$\lambda_{cv}/\lambda_{eff} \ll 1 \tag{3.6}$$

As explained by Gibson and Ashby (1999), the works of Skochdopole (1961), Traeger (1967) and Baxter and Jones (1972) experimentally validated this assumption for foams having even bigger pores.

3.1.2.3 Radiation across the pores

Loeb (1954) suggested to assess the radiant conductivity through a pore with:

$$\lambda_{rp} = 4nd\varepsilon_p\sigma\bar{T}^3 \tag{3.7}$$

where ε_p, p, σ, $\bar{T}$ and n are the emissivity, the pore size, the Stephan's radiation constant (5.6704×10^{-8} $W.m^{-2}.K^{-4}$), the average absolute temperature in the pore and a geometrical factor ($= 2/3$ for spherical pores) respectively. As this conductivity increases with the cubic power of the temperature, the relative contribution of the radiant conductivity was assessed for a mean temperature of 1100 K (maximal allowable wall liner temperature). For 400 μm spherical pores, λ_{rp} is less than 8×10^{-2} W/m K. Consequently, it can also be assumed that the contribution of the radiant conductivity is negligible, even at high temperature:

$$\lambda_r/\lambda_{eff} \ll 1 \tag{3.8}$$

3.1.2.4 Summary

In the case of **metallic partially-sintered materials** filled with steady air and submitted to a uniform temperature gradient, **most of the heat is transferred by the mechanism of conduction through the solid phase:**

$$\boxed{\lambda_{eff} \simeq \lambda_{cs}} \tag{3.9}$$

As the solid phase effective conductivity $\lambda_{s,eff}$ from equation 1.1 can be identified to λ_{cs}, **experimental measurements of $\boldsymbol{\lambda_{\mathrm{eff}}}$ should be representative of $\boldsymbol{\lambda_{\mathrm{s,eff}}}$.**

3.2 Models of effective thermal conductivity

Koh and Fortini (1973) claimed that the irregularities in the architecture of the porous materials make the theoretical prediction of its effective thermal conductivity "rather difficult if not impossible". In the following section, some classical models of conductivity for composite materials are introduced. They are then compared to empirical laws.

3.2.1 Theoretical models

A porous material can be seen as a composite material made of two phases: a solid and a void or fluid phase. Various models of effective conductivity for composite material were developed by simplifying the geometry. If most of the models were originally dedicated to electrical conduction in two-phase materials, the physical analogy between the phenomena allows them to be applied for thermal conduction.

3.2.1.1 Lower- and upper-bounds of the conductivity in two-phase materials

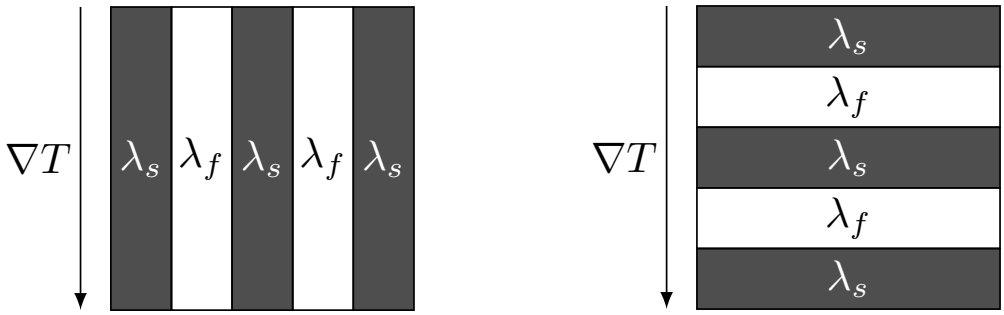

(a) Parallel model **(b)** Serial model

Figure 3.1: Models of conductivity of Wiener (1912)

The simplest models are the parallel (equation 3.10) and the serial (equation 3.11) models of Wiener (1912). He assumed that the conductivity could be predicted from the knowledge of the volume fraction of each one of the phases. In the parallel model (figure 3.1a), a two-phase medium is supposed to be represented by a succession of layers parallel to the temperature gradient. The effective conduction is in this case:

$$\lambda_{eff} = \varepsilon\lambda_f + (1-\varepsilon)\lambda_s \tag{3.10}$$

In the serial model (figure 3.1b), these layers are perpendicular to the temperature gradient

and the effective conduction is assessed as:

$$\lambda_{eff} = \frac{\lambda_s \lambda_f}{\varepsilon \lambda_s + (1-\varepsilon)\lambda_f} \tag{3.11}$$

Despite the fact that these models are too simple to describe the properties of a two-phase medium, they give the upper- and lower-bounds of the effective thermal conductivity.

3.2.1.2 Maxwell-type models

More relevant models would be the ones based on the works of Maxwell (1873). He considered low concentrations spherical inclusions without any interaction (no contact) in an homogeneous matrix. An upper-bound limit can be obtained when lower conductivity particles are embedded in high conductivity matrix:

$$\lambda_{eff} = \lambda_s + \frac{\varepsilon}{\frac{1}{\lambda_f - \lambda_s} + \frac{1-\varepsilon}{3\lambda_s}} \tag{3.12}$$

The lower-bound defined the case where high conductivity particles are embedded in a low conductivity matrix:

$$\lambda_{eff} = \lambda_f + \frac{1-\varepsilon}{\frac{1}{\lambda_s - \lambda_f} + \frac{\varepsilon}{3\lambda_f}} \tag{3.13}$$

Based on the electrical theory, other authors (Rayleigh, 1892; Meredith and Tobias, 1961; Bruggeman, 1935) tried to take into account the interactions between the inclusions. As Maxwell (1873), they studied the effect of an inclusion in a matrix but they took into account the effects of the other inclusions by the mean of an equivalent mean field.

3.2.1.3 Bruggeman-type models

Firstly, Bruggeman (1935) suggested an asymmetric theory based on a differential method. The conductivity is assessed by assuming that the composite is obtained from infinitesimal addition of conductive spherical inclusions in a host matrix. The method principle is explained in figure 3.2. It leads to:

$$1 - \varepsilon = \frac{\lambda_{eff} - \lambda_f}{\lambda_s - \lambda_f} \left(\frac{\lambda_s}{\lambda_{eff}} \right)^{(\frac{1}{3})} \tag{3.14}$$

Bruggeman (1935) also introduced a symmetric model by using an equivalent mean field approach, later taken up by Landauer (1952). The conductivity is determined with a

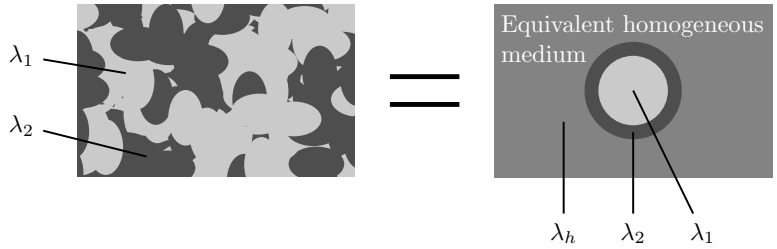

Figure 3.2: Principle of the asymmetric model of Bruggeman (1935). The grains of the phase 1 are surrounded by the phase 2 which is included in a mean phase having an intermediate composition which has the effective property of the two-phase material

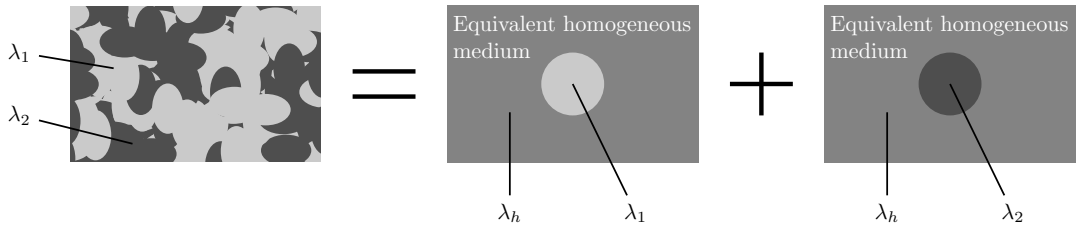

Figure 3.3: Principle of the symmetric model of Bruggeman (1935). The grains of the phase 1 and 2 are surrounded by a mean phase having an intermediate composition which has the effective property of the two-phase material

self-consistent process by computing the local field at the level of an element of the composite which is assumed to be embedded in a homogeneous medium. The homogeneous medium has the effective conductivity which has to be determined. The method principle is explained in figure 3.3. It leads to:

$$\frac{\lambda_s - \lambda_{eff}}{\lambda_s - 2\lambda_{eff}}(1-\varepsilon) + \frac{\lambda_f - \lambda_{eff}}{\lambda_f - 2\lambda_{eff}}\varepsilon = 0 \tag{3.15}$$

In the case of metallic partially-sintered materials, the conductivity of the fluid phase can be neglected compared to that of the metallic one. The previous relationships can then be reduced in terms of relative conductivity as it is introduced in table 3.1.

3.2.1.4 Other approaches

The models previously introduced suffer from the fact that they cannot take into account the particulate aspect of the partially-sintered materials. Jagota and Hui (1990) studied the effective conductivity of a random packed bed of spherical particles. They considered

Models	λ^*	
Wiener (1912) upper-bound	$1-\varepsilon$	(3.16)
Maxwell (1873) upper-bound	$1-\frac{3\varepsilon}{2+\varepsilon}$	(3.17)
Bruggeman (1935) asymmetric	$(1-\varepsilon)^{\frac{3}{2}}$	(3.18)
Bruggeman (1935) symmetric	$1-\frac{3}{2}\varepsilon$	(3.19)

Table 3.1: Theoretical models of effective thermal conductivity when the conductivity of the fluid phase can be neglected compared to the one of the solid phase

that the contact radii r_c were small compared to the radius of the particles R. and suggested the following relation:

$$\lambda_{eff} = \frac{1}{\pi R}(1-\varepsilon)N\lambda_s r_c \tag{3.20}$$

where N is the coordination number. However, as explained by Grootenhuis et al. (1952) and Biceroglu et al. (1976), the effective thermal conductivity of sintered metallic powders is well different from that of a packed bed. Indeed, in the latter, the single contact points involves huge thermal resistance and most of heat is conducted through the fluid phase. On the contrary, in the case of sintered metallic powders, the sintering necks create large contacts and the heat is therefore mostly conducted through the almost continuous metallic phase.

3.2.2 Empirical models

To avoid the issues related to the theoretical models, authors preferred to develop empirical models for partially-sintered metallic materials. Grootenhuis et al. (1952) measured the effective thermal conductivity of bronze materials having a porosity between 0 and 40%. They showed that the relative thermal conductivity λ^* of their materials could be satisfactorily predicted with the following empirical law:

$$\lambda^* = 1 - 2.1\varepsilon \tag{3.21}$$

This relationship only involves the porosity of the materials.

Later, Aivazov and Domashnev (1968) studied the effective thermal conductivity at room temperature of hot-pressed titanium-nitride specimens with a porosity ranging from 0 to 40%. They also suggested to correlate all their relative effective thermal conductivities with a function dependent on the porosity:

$$\lambda^* = \frac{1-\varepsilon}{1+n\varepsilon^2} \tag{3.22}$$

They introduced a geometrical constant n which would be a function of the distribution and shape of the pores. In a study made by the NASA and relative to the transpiration cooling for aerospace applications, Koh and Fortini (1973) carried out experimental measurements of effective thermal conductivity of copper and 304L stainless steel sintered powders and 304L stainless steel Rigidmesh materials. They studied materials with a porosity lower than 40%. They completed their data with thermal conductivity measured on metallic foams (Foametal®), sintered metallic fibers (Feltmetal®) and non-spherical sintered powders of other authors. They showed that the relation of Aivazov and Domashnev (1968) fitted well with their data if $n = 11$. Tye (1973) also claimed that $n = 11$ was the best value for the effective thermal conductivity of these materials. Biceroglu et al. (1976) measured effective thermal conductivity of stainless steel sintered powder but at a higher porosity level ranging from 33% to 60%. They also showed that the equation 3.22 was able to predict their data with less than 20% of error if $n = 11$.

Finally, Agapiou and DeVries (1989) measured the effective thermal conductivity of 304L stainless steel sintered powders with a porosity varying from 10% to 36%. They also explained that the relative effective thermal conductivity can be predicted thanks to the porosity but they suggested a new model to correlate all the data:

$$\lambda^* = \frac{1-1.88\varepsilon}{1+0.38\varepsilon-2.3\varepsilon^2} \tag{3.23}$$

As a conclusion, all the empirical laws found in the literature suggest that the relative thermal conductivity of porous metallic material can be predicted with only the use of the porosity.

3.2.3 Summary

The behavior of the different models previously introduced are represented altogether in a same graph (figure 3.4). Lower bound models are not represented since they predict a null conductivity for any porosity except for $\varepsilon = 1$.

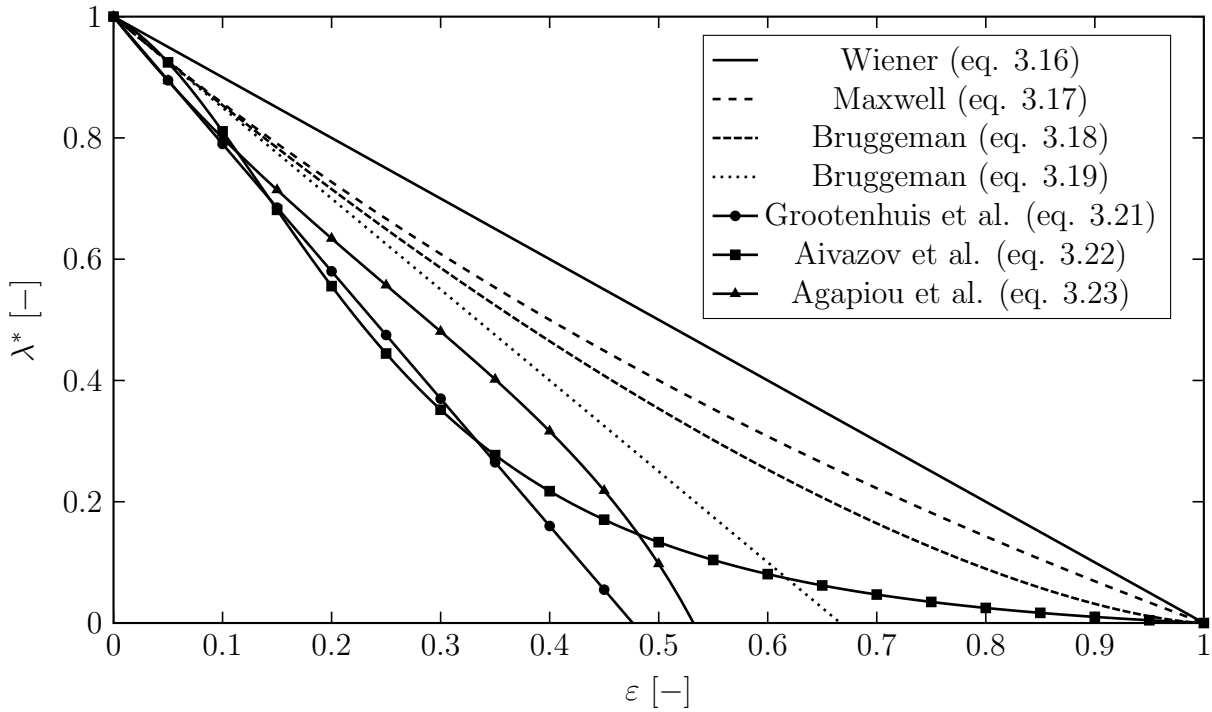

Figure 3.4: Comparison of the different models predicting the relative conductivity as a function of the porosity

It can be noticed that the theoretical models predict higher values of relative conductivity than the empirical ones. Moreover, some models predict a percolation threshold (equations 3.19, 3.21 and 3.23).

3.3 Experimental determination of the effective thermal conductivity

The effective thermal conductivity of partially-sintered metallic samples was indirectly assessed thanks to the experimental determination of their thermal diffusivities. The thermal diffusivity a, defined as:

$$a = \frac{\lambda}{\rho c_p} \tag{3.24}$$

was measurement with the flash method at the laboratory ONERA from Châtillon (France). Calorific capacities c_p found in the literature and additional density ρ measurements allowed the assessment of the effective thermal conductivity.

3.3.1 The flash method

3.3.1.1 The measurement principle

The flash method consists in producing a uniform light pulse on one side of a cylindrical sample and then in analyzing the evolution of the temperature on the other side. The flash method principle is summarized in figure 3.5.

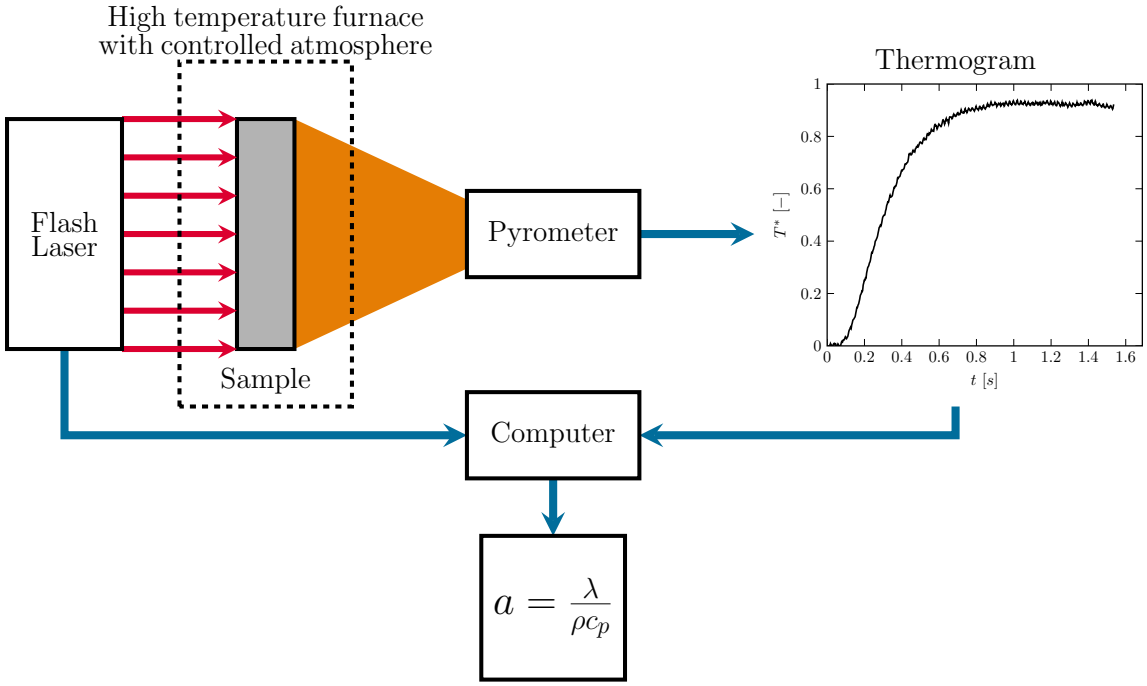

Figure 3.5: Principle of the flash method

The energy pulse is generated by a laser having the same diameter as the sample. The samples have to be homogeneous and opaque to the laser. The temperature sensor at the back side of the sample is a high sensitivity and ultra-fast pyrometer. The evolution of the back side transient temperature with time (thermogram) is compared to a theoretical model and the thermal diffusivity is then deduced. For more explanation about the flash method, the reader may refer to paper of Demange (1999). Contrary to the simplified method originally suggested by Parker et al. (1961), the thermal losses caused by possible convection are taking into account in the following measurements. Finally, due to the low temperature variation during a test ($\preceq 5\ K$), the thermophysical properties of the material are supposed to remain constant. In the following, the thermograms are plotted using a dimensionless temperature T^* defined as:

$$T^* = \frac{T \rho c_p L}{Q} \tag{3.25}$$

where Q is the energy delivered by the laser beam and L is the thickness of the sample.

3.3.1.2 The experimental benches

Two benches were developed at ONERA for measuring the diffusivity at temperatures varying between $20°C$ and $2500°C$. They are distinguished by their type of laser:

- Diffusimeter Quantel: uses phosphate glass pulse laser with a pulsed at 1.06 μm, at a maximal energy of 100 J for 0.5 ms;
- Diffusimeter Triagon: uses CO_2 continuous laser with pulses at 10.6 μm and a mean energy of 20 J.

Both apparatus are composed of:

- a high temperature vacuum furnace with graphite resistors;
- an optical detector HgCdTe;
- amplification and insulation electronic devices;
- a computer to control the measurements and post-process them.

The cylindrical test chamber is cooled with water and is linked to a vacuum pump allowing measurements under vacuum or under controlled atmosphere of inert gas.

3.3.2 The samples

The diffusivity of twelve cylindrical partially-sintered samples was measured. The samples were either bronze partially-sintered spherical powders (SP) or 316L stainless steel partially sintered irregular powders (IP). Pictures of some samples can be found in figure 3.6.

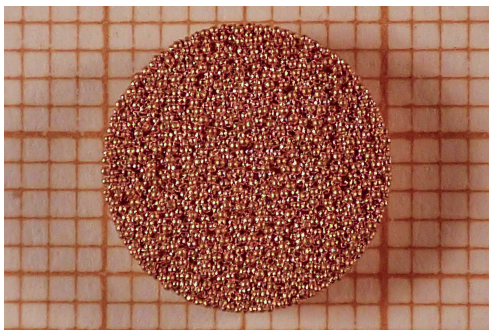

(a) Sample of partially-sintered bronze 300 μm spherical powders (1 cm diameter)

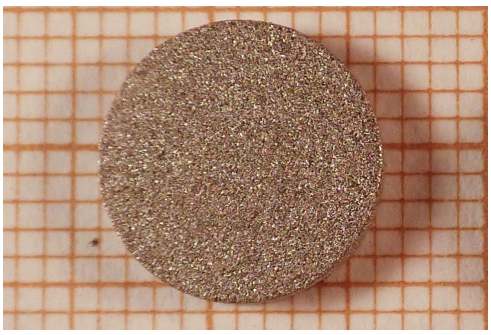

(b) Sample of partially-sintered stainless-steel 100 μm irregular powders (1 cm diameter)

Figure 3.6: Samples for diffusivity measurements

The diameter of the cylinders was about 1 cm and the thickness e varied between 1.8 and 3 mm depending on the samples. The characteristics of all the measured samples are summarized in table 3.2.

specimen #	powder type –	powder size $[\mu m]$	e $[mm]$	ε [%]
1	IP	30	2.1	24
2	IP	100	1.9	36
3	IP	100	1.9	37
4	IP	150	2.0	37
5	IP	400	2.0	41
6	IP	600	2.0	51
7	SP	50	2.0	36
8	SP	50	2.0	36
9	SP	150	2.1	33
10	SP	150	2.1	32
11	SP	300	3.0	38
12	SP	300	3.0	37

Table 3.2: Characteristics of the samples analyzed with the flash method (SP:partially-sintered spherical powder, IP: partially-sintered irregular powder)

3.3.3 Measurement at ambient condition

The diffusivity of each sample was measured at ambient temperature with ambient air. For repeatability, each sample was tested five times. The thermal conductivity was then deduced from the mean diffusivity thanks to the following relationship:

$$\lambda_{eff} = a(1-\varepsilon)\rho_{s,bulk}c_p \tag{3.26}$$

where $\rho_{s,bulk}$ is the density of the bulk material. In order to judge the accuracy of the measured diffusivity, figure 3.7 introduces thermograms of some samples. The thermogram obtained from experimental temperature measurements and the one from the theoretical model after fitting are plotted together as a function of the time.

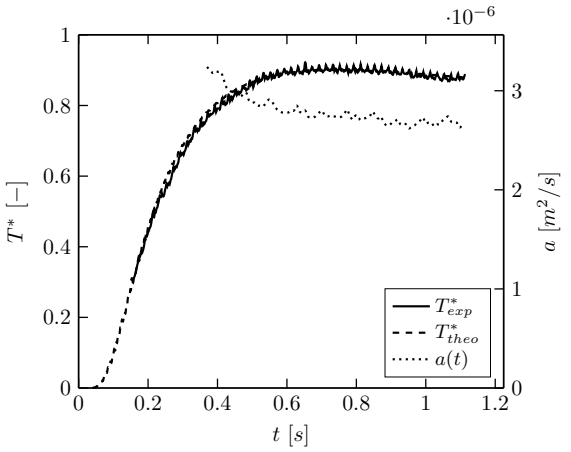

(a) specimen #1: IP 30 μm

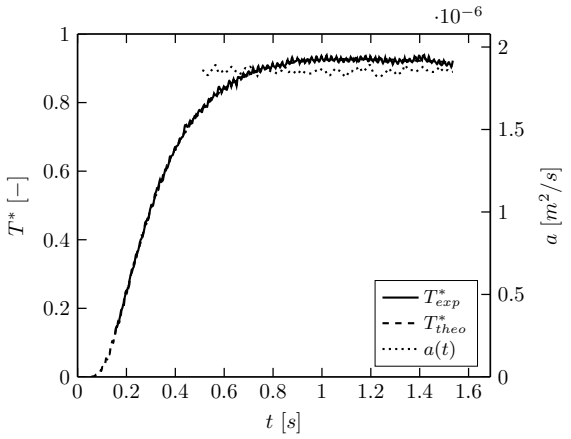

(b) specimen #5: IP 400 μm

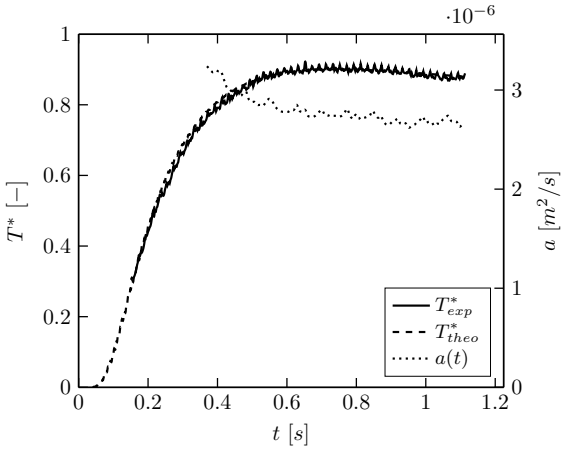

(c) specimen #6: IP 600 μm

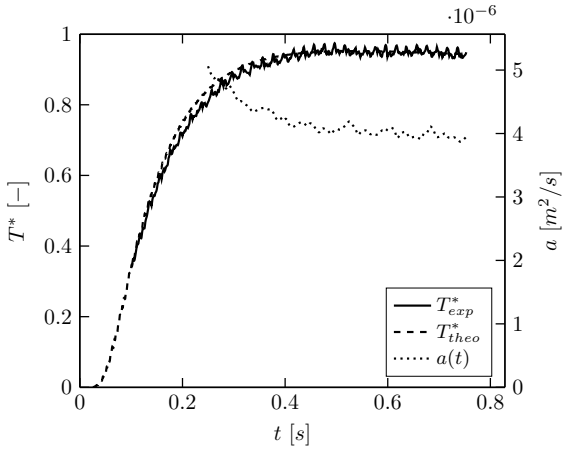

(d) specimen #7: SP 50 μm

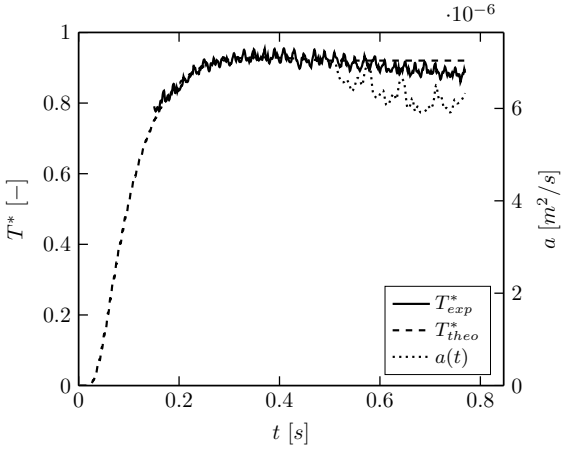

(e) specimen #10: SP 150 μm

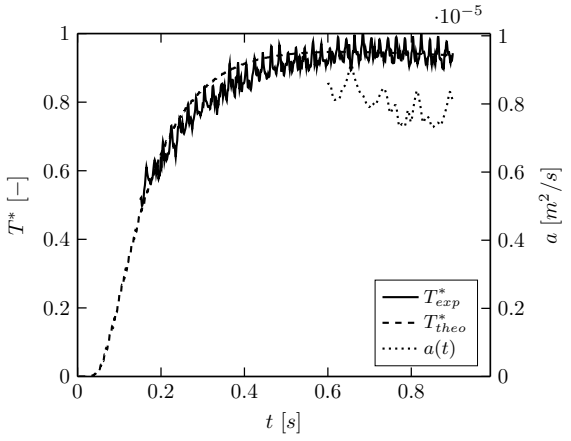

(f) specimen #12: SP 300 μm

Figure 3.7: Thermograms of different specimens

The first trials showed that the recorded dimensionless temperatures were not null at the initial time. This suggested that a part of the light pulse managed to pass through the samples and was then detected by the pyrometer. The opaque material assumption was therefore not respected and the accuracy of the measurements is reduced. To limit the errors, the signal was recorded only after a small time interval in order not to disrupt too much the fit with the theoretical model.

The diffusivity evolution is a good indicator of the quality of the measurements. For a homogeneous material and without any experimental anomalies, the diffusivity should stay constant over time. Variations of the diffusivity mean either a heterogeneous conductivity in the material, or experimental anomalies (bad assessment of heat losses, misalignement of the laser with the sample, delay of the clock compared to the laser pulse).

As regards the materials made of irregular particles, rather good fits are obtained between the experimental and the theoretical thermograms. The small fluctuations of the diffusivity ensure a rather accurate prediction of the conductivity.

Regarding the materials made of spherical powders, only the specimens with very small particles give really accurate results. With particle sizes of 150 μm and 300 μm, noisy experimental thermograms were recorded. Large discrepancies between the experimental and the theoretical temperature curves and important variations of the diffusivities can also be observed. As a result, less confidence was attributed to these measurements. Two reasons may explain this difference in behavior:

- the smooth surface around the bronze particles may help the light impulse to be reflected multiple times on the powder and thus to penetrate in the material. The bigger pores of the bronze samples may also help the penetration of the light impulse;
- bronze samples have bigger surface irregularities as it can be observed in figures 3.8a-b. The actual geometry is then further from the ideal theoretical model geometry.

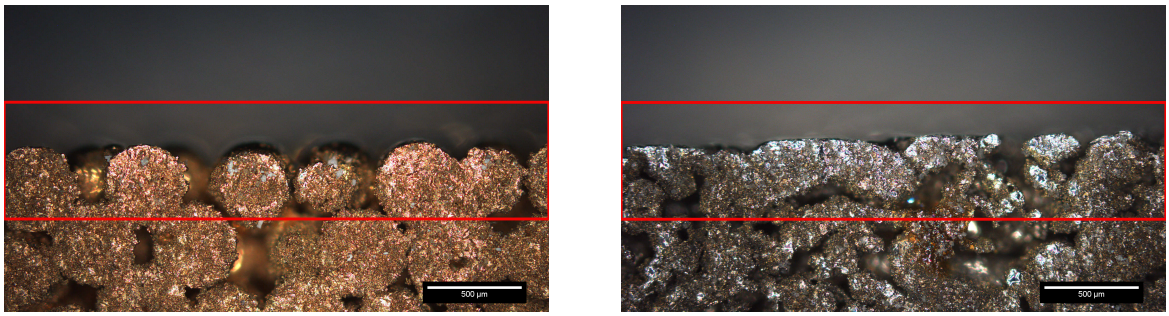

(a) Spherical particles of 400 μm **(b)** Irregular particles of 400 μm

Figure 3.8: Cross-sections of partially-sintered samples showing the irregularities at the surface

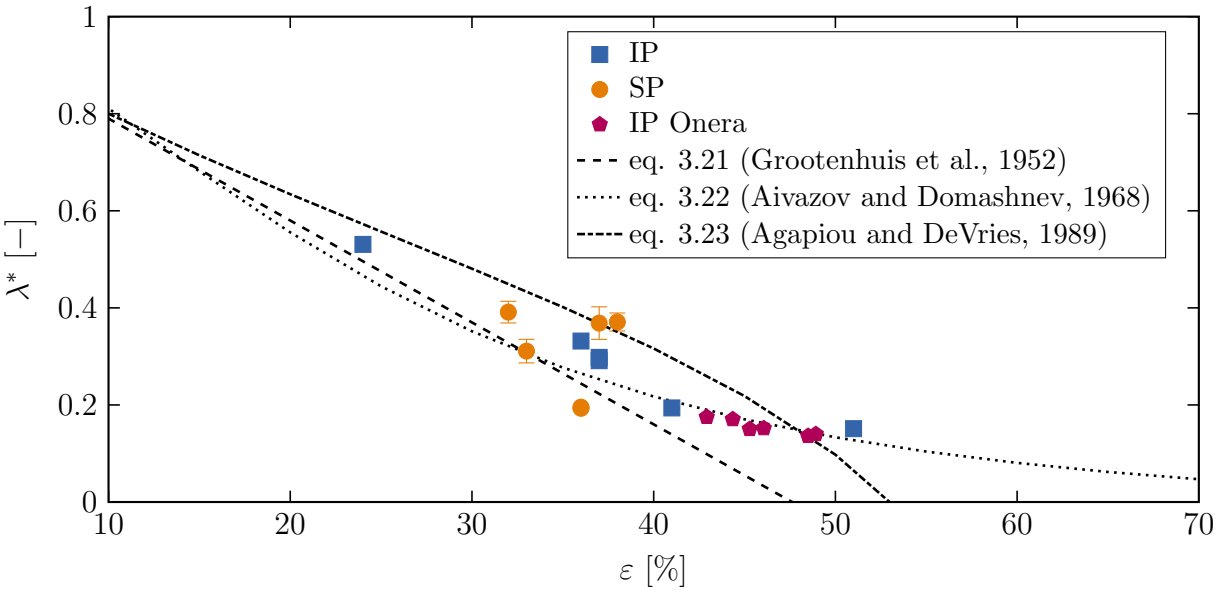

Figure 3.9: Relative effective thermal conductivities of SP and IP samples measured with the flash method. Data are compared to empirical laws from the literature.

The assessed relative effective thermal conductivities are shown figure 3.9. Additional data measured by ONERA on partially-sintered irregular Inconel 600 powders are also given. The experimental data can be compared with the empirical laws introduced in the previous section. The classical theoretical laws are not given since they overestimate too much the relative conductivity. **The effective thermal conductivity of the partially-sintered materials made of irregular powders (IP) agrees quite well with the empirical law of Aivazov and Domashnev (1968).** The law of Grootenhuis et al. (1952) predicts a cut-off porosity value at $\varepsilon = 0.48\%$ which does not seem appropriate for IP samples. The experimental data of partially-sintered spherical powder (SP) show a large discrepancy which can be justified with the reasons previously mentioned. At this point, even though the data of the SP samples remain close to what is predicted by the three empirical laws, it is difficult to favor an empirical model over the two others.

3.3.4 Measurement at different temperatures

The porous material is aimed to be used at temperatures far much higher than the ambient one. As a result, it is important to be able to predict the evolution of the relative conductivity with the temperature. If the effective thermal conductivity is mainly due to the contribution of the conduction in the solid phase, even at high temperature, there is no reason to detect an evolution of the relative conductivity. This was the conclusion

made by Koh and Fortini (1973) and Agapiou and DeVries (1989) after additional measurements of thermal conductivity at higher temperatures (up to 300 $°C$ for Agapiou and DeVries (1989) and up to 1000 $°C$ for Koh and Fortini (1973)). To test this assumption, additional diffusivity measurements were carried out in this PhD thesis on irregular powder samples (#3, 4 and 5) and at different temperatures (373, 473, 673, 873 and 1073 K). To avoid oxidation, the tests were carried out under vacuum. To satisfy a good temperature homogenization, the first measurement was performed 20 minutes after the temperature rise. The figure 3.10 gives the evolution with the temperature of the relative thermal conductivities of the specimens #3, 4 and 5. The data are completed with additional measurements made by ONERA with the flash method on partially sintered irregular Inconel 600 powders as well as with experimental measurements made by Agapiou and DeVries (1989) and Koh and Fortini (1973).

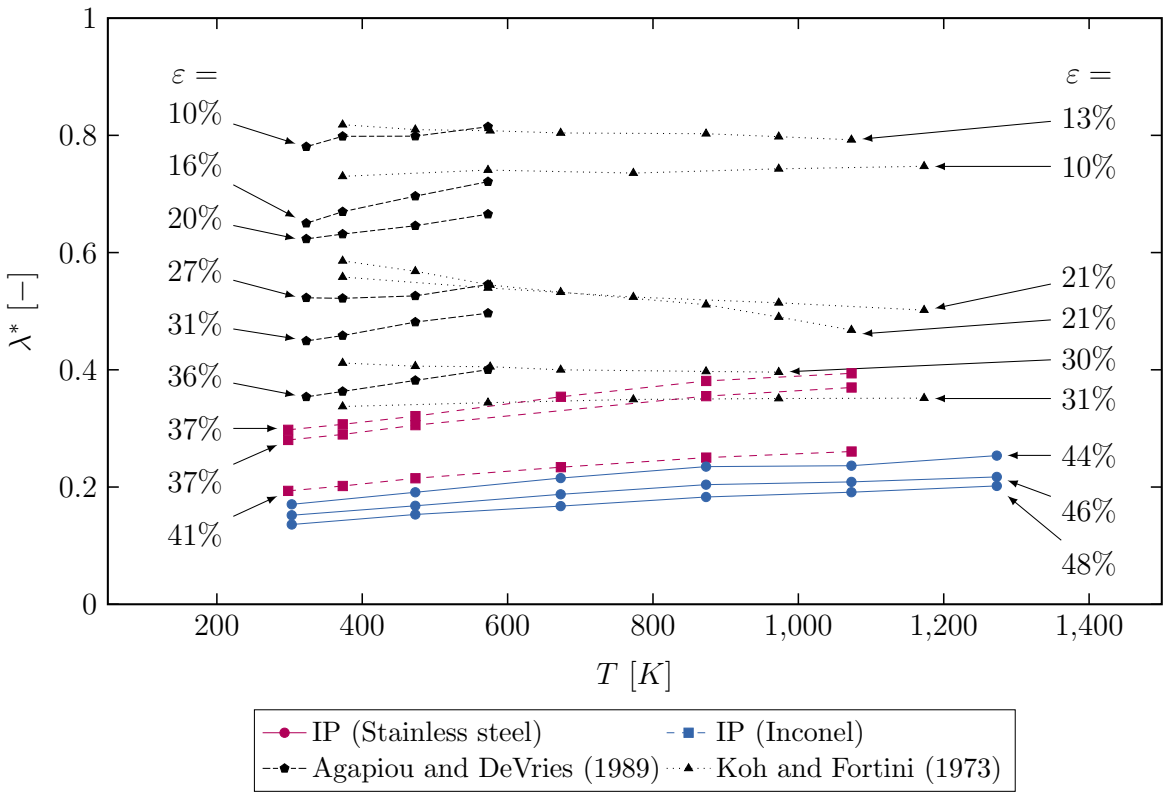

Figure 3.10: Relative thermal conductivity of partially sintered irregular powders of 316L stainless steel and Inconel 600 as a function of the temperature. The data are completed with the experimental measurements of Agapiou and DeVries (1989) and Koh and Fortini (1973). The porosity of each one of the tested porous materials is also given.

Once again, it can be noticed that the relative thermal conductivity clearly decreases

with the porosity at a given temperature. The relative thermal conductivity of the IP materials shows a slight increase with the temperature. This increase is against the idea of a constant relative effective thermal conductivity. However, the analysis of the data of Agapiou and DeVries (1989) seems also to show this increase. Regarding the works of Koh and Fortini (1973), an inverse trend can however be emphasized. A change in relative effective thermal conductivity could be associated to the increasing participation of one or more heat transfer mechanisms which were neglected (conduction and convection in the porous phase, mechanisms of radiation through the pores). Since these mechanisms can only increase the effective conductivity, it is quite unlikely to have a relative thermal conductivity which decreases with the temperature rise as in the works of Koh and Fortini (1973). Moreover, as the measurements made on IP materials were carried out under vacuum, conduction and convection through the void phase cannot take place. It was also shown in section 3.1.2.3 that the radiant conductivity through pores, even a high temperature, could be neglected compared to the conductivity in the solid phase. The slight variations of the relative thermal conductivity are therefore attributed to measurement uncertainties such as change in the material emissivity. **Based on these results, it will consequently be assumed in the following that the relative thermal conductivity of partially sintered metallic powders remains constant with the temperature in the porosity range of $10 - 50\%$.**

3.3.5 Summary

In this section, experimental measurements of effective thermal conductivity were performed with the flash method on partially-sintered spherical and irregular metallic powders. The results revealed that **the effective conductivity of irregular powders follows quite well empirical laws.** Moreover, it was shown that the **relative thermal conductivity of the studied partially-sintered materials could be considered as independent of the temperature for temperature up to 1300 K.** However, as the measurements carried out on partially-sintered spherical bronze powders were not satisfying enough, it was decided to complete the data with an electrical approach.

In pure metals, the free electrons are responsible for the electrical conductivity and most of the thermal conductivity. These two physical parameters are linked by the Wiedemann-Franz-Lorentz law (Koh and Fortini, 1973):

$$\lambda = \underbrace{L\sigma_{el}T}_{Electronic\ component} + \underbrace{C}_{Lattice\ component} \tag{3.27}$$

where L is the Lorentz constant, σ_{el} is the electrical conductivity and C is the lattice

component of thermal conductivity. Even though Koh and Fortini (1973) explained that the lattice component would depend on the kind of materials and on the porosity, its contribution remains low for good electrical and thermal conductors. Moreover, as the air is also a very bad electrical conductor, it does not participate to the effective electrical conductivity if the solid matrix is well interconnected. A simple relationship between the effective thermal conductivity and the effective electrical conductivity is therefore expected. Grootenhuis et al. (1952), Aivazov and Domashnev (1968) and Koh and Fortini (1973) showed that the relative thermal conductivity and the relative electrical conductivity of their samples were equal for temperature ranges where there is no magnetic transformation:

$$\boxed{\lambda^* = \sigma_{el}^*} \tag{3.28}$$

It was therefore decided too use this property to complete the data thanks to electrical conductivity measurements on different partially-sintered metallic powders.

3.4 Experimental determination of the effective electrical conductivity

The Ohm's law relates the ease of a material to transmit an electric current I when it is submitted to a voltage difference V_{el}:

$$V_{el} = IR \tag{3.29}$$

where R (Ω) is the resistance of the material, dependent on the material configuration. The electrical resistivity ρ_{el} is preferred when dealing with intrinsic material properties because of its geometry independence. For a constant cross-section specimen, it is related to R thanks to the following expression:

$$\rho_{el} = \frac{RA}{L} \tag{3.30}$$

where A and L are respectively the cross-sectional area and the length of the specimen. The electrical conductivity σ_{el} is simply the inverse of the electrical resistivity:

$$\sigma_{el} = \frac{1}{\rho_{el}} \tag{3.31}$$

The electrical conductivity of partially-sintered metallic samples was indirectly determined by the measurement of the electrical resistance R via the four-point probes method at the laboratory *SIMaP*.

3.4.1 The four-point probes method

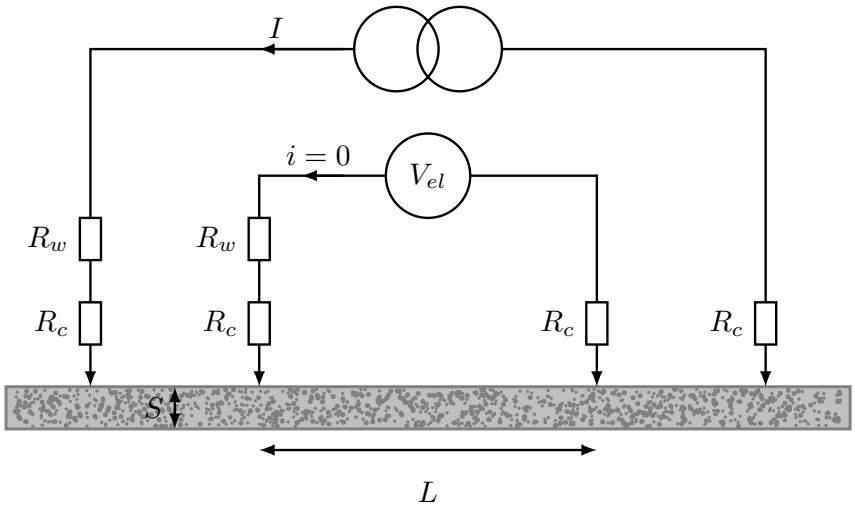

Figure 3.11: Schematic representation of the four-probes method apparatus

The principle of the four-point probes method is given figure 3.11. This method consists in measuring the electrical resistivity by using separate current-carrying and voltage-sensing electrodes. The cross-sectional area of the samples has to be known. This apparatus permits a more accurate measurement than the two-point probes method. Indeed, the use of a separated infinite impedance voltmeter ensures negligible effects of wire and contact resistances (R_w and R_c). As the apparatus measures the apparent electrical resistance of the sample between the two voltage-sensing probe, separated by a distance L, the electrical resistivity is in fact indirectly measured. In this study, voltage differences are measured for values of current intensity ranging from $-100\ mA$ to $100\ mA$. The electrical resistance is deduced from the slope of the linear relationship predicted by the Ohm's law (equation 3.29) between V and I as shown figure 3.12. Electrical resistances are then measured for different voltage-sensing spacings L. Since the cross-sectional area of the sample is known and constant, the electrical resistivity can be deduced from the slope of the $R - L$ curve using equation 3.30 as shown figure 3.13.

Thanks to the accuracy of both the voltmeter and the current generator and to the choice of the used apparatus, the uncertainties on the measured resistances can be neglected. Indeed, the main uncertainties in the assessment of the electrical resistivity take their origin in the measurement of both the sample cross-sectional areas and the spacing between the voltage-sensing probes. A reduction of the voltage-sensing probe spacing uncertainty was ensured by taking samples as long as possible and by measuring resistances at five different probe spacings.

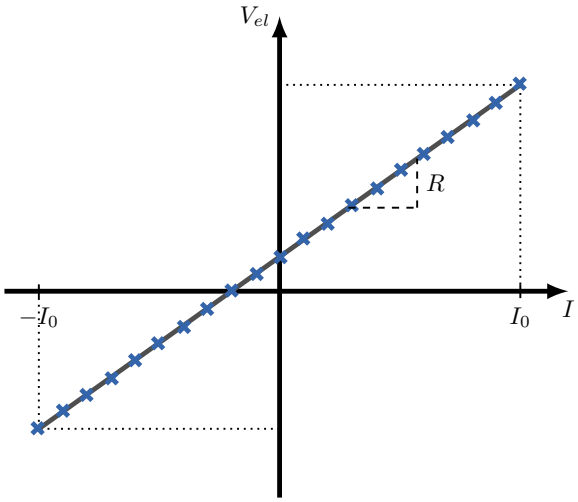

Figure 3.12: Determination of the electrical resistance for a given voltage-sensing spacing thanks to the V/I curve

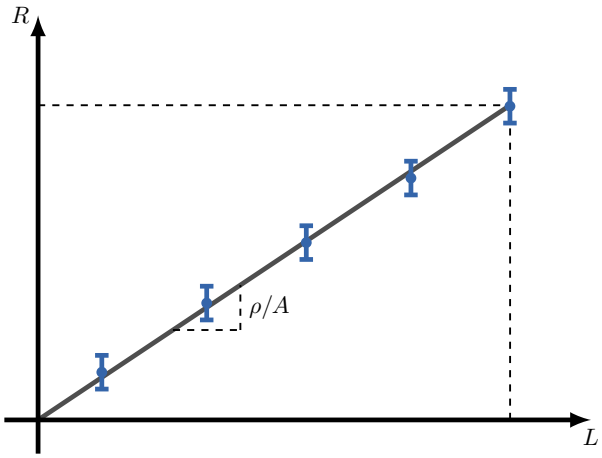

Figure 3.13: Determination of the electrical resistivity thanks to the R/L curve and knowing the cross-sectional area A of the sample

3.4.2 The samples

Partially-sintered materials made of spherical bronze powders and stainless steel irregular powders were analyzed with the four-point probes method. Two batches of samples were analyzed. The first one ($B1$) was composed of bars cut by Electrical Discharge Machining (EDM) from bigger disks (figures 3.14a and 3.14b). The EDM ensured a good surface quality of the cut faces and preserves the pores. Indeed, mechanical cuts tend to create plain surfaces, thus creating preferential electrical paths. The second batch ($B2$) was composed of 5 cm length preformed slabs (figure 3.14c). The characteristics of all the samples are introduced in table 3.3.

(a) EDM cut of a partially-sintered bronze bar (7 cm in length)

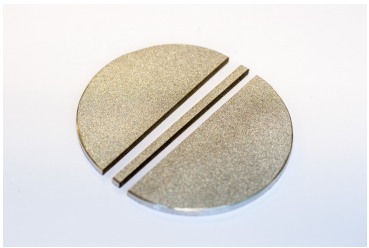

(b) EDM cut of a partially-sintered stainless steel bar (7 cm in length)

(c) Preformed slabs of partially-sintered bronze and stainless steel powders (5 cm in length)

Figure 3.14: Samples for electrical conductivity measurements

B1				B2							
powder				powder				powder			
type	size	S	ε	type	size	S	ε	type	size	S	ε
[−]	[μm]	[mm^2]	[%]	[−]	[μm]	[mm^2]	[%]	[−]	[μm]	[mm^2]	[%]
SP	200	7.9	36	SP	200	24.4	18	IP	300	28.6	21
SP	300	8.5	36	SP	200	23.8	15	IP	300	27.5	18
SP	400	8.5	38	SP	300	25.8	19	IP	300	28	19
IP	100	8.4	35	SP	300	27.3	20	IP	400	34.2	33
IP	150	7.6	30	SP	400	25.2	19	IP	400	30.2	25
IP	200	8.2	34	SP	400	26.9	21	IP	400	28.5	21
IP	300	8.6	38	IP	300	33.4	33	IP	400	28.1	20
IP	400	8.4	37	IP	300	29.8	24	IP	400	27.6	19

Table 3.3: Characteristics of the samples analyzed with the four-point probes method (powder type and size, surface area and porosity)

3.4.3 Measurement at ambient temperature

For reasons of simplicity, the electrical conductivities of the samples introduced in the previous section were only measured at ambient condition. The experimental results are plotted in figure 3.15.

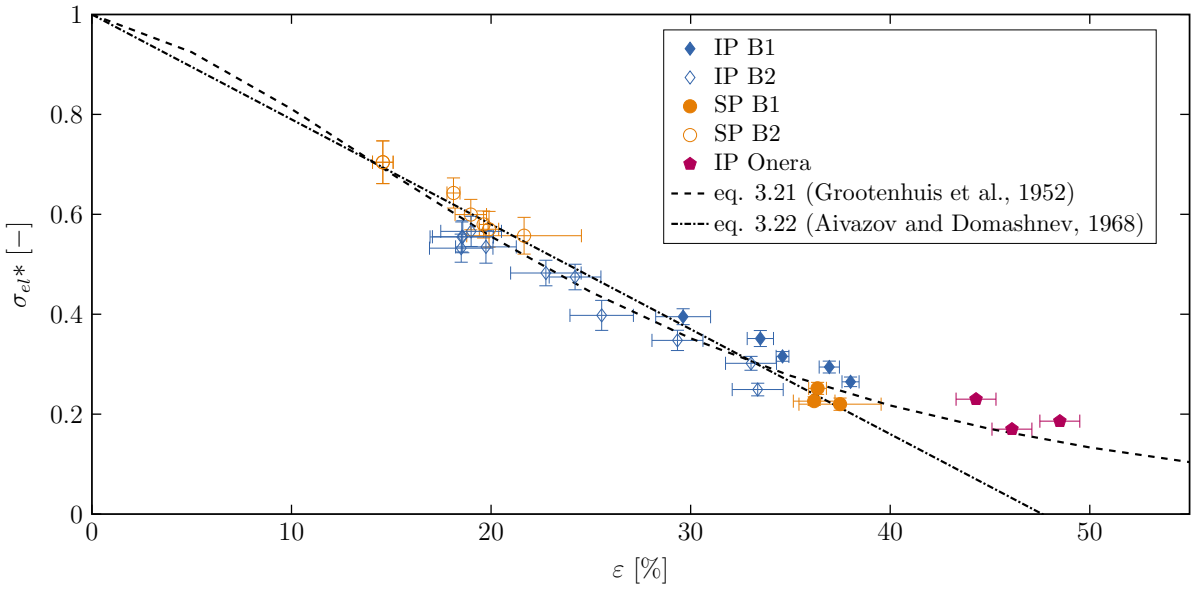

Figure 3.15: Effective electrical conductivities of SP and IP samples measured with the four-point probes method. Data are compared to empirical laws from the literature

.

Additional experimental data obtained by *ONERA* on partially-sintered irregular powders of Inconel 600 (IP Onera) are added to the graph. The data are compared to the empiral laws of Grootenhuis et al. (1952) (eq. 3.21) and Aivazov and Domashnev (1968) (eq. 3.22) which are also applicable to the relative effective electrical conductivity. Once again, **experimental data agree very well with both empirical laws up to a porosity of** 40%**. Beyond this threshold, the data measured by Onera on Inconel partially-sintered materials follow better the trend of the law of Aivazov and Domashnev (1968) (equation 3.22).** The shape of the powder as well as the metallic alloy employed do not impact sensitively the evolution of the relative electrical conductivity of the metallic partially-sintered materials.

3.5 Summary

The effective thermal and electrical conductivity of partially-sintered metallic materials were analyzed. It was shown that the effective thermal conductivity of the studied materials is mainly due to conduction through the solid phase, even at high temperature. The effective thermal conductivity can therefore be identified to the effective thermal conductivity of the solid phase $\lambda_{s,eff}$ appearing in the heat equation 1.1. It was also shown that **the temperature has little impact on the relative thermal conductivity** (ratio of the effective thermal conductivity to the thermal conductivity of the dense material). Moreover, the relative thermal or electrical conductivity of the tested samples **is mainly affected by porosity**. The relative conductivities of all the studied alloys follow a same trend. This evolution is well described by the empirical law of Aivazov and Domashnev (1968) for a $10 - 50\%$ porosity range and particle sizes varying from 30 to 600 μm. The method introduced in the figure 3.16 enables the assessment of the thermal conductivity of any partially-sintered metallic material at a given temperature. The relative effective thermal conductivity λ^* of a metallic architecture is computed from the equation of Aivazov and Domashnev (1968). The effective thermal conductivity $\lambda_{s,eff}$ at a given solid temperature T_s is then deduced from λ^* and from the conductivity of the constitutive material $\lambda_{s,bulk}$ computed at the temperature T_s.

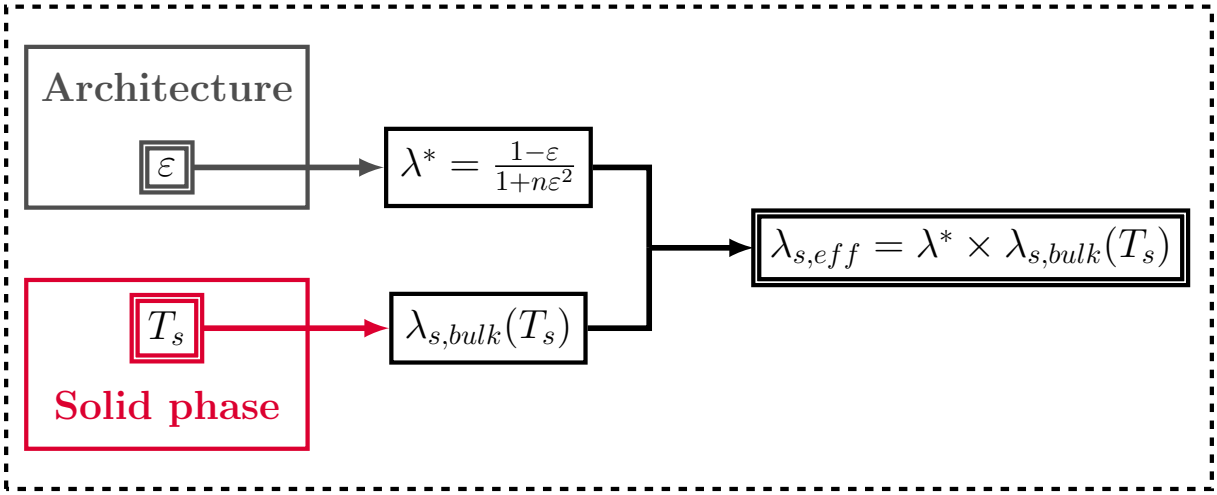

Figure 3.16: Method to assess the effective thermal conductivity of a partially-sintered metallic powder at a given temperature

Chapter 4

Permeability of partially-sintered materials

Contents

The permeability characterizes the ability of a porous material to let a fluid flow through it under the effect of a pressure difference. It has an important role in transpiration cooling:

- it determines the air flow rate which internally cools the liner;
- it determines the ejection velocity of the cooling air on the liner inner side which forms the protective boundary layer.

This chapter aims to study how the architecture of partially-sintered powders can impact their permeability.

4.1 Flow through a porous material

4.1.1 Introduction

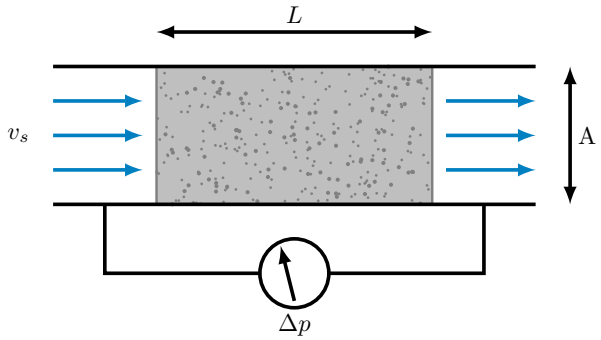

Figure 4.1: Flow through a porous media.

As shown in figure 4.1, if a pressure difference Δp is applied on a porous duct of length L and of cross-sectional area A, a flow is created with a **superficial velocity $\mathbf{v_s}$** defined as:

$$v_s = \frac{q_v}{A} \tag{4.1}$$

This superficial velocity is defined as the velocity that the fluid would have through the empty tube at the same volumetric flow rate q_v. **The challenge is to predict this superficial velocity when the pressure gradient is known and vice versa.**

Fluid flow problems are usually described and solved thanks to the well-known Navier-Stokes equation:

$$\rho_f \left[\frac{\partial \vec{v}}{\partial t} + \left(\overline{\overline{\nabla}} \vec{v} \right) . \vec{v} \right] = \rho_f \vec{g} - \overline{\nabla} p + \eta \overline{\Delta} \vec{v} + \frac{1}{3} \eta \overline{\nabla} (\overline{\nabla} . \vec{v}) \tag{4.2}$$

where ρ_f, η, $\vec{g}$, p, $\vec{v}$ are the fluid density, the fluid dynamic viscosity, the gravitational acceleration, the pressure and the velocity vector respectively. However, when flows through porous media are involved, the complexity of the architecture (scale and shape of the pores) can make this equation difficult to be solved analytically as well as numerically. To overcome this issue, macro-scale models have been developed to describe the behavior of the flow. The porous medium is then considered as a homogeneous medium with effective properties.

4.1.2 Flow regimes

A flow can be described by its regime: laminar, transitional or turbulent. It is generally determined thanks to the Reynolds number Re:

$$Re = \frac{\rho_f v l}{\eta} \tag{4.3}$$

where v is the flow velocity and l is a characteristic length (for instance the pipe diameter). This dimensionless number measures the ratio of inertial forces to viscous forces. At low Reynolds number, the flow is considered as laminar and can be described as parallel layers (figure 4.2a). Energy losses are mainly due to viscous drags. On the contrary, at high Reynolds number, the flow is considered as turbulent and is marked by the apparition of eddies, vortices and other flow instabilities which cause additional drags (figure 4.2b). Whatever the flow regime, it is important to emphasize the existence of a laminar boundary layer whose thickness decreases with the increasing Reynolds number.

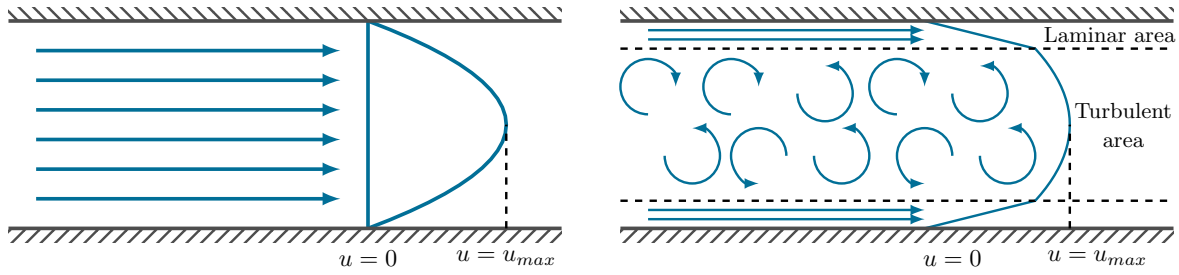

(a) Laminar flow in a pipe at low Reynolds number

(b) Turbulent flow in a pipe at high Reynolds number

Figure 4.2: Typical flow pattern in pipe at different regimes.

In porous flow problems, it is common to characterize the flow with the modified Reynolds number Re' defined as:

$$Re' = \frac{d_p \rho_f v_s}{(1-\varepsilon)\eta} \tag{4.4}$$

where d_p is the equivalent particle diameter and ε is the porosity. In the case of packed beds, the typical Reynolds number ranges are introduced in table 4.1.

Regime	Value
Laminar	$Re' < 10$
Transitional	$10 < Re' < 1000$
Turbulent	$Re' > 1000$

Table 4.1: Reynolds number boundaries for flow through packed beds (Ergun, 1952)

Note that another definition uses the square root of the permeability coefficient K, (which will be introduced section 4.1.3) as the characteristic length:

$$Re'' = \frac{\sqrt{K}\rho_f v_s}{\eta} \tag{4.5}$$

The threshold value to consider a flow as laminar is then $Re'' < 10$. This is the definition used by the software *GeoDict* which will be described in section 4.2.1. It has the advantage to not require to define a particle diameter. Other common definitions of Reynolds numbers can be found in the literature. Many of them are reported by Zeng and Grigg (2006).

In this chapter, only laminar flows through porous media will be considered. This assumption will be discussed later in the study.

4.1.3 Macro-scale description of the flow

The first macro-scale description of an incompressible flow through a porous medium is due to Darcy (1857). Based on water flow measurements through sands and at low Reynolds number, he proposed the following fundamental equation:

$$-\frac{\Delta p}{L} = \frac{\eta}{K} v_s \tag{4.6}$$

This equation predicts viscous losses with a linear relationship between the pressure gradient and the superficial velocity. It also involves **the permeability coefficient K** $[m^2]$ which is **only dependent on the porous geometry.**

Later, Forchheimer (1901) studied flow through porous media at higher Reynolds number. In order to model the appearance of inertial losses, due to laminar as well as

turbulent effects, he suggested to extend Darcy's law by adding a quadratic velocity term:

$$-\frac{\Delta p}{L} = \frac{\eta}{K} v_s + \beta \rho_f v_s^2 \tag{4.7}$$

The new term involves the **Forchheimer coefficient $\boldsymbol{\beta}$** $[m^{-1}]$ which is also **only dependent on the geometry of the porous architecture.** This equation, better known as the Darcy-Forchheimer equation, is widely accepted in the scientific domain to describe flow through various kind of porous materials: through ceramic filters (De Freitas et al., 2006), through metal foams (Reutter et al., 2008), through open-cellular materials (Bonnet et al., 2008), through fibrous media (Papathanasiou et al., 2001), etc. **However, the equation 4.7 does not allow the prediction of the pressure losses if the permeability coefficient and the Forchheimer coefficient have not been previously determined.** To overcome this issue, authors tried to develop specific semi-empirical models and thus expressed the permeability and the Forchheimer coefficients as a function of geometrical parameters:

$$\boxed{K,\beta = f(\text{architecture})} \tag{4.8}$$

Most of these efforts were focused on the description of flows through packed beds.

4.1.4 Geometrical models for K and β

4.1.4.1 The case of packed beds

The first attempts to develop a geometrical model of permeability may be attributed to Kozeny (1927) and Carman (1937). They were focused on low Reynolds flows through packed beds ($Re' < 10$). The porous phase was modeled as an equivalent group of tubes of length L_p and of hydraulic diameter d_h defined as:

$$d_h = \frac{4A_x}{p_w} \tag{4.9}$$

where A_x and p_w are the cross sectional area open to the flow and the wetted perimeter respectively. For monomodal packed beds of spherical particles:

$$d_h = \frac{2\varepsilon}{3(1-\varepsilon)} d_p \tag{4.10}$$

where d_p is the particle diameter. From the Hagen-Poiseuille equation, they derived the well known semi-empirical Kozeny-Carman equation (or Blake-Kozeny equation):

$$-\frac{\Delta p}{L} = 180 \frac{(1-\varepsilon)^2}{d_p^2 \varepsilon^3} \eta v_s \tag{4.11}$$

To deal with flow in packed beds, it is common to define a friction factor f as:

$$f = -\left(\frac{d_p}{L}\right)\frac{\varepsilon^3}{(1-\varepsilon)}\frac{\Delta p}{\rho_f v_s^2} \tag{4.12}$$

and the Carman-Kozeny equation can be rewritten as:

$$f = \frac{180}{Re'} \tag{4.13}$$

When the flow becomes turbulent, it was experimentally shown that the friction factor only depends on the roughness and not on the Reynolds number anymore. This flow regime ($Re' > 1000$) is then described by the Burke-Plummer equation (Ergun, 1952):

$$-\frac{\Delta p}{L} = 1.75\frac{(1-\varepsilon)}{d_p\varepsilon^3}\rho_f v_s^2 \tag{4.14}$$

which can also be rewritten under a dimensionless form:

$$f = 1.75 \tag{4.15}$$

Ergun (1952) claimed the existence of a smooth transition from all-laminar to all-turbulent flows and suggested to describe the pressure losses at any flow regime by simply adding the Burke-Plummer equation to the Kozeny-Carman one:

$$f = \frac{150}{Re'} + 1.75 \tag{4.16}$$

or

$$-\frac{\Delta p}{L} = A\frac{(1-\varepsilon)^2}{d_p^2\varepsilon^3}\eta v_s + B\frac{(1-\varepsilon)}{d_p\varepsilon^3}\rho_f v_s^2 \tag{4.17}$$

with A and B respectively equal to 150 and 1.75. Equation 4.17 was especially used by authors of the chemical engineering field (Niven, 2002), where packed beds are a common thing. The Ergun equation is also often introduced under another form. By using the fact that the mean particle diameter of packed beds can be expressed as:

$$d_p = \frac{6(1-\varepsilon)}{A_{sp}} \tag{4.18}$$

where A_{sp} is the specific surface area, the Ergun equation becomes then:

$$\boxed{\frac{\Delta p}{L} = h_k\frac{A_{sp}^2}{\varepsilon^3}\eta v_s + h_b\frac{A_{sp}}{\varepsilon^3}\rho_f v_s^2} \tag{4.19}$$

This equation has a convenient form because it does not require to define a characteristic particle diameter. The coefficients $\mathbf{h_k}$ and $\mathbf{h_b}$ are called the **Kozeny constant** and **the Burke-Plummer constant**. A lot of disagreements about their values can be found in

the literature. According to the original work of Kozeny (1927) and Carman (1937), h_k is equal to 5 for packed beds of spherical particles. However, Ergun claimed that h_k is equal to 4.2 and h_b is equal to 0.3. Later, Happel and Brenner (2012) explained that the Kozeny constant could vary from 4.2 to 6 for packed beds of spherical particles. In the end, Quinn (2014) reviewed a major part of the works referred in Ergun's paper. He explained that Ergun gave erroneous constant values and should have obtained larger ones.

4.1.4.2 Ergun-like equation

Many authors decided to use equations similar to 4.17 or 4.19 to characterize or compare other architectures than packed beds of spherical particles. They usually changed the values of the constants A, B, h_k or h_b and the definition of the particle diameter to obtain laws which fit well with their data. This is then referred as an Ergun-like relation.

Works using the form of equation 4.17:

Tadrist et al. (2004) fitted data through fibrous materials by using a coefficient A varying from 100 to 865 and a coefficient B varying from 0.65 to 2.6. Topin et al. (2006) fitted experimental permeability coefficients of metallic foams with a coefficient A equal to about 7200. The Forchheimer coefficients were defined as a linear function of the foam specific surface area. Dukhan et al. (2006) proposed an Ergun-like relation by adding exponent at the geometrical ratios to capture pressure losses in aluminum foams. Kumar et al. (2012) suggested new correlations for the coefficients A and B of open-cell foams.

Works using the form of equation 4.19:

Macdonald et al. (1979) claimed that the pressure losses through an unconsolidated porous material could be well predicted if the coefficients h_k and h_b were respectively taken at 5 and 0.3 for smooth particles and at 5 and 0.67 for rough particles. Meyer and Smith (1985) investigated partially sintered irregular powders and showed that the coefficient h_k could range from 2.95 to 22.1 and the coefficient h_b from 0.26 to 4.6. Papathanasiou et al. (2001) reported that the coefficient h_k could vary from 5 to 20 for fibrous materials. Nemec and Levec (2005) claimed that higher coefficients than $h_k = 5$ and $h_b = 0.3$ should be used for packed beds of non-spherical particles due to additional pressure losses caused by irregularities.

4.1.4.3 Flow through partially sintered materials

In the present PhD thesis, the partial sintering of spherical powders leads to the creation of necks which differ from the single contact points present in packed beds of spherical particles. Moreover, the use of irregular particles may increase the complexity of the flow path. Consequently, if the relationship linking the pressure losses to the flow velocity in partially sintered materials is described with an Ergun-like relation, different coefficients h_k and h_b to those suggested for packed beds of spherical particles should be expected.
Some experimental permeability works related to partially sintered metallic powders can be found in the literature. Meyer and Smith (1985) investigated irregular stainless steel powder based materials with porosities ranging from 0.18 to 0.67. Hwang and Chao (1994) studied bronze beads with porosities of 0.37 and 0.38. Jiang et al. (2004) carried out measurements on bronze porous channels with a porosity ranging from 0.402 to 0.463. Hetsroni et al. (2006) studied stainless steel rounded irregular powders based materials with porosities of 0.32 and 0.44. Liu et al. (2013) studied bronze and stainless steel porous plates with a porosity varying between 0.32 and 0.37. If Jiang et al. (2004) and Liu et al. (2013) tried to correlate their data to Ergun-like semi empirical laws with new constant h_k and h_b coefficients, Meyer and Smith (1985) were the only ones to admit that h_k and h_b could vary with the geometry and they thus suggested new semi-empirical correlations.

4.1.5 Objectives of the chapter

The aim of this chapter is to get a simple theory able to predict the behavior of flows through partially sintered materials made either of spherical or of irregular powders. To carry out this task, the chapter will try to answer two different questions:

- Can an Ergun-like equation be applied to partially-sintered powders ($K^{-1} = h_k \frac{A_{sp}^2}{\varepsilon^3}$ & $\beta = h_b \frac{A_{sp}}{\varepsilon^3}$) ?
- Is there a need to use other geometrical parameters than the porosity and the specific surface area to accurately predict the permeability ?

To answer these questions, flow simulations were performed on 3D digitized images of partially-sintered materials introduced in chapter 2. After testing the accuracy of the numerical method with experimental data, the permeability coefficient K and the Forchheimer coefficient β of each one of the architectures were assessed. They were then analyzed with the extracted geometrical parameters.

4.2 Simulation of the flow through porous material

4.2.1 Introduction to *FlowDict*

The computation of the flow through a porous material was performed thanks to the module *FlowDict* of the software Geodict (2014). This software has the particularity to perform computational fluid dynamics (CFD) on voxelized 3D-images. As the geometries are complex, time-consuming steps of meshing, normally required by more conventional commercial softwares, can thus be avoided. This module solves the steady Navier-Stokes equation thanks to a *FFT*[1]*-SIMPLE*[2] method. Information about the *SIMPLE* algorithm can be found in the book of Patankar (1980). Even though the software can record the non-linear behavior between the pressure difference and the superficial velocity (equation 4.7), it is not able to simulate a flow with turbulence. The use of a Fast Fourier Transform method requires periodic images. If the software *dp3D* allows the generation of periodic architectures, the digitized 3D-images of partially-sintered samples are clearly non-periodic. To be able to compute the flow field, the digitized images have first to be symmetrized according to the plan perpendicular to the main flow direction as it is shown figure 4.3. This symmetrization increases the computational time (the volume size is doubled). It can also create geometrical artifacts next to the plan of symmetry which can be non representative of the real material architecture.

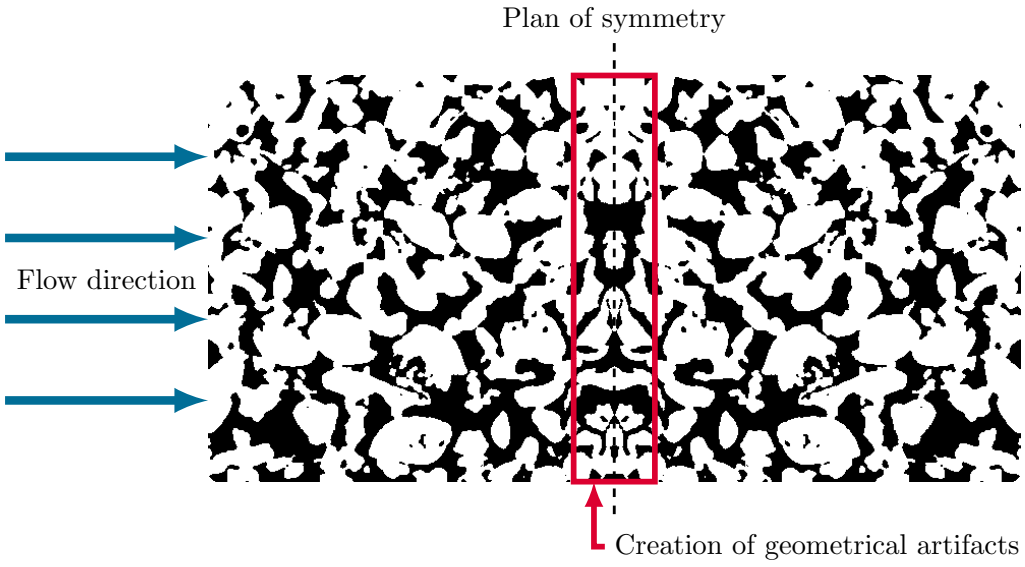

Figure 4.3: Scheme representing the symmetrization of a digitized 3D image.

[1]Fast-Fourier Transform
[2]Semi-Implicit Method for Pressure Linked Equations

As entry data, the main flow direction and the pressure difference between the two opposite faces of the volume are chosen. For the simulations at ambient condition, the properties of air are set at $\rho_f = 1.204\ kg/m^3$ and $\eta = 1.834 \times 10^{-5}\ Pa.s$. A no-slip boundary condition is imposed at each solid/fluid interfaces. **As the permeability coefficient and the Forchheimer coefficient only depend on the architecture of the porous material, there is no need to take into consideration the effects of temperature and compressibility at engine working conditions. The relationships $\mathbf{K}$,$\boldsymbol{\beta} = \mathbf{f}$(architecture) at ambient conditions will be valid for other conditions.** The superficial velocity of each geometry is computed at several pressure gradients in order to build a representative pressure gradient/velocity profile as it is represented in figure 4.4.

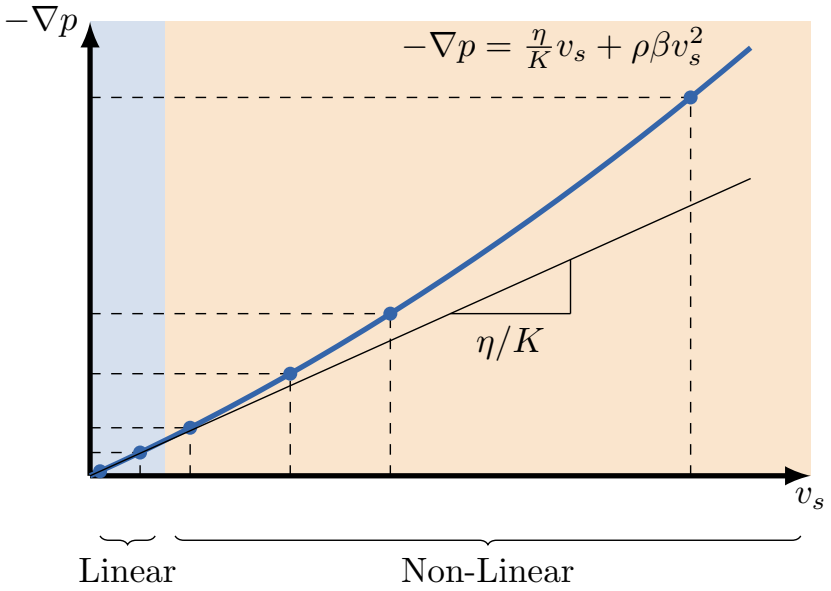

Figure 4.4: A typical velocity/pressure gradient profile.

By using equation 4.7, the permeability coefficient K can be deduced from the slope at the origin. In practice, a simulation is carried out for a very small pressure gradient (100 Pa/m), where Re' is very low, and K is deduced by using:

$$K = -\frac{\eta v_s}{\nabla p} \tag{4.20}$$

After ensuring there are enough points in the non-linear domain, the coefficient β is computed by fitting equation 4.7 to the data with a least square method. As the simulations are performed for the three space directions, each porous geometry is characterized by three permeability coefficients and three Forchheimer coefficients (K_{xx}, K_{yy}, K_{zz}, β_{xx},

β_{yy}, β_{zz}). In this thesis, the architectures are assumed to be isotropic enough to consider mean coefficients $\bar{K}$ and $\bar{\beta}$ (the isotropy assumption is justified in section 4.2.3):

$$\bar{K} = \left[\frac{1}{3}\left(\frac{1}{K_{xx}} + \frac{1}{K_{yy}} + \frac{1}{K_{zz}}\right)\right]^{-1} \tag{4.21}$$

$$\bar{\beta} = \frac{\beta_{xx} + \beta_{yy} + \beta_{zz}}{3} \tag{4.22}$$

4.2.2 REV, voxel size and computational time

To deal with computation on 3D images, one has to always find the best trade-off between the size of the image, the pixel size and the computational time. If reducing the pixel size allows a better description of the geometrical irregularities, it also increases the number of voxels included in the REV, the image memory size and thus the computational time. Flow simulations were performed on 3D images of 400 μm partially-sintered irregular powders having different size of volume of interest (VOI). The VOI size varied from 100^3 voxels to 600^3 voxels. All the simulations were performed on a unique computer (Intel X5660, 2.8 MHz, 96 Go RAM) and with one processor. Figure 4.5 represents the RAM required to run the simulations and their computational time (one main flow direction at one pressure gradient). The pressure gradient was fixed at 100 Pa/m for each VOI. The simulations were stopped once the mean velocity relative difference is less than 5×10^{-4}.

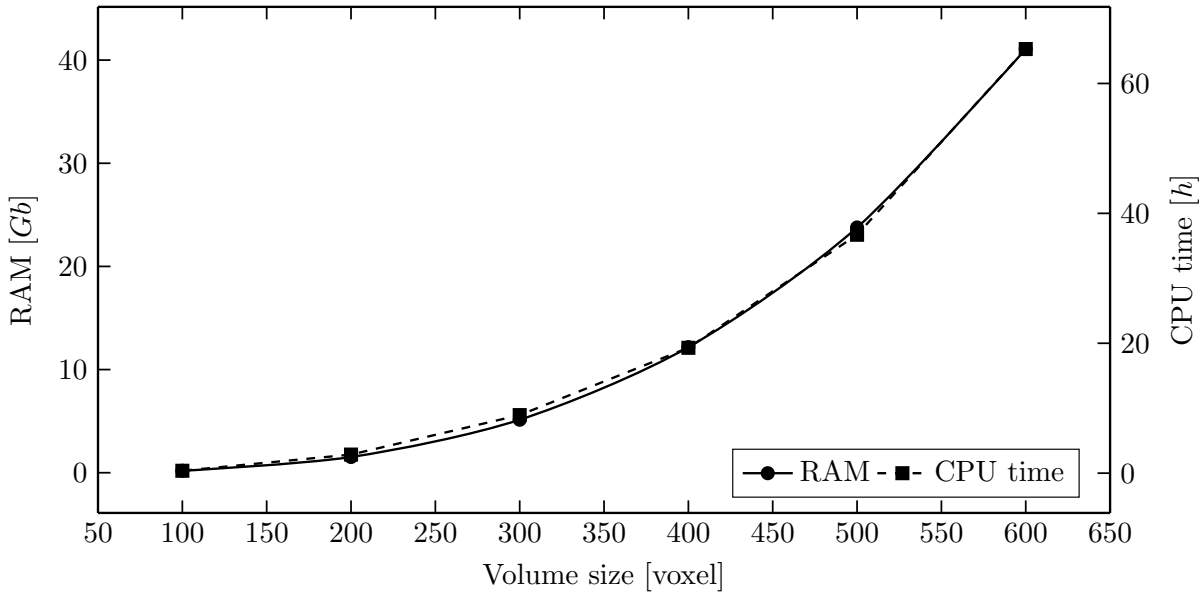

Figure 4.5: Evolution of the required RAM and CPU time to run a simulation as a function of the size of the cubical volume (expressed as the number of voxels along the cube edge)

Considering the high number of simulations required for this thesis, cubic volumes with a maximum number of 400 voxels along the edge were authorized. With this choice, five simulations could run simultaneously, offering a ratio of about 5 complete simulations a day. For comparison, choosing a maximum size of 500 voxels would have led to a ratio of less than 2 complete simulations a day. For information, in order to obtain a sufficient velocity/pressure gradient profile, simulations were performed at six different pressure gradients on each image and the process was repeated for the three main space directions. As a result, at least 18 simulations were required to completely characterize a geometry.

In section 2.3.4, it was shown that a VOI of 300^3 voxels with at least 50 voxels along the particle diameters was large enough to be considered as a REV for the porosity and the specific surface. However, the size of the REV depends on the measured property. It has therefore to be proved that a volume of 400^3 voxels could lead to representative values of permeability. This work was performed on two materials made of 150 μm and 400 μm irregular particles (IP). Because of the irregular geometry, at equivalent particle size distribution, it is expected to obtained a REV larger than for materials made of spherical particles (SP). The mean permeability and Forchheimer coefficients were assessed in cubical VOI of different sizes following the process introduced section 4.2.1. The relative differences of the measured coefficients are given tables 4.2 and 4.3. They are compared to the coefficient of the largest tested VOI (400^3 voxels). For both tested architectures, the relative differences between the coefficients of the 300^3 voxel size volume and those of the 400^3 voxel one are less than the threshold of 5%. A volume of 400^3 voxels can therefore be considered as large enough to give representative values of permeability and Forchheimer coefficients.

4.2.3 Isotropy of the digitized architectures

In section 4.2.1, isotropic properties of the digitized architectures were assumed. Thanks to the isotropy, a good statistical information of the properties could be obtained with only one image by repeating the computations in the three space directions. However, similar permeability values in the three space directions have to be measured to validate this assumption. Table 4.4 gives the values of permeability and Forchheimer coefficients of different digitized materials in each space direction.

A slight anisotropy of the permeability coefficient was in fact detected. Indeed, the coefficients in the x-axis direction, corresponding to thickness of the disk from which the samples were cut, are always a little bit different from the two other directions. This

VOI $[\text{voxel}^3]$	$\Delta\bar{K}/\bar{K}_{400}$ [%]	$\Delta\bar{\beta}/\bar{\beta}_{400}$ [%]
100^3	7.2	103.0
200^3	30.2	31.3
300^3	3.9	4.3

Table 4.2: Relative differences of permeability and Forchheimer coefficients as a function of the size of the cubical VOI of an IP material having a mean particle size of 150 μm (the coefficients are compared to those of the 400^3 voxel VOI).

VOI $[\text{voxel}^3]$	$\Delta\bar{K}/\bar{K}_{400}$ [%]	$\Delta\bar{\beta}/\bar{\beta}_{400}$ [%]
100^3	10.8	23.1
200^3	8.3	2.0
300^3	2.8	0.1

Table 4.3: Relative differences of permeability and Forchheimer coefficients as a function of the size of the cubical VOI of an IP material having a mean particle size of 400 μm (the coefficients are compared to those of the 400^3 voxel VOI).

		SP			IP		
d_p	$[\mu m]$	150	300	200	150	400	50
ε	[%]	36.3	33.9	21.2	36.5	40.0	23.5
K_{xx}		1.38	4.84	0.65	4.84	2.88	0.015
K_{yy}	$[\times 10^{-11}\ m^2]$	1.48	4.67	0.76	5.06	3.08	0.013
K_{zz}		1.49	4.63	0.73	5.08	3.08	0.014
β_{xx}		2.54	1.43	32.9	8.76	2.91	260
β_{yy}	$[\times 10^5\ m^{-1}]$	2.19	1.56	28.3	8.06	2.47	292
β_{zz}		2.17	1.52	27.5	7.55	2.73	292

Table 4.4: Simulated permeability and Forchheimer coefficients of digitized samples for the three main flow directions.

anisotropy may be due to the shaping process of the green body during which the gravity and the axial compression organize the powder compact. This anisotropy is the most pronounced with the less porous partially-sintered spherical powders (SP): $\simeq$ 13% of relative difference between the x-axis direction and the other ones. The anisotropy is less pronounced with the Forchheimer coefficient. A maximum relative difference between of $\simeq$ 13% is still observed for the less porous SP materials.

As the maximum relative difference between the directions is 13%, the samples were indeed considered as isotropic. Only the mean parameters $\bar{K}$ and $\bar{\beta}$ will be given in the following.

4.2.4 Accuracy of the numerical method

Section 4.2.2 aimed to prove that the flow computations were carried out on sufficiently representative volumes. However, it did not give any appreciation about the numerical method accuracy. This section therefore introduces comparison between numerical data and theoretical or experimental ones.

4.2.4.1 Comparison with theoretical values

The simplest way to assess the accuracy of the suggested numerical method may be to compare the data of flow through packed beds with the predictions made by the Ergun equation (equation 4.17). Monomodal packed beds with porosities ranging from 37.5 to 50% were generated following the process introduced section 2.2.2. The number of spherical particles was fixed at 400 and the particle diameter d_p at 100, 200 or 400 μm. Following the discussion of the section 4.1.4.1, numerically computed Kozeny and Forchheimer coefficients from the Ergun equation are compared to the **theoretical coefficients $\mathbf{h_k = 5}$** and $\mathbf{h_b = 0.3}$. After measuring the porosity and the specific surface area of a sample, the simulated Kozeny and Burke-Plummer coefficients ($\bar{h}_k$ and $\bar{h}_b$) are determined thanks to:

$$\bar{h}_k = \frac{\varepsilon^3}{A_{sp}^2 \bar{K}} \;\&\; \bar{h}_b = \frac{\varepsilon^3}{A_{sp}} \bar{\beta} \tag{4.23}$$

Some results are given in the table 4.5.

ε [−]	37.5			42.5			50.0		
d_p [μm]	100	200	400	100	200	400	100	200	400
$\bar{h}_k$ [−]	5.16	5.16	5.16	4.98	4.98	4.98	4.87	4.87	4.88
$\bar{h}_b$ [−]	0.40	0.41	0.38	0.38	0.37	0.34	0.32	0.31	0.28

Table 4.5: Numerical determination of the parameters $\bar{h}_k$ and $\bar{h}_b$ of packed beds of monomodal spherical particles generated with *dp3D*.

As regards the coefficients $\bar{h}_k$, no impact of particle size was noticed. Their values range from 4.84 to 5.18, which agrees well with the theory. A slight particle size effect was detected in the assessment of the coefficient $\bar{h}_b$. However, the maximum relative difference between particles of 100 μm and particles of 400 μm remains below 15%. $\bar{h}_b$ varies between 0.41 for a 37.5% porous geometry and 0.277 for a 50% porous geometry. This agrees also well with the theoretical values.

4.2.4.2 Comparison with experimental data

Partially-sintered materials have a more complex architecture than simple packed beds. The accuracy of the simulations performed on the digitized materials was therefore also assessed. The numerical results were compared to experimental data given by the company *Sintertech*. These experimental data were obtained according to the ISO 4022 standard. A picture of the experimental apparatus is introduced figure 4.6.

Figure 4.6: Permeability bench used by the company *Sintertech*.

The sample is a disk clamped between two gaskets. The mass flow is set up thanks to a flow vane and monitored by a mass-flow meter. The pressure difference is measured thanks to two manometers placed downstream and upstream the sample. The temperature of the air is measured upstream to compute its density and its dynamic viscosity. The experimental apparatus can discharge a maximum mass flow of 2000 L/h. Pressure differences are measured at different mass-flows so as to get a representative velocity/pressure gradient profile. The permeability and Forchheimer coefficients are then determined following a procedure similar to the one introduced in section 4.2.1.

Experimental permeability and Forchheimer coefficient values were given as confidence ranges. They allow the extrapolation of velocity/pressure gradient profiles. Figure 4.7 compares the numerical and experimental profiles of some SP and IP architectures. The extrapolated profiles were drawn until a critical velocity of about 1 m/s is reached. This critical velocity is defined as the maximum flow reachable on the experimental bench by

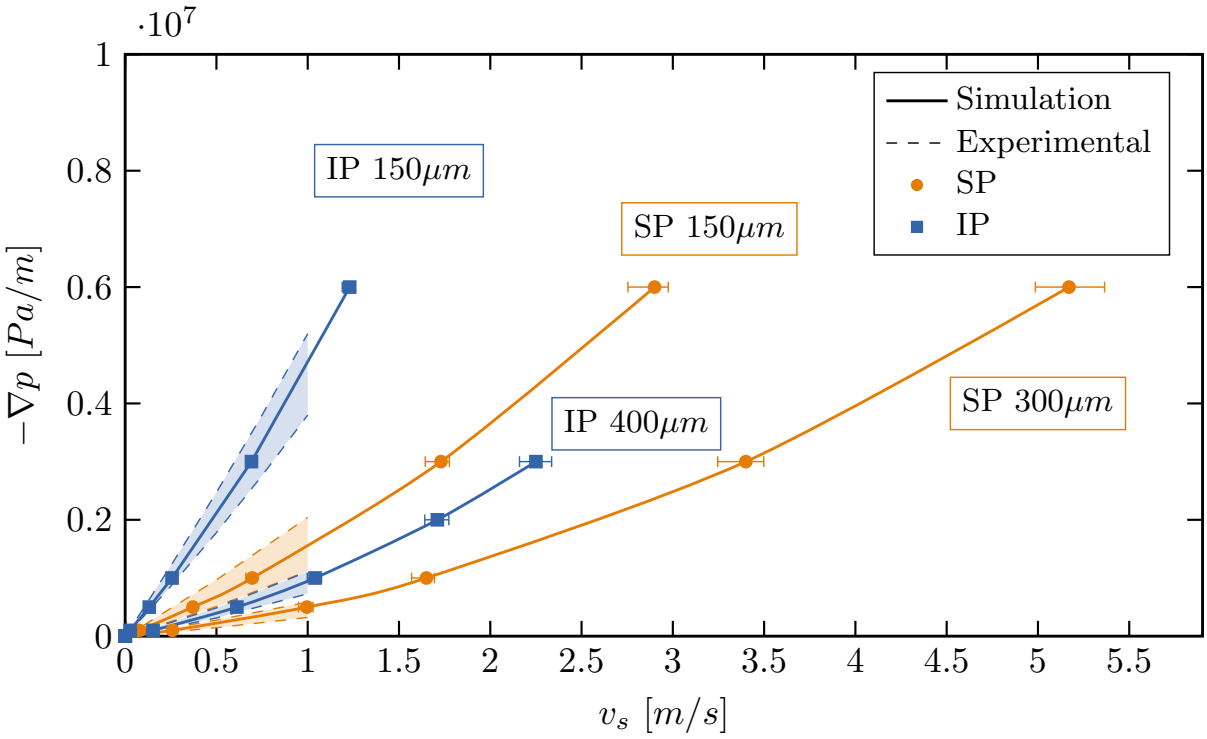

Figure 4.7: Comparison of velocity/pressure gradient profiles of SP ($d_p = 150$ and 300 μm) and IP ($d_p = 150$ and 400 μm) materials obtained from *FlowDict* simulations and from Sintertech's experimental data.

considering the apparatus flow capacity and the sample diameters.

Simulated profiles agree very well with the experimental ones up to the critical velocity. For a given powder type (spherical or irregular), the numerical simulations capture very well the change in particle size. They are also able to differentiate the powder type used at a given particle size.

4.2.4.3 Summary

Simulations were compared to theoretical and experimental data. **It was shown that the numerical method captures very well the pressure gradient/velocity relationships of partially-sintered architectures, even in the non-linear domain. Only laminar inertial effects cause additional pressure losses.** The method can therefore be used to extract and analyze the permeability and the Forchheimer coefficients of all the digitized materials.

4.3 Analysis of the numerical data

Numerical simulations were carried out on numerically generated and digitized three-dimensional images of partially-sintered materials. To develop predictive permeability laws, this section studies the simulated data and compares them to the measured geometrical parameters.

4.3.1 Respect of the assumption of a laminar flow

In section 4.2.1, it was explained that *FlowDict* was only able to perform flow simulations at a laminar regime. The study of only laminar flows was then assumed. In section 4.1.2, two definitions of Reynolds numbers were introduced. Re' is rather used for packed beds of spherical particles and Re'' is a more general definition. Figure 4.8 introduces the maximum Reynolds numbers obtained for each SP and IP geometries studied in the present work. These maximum values describe the flow at the maximum pressure gradients at which the samples were analyzed.

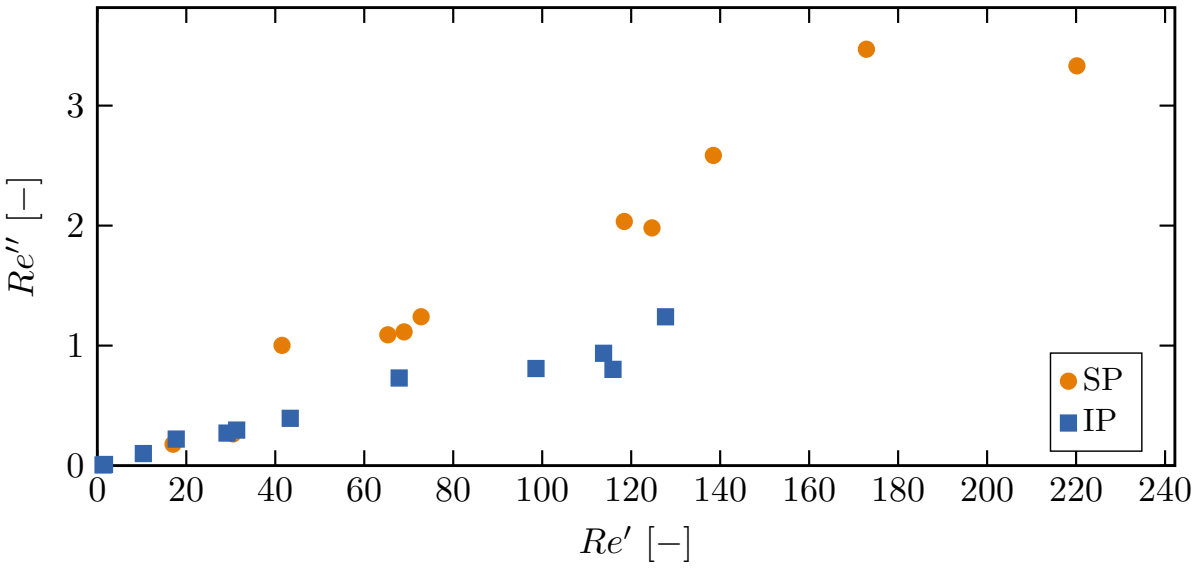

Figure 4.8: Maximum Re' and Re'' of the digitized partially-sintered samples.

As regards the maximum Re'' values, all samples have a value below the laminar threshold of 10. On the contrary, the maximum Re' values can be larger than the laminar threshold of 10. However, not only this definition was developed for packed beds but the values also remain at the beginning of the transitional regime. It can therefore be concluded that the simulations respect pretty much the assumption of a laminar flow.

4.3.2 Study of the numerical flow fields

Before looking for some relationships between the permeability coefficients and the geometrical parameters of partially-sintered materials, it seems important to give a global vision of how the flow behaves in each architecture.

4.3.2.1 Comparison of flow fields

The interstitial velocity v_i is defined as the mean flow velocity inside the porous materials. It is simply linked to the superficial velocity by:

$$v_i = \frac{v_s}{\varepsilon} \tag{4.24}$$

Figures 4.9 to 4.10 represent areas in which the local velocity v is twice or five times higher than the interstitial velocity v_i. These areas are shown for different SP and IP architectures and the simulations were performed for a pressure gradient of 100 Pa/m.

At equivalent porosity and particle size, the mean velocity is higher in materials made of spherical powders (SP) than in materials made of irregular particles (IP). The comparison of the interstitial velocities given in the captions illustrates well this point.

The figures showing the areas where $v > 2v_i$ show well that the porous phase of each architecture is well interconnected.

Much more areas where $v > 5v_i$ are highlighted in materials made of IP materials than in SP ones. For SP materials, almost all the pores participate to the flow and the velocities are close to the mean velocity v_i. However, in IP materials, the irregularities seem to more concentrate the flow in some preferential pores. There are therefore more areas in which the velocity is relatively much higher than the superficial velocity. The amount of areas where the velocity is at least five times higher than the superficial velocity seems also to rise with the decreasing porosity. That tends to show that a decreasing porosity concentrates even more the flow in some preferential pores.

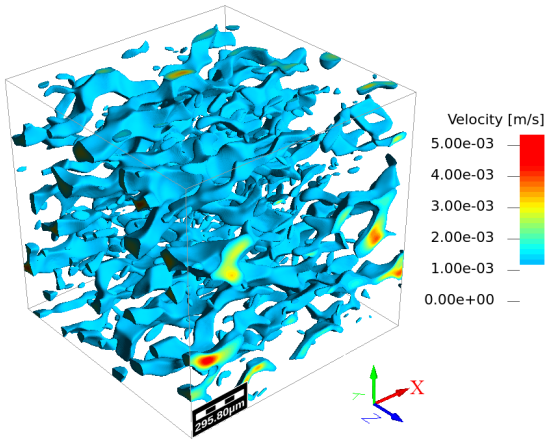

(a) SP, 200 μm, $\varepsilon = 38\%$, $v_i = 5.8 \times 10^{-4}$ m/s, $v > 2v_i$.

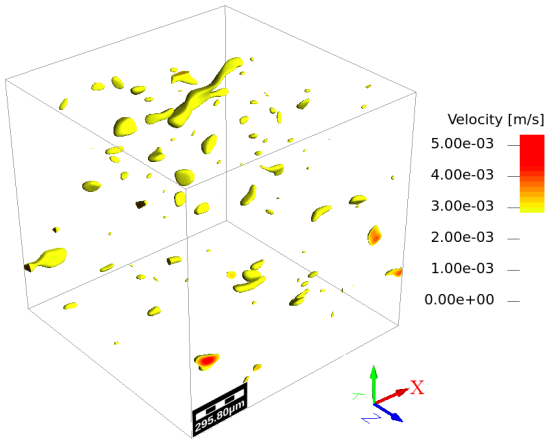

(b) SP, 200 μm, $\varepsilon = 38\%$, $v_i = 5.8 \times 10^{-4}$ m/s, $v > 5v_i$.

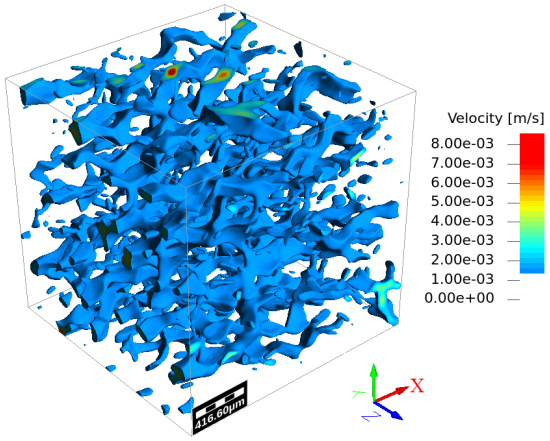

(c) SP, 300 μm, $\varepsilon = 35\%$, $v_i = 7.8 \times 10^{-4}$ m/s, $v > 2v_i$.

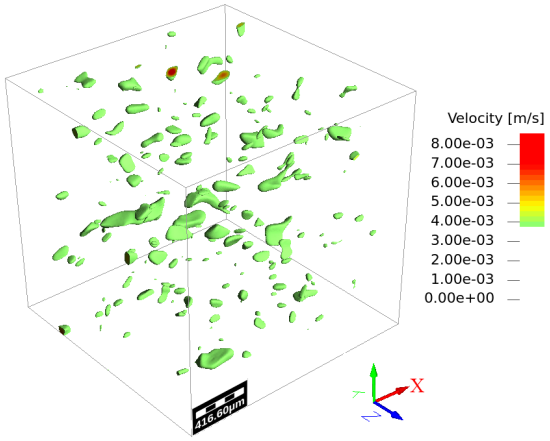

(d) SP, 300 μm, $\varepsilon = 35\%$, $v_i = 7.8 \times 10^{-4}$ m/s, $v > 5v_i$.

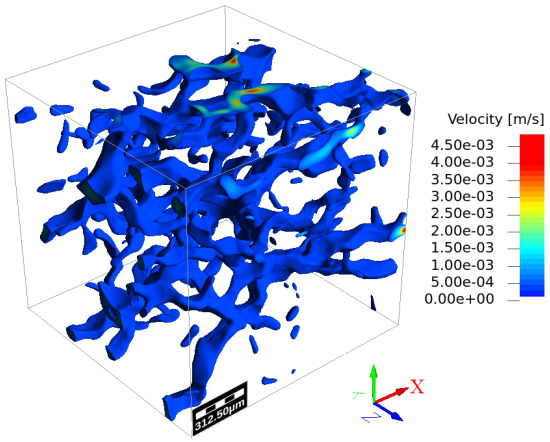

(e) SP, 200 μm, $\varepsilon = 22\%$, $v_i = 1.88 \times 10^{-4}$ m/s, $v > 2v_i$.

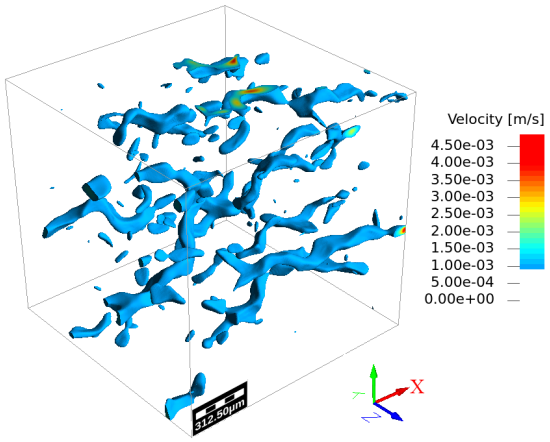

(f) SP, 200 μm, $\varepsilon = 22\%$, $v_i = 1.88 \times 10^{-4}$ m/s, $v > 5v_i$.

Figure 4.9: Areas in partially-sintered **spherical powders** where the velocity is at least n times higher than the interstitial velocity v_i. The pressure gradient is 100 Pa/m and is applied in the X-direction.

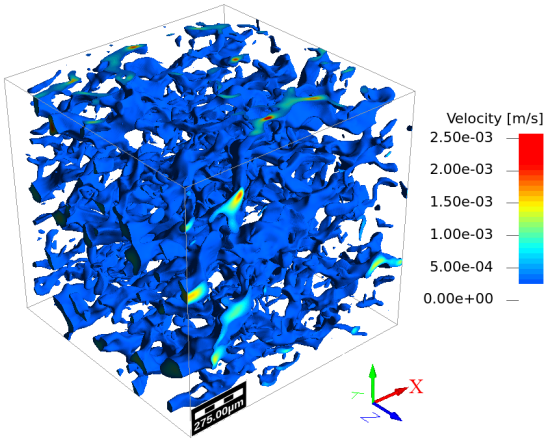

(a) IP, 200 μm, $\varepsilon = 38\%$, $v_i = 1.6 \times 10^{-4}$ m/s, $v > 2v_i$.

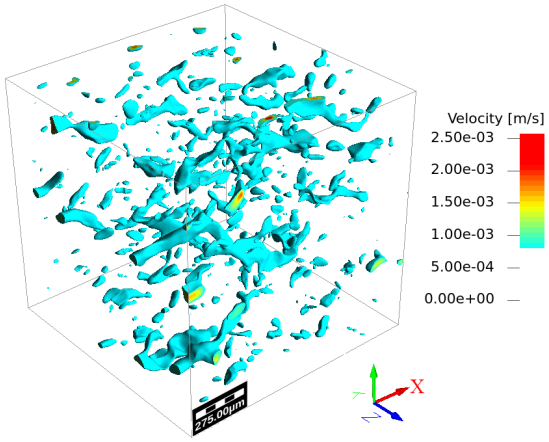

(b) IP, 200 μm, $\varepsilon = 38\%$, $v_i = 1.6 \times 10^{-4}$ m/s, $v > 5v_i$.

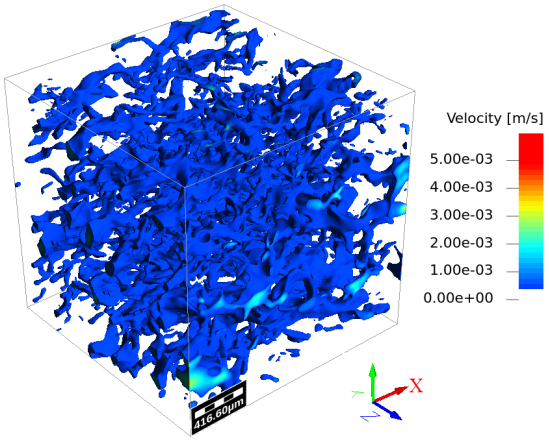

(c) IP, 300 μm, $\varepsilon = 35\%$, $v_i = 2.4 \times 10^{-4}$ m/s, $v > 2v_i$.

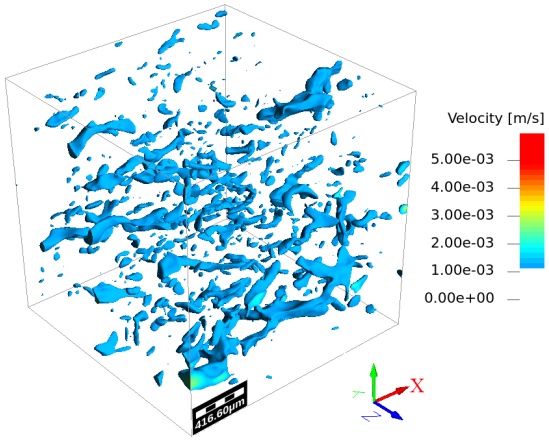

(d) IP, 300 μm, $\varepsilon = 35\%$, $v_i = 2.4 \times 10^{-4}$ m/s, $v > 5v_i$.

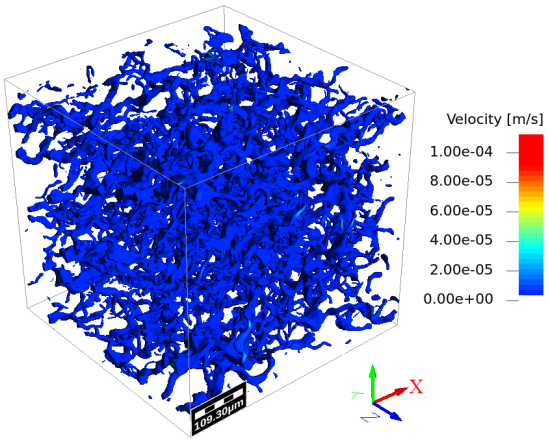

(e) IP, 50 μm, $\varepsilon = 20\%$, $v_i = 1.8 \times 10^{-6}$ m/s, $v > 2v_i$.

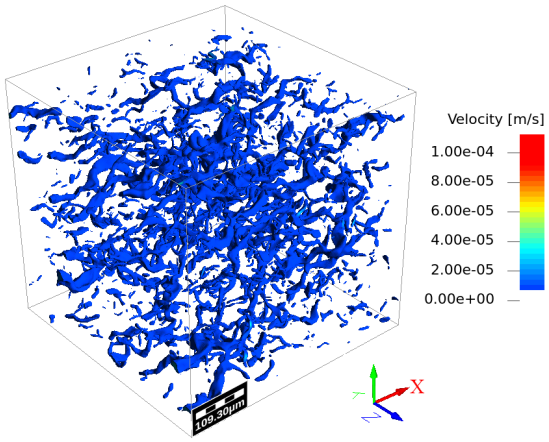

(f) IP, 50 μm, $\varepsilon = 20\%$, $v_i = 1.8 \times 10^{-6}$ m/s, $v > 5v_i$.

Figure 4.10: Areas in partially-sintered **irregular powders** where the velocity is at least n times higher than the interstitial velocity v_i. The pressure gradient is 100 Pa/m and is applied in the X-direction.

4.3.2.2 Comparison of streamlines

The complexity of the flow path in materials made of spherical (SP) or irregular powders (IP) can also be observed in the figure 4.11 where streamlines are represented for a pressure gradient of 100 Pa/m. The streamlines are defined as the lines parallel to the velocity vector. It seems that the streamlines of IP materials are more irregular than those of SP ones. This suggests that the fluid may need to travel a greater distance to go through an IP material. To check this assumption, the streamlines's tortuosities τ_{sl}, defined as the ratio of the streamline mean length to the thickness of the digitized sample, were computed. Some results are introduced in table 4.6.

		SP			IP		
d_p	$[\mu m]$	200	300	200	200	300	50
ε	[%]	38	35	22	38	35	24
τ_{sl}	$[-]$	1.26	1.30	1.56	1.40	1.39	1.75

Table 4.6: Computed streamline's tortuosities

It is shown that the relative length of the streamlines are indeed longer in IP materials than in SP ones at equivalent porosity. It is also shown that the length of the streamlines of both types of architecture seems to increase with the decreasing porosity. The amount of channels allowing the fluid to flow easily must reduce with the decreasing porosity. The fluid must then be forced to deviate a lot to go through the porous material.

4.3.2.3 Summary

As it was explained earlier, it is necessary to find simple relationships capable of linking the pressure gradient to the mean flow velocity of partially sintered powders. The previous analysis shows that the use of spherical or irregular powders leads to completely different flow fields and flow paths. **At equivalent porosity and particle size, the flow in partially-sintered irregular powders is much slower and more irregular. However, it is still impossible to know if the development of completely different relationships are necessary to predict the permeability of each architectural family.** This is the main topic of the following sections.

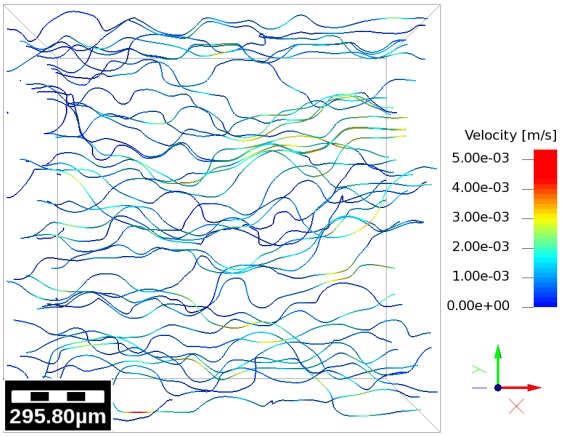

(a) SP, 200 μm, $\varepsilon = 38\%$.

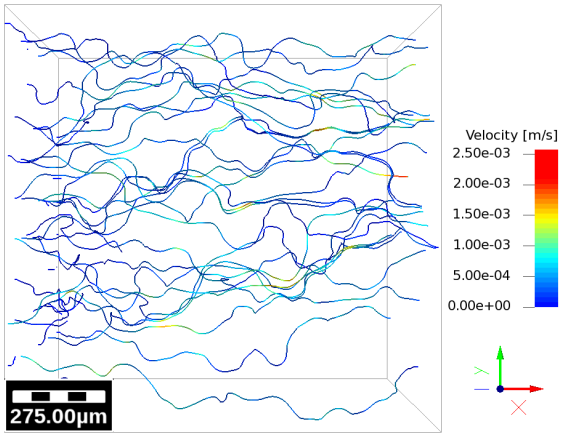

(b) IP, 200 μm, $\varepsilon = 38\%$.

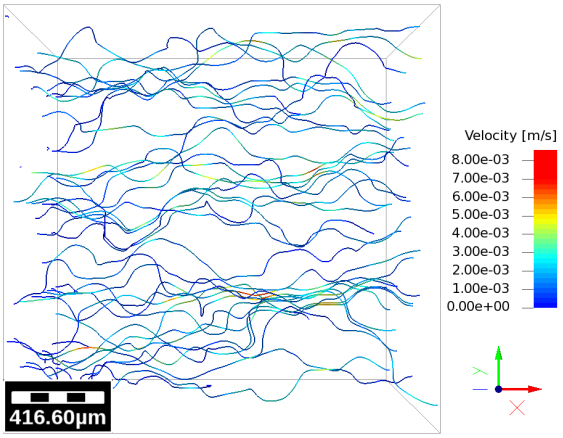

(c) SP, 300 μm, $\varepsilon = 35\%$.

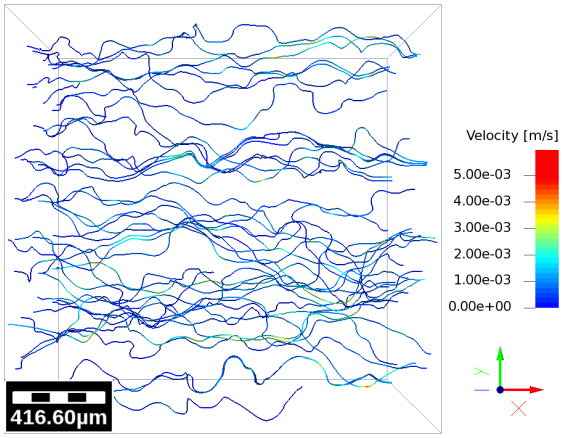

(d) IP, 300 μm, $\varepsilon = 35\%$.

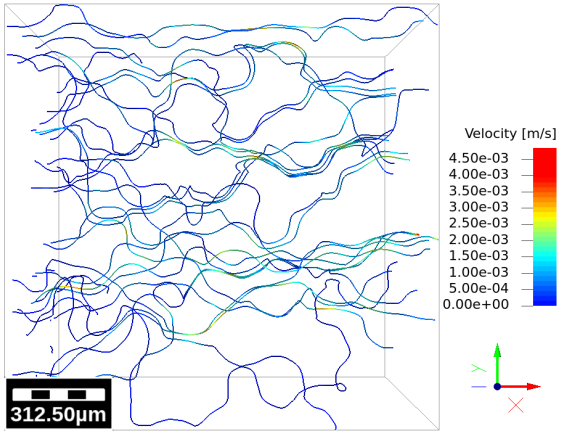

(e) SP, 200 μm, $\varepsilon = 22\%$.

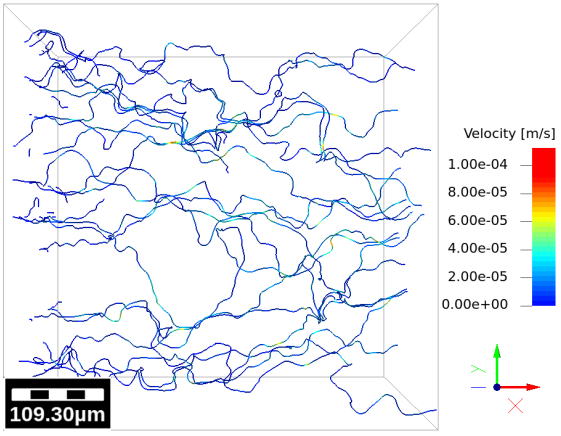

(f) IP, 50 μm, $\varepsilon = 20\%$.

Figure 4.11: Streamlines in partially-sintered materials. The pressure gradient is 100 Pa/m and is applied in the X-direction.

4.3.3 An Ergun-like relation for partially sintered materials ?

As it was stated section 4.1.5, the possibility to describe the flow through partially sintered spherical or irregular powders with an Ergun-like equation has first to be tested:

$$\frac{\Delta p}{L} = h_k \frac{A_{sp}^2}{\varepsilon^3} \eta v_s + h_b \frac{A_{sp}}{\varepsilon^3} \rho_f v_s^2 \tag{4.25}$$

For that purpose, the computed permeability coefficient $\bar{K}$ and the Forchheimer coefficient $\bar{\beta}$ of all the tested geometries are compared to their respective geometrical ratios ε^3/A_{sp}^2 and A_{sp}/ε^3 from equation 4.25. The ratios were assessed after numerically computing ε and A_{sp} with the methods described in the section 2.3. The porosity of the analyzed samples ranged from 20 to 40% and the specific surface area varied between 7500 and 75000 m^2/m^3.

4.3.3.1 Prediction of the permeability coefficient K

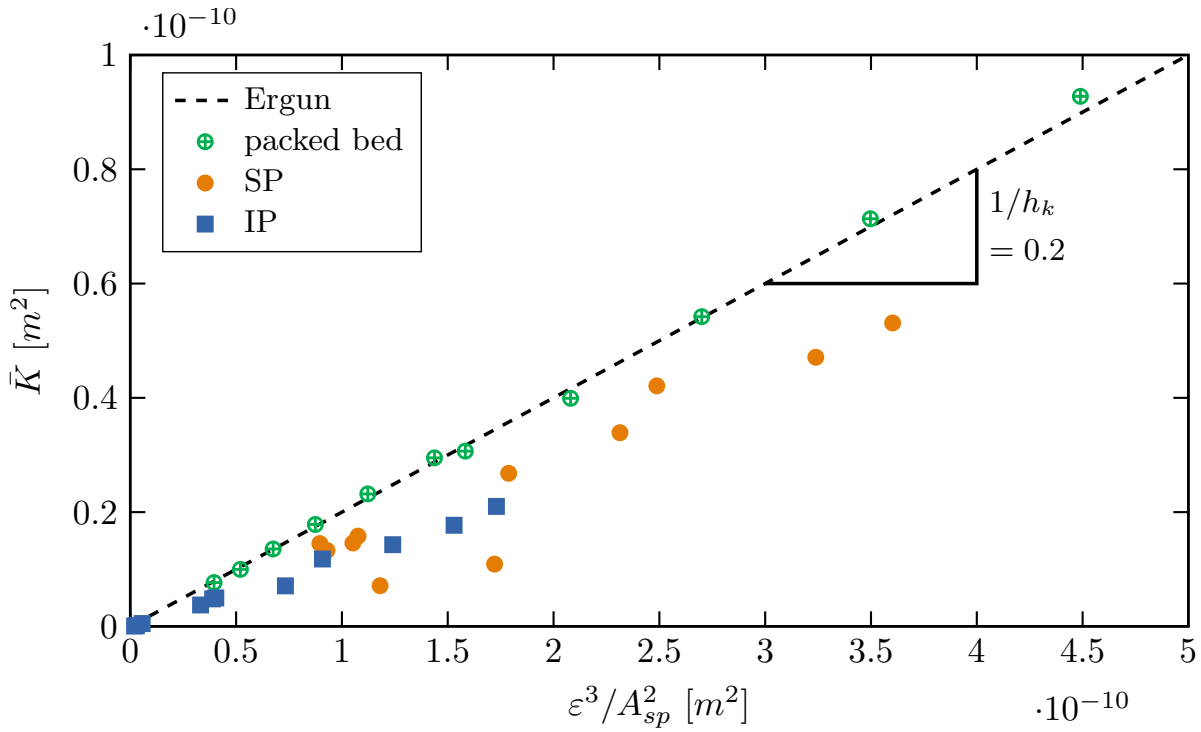

Figure 4.12: Computed mean permeability coefficient $\bar{K}$ as a function of the measured ratio ε^3/A_{sp}^2.

In the figure 4.12, the mean permeability coefficient $\bar{K}$ is plotted as a function of the ratio ε^3/A_{sp}^2. The dashed line corresponds to the theoretical relationship for packed beds

of spherical particles from the Ergun equation:

$$K = \frac{\varepsilon^3}{h_k A_{sp}^2} \tag{4.26}$$

The slope is $1/h_k = 1/5 = 0.2$. Once again, the simulations performed on numerical packed beds agree well with the theory since all the points are on the theoretical line. The coefficient $\bar{K}$ of SP and IP materials seems to go up with the increasing geometrical ratio. In the studied ranges of ε and A_{sp}, an almost linear relationship could be defined for the IP materials by using $\bar{h}_k(IP) = 8$. For SP samples, a visible discrepancy between the points limits the use of linear relationships. The two lower values correspond to the least porous SP samples.

4.3.3.2 Prediction of the Forchheimer coefficient β

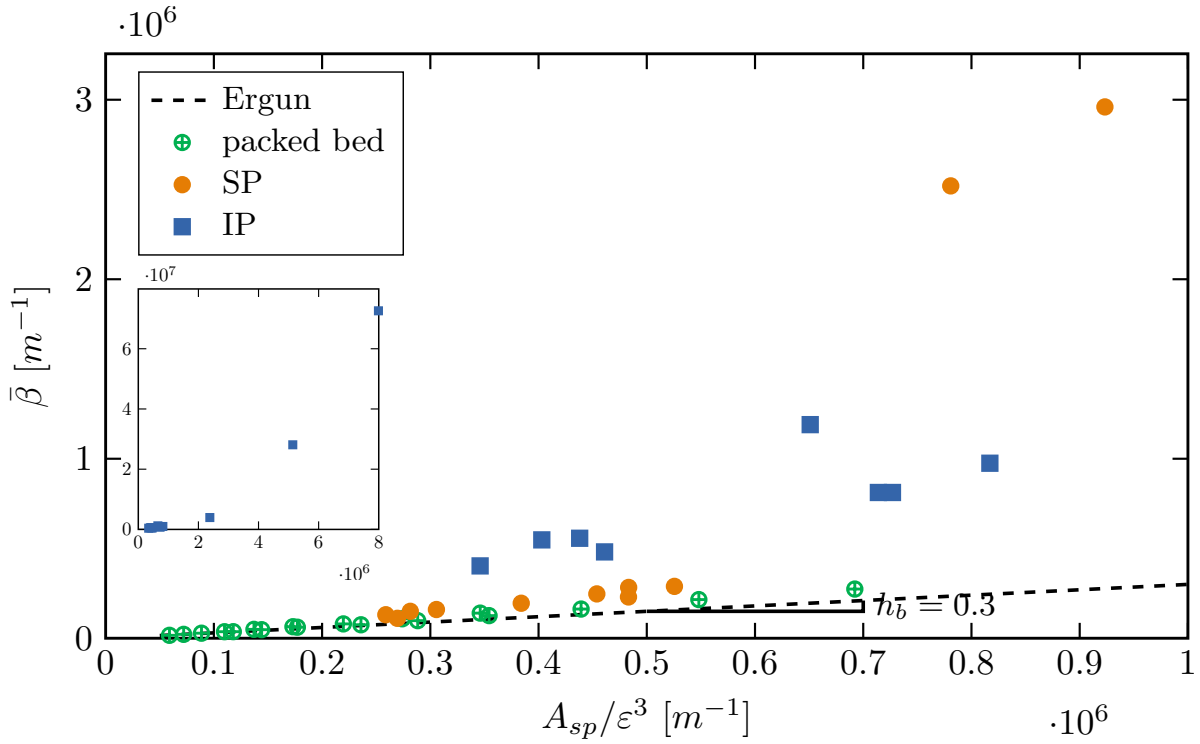

Figure 4.13: Computed mean Forchheimer coefficient $\bar{\beta}$ as function of the measured ratios A_{sp}/ε^3.

In the figure 4.13, the mean Forchheimer coefficient $\bar{\beta}$ is plotted as a function of the ratio A_{sp}/ε^3. The dashed line corresponds to the theoretical relationship for packed beds of spherical particles from the Ergun equation:

$$\beta = h_b \frac{A_{sp}}{\varepsilon^3} \tag{4.27}$$

The slope is $h_b = 0.3$. The additional small window shows the points of IP samples having very large ratio values. As already explained in the section 4.2.4.1, the computed coefficients $\bar{\beta}$ of packed beds agree also well with the theory.

As for the coefficient $\bar{K}$, the Forchheimer coefficients of partially-sintered materials seem to go up with the increasing A_{sp}/ε^3. If the coefficient $\bar{\beta}$ of SP materials slightly diverges from the one of packed beds for $A_{sp}/\varepsilon^3 < 6 \times 10^5\ m^{-1}$, larger differences can be observed for higher ratio values. The two higher values correspond to the least porous SP samples. Similar observations can be done for IP samples. However, the differences with the packed bed theoretical values are even more pronounced at low A_{sp}/ε^3.

4.3.3.3 Summary

It was shown that there is indeed a rise of the coefficients $\bar{K}$ and $\bar{\beta}$ with the increase of their respective geometrical ratios (ε^3/A_{sp}^2 and A_{sp}/ε^3). Despite the lack of linearity between the corresponding parameters, it could be nevertheless interesting to be able to predict K and β with relations similar to the Ergun one. For that purpose, **a coefficient $\bar{h}_k$ and a coefficient $\bar{h}_b$ are defined for each digitized architecture as:**

$$\boxed{\bar{h}_k = \frac{\varepsilon^3}{A_{sp}^2 \bar{K}}} \tag{4.28}$$

$$\boxed{\bar{h}_b = \frac{\varepsilon^3}{A_{sp}} \bar{\beta}} \tag{4.29}$$

and the next sections are focused on the analysis of $\bar{h}_k$ and $\bar{h}_b$. They aim to find the missing topological information which could enable their prediction.

4.3.4 $\bar{h}_k$ for partially sintered materials

4.3.4.1 Determination of h_k in the literature

According to Kozeny (1927), a packed bed can be modeled as an equivalent group of tubes and the coefficient h_k is:

$$h_k = h_{k0} \left(\frac{L_p}{L} \right)^2 = h_{k0} \tau^2 \tag{4.30}$$

where h_{k0} is a constant dependent on the cross-section shape of the equivalent tube, L_p is the effective hydraulic path length of the flow and L is the thickness of the sample and τ is the hydraulic tortuosity defined as:

$$\tau = \left(\frac{L_p}{L} \right) \tag{4.31}$$

Despite the apparent simplicity of equation 4.30, the hydraulic tortuosity is in fact extremely complex to measure. A lot of authors tried to assess it with more or less success. Indeed, τ depends on numerous geometrical parameters: the shape, the size, the distribution and the connectivity of the pores and channels. Its value is therefore generally found by coping a model with experimental data. Bartell and Osterhof (1928) considered the equivalent capillarity of packed beds as circular ($h_{k0} = 2$). They then assumed that $\tau = \pi/2$, which leads to $h_k = 4.9$. By looking at flow through packed beds, Carman (1937) noted that the fluid followed capillary tubes deviating from the main flow direction with an average angle of 45°. He then suggested $\tau = \sqrt{2}$ and $h_{k0} = 2.5$.

With the development of X-ray tomography, authors had access to the true architecture of their samples. They then attempted to assess a geometrical tortuosity thanks to various algorithms (Lindquist et al., 1996; Gommes et al., 2009; Sun et al., 2011). This geometrical tortuosity was always defined as the shortest path between the two opposite sides of a material. However, this definition cannot be equivalent to a hydraulic tortuosity since the no-slip boundary condition of the fluid mechanics also involves the size of the flow path section.

Other authors tried to assess a hydraulic tortuosity from computed streamlines (Koponen et al., 1996; Matyka et al., 2008; Ghassemi and Pak, 2011; Duda et al., 2011). They generally developed correlation laws between their measured tortuosities and the porosity of their architectures. However, even though their parameters were close to the definition of Kozeny (1927), none of the cited authors tried to link their tortuosities to the coefficient h_k.

Consequently, as the relationship between a tortuosity and h_k is still unclear and that the tortuosity is not a parameter easy to determine, a simpler approach was adopted in the present work.

4.3.4.2 Analysis of h_k

In order to enrich the database, additional flow simulations were performed on numerical partially-sintered spherical powders (SPnum). These architectures were generated with the process detailed in section 2.2.2. The generation of the architectures followed the manufacturing process of the company *Sintertech*: sintering reduces the porosity by about 6%. Green-bodies of monomodal spherical particles were first generated. Their porosity varies from 38.5% to 51%. The minimum porosity of the green-body was limited to 38.5% because it is already close to the limited value of 36% reachable by a random packing. Obtaining a less porous green-body would have led to a considerable computa-

tion time. The porosity of the final architecture ranges from 32.5% to 45%. Images of SPnum geometries are introduced in the figure 4.14.

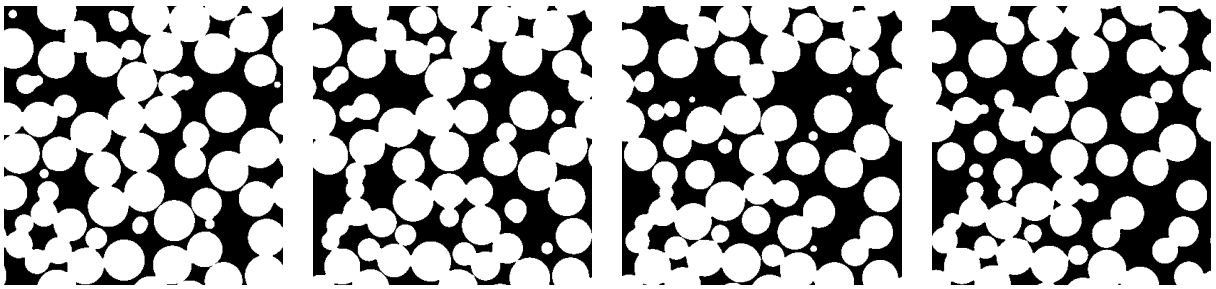

(a) $\varepsilon = 32.5\%$ **(b)** $\varepsilon = 35\%$ **(c)** $\varepsilon = 40\%$ **(d)** $\varepsilon = 45\%$

Figure 4.14: SPnum geometries numerically generated by following the manufacturing process of *Sintertech*.

In figure 4.15, the coefficient h_k is plotted as a function of the porosity and of the architectural family (SP, SPnum and IP). The theoretical constant value $h_k = 5$ for packed beds of spherical particles is also given.

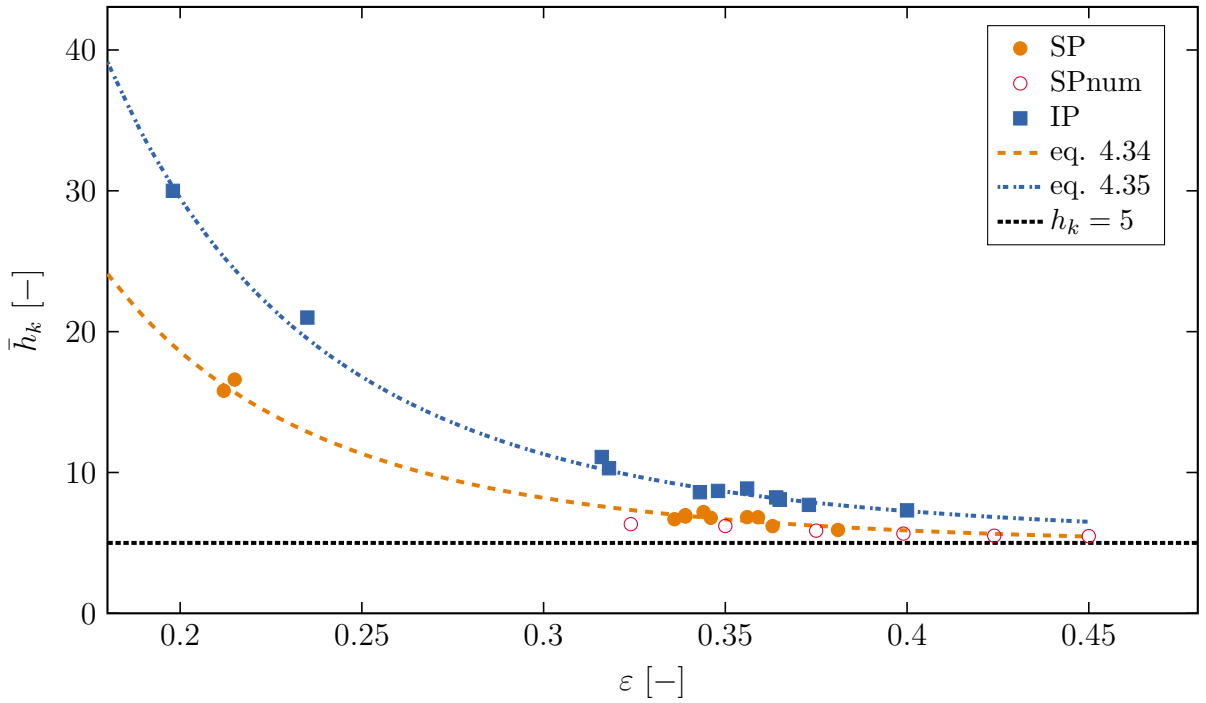

Figure 4.15: Variation of the coefficient $\bar{h}_k$ of different porous materials (SP, SPnum and IP) with the porosity.

Firs of all, it is shown that SP geometries can be easily discriminated from IP ones. Indeed, at a given porosity:

$$\boxed{\bar{h}_k(IP) > \bar{h}_k(SP)} \tag{4.32}$$

Next, **it appears that the coefficient $\mathbf{h_k}$ of each architectural family seems to be correlated to the porosity.** The coefficient $\bar{h}_k$ goes up with the decreasing porosity. This evolution must be due to changes in the overall architecture which are caused by the level of green-body compaction. Contrary to the works of Jiang et al. (2004) and Liu et al. (2013), **the coefficient h_k cannot be considered as constant**. This observation agrees with the experimental data of Meyer and Smith (1985) obtained for other partially-sintered irregular powder materials. Their $\bar{h}_k$ varied from 7, for a porosity of 39%, to 19, for a porosity of 20%.

The coefficients of SPnum samples are extremely close to those of SP samples up to $\varepsilon > 33\%$. The partially-sintered spherical powder geometry can therefore be modeled with the numerical generation using the discrete element method (DEM) for $\varepsilon > 33\%$. SP samples with a lower porosity are obtained with a high compression of the green body which deforms the spherical powders. Since the DEM has to consider perfectly spherical particles, less porous architecture cannot be numerically generated. The coefficients of SPnum geometries are also very close to the theoretical values of packed beds of spherical particles ($h_k = 5$) for porosity larger than 40%.

The variation of $\bar{h}_k$ of partially sintered materials was captured in the **20-45% porosity range** with relations having the following form:

$$\bar{h}_h = a + b\frac{0.45 - \varepsilon}{\varepsilon^n} \tag{4.33}$$

where a, b and n are constants specific of the architectural family.

For **partially-sintered spherical powders (SP)**, the following relationship is suggested:

$$\boxed{\bar{h}_k = 5.45 + 0.8\frac{0.45 - \varepsilon}{\varepsilon^{2.6}}} \tag{4.34}$$

The constant a was fixed with the $\bar{h}_k$ value of the 45% porous SPnum architecture. The relationship is represented in the figure 4.15. The maximum error between $\bar{h}_k$ values predicted with equation 4.34 and the numerical ones is about 10%.

Data obtained for **partially-sintered irregular powders (IP)** are correlated with:

$$\boxed{\bar{h}_k = 6.5 + 1.4\frac{0.45-\varepsilon}{\varepsilon^{2.6}}} \tag{4.35}$$

No data of partially-sintered irregular powders with a porosity larger than 40% were obtained. However, and to homogenize both relationships, data of IP materials were extrapolated up to a porosity of 45%. The relationship is represented in the figure 4.15. The maximum error between $\bar{h}_k$ values predicted with equation 4.35 and the numerical ones is also about 10%.

4.3.5 $\bar{h}_b$ for partially-sintered materials

4.3.5.1 Determination of h_b in the literature

Very few works were found to correlate the coefficient h_b to the geometry. Meyer and Smith (1985) suggested to extend the theory of turbulent friction in corrugated pipes to porous media. They studied the inertial losses in partially-sintered irregular powders. They suggested to predict h_b thanks to a relation having the following form:

$$h_b = \tau\left[c + b\left(\frac{q'}{d_h}\right)^n\right] \tag{4.36}$$

where a, b and n are constants experimentally determined, $d_h = 4\varepsilon/A_{sp}$ is the hydraulic diameter of the flow and q' is an effective particle roughness. They defined the particle roughness as:

$$q' = \left[\int (r - r_{eq})^2 dS / \int dS\right]^{1/2} \tag{4.37}$$

where r_{eq} and S are the volume equivalent spherical particle radius and the surface area corresponding to r_{eq} respectively as shown figure 4.16.

Despite the physical meaning of this relation, several issues can be emphasized. First of all, the relationship involves a tortuosity defined by Meyer and Smith (1985) as $h_k = 2\tau$. The issues related to this definition were given in section 4.3.4.1. Next, the relevance of the effective particle roughness can be questioned with particles more or less elongated as with the irregular particles studied in this thesis (see figure 2.1b). Finally, Meyer and Smith (1985) assumed that the ratio q'/d_h was the same for all their consolidated porous materials made of irregular powders without any justification of how they measured it.

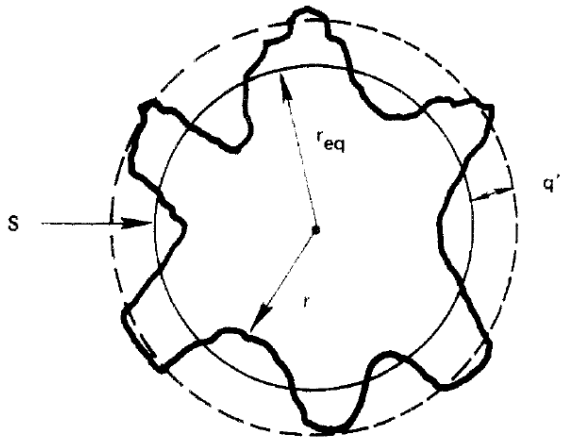

Figure 4.16: The effective particle roughness of Meyer and Smith (1985).

4.3.5.2 Analysis of $\bar{h}_b$

In the present study, $\bar{h}_b$ was analyzed with an approach similar to that used for $\bar{h}_k$. In figure 4.17, the coefficient h_b is plotted as a function of the porosity and of the architectural family (SP, SPnum and IP). The numerically generated partially-sintered sperical powders (SPnum) are the same as those studied in the analysis of h_k (section 4.3.4.2). The theoretical coefficient $h_b = 0.3$ of packed beds of spherical particles is represented.

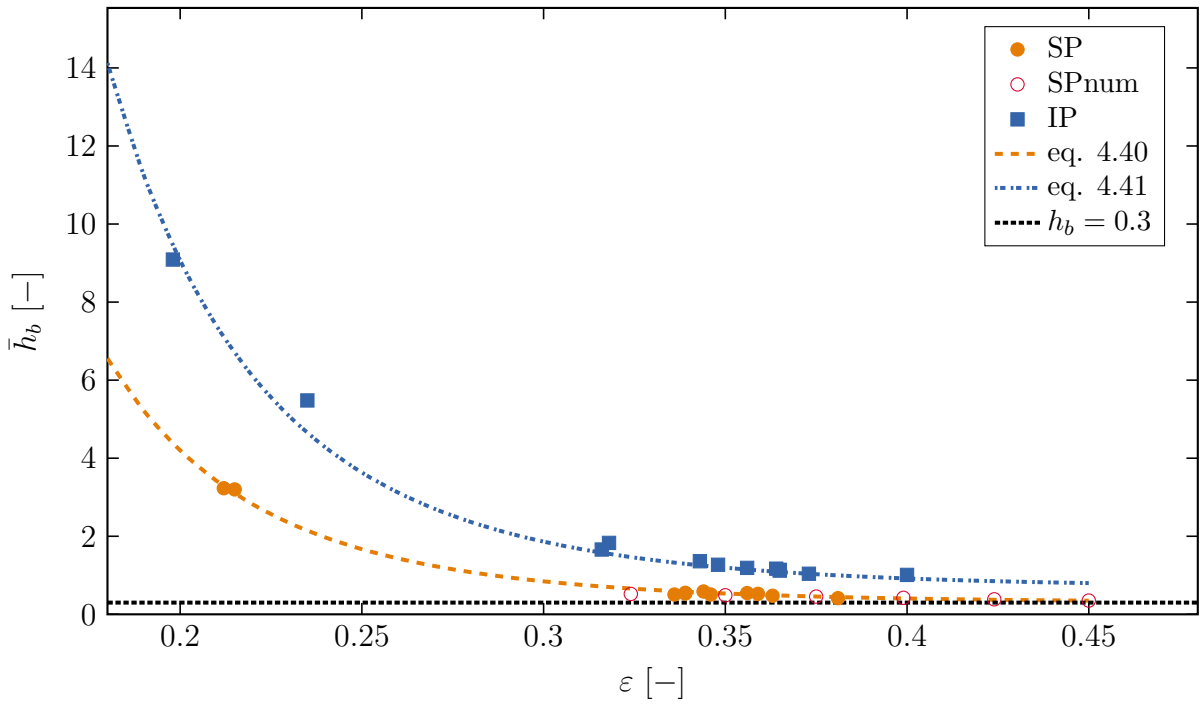

Figure 4.17: Variation of the coefficient $\bar{h}_b$ of different porous materials (SP, SPnum and IP) with the porosity.

Similar observations to that given for $\bar{h}_k$ can be made. SP geometries can be discriminated from IP ones. Indeed, at a given porosity, partially-sintered irregular powders have much higher coefficients than spherical powders.

$$\boxed{\bar{h}_b(IP) > \bar{h}_b(SP)} \tag{4.38}$$

The coefficient $\mathbf{h_b}$ of each architectural family can be correlated to the porosity. The manufacturing process must be responsible for some modifications in the overall architecture. That would cause the coefficient $\bar{h}_b$ to rise with the decreasing porosity. This agrees with the observations of Meyer and Smith (1985). Experimental $\bar{h}_b$ obtained for other partially-sintered irregular powder materials ranged from 0.85, for a porosity of 39%, to 3.15, for a porosity of 20%.

The coefficients $\bar{h}_b$ of the SPnum geometries are very similar to those of SP for porosities ranging from 32.5 to 40%. In this porosity range, both architectures have $\bar{h}_b$ close to the theoretical value of packed bed ($h_b = 0.3$). The difference declines with the increasing porosity.

The variation of $\bar{h}_b$ of partially sintered materials was captured in the **20-45% porosity range** with relations having the following form:

$$\bar{h}_b = a + b\frac{0.45 - \varepsilon}{\varepsilon^n} \tag{4.39}$$

where a, b and n are constants specific of the architectural family.

For **partially-sintered spherical powders (SP)**, the following relationship is suggested:

$$\boxed{h_b = 0.35 + 0.034\frac{(0.45 - \varepsilon)}{\varepsilon^{3.8}}} \tag{4.40}$$

The relationship is represented in the figure 4.17. The maximum error between the prediction of equation 4.40 and the simulated values is 13%.

Data of **partially-sintered irregular powders** are correlated with:

$$\boxed{h_b = 0.8 + 0.073\frac{(0.45 - \varepsilon)}{\varepsilon^{3.8}}} \tag{4.41}$$

The relationship is represented in the figure 4.17. The maximum error between the prediction of equation 4.41 and the simulated values is 16%.

4.4 Summary

This chapter was focused on the permeability of partially-sintered materials made from spherical (SP) and irregular particles (IP). Numerical flow simulations were performed on three-dimensional digitized and numerically generated images. The numerical predictions of the flow velocity at given pressure gradients agreed well with experimental data. Simulations showed that the manufacturing process of porous plates led to almost isotropic properties. It was then explained that **an Ergun-like relation is adapted** to describe the pressure losses through both types of studied partially sintered materials:

$$\frac{\Delta P}{L} = \underbrace{h_k(\varepsilon)\frac{A_{sp}^2}{\varepsilon^3}}_{1/K}\eta v_s + \underbrace{h_b(\varepsilon)\frac{A_{sp}}{\varepsilon^3}}_{\beta}\rho_f v_s^2 \tag{4.42}$$

Contrary to packed beds of spherical particles, h_k **and** h_b **are functions of the porosity**. Specific relationships were developed for each architectural family (SP or IP) and for a porosity range of $20 - 45\%$. They take into account the growing complexity of the flow path caused by an increasing level of green-body compaction.

The method introduced in the figure 4.18 summarizes how the permeability coefficient K and the Forchheimer coefficient β of partially-sintered materials can be assessed. Depending on the architectural family, different equations are used to compute the coefficients h_k and h_b from the porosity. K and β are then assessed as in the Ergun-like equation by using the values of porosity, specific surface area and the coefficient h_k and h_b previously calculated.

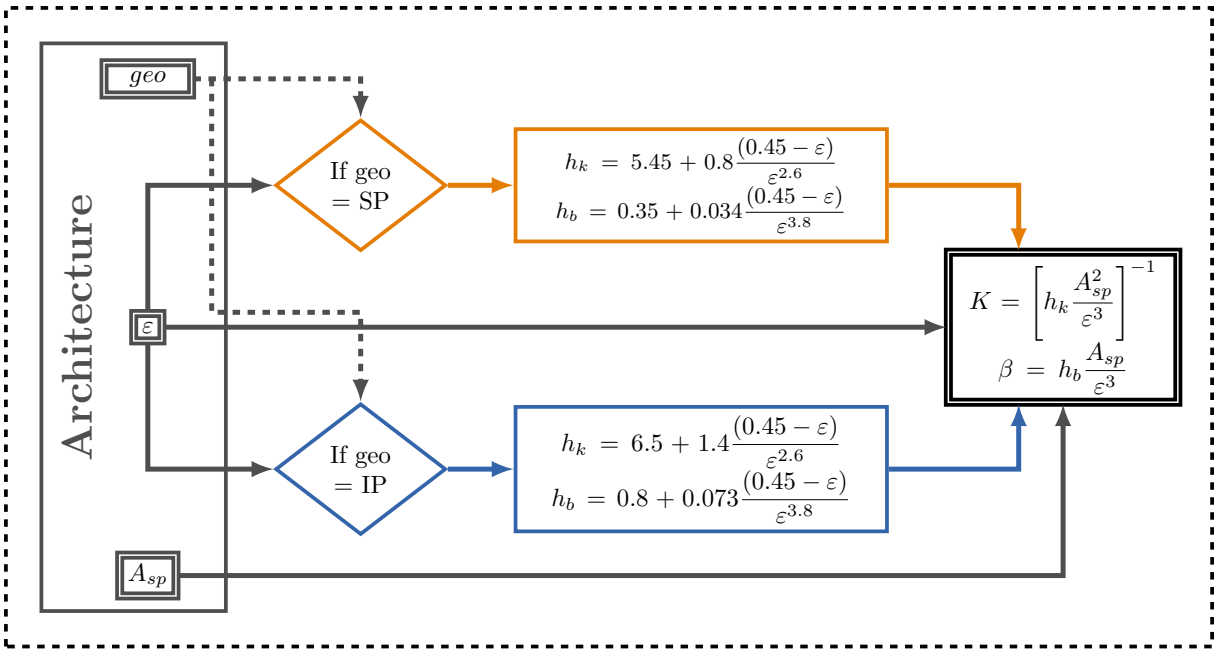

Figure 4.18: Method to assess the permeability and the Forchheimer coefficients of partially-sintered powders

Chapter 5

Volumetric heat transfer coefficients of partially-sintered materials

Contents

Convective heat transfer between the fluid phase and the solid phase are the heart of the concept of transpiration cooling. Thanks to the large specific surface area of the porous materials, a substantial amount of heat is expected to be exchanged in small volumes. **This chapter aims to study how the architecture of partially-sintered materials impacts the way the fluid removes heat from the solid phase by internal convection.**

5.1 Introduction

5.1.1 Generalities

Convection is defined as a heat transport from one place to another by the movement of a fluid (a mass transport). The convection is considered as natural or free when the flow is only caused by density differences, due to temperature, or concentration gradients. When the driving force is not a temperature gradient, it is question of forced convection. In the present study, a forced convection is caused by a pressure difference between both sides of the flame tube liner. Convective heat transfers are also closely linked to the flow regime. However, whatever the convection mode (natural or forced) and the flow regime, convective heat fluxes φ through a surface S are generally modeled with the following equation:

$$\varphi = hS\Delta T \tag{5.1}$$

where h $[W/(m^2.K)]$, S and ΔT are the heat transfer coefficient, the surface area and the temperature difference between the solid and the fluid respectively. Although equation 5.1 has a simple form, convection heat fluxes are difficult to assess because the heat transfer coefficient h is difficult to determine. Indeed, it is directly linked to the characteristics of the flow (thermal properties of the fluid, flow regime, velocity and patterns, rugosity of the surface) and depends on many variables. As the theoretical computation of the heat transfer coefficient is extremely complex, it is generally determined thanks to experimental correlation laws. A dimensional analysis shows that the relation linking the heat transfer coefficient to its variables can be expressed in terms of three dimensionless numbers: the Nusselt number $Nu_l = hl/\lambda_f$, the Reynolds number $Re_l = \rho_f lv/\eta$ and the Prandtl number $Pr = c_p\eta/\lambda_f$:

$$\boxed{Nu_l = \frac{hl}{\lambda_f} = f(Re_l,Pr)} \tag{5.2}$$

l, λ_f, c_p and η are the characteristic length of the flow, the fluid thermal conductivity, the fluid calorific capacity and the fluid dynamic viscosity respectively. Nu_l represents the ratio of the convective thermal resistance to the conductive thermal resistance. Pr is the ratio of momentum diffusivity to thermal diffusivity. Re_l is the ratio of inertial forces to viscous forces. **In this chapter the subscripts used for the Nusselt and the Reynolds number refer to the corresponding characteristic length.**

As explained in section 1.2.3, forced convection in porous materials can lead to a situation where the solid phase and the fluid phase are locally at different temperatures. This phenomenon is generally modeled by the Local Thermal Non-Equilibrium (LTNE) model which involves the coupled equations 1.1 and 1.2. In this model, the convective heat transfers between the fluid phase and the solid phase are modeled with a volumetric source term q similar to equation 5.1:

$$q = h_v(T_s - T_f) \tag{5.3}$$

This term involves a volumetric heat transfer coefficient h_v $[W/(m^3.K)]$ which can also be expressed as a function of a heat transfer coefficient h and of the specific surface area A_{sp}:

$$\boxed{h_v = hA_{sp}} \tag{5.4}$$

The solid temperature introduced in the LTNE model is a mean solid temperature and not the temperature at the interface. Dixon and Cresswell (1979) explained that the interfacial heat transfer coefficient h_{sf} (true fluid/solid film heat transfer) and the particle conductivity λ_s contribute to the the heat transfer coefficient h:

$$\frac{1}{h} = \frac{1}{h_{sf}} + \frac{d_p/\gamma}{\lambda_s} \tag{5.5}$$

where d_p is the size of the particle and γ is a shape factor (= 10, 8 and 6 for spheres, cylinders and slabs respectively). The heat conduction in the particles acts as a parallel thermal resistance and limits the rate at which heat can be exchanged between the solid and the fluid. In the case of metallic powders smaller than 400 μm, it was assumed that the thermal conductivity in particles was not a limiting mechanism and that:

$$\boxed{h = h_{sf}\left(\frac{1}{1 + \frac{d_p h_{sf}}{\gamma \lambda_s}}\right) \simeq h_{sf}} \tag{5.6}$$

This assumption is checked later in this chapter in section 5.3.3.

Quintard et al. (1997) managed to develop a general model from volume averaged equations and tried to theoretically determine the effective properties on periodic sphere arrays. However, the complexity of their work, even for a regular architecture, clearly illustrates the fact that the theoretical determination of h_v is extremely difficult. Despite the fact that the experimental measurement of h_v is not easy either, it has been preferred over the years.

5.1.2 Experimental determination of a heat transfer coefficient in the literature

As explained by Achenbach (1995), many parameters influence convective heat transfer in porous media: the Reynolds and Prandtl numbers, the porosity, the ratio of particles diameter to bed height or bed diameter, the existence of radiation, the contact conduction, the surface roughness,etc. The large amount of parameters could be the first cause to explain a large discrepancy between all the experimental data found in the literature. The second one would be the fact that all the authors do not give all the details of their experiments, making difficult a good interpretation of their results. Indeed, Kaviany (2012) explained that the definition of the measured heat transfer coefficient is not always clear. Eroshenko and Yaskin (1976) pointed out that the choice of the method used to determine the heat transfer coefficient (use of heat transfer model or analogy with flow in a tube), as well as the choice of the characteristic length for the dimensionless numbers, make the comparison of all the data almost impossible. Nevertheless, the following section gives an overview of the experimental works carried out on convective heat transfer in porous media in order to introduce data which help the validation of the numerical method suggested in the present study.

5.1.2.1 Experimental measurements for unconsolidated porous media

A lot of efforts were given to the study of convective heat transfer in unconsolidated porous media. Many early works can be found in the papers of Whitaker (1972) and Wakao and Kagei (1978). The paper of Wakao and Kagei (1978) gives a good overview of the different experimental techniques used to characterize convective heat transfer in packed beds: steady measurements based on simultaneous mass and heat transfer, conduction in bed with no heat-generating particles, ohmic-,induction-, or micro-wave induction heating particles as well as unsteady methods based on frequency, step or shot responses are referenced.

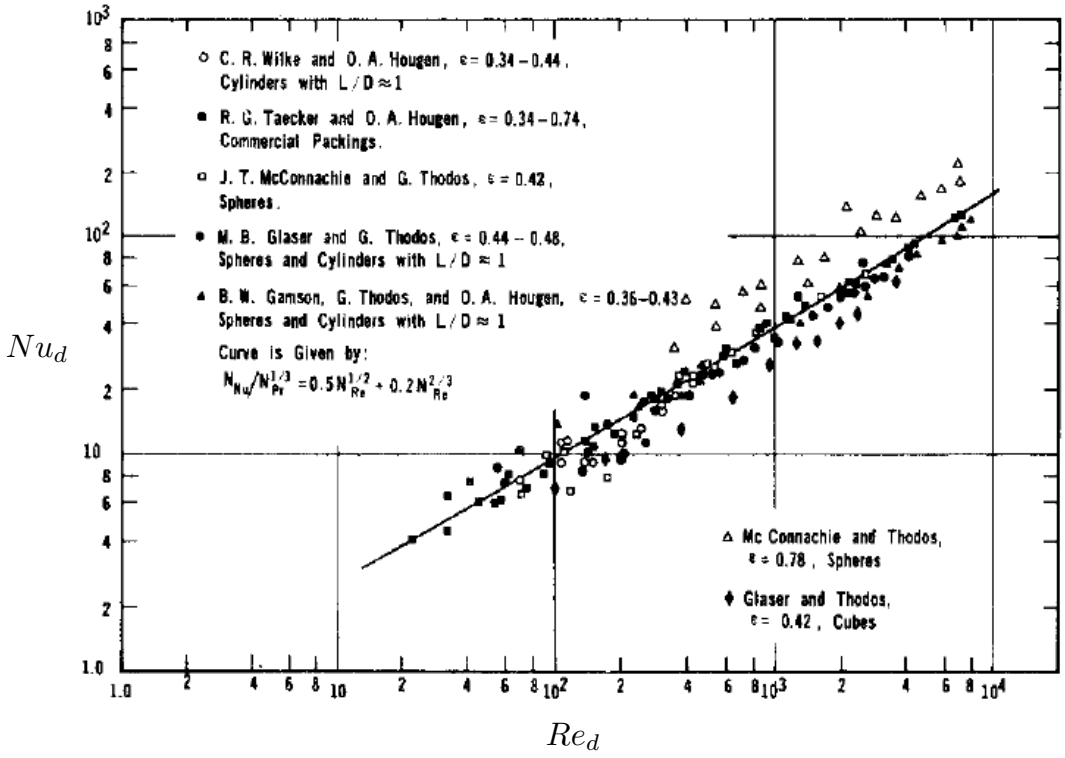

Figure 5.1: Experimental data collected by Whitaker (1972) and his correlation for $10 < Re_d < 10^4$ and $0.34 < \varepsilon < 0.74$ (apology for the poor image quality).

After analyzing all the data he gathered (figure 5.1), Whitaker (1972) suggested a dimensionless law to predict heat transfer coefficients of random packed beds with an accuracy of $\pm 25\%$ and for $10 < Re_d < 10^4$ and $0.34 < \varepsilon < 0.74$:

$$Nu_d = (0.5Re_d^{1/2} + 0.2Re_d^{2/3})Pr^{1/3} \tag{5.7}$$

with:

$$Nu_d = \frac{hd\varepsilon}{\lambda_f(1-\varepsilon)} \tag{5.8}$$

$$Re_d = \frac{\rho v_s d}{\eta(1-\varepsilon)} \tag{5.9}$$

$$d = \frac{6(1-\varepsilon)}{A_{sp}} \tag{5.10}$$

The characteristic length is here the equivalent particle diameter d of the packed bed. In the case of a packed bed of monosized spherical particles, the equivalent diameter is equal to the size of the particles.

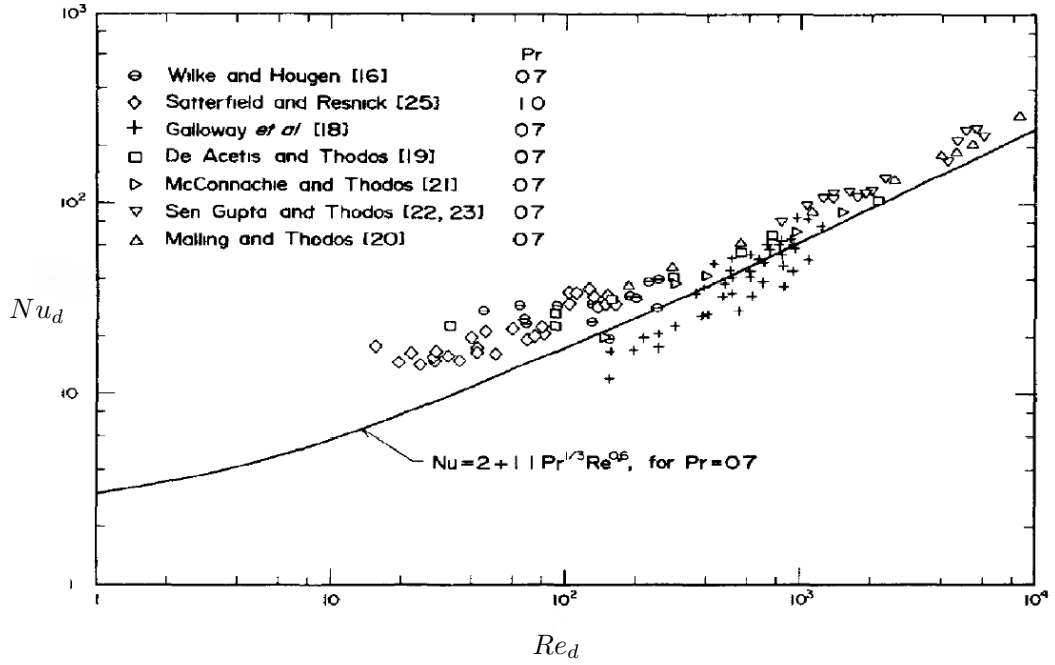

Figure 5.2: Experimental data collected by Wakao and Kagei (1982) and their correlation for $10 < Re_{d_p} < 10^4$.

Wakao and Kagei (1978) also studied data from the literature. For cause of technical problems encountered during the experiments, assumption issues or lake of clarity, they only analyzed, among all their referenced experimental techniques, the data obtained by water evaporation, catalytic decomposition of hydrogen peroxide or step and frequency response. After correcting the collected data (figure 5.2), they established another dimensionless relationship for $10 < Re_{d_p} < 10^4$:

$$Nu_{d_p} = 2 + 1.1 Re_{d_p}^{0.6} Pr^{1/3} \tag{5.11}$$

$$Nu_{d_p} = \frac{h d_p}{\lambda_f} \tag{5.12}$$

$$Re_{d_p} = \frac{\rho v_s d_p}{\eta} \tag{5.13}$$

where d_p is the particle diameter. The correlation gives a limit value of 2 when $Re_{d_p} \to 0$. If Fu et al. (1998) claimed that this limit cannot be valid, Kaviany (2012) thought that this assessment is more reasonable than $h_{sf} \to 0$. Indeed, he explained that as the Reynolds number gets low, the convection term becomes insignificant, which leads to experimental uncertainties.

Achenbach (1995) extended the data on packed beds with a mass transfer technique at low Reynolds number and an electrically heated single sphere method at high Reynolds number. He suggested to correlate heat transfer through packed beds for $1 < Re_{d_p}/\varepsilon < 7.7 \times 10^5$ with:

$$Nu_{d_p} = \left\{ (1.18 Re_{d_p}^{0.58})^4 + \left[0.23 \left(\frac{Re_{d_p}}{1-\varepsilon} \right)^{0.75} \right]^4 \right\}^{1/4} \tag{5.14}$$

5.1.2.2 Experimental measurements for consolidated porous media

Many experimental characterizations of convective heat transfer carried out on consolidated porous materials can also be found in the literature. Fu et al. (1998) claimed that most intention was given to heat transfer in sintered materials because of their potential application in gas turbines. Koh et al. (1973) assessed a volumetric heat transfer coefficient thanks to an energy balance in partially-sintered 304L stainless steel spherical powders. Eroshenko and Yaskin (1976) gave a good summary of the early characterizations of sintered materials. The data they collected were obtained by radiation, conduction or ohmic steady heating or non-stationary cooling methods. By studying transpiration cooling, Kar (1981) also experimentally measured heat transfer coefficients in porous materials. Hwang and Chao (1994) and Jiang et al. (2004) studied convective heat transfer in a rectangular channel filled with a bronze sintered material. By measuring the temperature at different locations of a copper plate in contact with the porous material submitted to a heat flux, they assessed local heat transfer coefficients. Jiang et al. (2004) claimed that the particle diameter has little effect on the convective heat transfer of sintered materials. Hetsroni et al. (2006) studied forced convection in rectangular channel filled with stainless steel sintered materials having a porosity of 32 or 44%. They measured an average heat transfer coefficient by using average wall and fluid temperatures. Bellettre et al. (2000) assessed the internal heat exchange in partially-sintered irregular stainless steel powders and highlighted the effect of the specific surface area of the materials.
The data given by all these authors are extremely complex to compare altogether because of the following reasons:

- Diversity of partially-sintered materials analyzed with few geometrical data given;
- Diversity of experimental methods in which the impact of the different involved heat transfer mechanisms cannot be easily isolated;
- Diversity of the heat transfer coefficient definitions, notably due to the various possibilities to define the fluid/solid temperature difference.

Although most of the introduced studies suggested dimensionless relationships between the Nusselt, the Reynolds and the Prandtl numbers, the previous reasons prevent a universal law to be found. Nevertheless, it is interesting to note that authors generally predict the Nusselt numbers of sintered materials with relationships having the following form:

$$\frac{Nu}{Pr^{1/3}} = A + BRe^n \tag{5.15}$$

where A and B are two empirical constants. Table 5.1 gives a comparative study of the exponent used for the Reynolds number. It shows that the exponent n for sintered materials is equal to 1 for high Reynolds number and ranges from 1 to 2 for small Reynolds number. It can also be noticed that these relations have larger exponents than the empirical laws introduced in the previous section and developed for packed beds of spherical particles. Indeed, the latter architectures have exponents ranging from 0.5 to 0.75.

Authors	Characteristic length	n	Validity domain of Re	Material
Koh et al. (1973)	d_h	1	1-100	Stainless steel (spherical powders) $\varepsilon = 21 - 31\%$
Kar (1981) (from Bellettre et al. (2000))	d_p	1.06	1-100	stainless steel $\varepsilon = 28 - 65\%$
		1.60	0.1-10	nickel $\varepsilon = 35 - 51\%$
		1.40	0.1-10	copper $\varepsilon = 45 - 58\%$
Bellettre et al. (2000)	d_h	1	0.01-1	Stainless steel (Irregular powders) $\varepsilon = 30 - 40\%$
Hetsroni et al. (2006)	d_h	1	500-3000	Stainless steel (Irregular powders) $\varepsilon = 32 - 44\%$

Table 5.1: Comparative study of correlation laws referenced in the literature and developed for partially sintered materials ($Nu/Pr^{1/3} = A + BRe^n$). d_p is the mean particle diameter and d_h is the hydraulic diameter.

5.1.3 Numerical determination of a heat transfer coefficient

Few numerical determinations of heat transfer coefficient in porous materials are reported in the literature. Most of them were performed on small unit cell of periodic geometry. Kuwahara et al. (2001) determined the interfacial heat transfer coefficient in two-dimensional periodic square arrays. An infinite conductivity in the solid phase was assumed in order to consider the rods as isothermal heat sources. They thus developed the following correlation for $0.2 < \varepsilon < 0.9$ similar to that of Wakao and Kagei (1978):

$$Nu_{d_p} = \left(1 + \frac{4(1-\varepsilon)}{\varepsilon}\right) + \frac{1}{2}(1-\varepsilon)^{1/2} Re_{d_p}^{0.6} Pr^{1/3} \tag{5.16}$$

No heat transfer simulation attempt in digitized partially-sintered materials was found.

5.2 Computation of a volumetric heat transfer coefficient

5.2.1 General idea

In this work, a method is suggested to numerically assess the volumetric heat transfer coefficient $\mathbf{h_v}$ of porous metallic materials thanks to their three-dimensional voxelized images. This computation is based on the assumption introduced in section 5.1.1:

$$\boxed{h_v = hA_{sp} = h_{sf}A_{sp}} \tag{5.17}$$

which claims that the thermal conductivity in the metallic particles does not limit the process of heat transfer by convection at the solid/fluid interfaces. Moreover, as the aim is to assess h_v and to predict the effect of the architecture, **only incompressible flow with constant thermal properties are considered**. The full description of the temperature field in both phases will not be studied either.

The general idea is to assess the volumetric heat transfer coefficient $\mathbf{h_v}$ by looking at the temperature evolution of a fluid when it enters and flows in a hotter and isothermal porous material. The heat equation is then only solved in the fluid phase of a digital 3D porous material image. h_v is extracted from the computed temperature field thanks to the use of a one-dimensional heat tranfer model. The numerical process is summarized in the flow chart introduced in figure 5.3. The different steps of the computation of the volumetric heat transfer coefficient are detailed in the next sections.

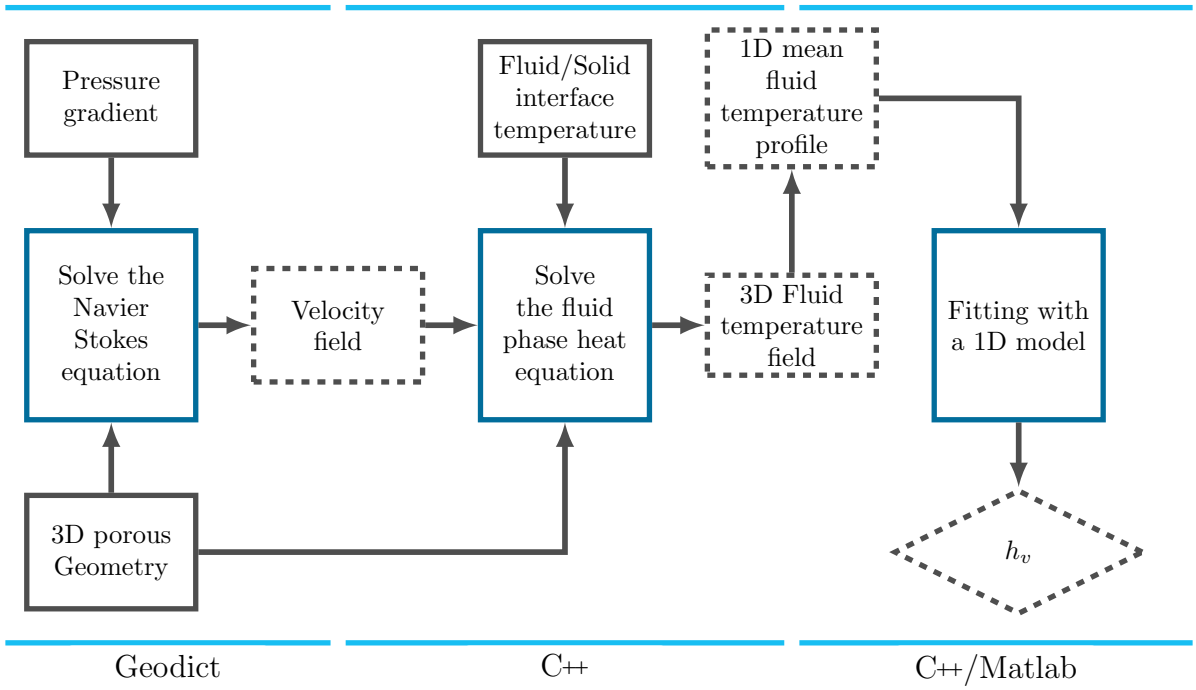

Figure 5.3: Flow chart to assess the volumetric heat transfer coefficient of a geometry and at a given pressure gradient.

5.2.2 Computation of the fluid phase three-dimensional temperature field

The first step of the suggested numerical method is the computation of the three-dimensional temperature field. The model and the required numerical tools enabling this computation are detailed in this section.

5.2.2.1 The fluid phase heat equation and its discretization

The fluid is supposed to enter and flow in a porous material maintained at a hotter and isothermal temperature. By assuming a steady and incompressible flow without any chemical reaction, the energy equation governing the heat transfer in the fluid phase can be reduced to equation 5.18:

$$\vec{\nabla}.\left(\rho_f c_p T_f \vec{v} - \lambda_f \vec{\nabla} T_f\right) = 0 \tag{5.18}$$

As small temperature variations are encountered in the method, **constant thermal properties** (ρ_f, c_p, λ_f, η) are considered. The equation 5.18, better known as the convection-diffusion equation, has four unknown variables: the temperature and three

velocity components. As a result, the equation has to be associated to the mass conservation law (equation 5.19) as well as to the Navier-Stokes equation (equation 5.20):

$$\vec{\nabla}.\vec{v} = 0 \tag{5.19}$$

$$\left(\rho_f \vec{v}.\vec{\nabla}\right)\vec{v} = -\vec{\nabla}p + \eta\nabla^2\vec{v} \tag{5.20}$$

As the fluid thermal properties are supposed to be independent of the temperature, equations 5.19 and 5.20 can be solved independently of equation 5.18. **The flow field is therefore computed in voxelized images with the module *FlowDict* of *GeoDict*** (see chapter 4) and then used to solve equation 5.18.

The fluid phase heat equation is discretized with a finite volume method and a power-law differencing scheme. Discrete temperature values are defined at the core of the voxels whereas discrete velocity component values, previously calculated with the software Geodict, are defined at the voxel faces. More information about this method and the differencing schemes are given in the appendix A. Higher order schemes, as the Quadratic Upstream Interpolation for Convective Kinematics scheme (QUICK), could also have been considered. By involving more neighboring points, these methods minimize the false diffusion error. However, the ease of implementation and the satisfying accuracy justify the fact that the power-law scheme was selected to discretize the energy equation in this work.

5.2.2.2 Boundary conditions

To be able to solve the energy equation, boundary conditions have to be applied at each one of the interfaces. All the existing interfaces to take into consideration are represented in figure 5.4. The boundary conditions defined at each of these interfaces are introduced in this section.

Flow inlets: As the flow is assumed to enter the porous domain with a known temperature T_0, a Dirichet condition is imposed at each one of the inlets:

$$T_f(x = 0) = T_{f,0} \tag{5.21}$$

Flow outlets: When the fluid goes out from the porous medium, no more heat transfer takes place between the solid and the fluid phases. No temperature variation in the flow

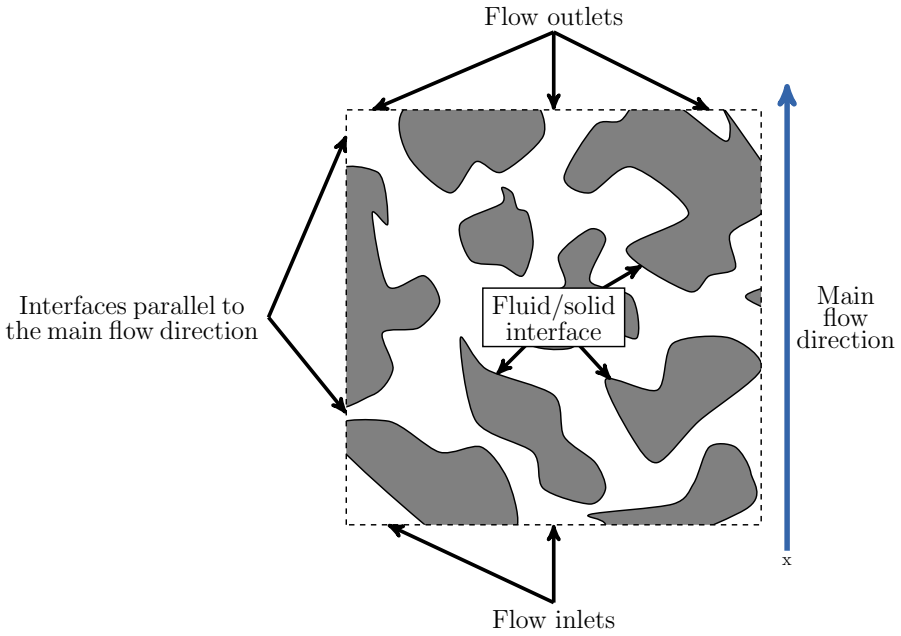

Figure 5.4: The different interfaces where boundary conditions have to be applied.

direction is then assumed and a Neumann condition is applied at each one of the outlets:

$$\left.\frac{\partial T_f}{\partial x}\right|_{x=L} = 0 \tag{5.22}$$

Faces parallel to the main flow direction: The computation of the flow field is performed with the module *FlowDict* of *Geodict* which requires periodic boundary conditions. As explained chapter 4, if the original image is not periodic, it has first to be symmetrized. As a result, different thermal boundary conditions are applied to the fluid interfaces parallel to the flow direction depending on the periodicity of the original image:

- If the original image is periodic, a periodic boundary condition is applied at the faces parallel to the main flow direction: the cell which is on the opposite side of the geometry is virtually used as one of the neighboring cells during the discretization step (figure 5.5).
- If the original image is not periodic, the mathematical symmetrization made by *FlowDict* leads to no normal flux at the inteface:

$$v_n = 0 \tag{5.23}$$

$$\frac{\partial T_f}{\partial x_n} = 0 \tag{5.24}$$

where n means the direction normal to the interface.

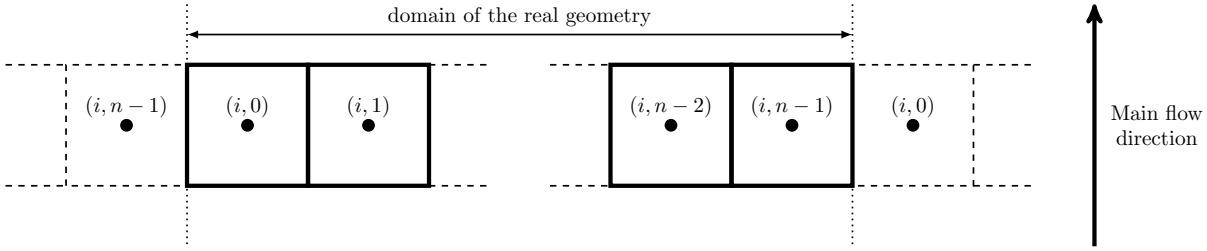

Figure 5.5: Use of the opposite cells to discretize the heat equation at a periodic interface.

Fluid-solid interfaces: The solid phase is supposed to be maintained at an arbitrary uniform temperature T_s, hotter than the fluid inlet temperature T_0. A Dirichlet boundary condition is therefore imposed at the fluid/solid interface. ΔT is defined as the temperature difference between the interface temperature T_s and the fluid inlet temperature $T_{f,0}$:

$$T_s = T_{f,0} + \Delta T \tag{5.25}$$

ΔT is sufficiently low (typically 10 K) to consider constant fluid thermal properties.

5.2.2.3 Linear system solver

The discretization of the fluid phase energy equation leads to a linear system which can be written under a matrix form:

$$M\tilde{T} = S \tag{5.26}$$

where $\tilde{T}$ is a column vector $(n \times 1)$ which includes the n unknown temperature variables, M is a square matrix $(n \times n)$, and S is a column matrix $(n \times 1)$. All the temperatures are found by solving the linear system. The computation was performed with a C++language and with the specific library *Eigen*. This library is specialized in linear algebra and easily manipulates sparse linear system. The system was solved with a bi-conjugate gradient stabilized solver (BiCGSTAB algorithm).

5.2.3 The one-dimensional equivalent model and the computation of h_v

After solving the energy equation, a volumetric heat transfer coefficient h_v has to be extracted from the resulting three-dimensional temperature field. This section explains how this parameter is assessed.

5.2.3.1 A mean temperature profile

First of all, a one dimensional temperature profile is extracted from the temperature field. This mean profile is obtained by averaging the fluid temperature of each plane perpendicular to the main flow direction as shown in figure 5.6.

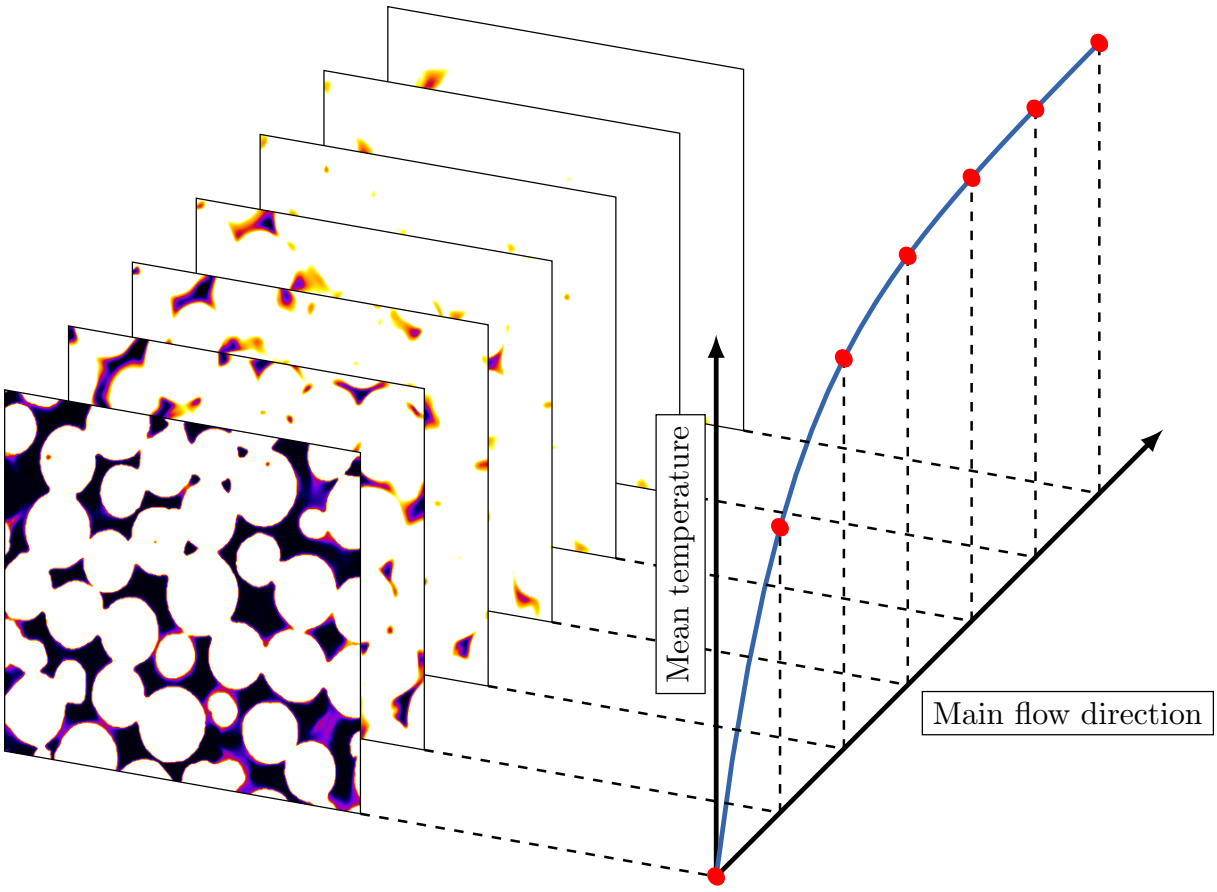

Figure 5.6: Construction of the mean 1D temperature profile from the 3D field.

Some questions arise regarding the way to average the temperature. In the homogenization theory, the mean temperature is defined as:

$$\bar{T}_f = \frac{1}{V_f} \int_{V_f} T_f dV \tag{5.27}$$

where V_f represents the volume of the fluid phase in the overall representative volume of integration. This mean temperature definition was used in the numerical works of Quintard et al. (1997); Wakao and Kagei (1978); Nakayama et al. (2002); Alshare et al. (2010) who tried to close the LTNE model from the intrinsic volume-averaged model. It

would therefore have been natural to define the mean temperature as:

$$\bar{T_f} = \frac{1}{S_f} \int_{S_f} T_f dS \tag{5.28}$$

where S_f is the surface occupied by the fluid phase. However, the mixed temperature definition was preferred in the present work:

$$\boxed{\bar{T_f} = \frac{\int_{S_f} \rho_f c_p v_x T_f dS}{\int_{S_f} \rho_f c_p v_x dS}} \tag{5.29}$$

where v_x is the velocity component parallel to the main flow direction. This mixed temperature is a measure of the energy transported by the flow. Such a temperature is closer to the experimentally measured temperatures and the assessed volumetric heat transfer coefficients should then agree more with experimental data from the literature.

5.2.3.2 Comparison with a one-dimensional model

In the simple case where the solid phase is supposed to be at an isothermal temperature, heat transfer through the fluid phase can be represented with the following one-dimensional model:

$$\rho_f c_p u_x \frac{dT_f(x)}{dx} - h_v(T_s - T_f(x)) = 0 \tag{5.30}$$

and with

$$T_f(x = 0) = T_{f,0} \tag{5.31}$$

This equation is similar to equation 1.2 with the exception that the conductive heat transport in the fluid phase was neglected compared to the advection term. This assumption can be justified with the computation of a macroscopic Peclet numbers:

$$Pe_L = \frac{c_p \rho_f u_x L}{\lambda_f} \tag{5.32}$$

where L is the size of the sample. This Peclet number measures the ratio of the rate of advection to the rate of diffusion. In each simulation, this Peclet number was indeed much larger than unity. This shows that the heat was mainly transported through the material by advection and not conduction. Equation 5.30 admits a simple analytic solution:

$$\boxed{\frac{T_f(x) - T_{f,0}}{\Delta T} = 1 - \exp\left(- St_v \frac{x}{L} \right)} \tag{5.33}$$

where L is the thickness of the material and $St_v = h_v L / \rho c_p u_x$ the Stanton number of the flow. The Stanton number is a dimensionless number which characterizes the ratio of heat

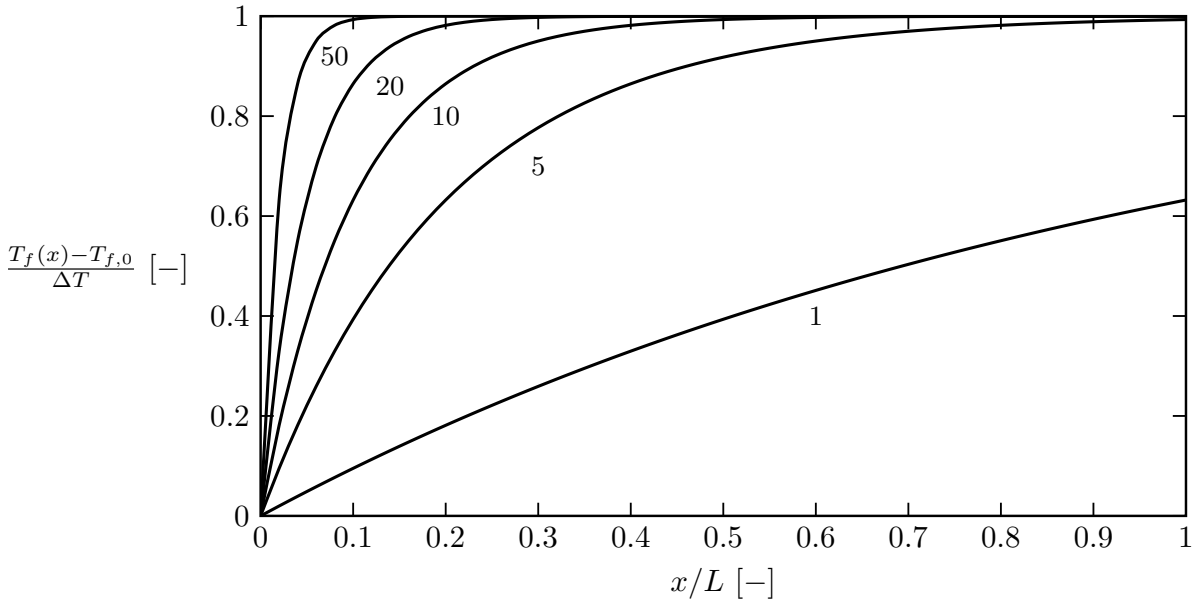

Figure 5.7: One-dimensional temperature profile in the porous material for different Stanton numbers ($St_v = 1$, 5, 10, 20, 50).

transferred by convection to the fluid thermal capacity in forced flow. Figure 5.7 gives the typical one-dimensional temperature profile in porous materials as a function of St_v.

Only the volumetric heat transfer coefficient is unknown in the analytical solution 5.33. The idea is then to tune the coefficient h_v from equation 5.33 to find the value which best copes with the mean temperature profile extracted from the 3D-simulation. h_v is obtained thanks to a non-linear least-squares solver (function *lsqcurvefit* of the software *Matlab*) which consists in finding the value of h_v by minimizing the following function $f(h_v)$:

$$f(h_v) = \sum_{x_i} \left(\bar{T}_f(x_i) - T_f(x_i,h_v)\right)^2 \tag{5.34}$$

where $T(x_i,h_v)$ is the temperature of the one-dimensional model at a position x_i and for a value of volumetric heat transfer coefficient h_v.

5.2.4 Summary

This section introduced the numerical method which was set up to assess the volumetric heat transfer coefficient of partially-sintered materials from voxelized 3D images. This method consists in fitting a one-dimensional heat transfer model with a mean tempera-

ture profile extracted from a three-dimensional heat transfer simulation. **The method assumes that the volume is large enough to extract a representative value of volumetric heat transfer coefficient. As the studied volumes are REVs for the permeability, it is assumed that they are also REVs for the volumetric heat transfer coefficient.** Before being able to analyze any architecture, it is now essential to show the accuracy of the computational process. This is carried out in the next section.

5.3 Accuracy of the numerical method

In order to check the accuracy of the suggested numerical method, several tests were carried out on simple packed beds of spherical particles. The tests were performed on packed beds because comparative data are available in the literature (section 5.1.2.1) and because this type of architecture is easily reproducible.

Three-dimensional images of 39, 43 or 50% porous periodic packed beds made of 400 monosized spherical particles were generated with the process introduced in section 2.2.2. For each geometry, the use of three different voxel sizes (respectively 2, 4, & 8 μm) allows the numerical method to be tested for three particle diameters (100, 200 & 400 μm). Cross sections of the packed beds are represented figure 5.8.

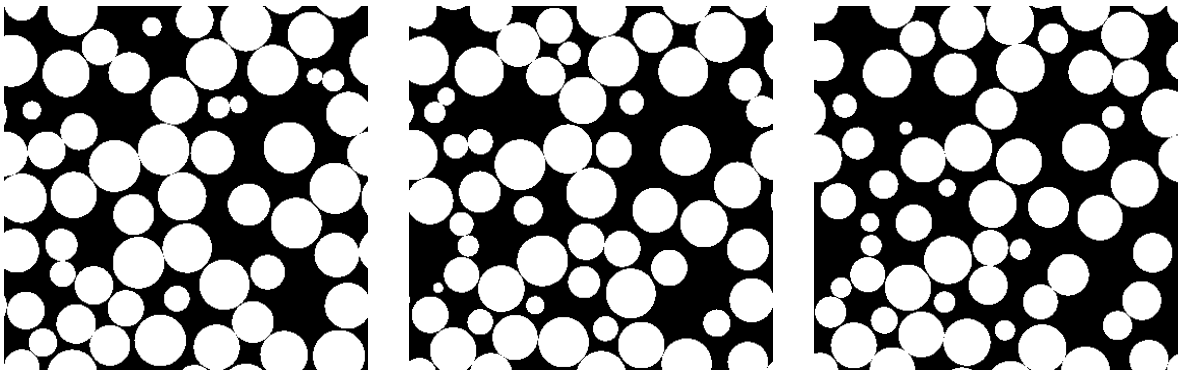

(a) $\varepsilon = 0.39$ **(b)** $\varepsilon = 0.43$ **(c)** $\varepsilon = 0.50$

Figure 5.8: Cross-sections of the generated packed beds of sphere particles.

5.3.1 Tests at ambient condition

Tests were first run at ambient conditions (300 K and 1 bar). For each porosity and particle diameter, flow simulations were performed with the module *FlowDict* of *Geodict*. The pressure gradients ranged from 1×10^6 to $1.2 \times 10^7 Pa/m$. The inlet air temperature

of the thermal simulation was fixed at 300 K and the solid temperature at 310 K. As the temperature difference is only 10 K, the thermal properties could indeed be considered as constants. The thermal properties of air at ambient conditions are introduced in table 5.2

ρ_f $[kg/m^3]$	η $[Pa.s]$	c_p $[J/(kg.K)]$	λ_f $[W/(m.K)]$
1.20	1.83×10^{-5}	1000	2.62×10^{-2}

Table 5.2: Thermal properties of the air at ambient conditions ($T = 300\ K$ and $p = 1\ bar$).

5.3.1.1 Quality of the fit of the 1D-model with the 1D mean temperature profile

The quality of the volumetric heat transfer coefficient value given by the least square method depends on how the theoretical 1D model fits with the extracted 1D mean temperature profile. Figure 5.9 shows comparisons between extracted 1D mean temperature profile and the 1D model after applying the least square method. The comparisons are done for different particle diameters of the 43% porous packed beds and for different pressure gradients.

The exponential profile of the 1D heat transfer model captures very well the evolution of the air temperature through packed beds for high pressure-gradient. Slight differences can be observed for the smallest particle size (100 μm) and the lowest pressure gradient ($1 \times 10^6\ Pa/m$). Nevertheless, the way the 1D model captures the 1D mean temperature profile remains satisfying enough. In the following, it is considered that the one-dimensional model can be used to fit the 1D mean temperature profile.

5.3.1.2 Comparison with literature data

To validate the accuracy of the computational method, the results obtained at ambient conditions for packed beds of spherical particles are compared to the empirical laws of Whitaker (1972) (equation 5.7), Wakao and Kagei (1978) (equation 5.11) and Achenbach (1995) (equation 5.14). The data are compared in figures 5.10a-5.10c in terms of Nusselt number Nu_{d_p} as a function of the Reynolds number Re_{d_p}. Both dimensionless numbers are based on the particle diameter d_p.

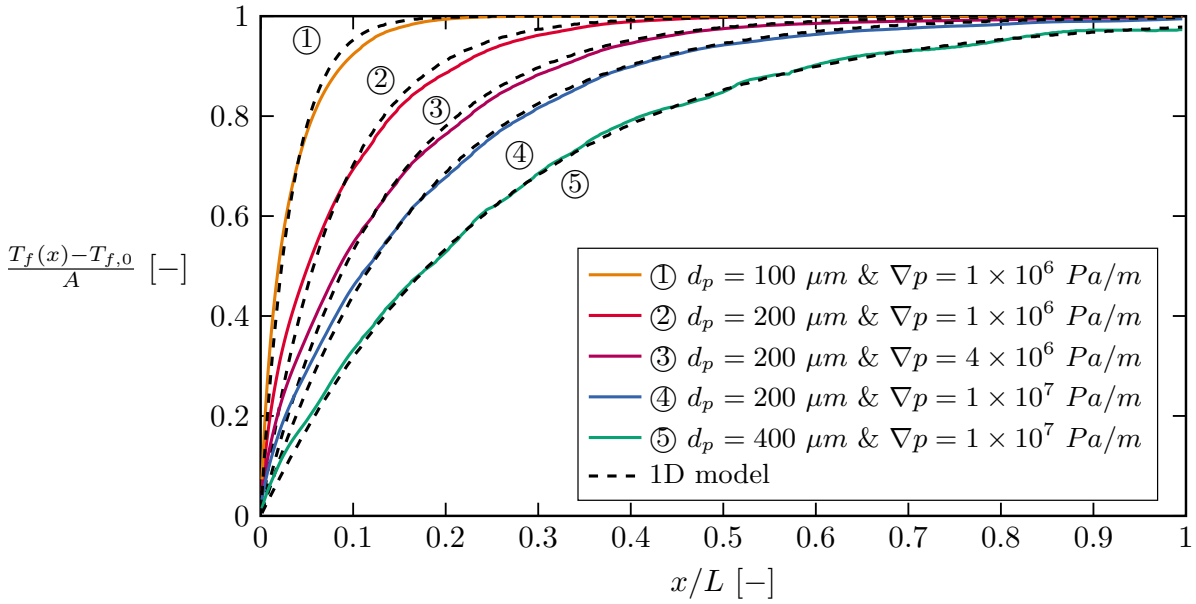

Figure 5.9: Comparison between the 1D temperature profiles extracted from the 3D temperature field and the fits with 1D model on the 43% porous geometry

The different empirical laws can first be compared altogether. Because of its limit value of 2 when $Re_{d_p} \to 0$, the empirical law of Wakao and Kagei (1978) is always higher than the other ones at very low Reynolds numbers. If the correlation laws are in good agreement for the lowest porosities, the differences increase with the porosity rise. At a porosity of 50%, the prediction of Whitaker gives Nusselt numbers about 50% lower than the two other laws.

The voxel size has no impact on the prediction of the Nusselt number. Indeed, for a given porosity, all the points follow the same trend whatever the particle diameter.

Despite a slight overestimation at the lowest porosity (39%), the simulation results are always very close to the prediction of Wakao and Kagei (1978) and Achenbach (1995). **The suggested numerical method is therefore considered in the following as accurate enough.**

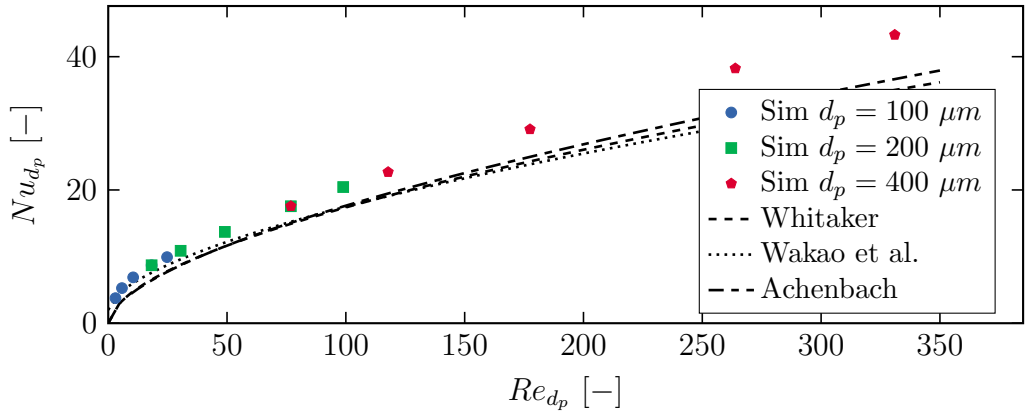

(a) $\varepsilon = 0.39$

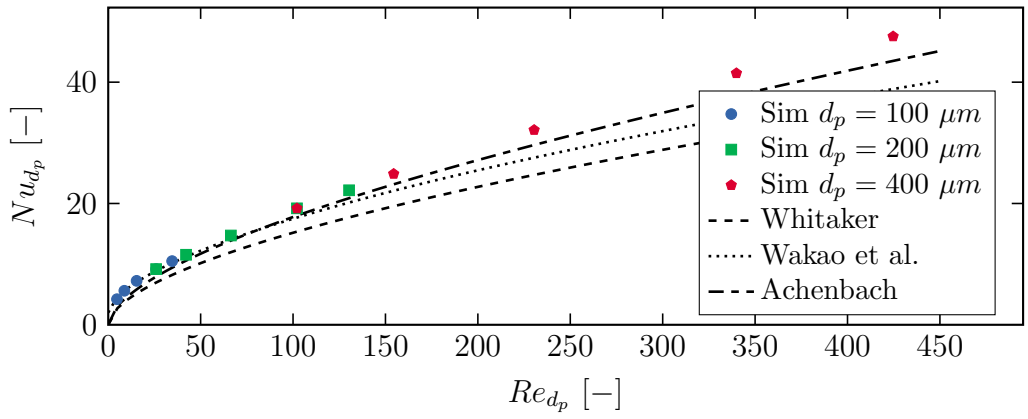

(b) $\varepsilon = 0.43$

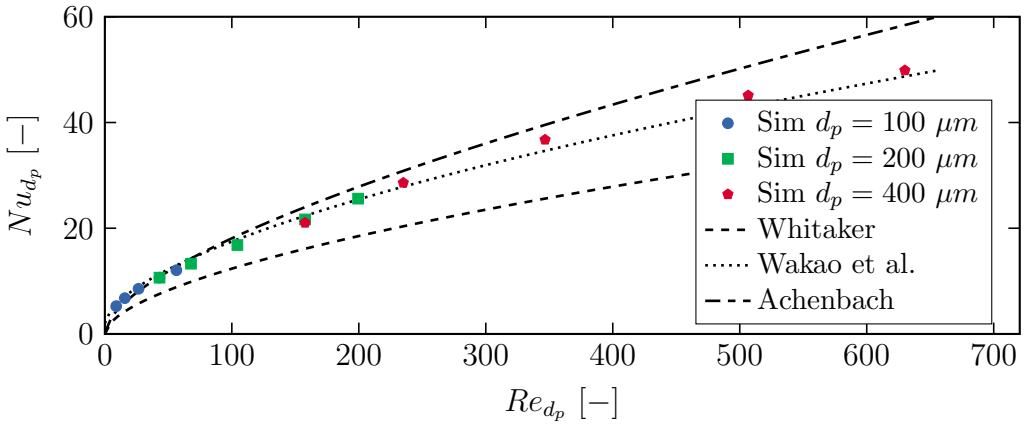

(c) $\varepsilon = 0.50$

Figure 5.10: Comparison of Nusselt numbers obtained by numerical simulation on digital packed beds of spherical particles (particle size: 100 μm, 200 μm or 400 μm) with empirical laws from the literature (Whitaker (1972) (equation 5.7), Wakao and Kagei (1978) (equation 5.11) and Achenbach (1995) (equation 5.14)).

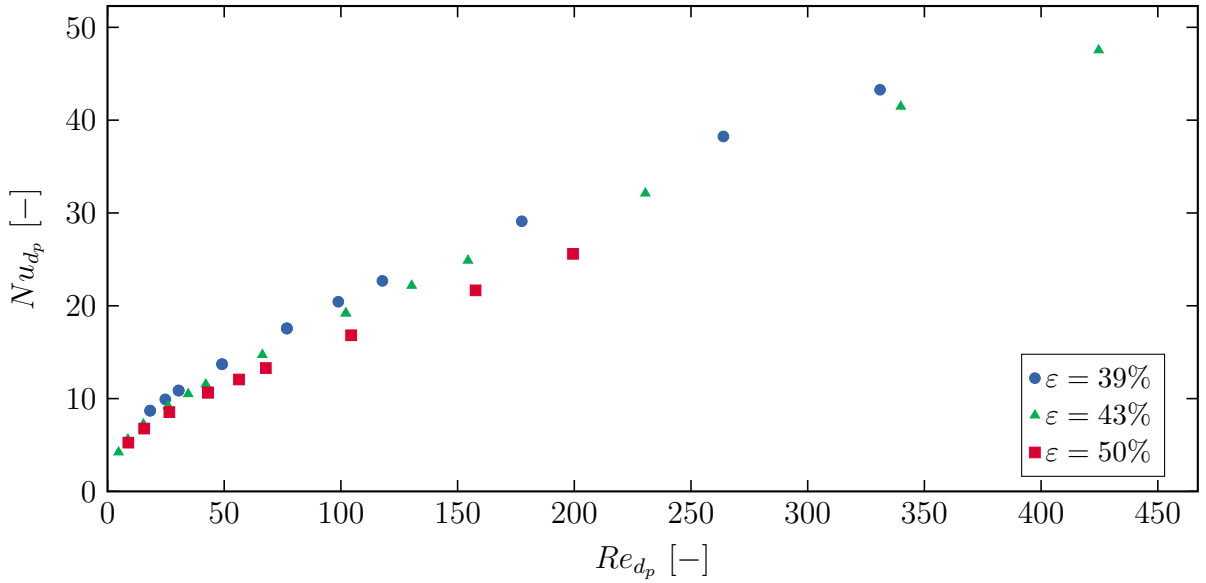

(a) Dimensionless numbers based on the particle diameter d_p.

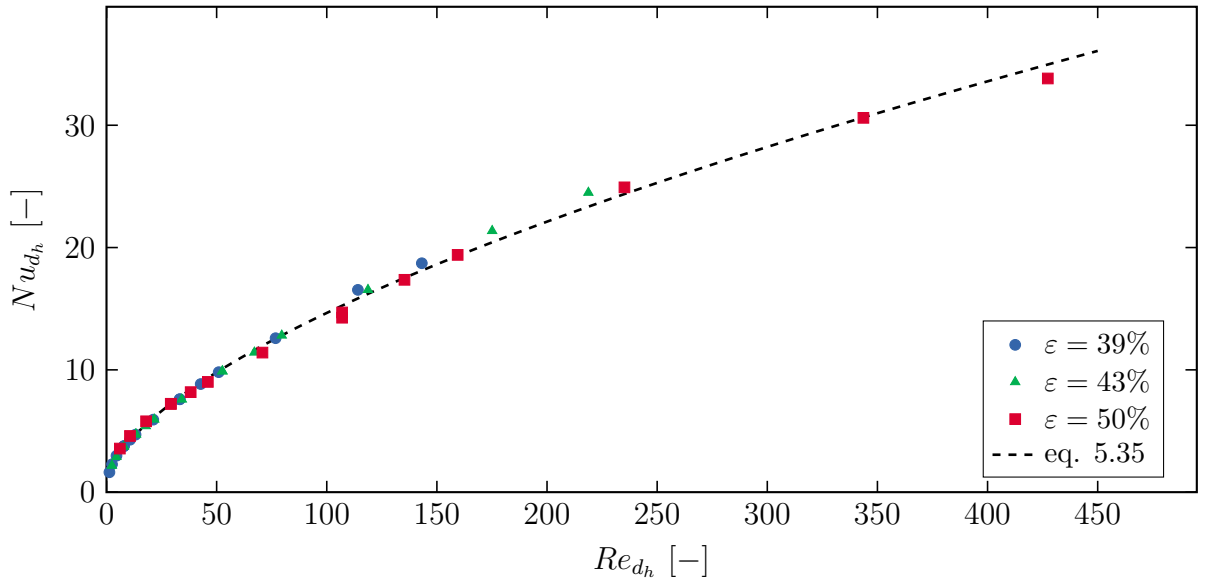

(b) Dimensionless numbers based on the hydraulic diameter d_h.

Figure 5.11: Nusselt numbers of packed beds of spherical particles as a function of the porosity, the Reynolds number and the characteristic length.

In figure 5.11a, all the simulated Nu_{d_p} are plotted in a unique graph as a function of Re_{d_p}. It is shown that the only use of the particle diameter is not sufficient to well predict the packed bed heat transfer coefficients. As in the law of Whitaker (1972) and Achenbach (1995), the role of the porosity must have to be taken into account **As the convective heat transfers are function of the flow, it could be interesting to use dimensionless numbers based on a parameter which better characterizes**

the geometry of the porous phase. Following the work done for the permeability (see chapter 4), **a hydraulic diameter $\mathbf{d_h = 4\varepsilon/A_{sp}}$ can be defined as the characteristic length.** The simulated Nusselt and Reynolds numbers based on the hydraulic diameter are introduced in figure 5.11b. By using this new characteristic length, all the points follow a same trend. A predictive law for packed beds of spherical particles can then be suggested for $Re_{d_h} > 1$:

$$\boxed{Nu_{d_h} = 0.75 + 0.90 Re_{d_h}^{0.62} Pr^{1/3}} \tag{5.35}$$

The use of the Prandtl number at the power 1/3 permits the equation to be consistent with most of Nusselt number empirical correlations. For $Re_{d_h} > 10$, the relative error between the simulated Nusselt numbers and equation 5.35 is lower than 5%. Otherwise, it remains below 10%. The form of the suggested equation is very close to the one given by Wakao and Kagei (1982). A limit value of 0.75 is used at low Reynolds number and the Reynolds number has a power close to 0.6.

5.3.2 Test at engine conditions

The previous simulations were carried out at ambient conditions. However, the conditions of pressure and temperature in an engine combustion chamber are very different from ambient and from the experimental conditions found in the literature. During cruise, the temperature of the air at the compressor outlet is about 800 K and its pressure is about 30 bar. The temperature difference between the solid phase and the fluid inlet temperature is once again fixed at 10 K. The air properties at these conditions are called *engine conditions* and are introduced in table 5.3:

ρ_f $[kg/m^3]$	η $[Pa.s]$	c_p $[J/(kg.K)]$	λ_f $[W/(m.K)]$
13.1	3.62×10^{-5}	1100	5.78×10^{-2}

Table 5.3: Thermal properties of the air at engine condition ($T = 800\ K$ and $p = 30\ bar$).

At engine conditions, the Prandtl number is similar to that at ambient condition ($Pr \simeq 0.7$). To agree with the literature and with equation 5.35, the same evolution of Nu_{d_h} with Re_{d_h} must then be observed at engine conditions as at ambient conditions. Additional simulations were performed at engine conditions on the three packed beds made of 200 μm spherical particles. The simulated Nusselt numbers at engine conditions

are displayed in figure 5.12a and compared to those at ambient condition. It can indeed be observed that all the Nusselt number follow the same trend. As a result, a correlation developed at ambient condition ($Nu = f(Re,Pr)$) can be used at other temperature and pressure conditions. Figure 5.12b shows the evolution of the heat transfer coefficient h with the Reynolds number at ambient and engine conditions. **At an equivalent Reynolds number, a dramatic increase of the heat transfer coefficient can be noticed at engine conditions (+150% in average)**. Moreover, its rate of increase with the Reynolds number is also higher. This improvement is surely due to the rise of the air thermal conductivity.

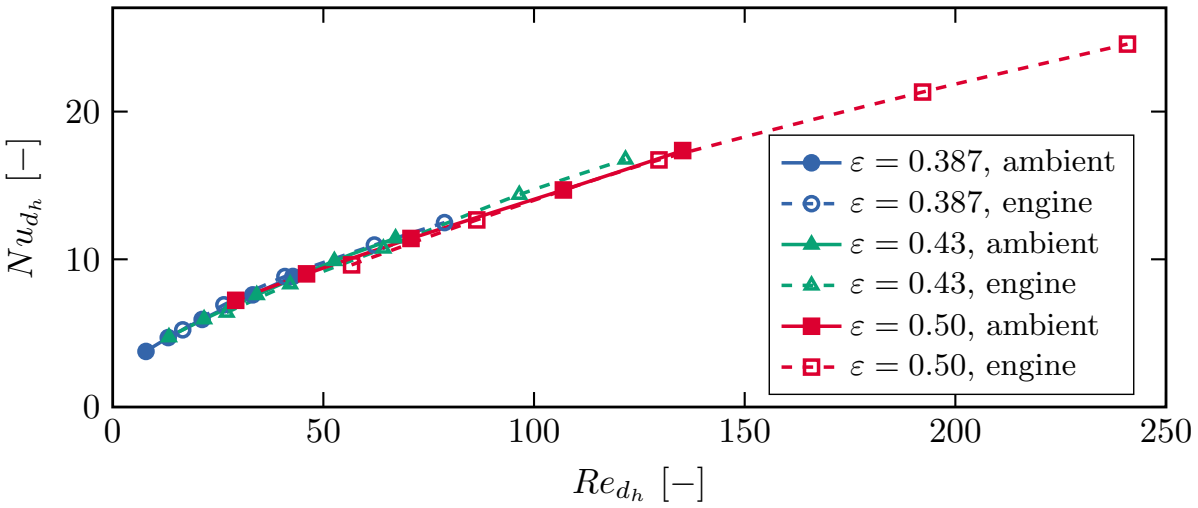

(a) Nusselt number.

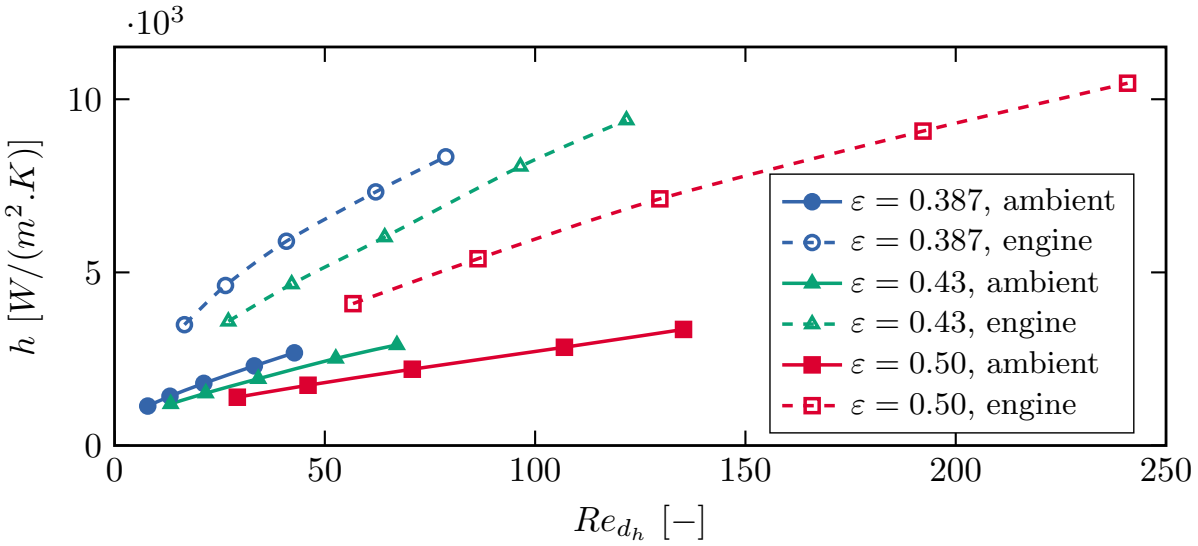

(b) Heat transfer coefficient.

Figure 5.12: Nusselt numbers and heat transfer coefficients of packed beds of 200 μm spherical particles at ambient and engine conditions as a function of the Reynolds number and the porosity.

5.3.3 Assumption $h = h_{sf}$

In sections 5.1.1 and 5.2, it was explained that the computed volumetric heat transfer coefficient $h_{sf}A_{sp}$, assessed with the numerical method, is representative of the actual coefficient $h_v = hA_{sp}$ if the conductivity in the metallic particles does not limit the process of convection. The most critical simulation was performed at ambient condition on a 50% porous packed bed made of 400 μm particles and for a pressure gradient of 1.2×10^7 Pa/m. The measured interfacial heat transfer coefficient was about 3300 $W/(m^2.K)$. At these conditions, the thermal conductivity λ_s of Hastelloy X is about 9.1 $W/(m.K)$). From equation equation 5.5, it can be shown that in this case:

$$h \simeq 0.986 h_{sf} \tag{5.36}$$

It is therefore reasonable to assume that for metallic particles no larger than about 400 μm :

$$h = h_{sf} \tag{5.37}$$

5.4 Determination of volumetric heat transfer coefficients for partially-sintered materials

The process to compute volumetric heat transfer coefficients, detailed in sections 5.2 and 5.3, was applied to the three-dimensional digitized images of partially-sintered materials. The simulations results and the analysis of the data are introduced in this section.

5.4.1 Simulations and results

The partially-sintered materials made of spherical or irregular powders already studied in the previous chapters were investigated. Because of computational time issues during the fluid dynamics simulation, heat transfer coefficients were assessed for only one main flow direction. In the chapter 4, it was explained that the permeability properties of all the digitized materials could be considered as isotropic. It is then reasonable to assume that the volumetric heat transfer coefficients of these digitized materials are also isotropic. Thus, it is considered that the computation of the h_v with only one flow direction gives a representative value.

The thermal simulations were carried out at ambient conditions with the fluid thermal properties introduced in table 5.2. In this work, it is suggested to represent the data with dimensionless numbers based on the hydraulic diameter d_h. All the simulated data are

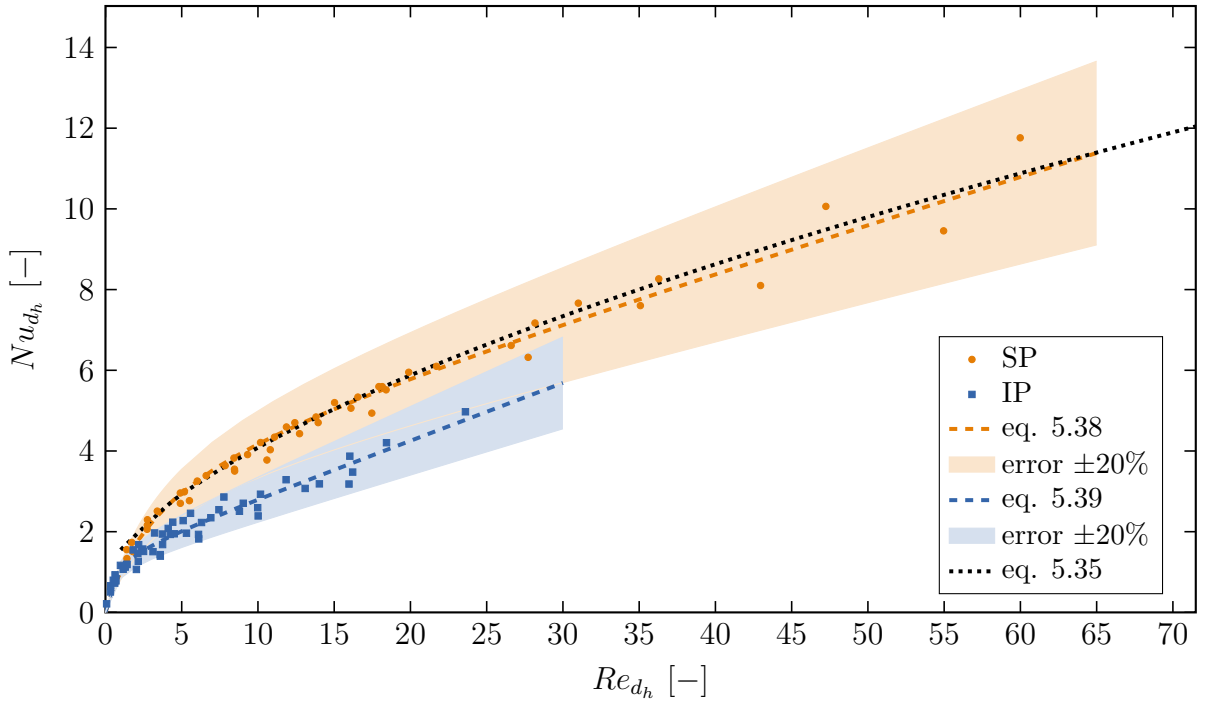

Figure 5.13: Nusselt numbers of partially-sintered spherical and irregular powders as a function of the Reynolds number. The equation 5.35 developed for packed bed is given for comparison.

plotted in figure 5.13. The relationship 5.35 developed for packed beds is also given for comparison.

5.4.2 Analysis of the data

Despite some slight discrepancies, **all the Nusselt numbers of a given geometrical family follow a similar evolution with the Reynolds number.** The relationships linking the Nusselt and the Reynolds numbers of partially-sintered spherical powders and packed beds are very similar. In section 5.1.2.2, it was explained that the literature often reports a linear dependence of the Nusselt number with the Reynolds number for high regimes. This trend be can observed in figure 5.13 for both types of architecture and for Reynolds numbers higher than 10.

At low Re values, the linear relationship does not exist. Moreover, and contrary to packed beds, the Nusselt numbers of partially-sintered powders tend toward zero when the Reynolds number becomes really small. This trend is more pronounced for materials made of irregular particles. This questions one more time the use or not of a non-zero limit value at low Reynolds number. Moreover, at low Reynolds number, the Nusselt number does not follow a power law with an exponent included between 1 and 2 as it was

suggested in section 5.1.2.2.

In the end, it was decided to predict the Nusselt number of both architectural families with functions tending to a **limit value of 0 for low Reynolds number and to a linear asymptote at higher Reynolds number**. Rational functions seemed well adapted to capture this behavior. The following relationship were established for **partially-sintered spherical powders**:

$$\boxed{Nu_{d_h} = \left(\frac{0.13Re_{d_h}^2 + 5.08Re_{d_h}}{Re_{d_h} + 3.6}\right) Pr^{1/3}} \tag{5.38}$$

For **partially-sintered irregular powders**, this relationship fitted well with the numerical data:

$$\boxed{Nu_{d_h} = \left(\frac{0.16Re_{d_h}^2 + 1.73Re_{d_h}}{Re_{d_h} + 0.59}\right) Pr^{1/3}} \tag{5.39}$$

As for equation 5.35, the effect of the thermal boundary layer is represented with a Prandtl number raised at the power 1/3. Both equations are represented in the figure 5.13. They are able to predict the simulated results with an accuracy of $\pm 20\%$.

As explained in section 5.1.2.2, a comparison of the results with literature data is quite difficult. Bellettre et al. (2000) found extremely low specific surface areas and he highlighted the fact that the volumetric heat transfer coefficient he measured were several magnitude orders lower than other data from the literature. The data of Hwang and Chao (1994) and Jiang et al. (2004) are related to bigger spherical particles and the specific surface areas of their samples are not given. Hetsroni et al. (2006) investigated much higher flow regimes in sintered porous materials and the definitions of his dimensionless numbers are not clear. Koh et al. (1973) gave some experimental Nusselts numbers obtained with a 22% porous irregular partially-sintered material. For a Reynolds number varying from 5 to 60, the Nusselt number ranges from 1 to 10. These experimental data underestimate the present results. However, the difference may be explained by the fact that the experimental dimensionless numbers were based on a hydraulic diameter using a specific surface area deduced from mercury penetration measurements. This latter method generally gives specific surface areas different from the present work method.

The ability of both architectural families to exchange energy can be compared. Despite the fact that the porosity is not taken into consideration, figure 5.14a clearly proves that the partially-sintered irregular powders (IP) have larger specific surface areas than

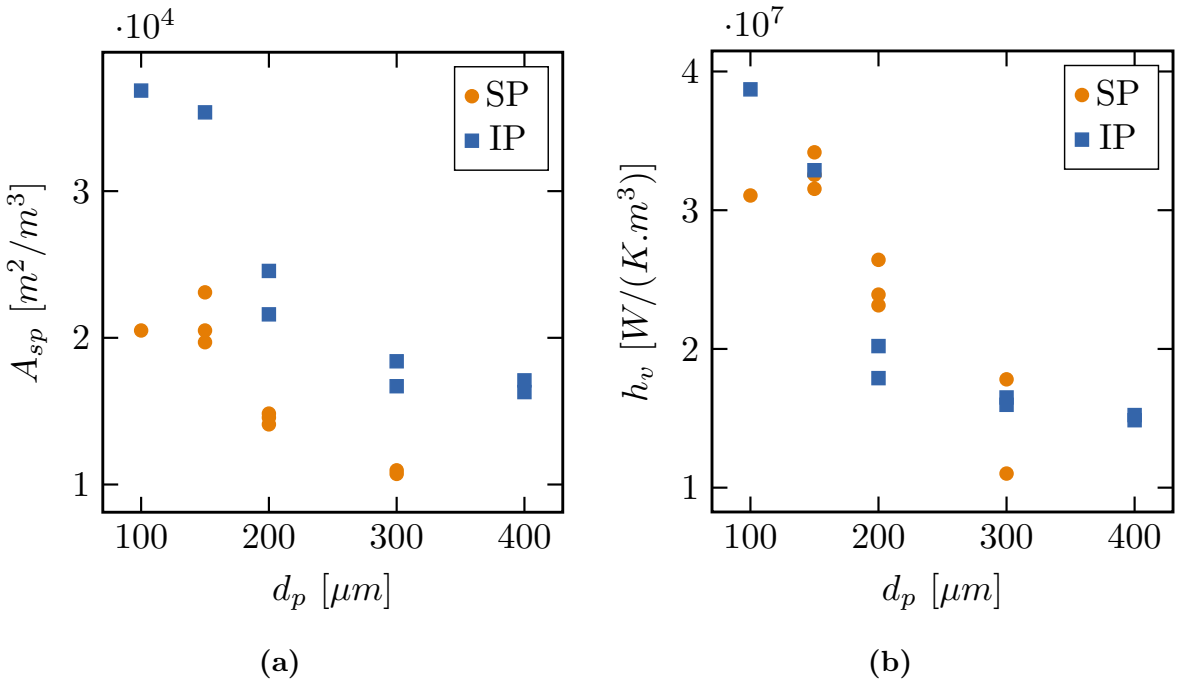

Figure 5.14: Specific surface areas and volumetric heat transfer coefficients for a pressure gradient of $4 \times 10^6\ Pa/m$ as functions of the particle size of SP and IP geometries

partially-sintered spherical powders (SP) for any particle size. The specific surface area is approximately 50% larger at a given particle size. However, the figure 5.14b, which gives the volumetric heat transfer coefficients for a pressure gradient of $4 \times 10^6\ Pa/m$, shows that the IP architectures do not have higher coefficient than SP ones. The high irregularity of the IP architecture may create a lot of areas were the fluid cannot flow. In these areas, the stagnant fluid acts like an insulation layer which may prevent the energy from the solid phase to be efficiently exchanged with the main flow. Moreover, the irregularities also create smaller hydraulic channels and the velocity of the flow is globally lower in IP architectures. That also limits the rate at which energy can be exchanged. At a given pressure gradient, partially-sintered irregular powders lead to volumetric heat transfer coefficients equivalent to that of partially-sintered spherical powders. However, their fluid mass flow is reduced. The choice between both types of architecture for a transpiration cooling application is then a trade-off between reduction of the mass-flow and efficiency of the protective boundary layer.

5.5 Summary

In this chapter, the prediction of the volumetric heat transfer in partially-sintered materials was investigated. **A numerical method was set up to predict this material parameter from three-dimensional images of porous architectures.** Firstly, the three-dimensional temperature field was solved thanks to a finite volume method with the following conditions:

- the fluid properties are considered as constant;
- the flow field is previously solved with Geodict;
- an isothermal solid phase temperature is considered;
- the fluid enters the porous material at a temperature lower than the solid phase temperature.

A one-dimensional fluid temperature profile is then extracted from the 3D temperature field. Finally, the profile is compared to a theoretical model in order to deduce the volumetric heat transfer coefficient. The numerical method was tested on packed beds of spherical particles. **A comparison of the computed results with empirical correlations found in the literature showed the accuracy of the method.**

Computations were finally carried out on three-dimensional images of partially-sintered spherical and irregular powders. **Specific laws for each architectural family was defined in order to predict the volumetric heat transfer coefficient from the porosity, the specific surface area and the properties of the flow.** The process to compute the volumetric heat transfer coefficient is summarized in the flow chart of the figure 5.15. The hydraulic diameter is assessed thanks to the porosity and the specific surface area of the architecture. The superficial velocity of the flow is used to compute the hydraulic diameter based Reynolds number. Depending on the architectural family of the partially-sintered material, a Nusselt number is then calculated using the laws developed in this chapter. This Nusselt number finally allows the evaluation of the volumetric heat transfer coefficient.

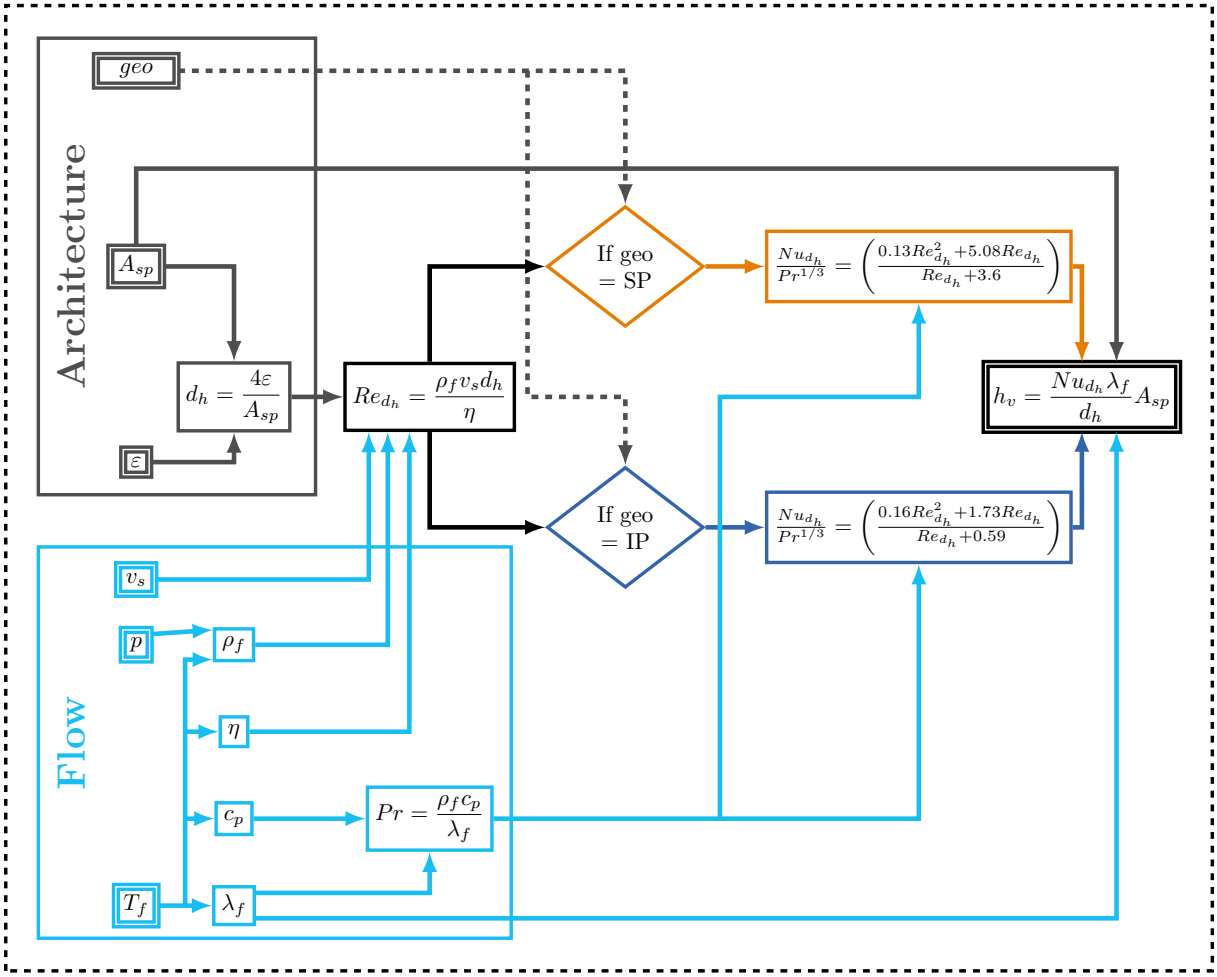

Figure 5.15: Method to assess the volumetric heat transfer coefficient of partially-sintered powders

.

Chapter 6

Optimization of the partially-sintered architecture for transpiration cooling

Contents

This chapter is focused on the optimization of the architecture of partially-sintered materials for transpiration cooling in future aero-engine combustion chambers. Since the performance of a design is strongly dependent on the way the energy is removed from the liner, a heat transfer model is first of all introduced. The optimization problem is then explained in details. The chapter finishes with an analysis and a selection of optimal designs.

6.1 Modelization of heat transfer during transpiration cooling

The simulation of heat transfer in combustion chambers is extremely difficult since it involves multi-physical and multi-scale phenomena. The combustion features complex turbulent flow patterns with chemical reactions and radiation. The cooling leads to interactions and mixes between different flows. The study of transpirating materials makes the problem even more difficult since it requires to study flows and heat transfer at a scale much smaller than the combustion chamber dimensions. For a matter of simplicity and in order to get a better understanding on how the architecture of partially-sintered materials impacts the transpiration cooling performance, a one-dimensional heat transfer model is here considered. This hypothesis can be easily criticized by the fact that the temperature and the composition of the flame as well as the profile of the boundary layers vary a lot in the combustion chamber. However, it was found useless to develop a more complex model considering the fact that this study is not about sizing a combustion chamber but highlighting some architectures which have a potential for transpiration cooling. Moreover, and despite numerous studies related to this subject, remaining interrogations regarding the interactions between the boundary layers on both liner sides and the porous materials, encouraged this choice.

6.1.1 General description of the problem

The simplified problem which is considered in the present work is introduced in figure 6.1. By comparing the liner thickness to the chamber size, the liner can be represented as a planar and homogeneous porous material having a thickness L. This assumption is also justified by the fact that most experimental tests carried out on multi-perforated or porous walls are made with planar samples. The flow through the liner is forced by a pressure difference Δp. The inner side of the wall is submitted to a radiative flux emit-

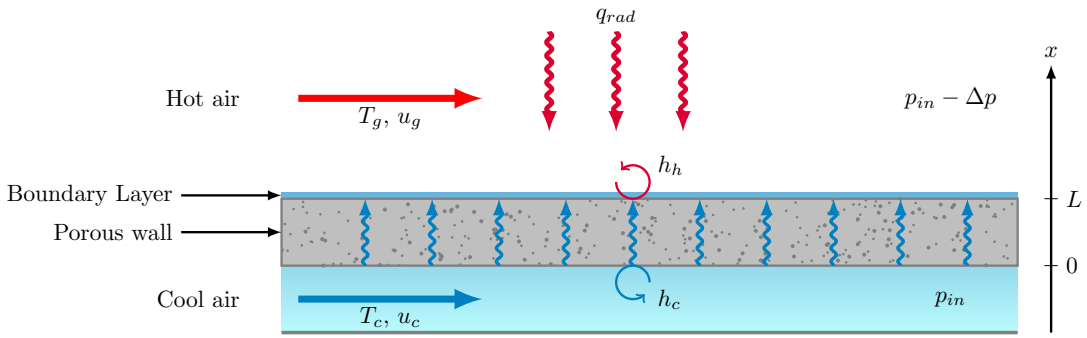

Figure 6.1: Reprensentation of heat transfer during transpiration cooling

ted by the hot gases q_{rad} and to hot convective heat transfer (heat transfer coefficient h_h). The outer side exchanges energy by convection with the cooling air (heat transfer coefficient hc). The outer side of the wall is expected to have a temperature close to the initial coolant temperature. Consequently, the radiation from the liner to the casing must be quite small compared to the external convective heat transfer (Lefebvre and Ballal, 2010) and are neglected. In order to simplify the writing of the following relationships, the subscripts $_0$ and $_L$ will respectively refer to the position $x = 0$ and $x = L$.

It is important to remind that transpiration cooling is aimed to be used in lean combustion chambers. As a result, and by referring to the figure 5, from the general introduction of this manuscript, the temperature of the hot gases will be lower than in a current combustion chamber. A temperature of $T_g = 1900\ K$ will be considered. The pressure and the temperature of the air which goes out from the compressor are taken at cruise regime ($p_{in} = 30 \times 10^5\ Pa$ and $T_c = 800\ K$). u_h and u_c refer to the flow velocities of the hot and the cold streams respectively.

6.1.2 Internal heat transfer

Heat transfer mechanisms in the porous wall can be modeled with the local thermal non-equilibrium model introduced in section 1.2.3. This choice of model can be justified with the argument of L'Ecuyer and Colladay (1972) and Colladay and Stepku (1971) who showed that a difference between the inner wall temperature and the cooling air outlet temperature could exist. By taking into account the large variations of pressure and temperature through the liner thickness, the thermal properties cannot be taken as constant. Effects of air compressibility at low Mach number are considered. The governing equations in a one-dimensional case are then:

Energy equation in the solid phase:

$$\frac{d}{dx}\left(\boldsymbol{\lambda}_{\mathbf{s,eff}}\frac{dT_s}{dx}\right) - \mathbf{h_v}(T_s - T_f) = 0 \tag{6.1}$$

Energy equation in the fluid phase:

$$\frac{d}{dx}\left(\rho_f c_p v_s T_f\right) - \varepsilon\frac{d}{dx}\left(\lambda_f\frac{dT_f}{dx}\right) - \mathbf{h_v}(T_s - T_f) = 0 \tag{6.2}$$

Conservation of mass:

$$\frac{d}{dx}(\rho_f v_s) = 0 \tag{6.3}$$

Fluid momentum equations:

$$\frac{1}{\varepsilon^2}\frac{d}{dx}(\rho_f v_s^2) = -\frac{dp}{dx} + \frac{1}{\varepsilon}\frac{4}{3}\frac{d}{dx}\left(\eta\frac{dv_s}{dx}\right) - \frac{\eta}{\mathbf{K}}v_s - \rho_f\boldsymbol{\beta}v_s^2 \tag{6.4}$$

Ideal gas law:

$$p = \rho_f r T_f \tag{6.5}$$

where T_s, T_f, ρ_f, c_p, η, v_s, p, λ_f, $\lambda_{s,eff}$, h_v, K and β are the solid phase temperature, the fluid phase temperature, the air density, the air calorific capacity, the air dynamic viscosity, the superficial velocity, the pressure, the air thermal conductivity, the effective thermal conductivity of the solid phase, the volumetric heat transfer coefficient, the permeability coefficient and the Forchheimer coefficient respectively. **The effective parameters $\boldsymbol{\lambda}_{\mathbf{s,eff}}$, K & $\boldsymbol{\beta}$, and $\mathbf{h_v}$ are computed following the process detailed in their corresponding chapters (chapters 3 to 5) by considering now varying fluid thermal properties.** In chapter 4 and chapter 5, the porosity and the specific surface area of the open porous phase were investigated whereas the overall porosity was measured in the study of the effective thermal conductivity in the chapter 3. For a matter of simplicity and by taking into account the low closed porosity of the partially-sintered materials, the effective thermal conductivity was considered to be reasonably assessed by identifying the overall porosity to the open porosity.

6.1.3 Boundary conditions

One of the major difficulties with such a one-dimensional model is to apply boundary conditions sufficiently representative of the complex three-dimensional problem.

6.1.3.1 Coolant side boundary conditions

As the behavior of the flow during suction in a porous materials is rather unknown, the fluid is assumed to perfectly enter the porous wall in the x direction. No axial velocity component or additional pressure losses caused by the entry of the fluid are considered. The inlet pressure is imposed at p_{in}, the compressor outlet pressure:

$$p_0 = p_{in} \tag{6.6}$$

Some convective heat transfers exist between the outer side of the wall and the cooling air. As explained by Von Wolfersdorf (2005), the coolant temperature rise can be neglected in the case of a large enough and well mixed coolant mass flow. Thus the inlet coolant temperature is assumed to be at the compressor outlet temperature T_c:

$$T_{f,0} = T_c \tag{6.7}$$

The convective heat transfers between the outer wall side and the cooling air are taken into account using the following boundary condition equation:

$$-\lambda_{s,eff} \frac{dT_s}{dx}\bigg|_0 = h_c(T_c - T_{s,0}) \tag{6.8}$$

Following the approach described by Lefebvre and Ballal (2010) or Glass et al. (2001), the coolant heat transfer coefficient h_c can be assessed with a fully developed turbulent boundary layer model thanks to:

$$Nu_c = \frac{h_c d_c}{\lambda_f} = 0.027 Re_{d_c}^{4/5} Pr^{1/3} \tag{6.9}$$

where Nu_c, $Re_{d_c} = (\rho_f d_c u_c)/\eta$ and $Pr = \eta c_p/\lambda_f$ are the Nusselt number on the outer side of the liner, the Reynolds number of the coolant flow and the Prandtl number respectively. d_c is the channel hydraulic diameter of the annulus and it is assessed to not be smaller than 1.5 cm (Lefebvre and Ballal, 2010). In multi-perforated walls, the coolant velocity u_c is a little bit larger than that of the hot mainstream. As its value is the result of a complex combustion chamber design optimization, the most adapted value for transpiration cooling is still unknown. As a result, the coolant velocity is taken as the same value as the hot main stream velocity u_g.

6.1.3.2 Hot gases side boundary conditions

The pressure difference between both sides of the liner is caused by pressure losses created by the combustion. These pressure losses are assessed to be approximately $r_{cc} = 2\%$ of

the compressor outlet pressure. The liner outlet pressure is then supposed to be equal to:

$$p_L = p_{in} - \Delta p = (1 - r_{cc}) \times p_{in} \tag{6.10}$$

The inner side of the wall is submitted to a radiant heat flux q_{rad} as well as to convective heat transfer with the hot gases:

$$-\lambda_{s,eff} \left. \frac{dT_s}{dx} \right|_L = -q_{rad} + h_h(T_g - T_{s,L}) \tag{6.11}$$

More details about q_{rad} and the hot heat transfer coefficient h_h are given in the following.

Radiative heat transfer $\mathbf{q_{rad}}$:

According to Lefebvre and Ballal (2010), the radiative heat flux q_{rad} can be expressed as:

$$q_{rad} = 0.5\sigma(1 + \varepsilon_w)\left(\varepsilon_g T_g^4 - \alpha_g T_{s,L}^4\right) \tag{6.12}$$

where $\sigma = 5.67 \times 10^8\ W/(m^2K^4)$, ε_g, α_g and ε_w are the Stefan-Boltzmann constant, the gas emissivity at the hot gases temperature T_g, the gas absorptivity at the inner wall temperature and the effective emissivity of the inner wall surface respectively. Lefebvre and Ballal (2010) also explain that it is sufficiently accurate to link α_g with ε_g thanks to:

$$\frac{\alpha_g}{\varepsilon_g} = \left(\frac{T_g}{T_{s,L}}\right)^{1.5} \tag{6.13}$$

The radiative emission generated during combustion can be divided into two components:

- a non-luminous radiation emitted by heteropolar gases (mainly carbon dioxide and water vapor);
- a luminous radiation emitted by soot particles.

The participation of both radiative components is taken into account with the following expression of gas emissivity:

$$\varepsilon_g = 1 - \exp\left[-290 P \gamma (q l_b)^{0.5} T_g^{-1.5}\right] \tag{6.14}$$

where P, γ, q and l_b are the gas pressure in kPa, a luminosity factor, the fuel/air mass ratio and the beam length respectively. In the case of an annular combustion chamber, the beam length is:

$$l_b = d_l \quad \text{for the inner liner} \tag{6.15}$$

$$= 1.2 d_l \quad \text{for the outer liner} \tag{6.16}$$

where d_l is the annular height ($\simeq 48\ cm$, courtesy of *SAFRAN*). For a lean combustion, the fuel/air mass ratio can be assessed at 0.04. For kerosine, the luminosity factor is 1.7 (Lefebvre and Ballal, 2010).

Hot convective heat transfer coefficient h_h

Convective heat transfers between the inner side of the wall and the hot gases depend on the efficiency of the boundary layer. Indeed, the role of the boundary layer is to insulate the wall from the hot gases. As it was already explained in section 1.2, the efficiency of the protective boundary layer and the effects of the blowing ratio F were investigated in many studies. The blowing ratio is defined as the ratio of the coolant mass flux to the mainstream mass flux:

$$F = \frac{(\rho_f v_s)}{\rho_g u_g} \tag{6.17}$$

By assuming an equilibrium temperature between the coolant and the porous wall, Eckert and Livingood (1954) expressed the reduction in convective heat transfer on the hot side as a function of the blowing ratio:

$$\frac{St}{St_{wc}} = \frac{h_h}{h_{h,wc}} = \frac{F/St_{wc}}{e^{F/St_{wc}} - 1} \tag{6.18}$$

where

$$St = \frac{h_h}{(\rho_f u c_p)_g} \tag{6.19}$$

is the Stanton number which characterizes the ratio of heat transferred by convection to the thermal capacity of the fluid in forced flow. The subscript $_{wc}$ describes the case without cooling. However, L'Ecuyer and Colladay (1972) and Colladay and Stepku (1971) then showed that the coolant leaving the wall can be at a temperature lower than the inner wall temperature. This thermal non-equilibrium is responsible for more heat removed from the hot wall and to lower external heat transfer with the hot gases. To take into account this phenomena, they added a correction factor to the equation 6.18:

$$\frac{St}{St_{wc}} = \frac{F/St_{wc}}{e^{F/St_{wc}} - 1} f(\eta_{eff}) \tag{6.20}$$

with

$$f(\eta_{eff}) = \left[\frac{e^{F/St_{wc}} - 1/\eta_{eff}}{e^{F/St_{wc}} - 1} + \frac{1/\eta_{eff} - 1}{F/St_{wc}} \right]^{-1} \tag{6.21}$$

and where η_{eff} is the cooling efficiency defined as:

$$\eta_{eff} = \frac{T_{f,L} - T_c}{T_{s,L} - T_c} \tag{6.22}$$

In the present work, **the hot side heat transfer coefficient is assessed with equation 6.20.** According to Moffat and Kays (1968), the Stanton number without blowing can be computed with the following relationship:

$$St_0 = 0.0292 Re_z^{-0.2} Pr^{-0.4} \tag{6.23}$$

where $Re_z = \rho_g u_g z / \eta_g$ represents the Reynolds number based on the distance z, downstream distance from the start of the boundary layer. The evolution of the Stanton number with z gives one of the limit of the one-dimensional model. However, a value of $z = 1\ cm$ was chosen for the numerical application. Experimental tests, which will be introduced in the works of Lambert (2017), will show that the protective boundary layer is almost fully established at such an upstream distance.

To take into account the fact that the air injection is not present as soon as the beginning of the boundary layer, models based the enthalpy thickness on could have been considered (Simpson et al., 1969; Whitten et al., 1970; Landis and Mills, 1972). For more explanation, the reader may refer to the work of Bellettre et al. (2000).

6.1.4 Summary

This section introduced the one-dimensional model which was developed for the simulation of transpiration cooling in a lean combustion chamber. All the parameters which were chosen to represent the conditions in the engine are summarized in the table 6.1. The **thermal properties of the Hastelloy X** were used in the following.

T_g	1900 K	T_c	800 K
p_{in}	30×10^5 Pa	r_{cc}	2%
q	0.04	u_g	30 m/s
d_l	48 cm	d_c	1.5 cm
ε_w	0.8	γ	1.7

Table 6.1: Conditions for the simulation

6.2 Numerical methods for the simulations

6.2.1 Discretization of the equations

Equations 6.1, 6.2 and 6.4 were discretized with a finite volume method (see appendix A for more explanation about the method). The space was uniformly discretized with n nodes from $x = 0$ to $x = L$. A power law scheme was used for the discretization of the fluid energy conservation equation. Central differencing schemes were preferred for the momentum conservation equation and the solid phase energy.

6.2.2 Resolution of the system

After discretization of equation 6.4, and by taking into account the fact that the mass flow rate $\dot{m} = \rho_f v_s$ is constant (equation 6.3), the resolution of the coolant mass flow consists in solving the following second order polynomial:

$$A\dot{m}^2 + B\dot{m} - \Delta p = 0 \tag{6.24}$$

where

$$A = \sum_{0}^{n-2} \left[\frac{1}{\varepsilon^2 \rho_{f,i+1}} - \frac{1}{\varepsilon^2 \rho_{f,i}} + \frac{2\delta_x \beta}{\rho_{f,i+1} + \rho_{f,i}} \right] \tag{6.25}$$

and

$$\begin{aligned} B = \frac{1}{\varepsilon} \sum_{0}^{n-3} \left[-\frac{8\eta_{i+1}}{3\delta_x} \left(\frac{1}{\rho_{i+2}} - \frac{1}{\rho_i} \right) \right] - \frac{4\eta_{n-1}}{3\delta_x \varepsilon} \left(\frac{1}{\rho_{n-1}} - \frac{1}{\rho_{n-2}} \right) \\ + \frac{4\eta_0}{3\delta_x \varepsilon} \left(\frac{1}{\rho_1} - \frac{1}{\rho_0} \right) + \frac{1}{\varepsilon} \sum_{1}^{n-2} \left[\frac{8\eta_{n-2}}{3\delta_x} \left(\frac{1}{\rho_{n-1}} - \frac{1}{\rho_{n-3}} \right) \right] \\ + \sum_{0}^{n-2} \left[\frac{1}{K} \frac{\eta_{i+1} + \eta_i}{\rho_{i+1} + \rho_i} \delta_x \right] \end{aligned} \tag{6.26}$$

In order to solve both coupled heat equations 6.1 and 6.2, a column vector Θ $(2n \times 1)$ can be defined as:

$$\Theta = [T_f, T_s] \tag{6.27}$$

The coupled equations can then be represented as a unique linear system:

$$M\Theta = S \tag{6.28}$$

where M is a matrix $(2n \times 2n$)and S a column vector $(2n \times 1)$. As the thermal properties are supposed to be functions of the temperature, an iterative process was set up until the

following convergence criterion of the temperature is reached:

$$\frac{||T_{f,t-1} - T_{f,t}||_2}{||T_{f,t-1}||_2} < \epsilon_f \text{ and } \frac{||T_{s,t-1} - T_{s,t}||_2}{||T_{s,t-1}||_2} < \epsilon_s \tag{6.29}$$

where the subscripts t is the iterative step, $||.||_2$ is the Euclidian norm and ϵ_f and ϵ_s are two convergence criteria (typically 10^{-4}).

The flow chart of the calculation program is introduced figure 6.2. The system is inverted with the linear solver *BiCGSTAB* (bi conjugate gradient stabilized solver) from the library *Eigen* of C++.

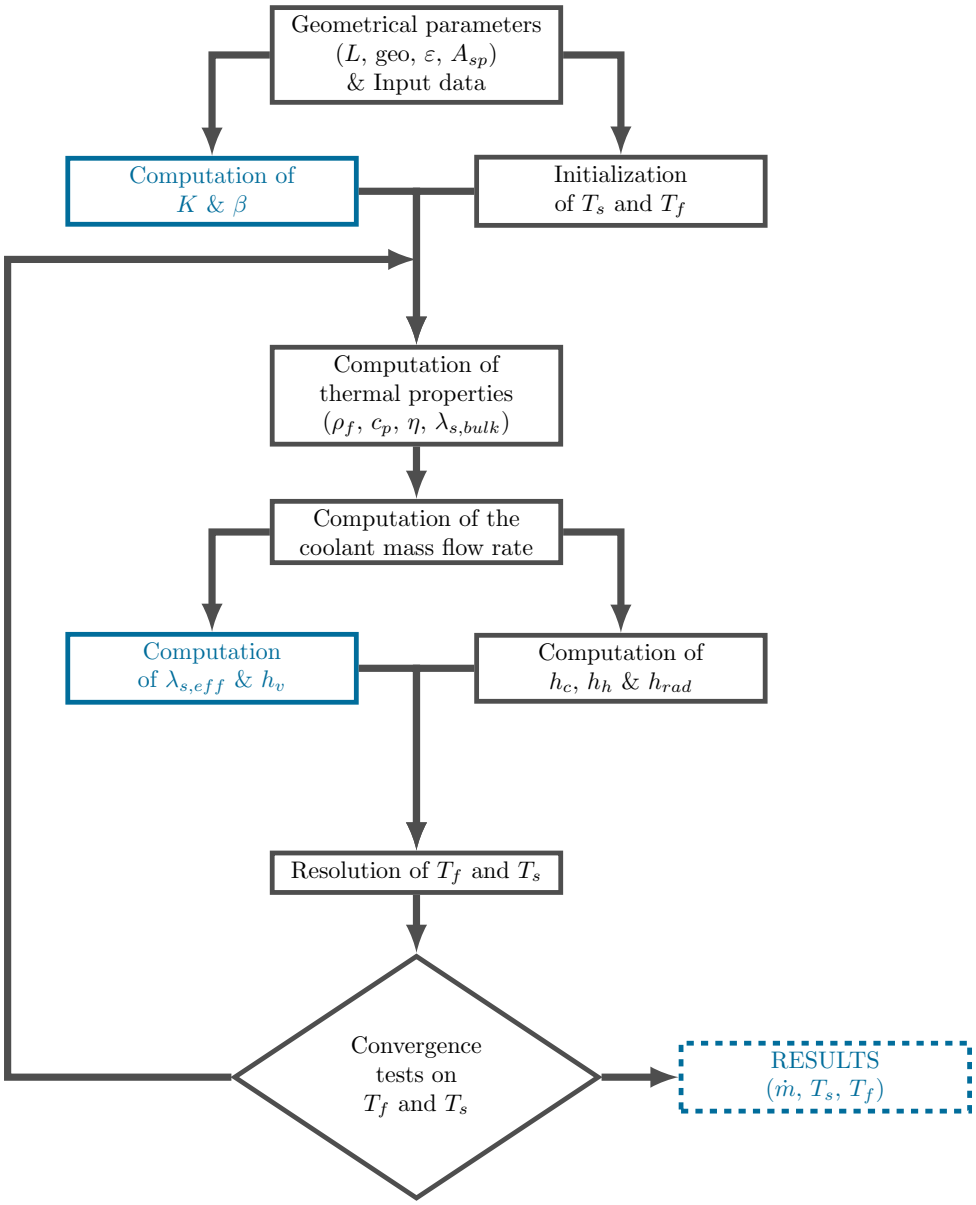

Figure 6.2: Flow chart of the calculation program

6.2.3 Linearization of the radiative boundary condition

An issue was encountered with the radiative boundary condition q_{rad} which has to be linearized. q_{rad} was transformed as:

$$q_{rad} = h_{rad}(\phi T_g - T_{s,L}) \tag{6.30}$$

with

$$h_{rad} = 0.5\sigma(1+\varepsilon_w)\alpha_g(\phi T_g + T_{s,L})\big((\phi T_g)^2 + T_{s,L}^2\big) \tag{6.31}$$

and

$$\phi = \left(\frac{\varepsilon_g}{\alpha_g}\right)^{1/4} \tag{6.32}$$

Due to its low sensitivity to $T_{s,L}$, h_{rad} can be considered as a heat transfer coefficient which is recalculated at each iteration step of the simulation.

6.2.4 Grid convergence study

Before being able to analyze any simulated result, it has to be verified that the choice of the grid size (N nodes) has no impact on the simulated temperature profiles. If the mesh is too coarse, steep variations of the temperatures are not well captured. On the contrary, a too fine mesh leads to additional computational time without any sensitive accuracy gain. A grid convergence study permits a good accuracy/computational time trade-off to be found. The grid convergence analyses were carried out with two extreme simulation cases:

- case 1: $\varepsilon = 40\%$ and $A_{sp} = 10{,}000\ m^{-1}$ and $geo = IP$;
- case 2: $\varepsilon = 25\%$ and $A_{sp} = 50{,}000\ m^{-1}$ and $geo = IP$;

In both cases, the wall thickness was 2 mm. The impact of the grid can be observed in figures 6.3a and 6.3b. In case 1, the permeability is high. The temperatures are not subjected to drastic variations. It can be noticed that the choice of the number of cells has a low impact on the results. On the contrary, in case 2 where the permeability is really low, the fluid temperature varies very quickly at the inlet of the material. It can therefore be noticed that increasing the number of nodes allows the convergence of the temperature profiles. The temperature profiles obtained with 600 nodes and 1000 nodes cannot be distinguished. Consequently, the use of 300 nodes/mm is considered in the following as a good trade-off for the spatial discretization.

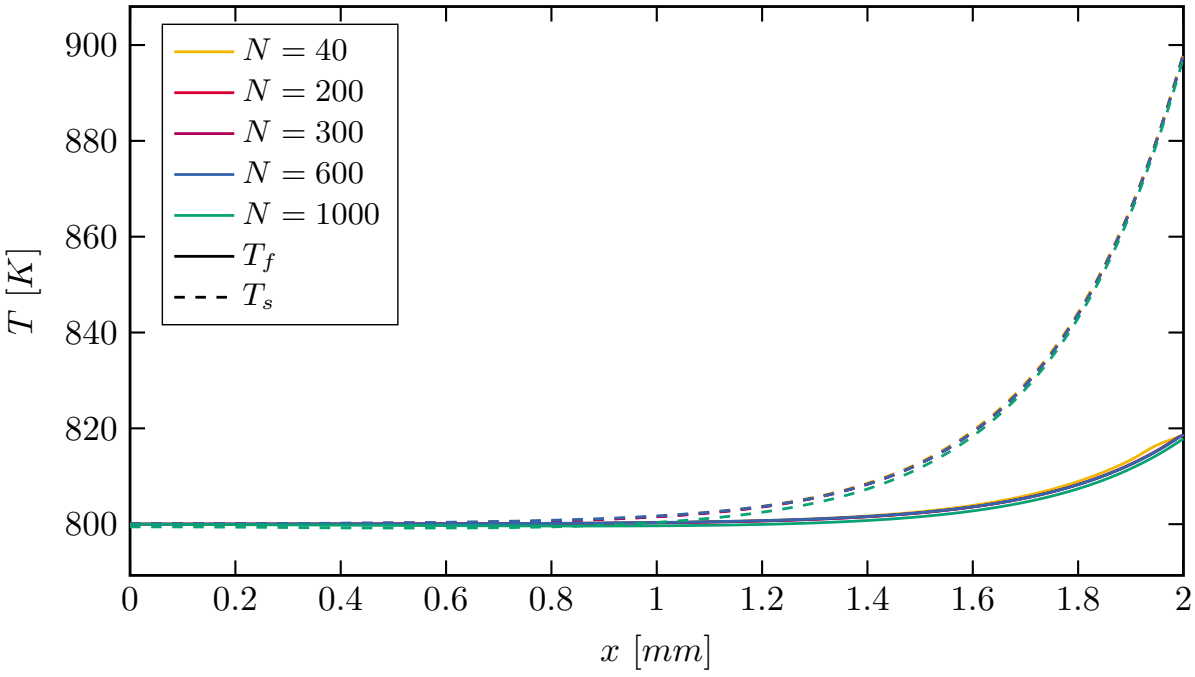

(a) case 1: $\varepsilon = 40\%$ and $A_{sp} = 10{,}000\ m^{-1}$.

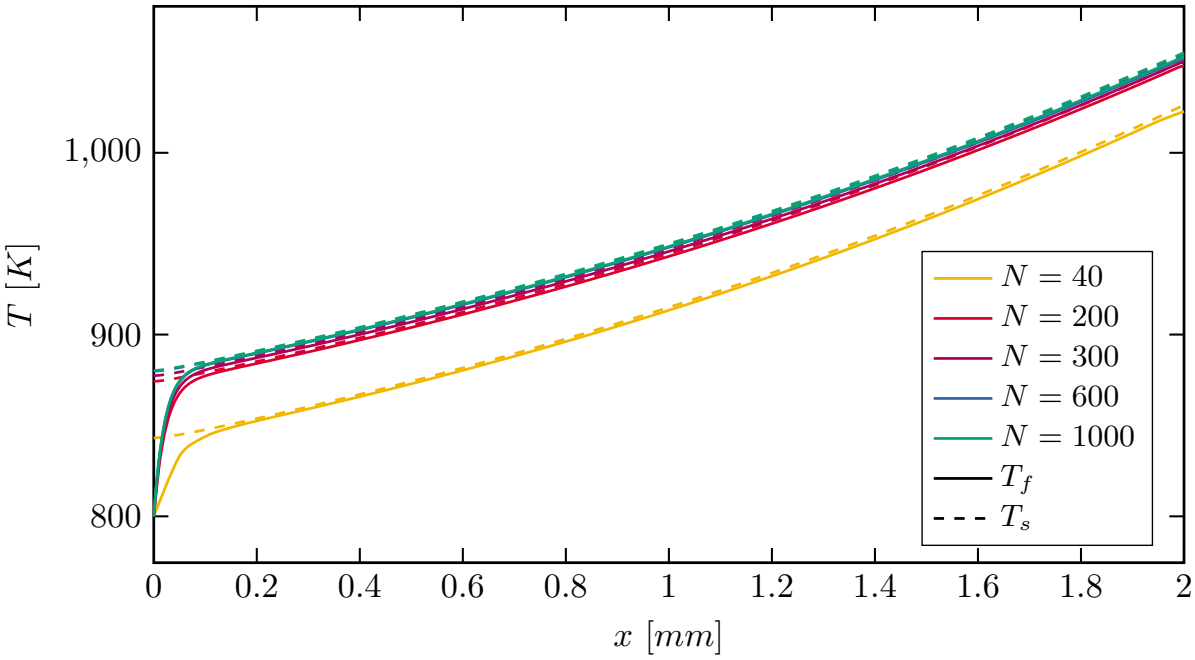

(b) case 2: $\varepsilon = 25\%$ and $A_{sp} = 50{,}000\ m^{-1}$.

Figure 6.3: Impact of the number of nodes N used to discretize the spatial domain on the simulated temperature profiles for two extreme cases.

6.3 The multi-objective optimization

The optimization of the partially-sintered architecture in view of a transpiration-cooling application can involve a lot of conflicting parameters. To take into consideration as most parameters as possible, a multi-objective optimization is considered.

6.3.1 Introduction to multi-objective optimization

A multi-objective optimization is an optimization problem in which more than one objective function f_i have to be simultaneously minimized. The optimization can involve n variables x_s which are represented by the design vector $\vec{x}$:

$$\vec{x} = (x_1,x_2,...,x_n) \tag{6.33}$$

A multi-objective problem can be formulated as follows:

$$\min(f_i(\vec{x})) \quad i = 1,...,l \tag{6.34}$$

$$g_j(\vec{x}) \leq 0 \quad j = 1,...,m \tag{6.35}$$

$$h_k(\vec{x}) = 0 \quad k = 1,...,p \tag{6.36}$$

$$x_s^{inf} \leq x_s \leq x_s^{sup} \quad s = 1,...,n \tag{6.37}$$

where g_j and h_k are constraint functions which defined the set of feasible solutions. x_s^{inf} and x_s^{sup} are respectively the lower and the upper bound of each variable.

Contrary to a single objective optimization which gives a unique optimum, the conflicting objectives of a multi-objective optimization lead to **a set of optimal solutions** called the **Pareto front**. Pareto optimal solutions are solutions for which none of the objective functions can be improved without degrading at least one of the other ones. The Objective Function Vector $\vec{F}$ is defined as:

$$\vec{F} = \{f_1(\vec{x}), f_1(\vec{x}),..., f_l(\vec{x})\} \tag{6.38}$$

If two feasible solutions $\vec{x}_1$ and $\vec{x}_2$ are taken into account:

- $\vec{x}_1$ dominates $\vec{x}_2$ if $f_i(\vec{x}_1) \leq f_i(\vec{x}_2)$ for all $i \in \{1,...,l\}$ and if $f_j(\vec{x}_1) < f_j(\vec{x}_2)$ for at least one index $j \in \{1,...,l\}$;
- $\vec{x}_1$ and $\vec{x}_2$ are **Pareto equivalent** if some components of $\vec{F}(\vec{x}_1)$ are smaller than the corresponding components of $\vec{F}(\vec{x}_2)$ and some others are greater. From the designer point of view, the two designs are in this case a trade-off between the different objective functions.

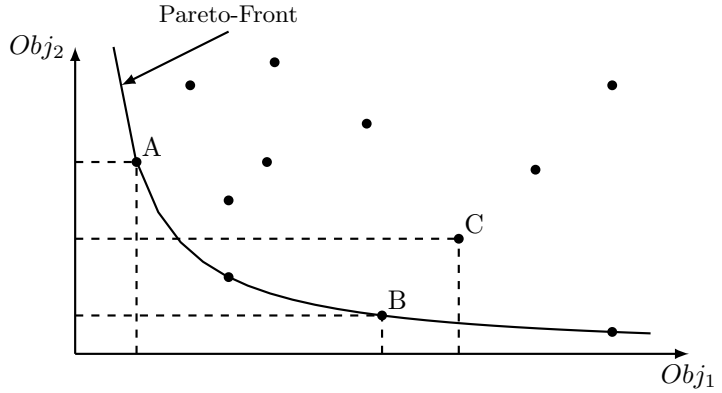

Figure 6.4: A typical Pareto front of a two-objective optimization problem.

An example of a typical two-objective optimization problem Pareto front is given in figure 6.4. The design C is here dominated by the design B. A and B or A and C are Pareto equivalent. Finally, the designs A and B are on the Pareto-Front.

6.3.2 Definition of the problem

In order to find the set of optimal architectures, it is essential to clearly define the objectives and the constraints related to the transpiration cooling process.

6.3.2.1 The objective functions

Minimization of the cooling air mass flow: The main goal of transpiration cooling is to reduce the amount of air required to cool the combustion chamber liner. The first objective function is therefore the liner outlet mass flux (mass flow rate per unit surface area) defined as:

$$\boxed{\textbf{Obj-Flux} = \textbf{Min}\Big(\rho_f v_s\Big) \quad \big[kg/(m^2.s)\big]} \tag{6.39}$$

Minimization of the mass of the liner: In aeronautical applications, the mass is a crucial parameter. Indeed, every gain in weight can for instance lead to a fuel consumption reduction or can permit more passengers to be carried. The second objective function is the surface density of the liner defined as:

$$\boxed{\textbf{Obj-Density} = \textbf{Min}\Big(\rho_{s,bulk}(1-\varepsilon)L\Big) \quad \big[kg/m^2\big]} \tag{6.40}$$

where $\rho_{s,bulk}$ is the bulk material density. The bulk Hastelloy X density is $8.22\times10^3\ kg.m^3$.

Maximization of the pore size: Aero-engine components are not supposed to suffer from rapid obstruction due to dust. As exposed by Lefebvre and Ballal (2010), blockage by airborne debris (sand, volcanic ash,etc.) is one of the barriers for the application of porous materials in combustion chambers. According to Wilcox et al. (2010), the typical atmospheric dust size distribution ranges from 0.1 to 100 μm. In environments where sand or ash can be carried by the wind, even bigger particles can be sucked in by the engine. With 500 μm diameter holes, multi-perforated walls resist well to obstruction. However, as the channels of the porous materials are expected to be much smaller, issues can easily appear. It is therefore important to have an architecture with a pore size d_{pores} as big as possible. The third objective is then:

$$\boxed{\textbf{Obj-PoreSize} = \textbf{Max}\left(d_{pores}\right) \ [\mu m]} \tag{6.41}$$

To agree with the definition of the multi-objective optimization given in section 6.3.1, maximizing an objective function is equivalent to minimize the opposite value of the function ($min(-d_{pores})$). The pore size is defined as the median pore size measured with the numerical porosimetry method introduced in section 2.3.3. The figure 6.5 shows that the pore size of partially sintered materials made of spherical or irregular particles can be correlated to their hydraulic diameters $d_h = 4\varepsilon/A_{sp}$ with the following law:

$$d_{pores} = 0.6 d_h \tag{6.42}$$

Maximization of the cooling air outlet temperature: Near the inner part of the liner, the low temperature of the ejected fluid can locally block the combustion and favor the appearance of carbon monoxide. As this phenomenon can hardly be taken into account in this one-dimensional model, the optimization only takes into consideration the maximization of the cooling air outlet temperature. The fourth objective is then defined as:

$$\boxed{\textbf{Obj-Outlet-T}^\circ = \textbf{Max}\left(T_{f,L}\right) \ [K]} \tag{6.43}$$

Taking into account the issues of pore size and cooling air outlet temperature as objectives and not as constraints can be discussed. In the present study, the use of constraints was considered as too restrictive because, at this point, there is no determined critical values for both parameters. Moreover, as it is shown in the following, the use of objective functions allows the designer to easily study the impact of additional conditions on the choice of optimal designs.

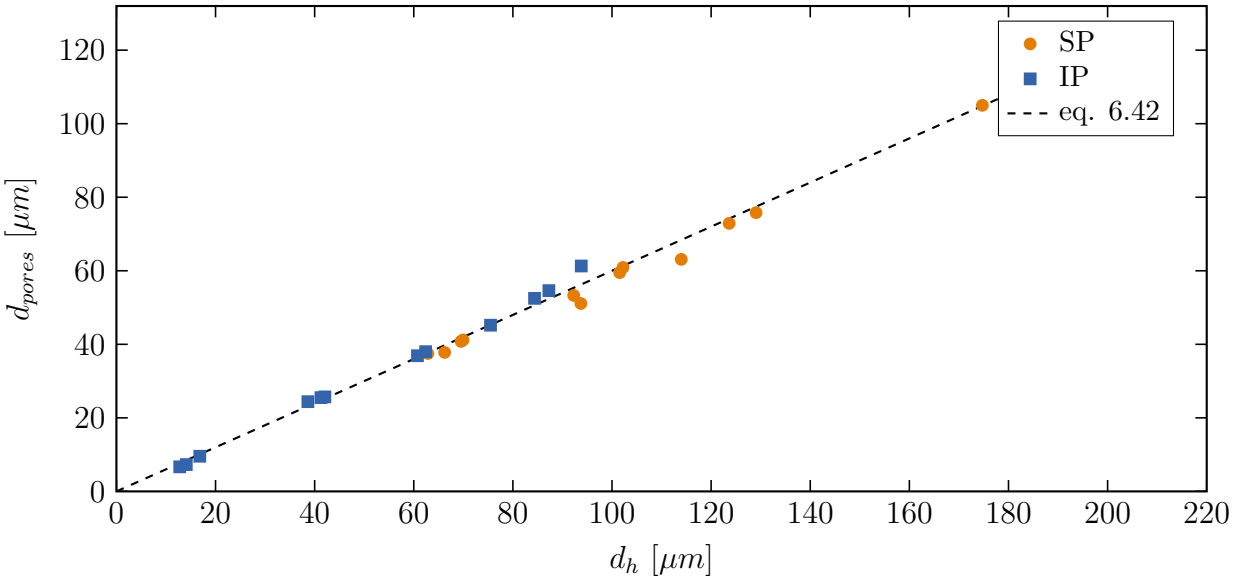

Figure 6.5: Variation of the pore size with the hydraulic diameter of digitized partially-sintered materials made of spherical particles (SP) or irregular particles (IP).

6.3.2.2 The wall temperature constraint

As it was explained in the general introduction, the operating temperature of the superalloys which composed the current multi-perforated liner should not be higher than 1100 K. Indeed, the mechanical strength of the materials decreases rapidly beyond this temperature. Another issue can appear with partially-sintered materials when there are placed in a hot atmosphere. Since the sintering of the powder is incomplete, densification could appear during their use. However, 1100 K is still much lower than the temperature at which densification by sintering appears. **As a conclusion, only the designs with $\mathbf{T_{s,L} < 1100\ K}$ will be considered as viable.**

6.3.2.3 Design variables

According to the previous chapters, the studied partially sintered material effective properties can be predicted thanks to the porosity (ε $[\%]$), the specific surface area (A_{sp} $[m^2/m^3]$) and the architectural family (geo = SP or IP). These three parameters are therefore the first three variables of the design vector. The thickness of the liner (L $[mm]$) is the fourth variable of the design vector. The range of variability of the four variables and the step sizes used for the discretization of the variable space are introduced in table 6.2.

Variable	Min	Max	step size
L $[mm]$	1	4	0.5
ε [%]	20	40	1
A_{sp} $[m^2/m^3]$	6000	50000	2000
geo		SP or IP	

Table 6.2: Range of variability of the four variables and their step size.

6.3.3 Building of the optimal designs set

By taking into account the fact that the time required to complete a simulation is quite short (less than two minutes), the performance of all the designs introduced in the table 6.2 was computed without any use of optimization algorithms. 6762 simulations were run using the parameters given in the section 6.1. The four objective functions were assessed for each design and an optimal set of 713 designs was generated. These optimal designs are analyzed in the next section.

6.4 Analysis of the optimal architectures

Even though the optimization step is essential in the design process, the analysis of the results is even more important since it will guide the future choices of the designer. Multi-objective optimization tends to generate a large amount of multi-dimensional data. It is then crucial to have tools well adapted to their analysis.

In the present work, the data mining was performed thanks to "parallel coordinates", a multi-dimensional visualization technique developed by Inselberg (1985). This method offers the possibility to display data with a large number of dimensions on a unique two-dimensional graph. Siirtola and Räihä (2006) claimed that the popularity of "parallel coordinates" is mainly due to the fact that the multiple dimensions are treated in a uniform way and to the fact that the user can easily interact with the data.

6.4.1 Principle of parallel coordinates

With parallel coordinates, a n-dimensional space is represented with n parallel axis. Each axis represents a dimension. A multidimensional point $M(x_1,...,x_n)$ of the n-dimensional space is then represented with a polyline crossing the axis i at the corresponding coordinate

x_i. The figure 6.6 is an example of 4-dimensional points represented in the "parallel coordinates" space.

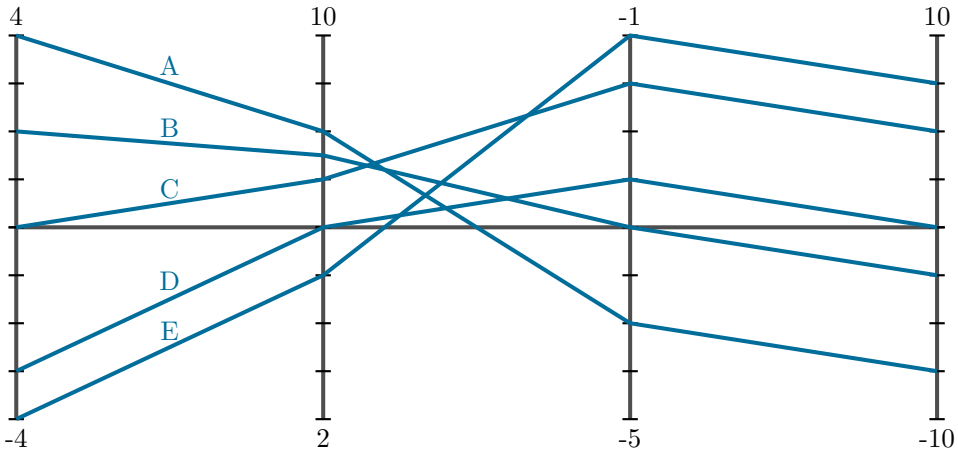

Figure 6.6: Reprensentation of the 4-dimensional points A(4,8,-4,-7.5), B(2,7.5,-3,-2.5), C(0,7,-1.5,-6), D(-3,6,-2.5,0) and E(-4,5,-1,7.5) in the parallel coordinate space.

This visualization technique also offers the possibility to easily detect relationships between two variables. Figures 6.7a-f show the relationships between lines from a two-dimensional space and their representations in parallel coordinates. To summarize these figures, a positive correlation ($m > 0$) between two variables leads to polylines which intercept each other outside the pair of vertical axis whereas this interception is between the axis in the case of a negative correlation ($m < 0$).

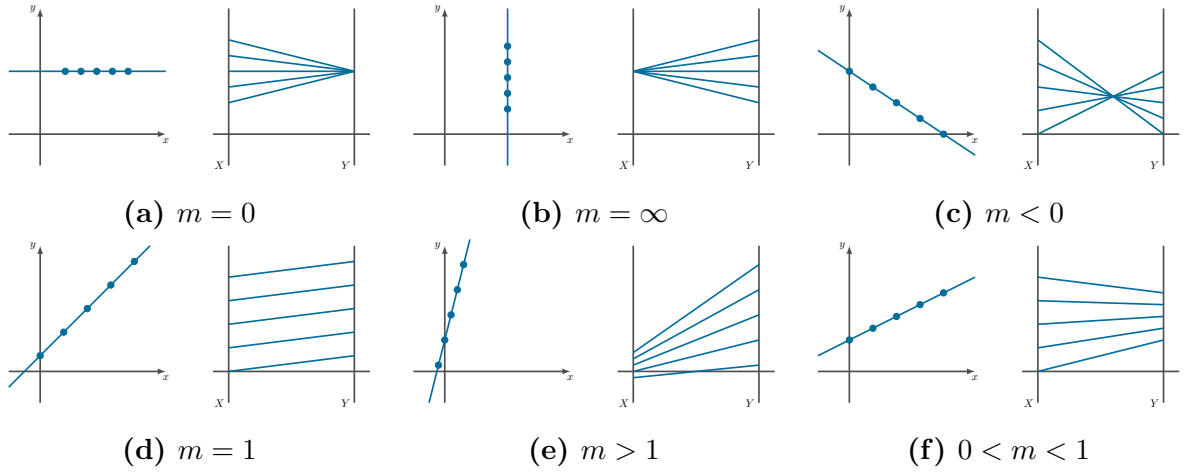

(a) $m = 0$ **(b)** $m = \infty$ **(c)** $m < 0$

(d) $m = 1$ **(e)** $m > 1$ **(f)** $0 < m < 1$

Figure 6.7: Relationships of shape between a line of equation $y = mx + b$ in a two-dimensional space and its projection in parallel coordinates.

6.4.2 Interaction with data

The open source software *Xdat* (Xdat, 2016) was used. Even though it does not offer all the interactions considered as primordial by Siirtola and Räihä (2006), this software permits the user to analyze the data with the help of two fundamental interaction techniques.

The user can perform an interval query and select a particular range on a axis in order to highlight the polylines passing through this interval.

To help the research of relationships, the user can also rearrange the axes:

- Since relationships between variables are more visible when the axes are adjacent, the user can permute the order of the axes;
- Since the intersections are more visible when they occur between the two corresponding axes, the user can invert the orientation of the axes;
- If a variable does not seem to influence the objective functions, the user can hide its axis and focus on the relevant ones.

6.4.3 Analysis of the optimal data set

This section introduces an analysis which highlights a methodology to help the designer in selecting some designs among the 713 optimal ones available.

6.4.3.1 The complete optimal data set

All the optimal architectures are represented in the figure 6.8. The red lines with the red arrows highlight the studied value ranges of each axis. The first four axes are the four geometrical parameters: the thickness of the liner L $[mm]$, the porosity ε [%], the specific surface area A_{sp} $[m^2/m^3]$ and the architectural family (geo = SP or IP). The next four axis are the four objectives of the optimization (Obj-Flux= $\rho_f v_s$ $[kg/(m^2.s)]$, Obj-Density= $\rho_{s,bulk}(1-\varepsilon)L$ $[kg/m^2]$, Obj-PoreSize= d_{pores} $[\mu m]$ and Obj-Outlet-T° = $T_{f,L}$ $[K]$.

Interesting patterns appear when the first objective is plotted with the hot side heat transfer coefficient (h_h $[W/(K.m^2)]$)) and the inner wall temperature ($T_{s,L}$ $[K]$)) (figure 6.9). Correlations between Obj-Flux, h_h ans $T_{s,L}$ are emphasized. This shows that the inner wall temperature of the optimal designs is directly linked to the efficiency of the protective boundary layer and therefore to the mass flow rate of cooling air (the lower h_h is, the more efficient the protective boundary layer is). If too much cooling air is injected through the porous liner, the wall temperature is much lower than the threshold temperature of 1100 K, which is a waste of energy.

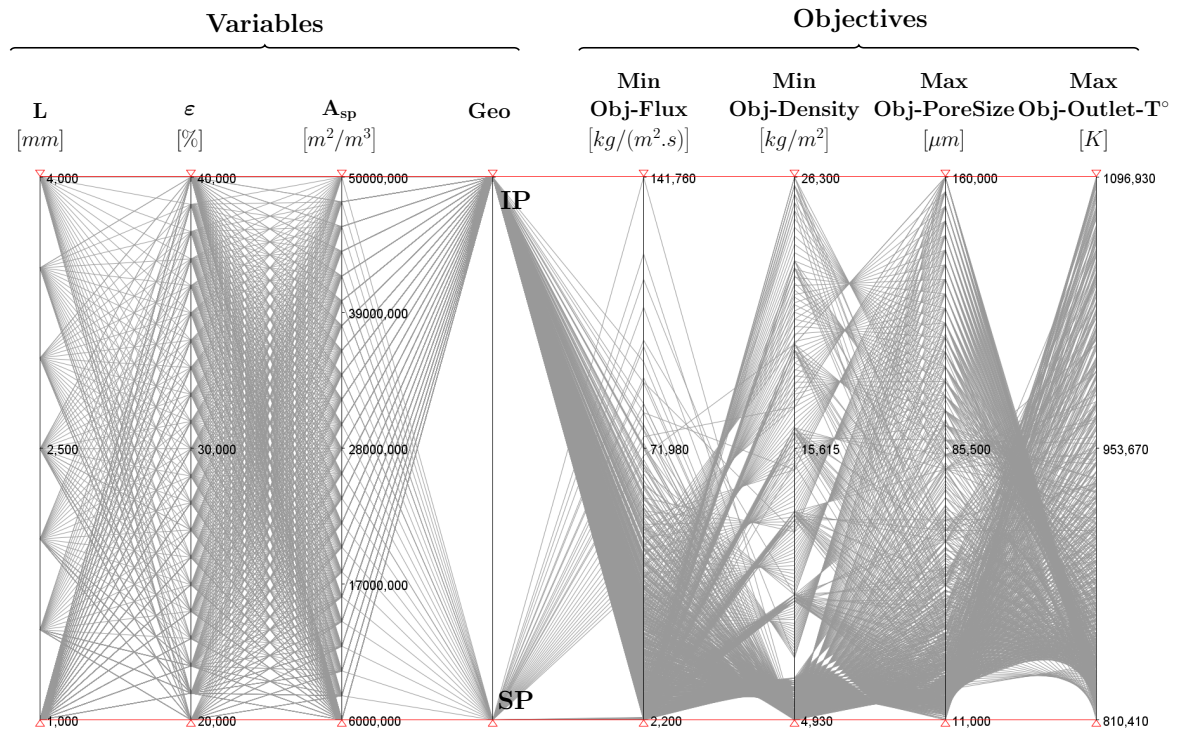

Figure 6.8: The overall optimal data set. (Apology for the three digits after the decimal point imposed by the software).

The optimal architecture having the theoretically least effective boundary layer has a hot heat transfer coefficient of $\sim 40\ W/(K.m^2)$. This optimal design has also the hottest inner wall liner temperature. Even though the protection of the boundary layer is not complete, h_h represents only 6% of the heat transfer coefficient without any protective boundary layer $h_{h,wc}$. Figure 6.10 also emphasizes the decrease of the optimal design air cooling outlet temperature with the increasing coolant mass flux.

One of the most important issues to implement transpirating systems in aero-engine is the porous material blockage (Lefebvre and Ballal, 2010). The figure 6.8 shows that the largest pore size reachable by the overall studied design range is 160 μm. This maximum pore diameter is not much bigger than the size of the typical atmospheric dust particles (up to 100 μm). Besides, engine manufacturers perform tests with particles having a size up to 150 μm to assess the ability to resist to dust. Consequently, **the transpiration with partially-sintered materials will require the use of an upstream filtration system.** Filtration systems have a cost since they cause additional pressure losses, increase the weight of the engine and require maintenance.

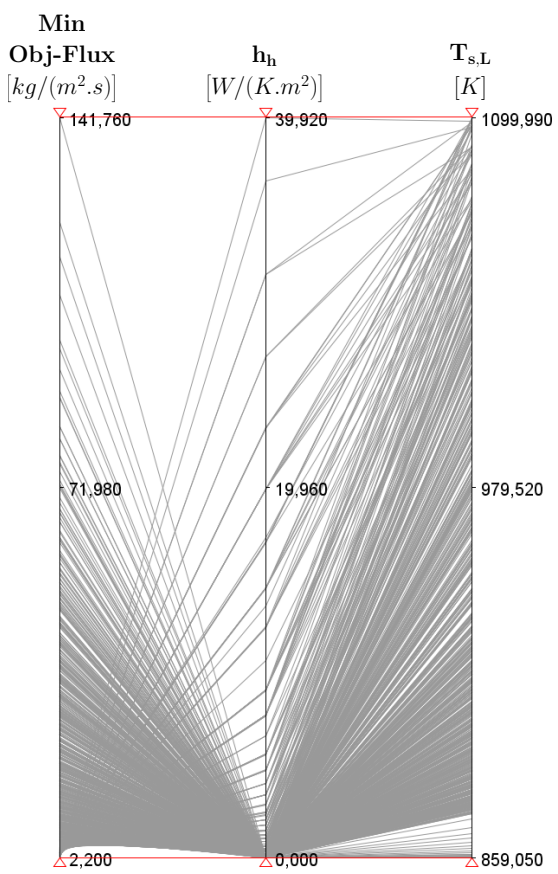

Figure 6.9: Relationship between Obj-Flux, the hot heat transfer coefficient h_h and the inner wall temperature $T_{s,L}$ of the optimal architectures.

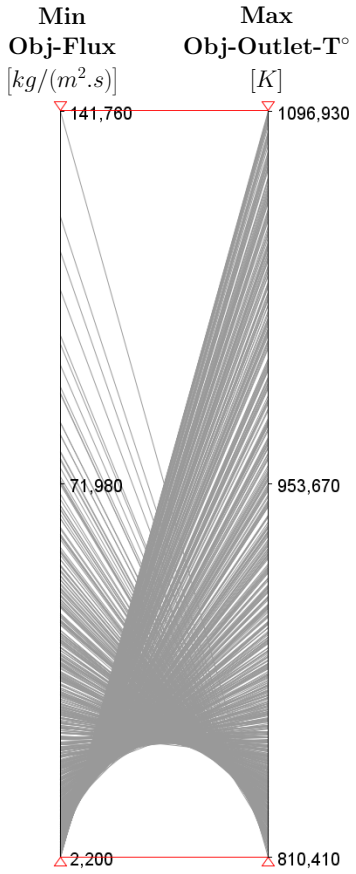

Figure 6.10: Relationship between Obj-Flux and Obj-Outlet-T° of the optimal architectures.

6.4.3.2 Improvement compared to the multi-perforated solution

From the manufacturer point of view, transpiration cooling provides an interesting advantage only if the technology allows a reduction of the cooling air mass flow and if the porous solution is not much heavier than the multi-perforated wall. To take these requirements into consideration and keep the most adapted architectures, additional conditions were applied on the optimal designs.

Reduction of the cooling air mass flow: In engine current combustion chambers, the cooling air is ejected from the multi-perforated wall (MPW) with a velocity u_c of $50 - 100\ m/s$ forming an angle α of 30° with the main hot stream direction (see figure 6.11). Moreover, the wall has a porosity of $\varepsilon_{MPW} = 3.5\%$. With a coolant density ρ_c of

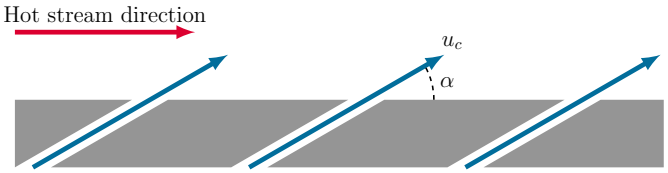

Figure 6.11: Injection of coolant through the multi-perforated wall.

about 13 kg/m^3, the mass flow rate of the multi-perforated wall can then be assessed to:

$$\text{Obj-Flux}_{MPW} = \rho_c u_c \varepsilon_{MPW} \sin(\alpha) \simeq 17 \ kg/(m^2.s) \tag{6.44}$$

In the following, all the optimal architectures having therefore a mass flow rate higher than Obj-Flux$_{MPW}$ = 17 $kg/(m^2.s)$ are considered as not interesting. The figure 6.12 shows the remaining optimal designs after applying the additional condition on Obj-Flux (cf. blue arrow).

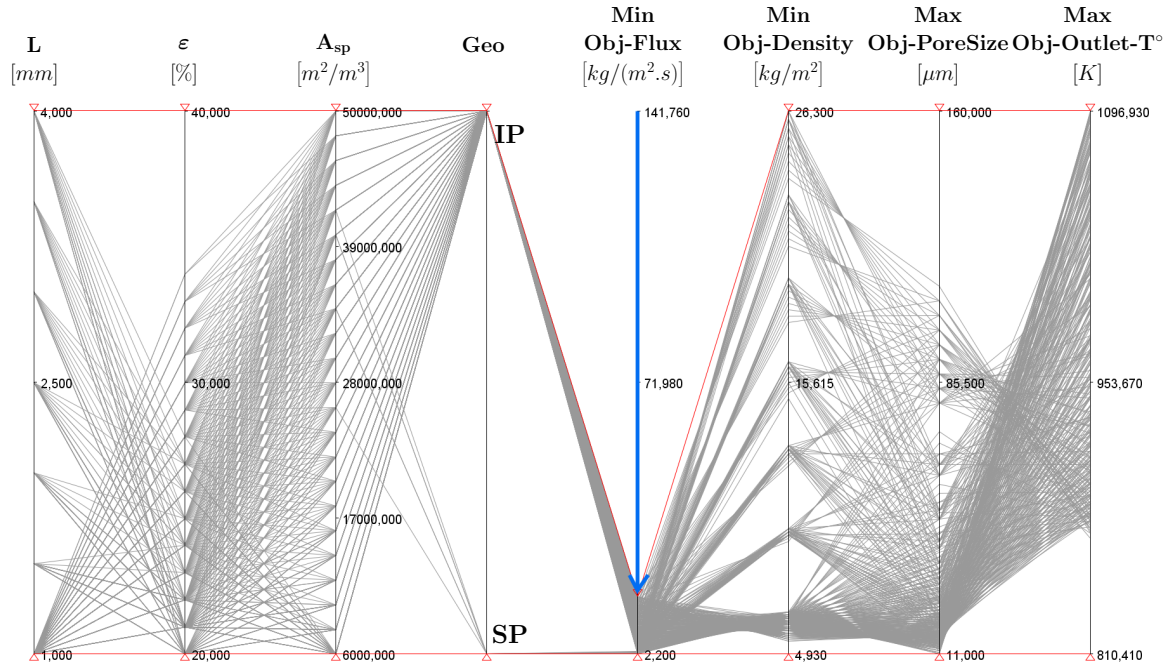

Figure 6.12: Remaining optimal architectures after applying the additional condition Obj-Flux< 17 $kg/(m^2.s)$ (cf. blue arrow).

A direct consequence of the additional condition was that all the optimal designs having a porosity higher than 34% were removed. Unfortunately, these designs also had the biggest pore sizes. Only the optimal designs with pore sizes smaller than 112 μm remain. It can also be noticed that very few optimal architectures made of spherical particles (SP)

are still viable. At equivalent porosity and specific surface area, SP architectures have a higher permeability. All the remaining designs have a permeability coefficient K which is lower than 4.7×10^{-11} m^2. Finally, only the optimal designs leading to a cooling air outlet temperature hotter than 870 K remain.

Weight of the porous wall: The thickness of the current aircraft combustion chamber liner is about 1.2 mm (courtesy of *SAFRAN*). As its porosity is $\varepsilon_{MPW} = 3.5\%$, the multi-perforated wall second objective can be assessed at Obj-Density$_{MPW} = 9.5$ kg/m^2.

However, developing a lighter cooling solution is not the major priority. Indeed, a slight gain in weight can be authorized if a more efficient cooling leads to more energy saving. As a result, removing all the designs having an objective function higher than this value is too restrictive. In the present work, it was decided to apply a tolerance margin of about 50% to Obj-Density$_{MPW}$. In the following, all the optimal designs having Obj-Density$<$ 14.4 kg/m^2 are then considered as interesting. The figure 6.13 shows the remaining designs after applying the additional condition on the Obj-Density (cf. blue arrow). It can be seen that the additional condition applied on Obj-Density imposed a maximum thickness of 2 mm. It also reduced the maximum pore size to 100 μm.

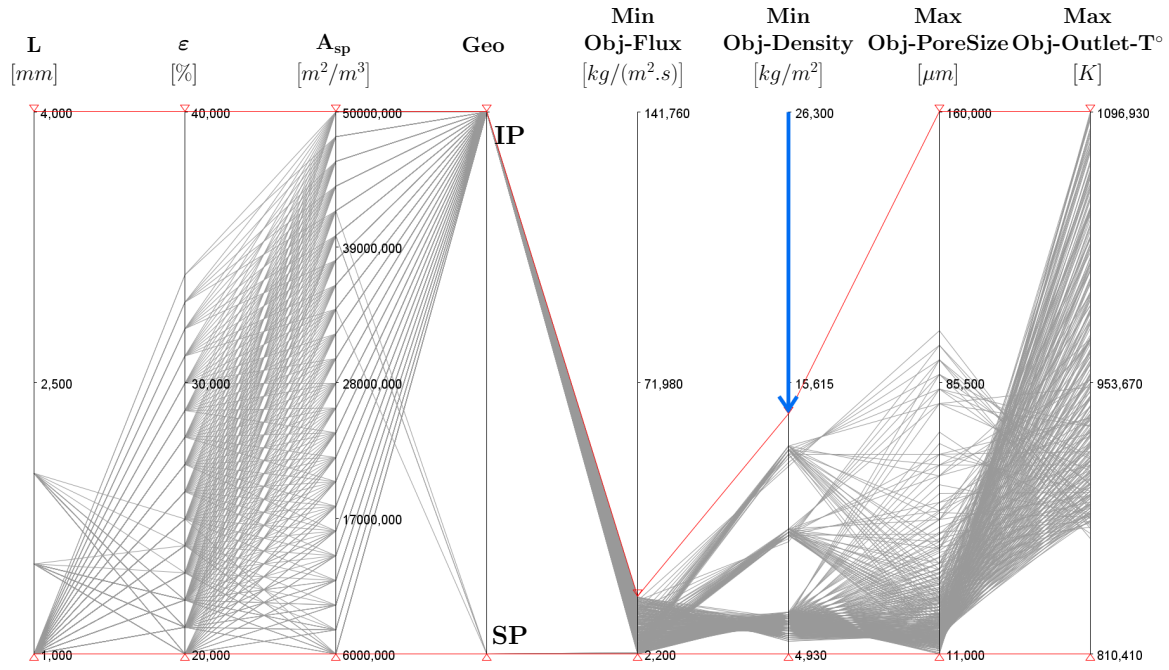

Figure 6.13: Remaining optimal architectures after applying the additional condition Obj-Density$<$ 14.4 kg/m^2 (cf. blue arrow).

Additional condition on the thickness of the designs: No mechanical aspect has-been raised in this work. However, it has to be reminded that the thickness of the multi-perforated wall is about 1.2 mm. As a result, it is unlikely to consider a porous design thinner than 1.2 mm as viable. Consequently, all the optimal designs with a thickness of 1 mm were removed. The figure 6.14 shows the remaining designs after applying an additional condition on the thickness variable (cf. blue arrow).

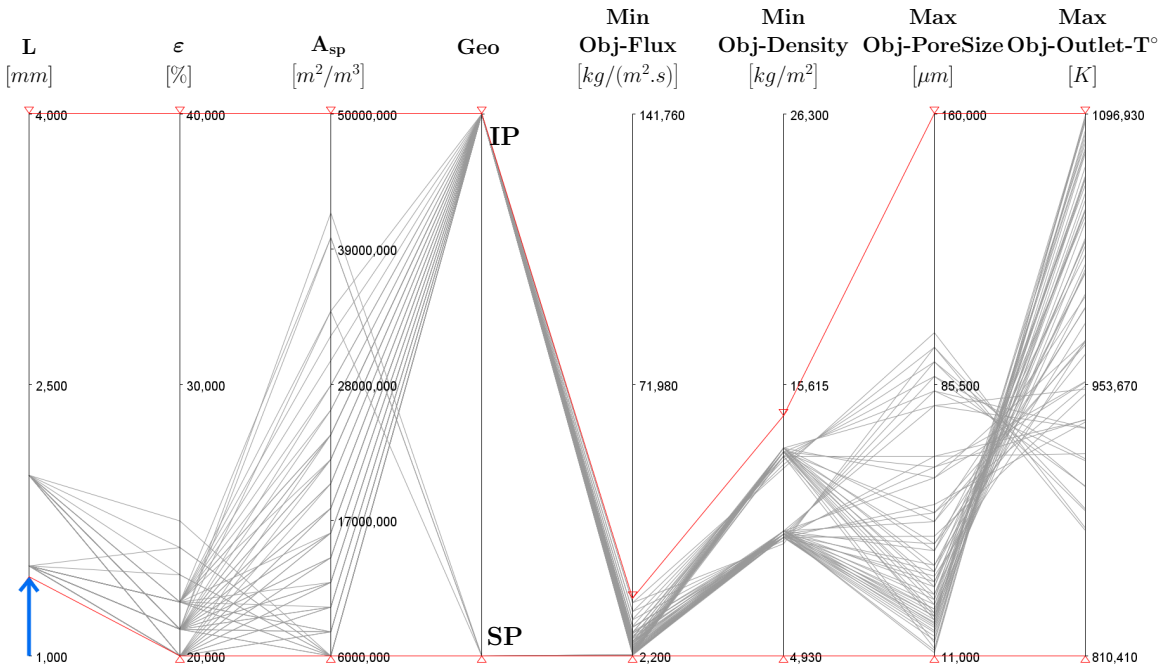

Figure 6.14: Remaining optimal architectures after applying the additional condition $L \geq 1.2\ mm$ (cf. blue arrow).

This additional condition removed a lot of designs. The porosity and the specific surface area of the remaining designs have now to be less than 25% and 42,000 m^2/m^3 respectively. The lightest designs were deleted and the Obj-Density ranges then from 1.12 to 1.6. This result justifies somehow the 50% margin applied on the threshold value of Obj-Density.

Summary: The three additional conditions applied on Obj-Flux, Obj-Density and on the liner thickness lead to a reduced number of remaining optimal designs (60 designs). These designs have a thickness ranging from 1.5 to 2 mm, a porosity ranging from 20 to 25% and a specific surface area lower than 42,000 m^2/m^3. Selecting some designs from the remaining ones depends now on the trade-off the designer is prepared to apply.

6.4.3.3 Selection of some optimal designs

For aircraft combustion chamber applications, the issues related to blockage by dust are highly constraining. In the following, some interesting optimal designs are highlighted according to the acceptable level of upstream filtration which can be set up. The effect of three filtration systems are studied.

Low filtration system ($d_{pore} > 75\ \mu m$): In a situation where the engine cannot have a sophisticated filtration system, a minimum acceptable pore size of 75 μm can be assumed. The figure 6.15 shows the remaining optimal designs. Only partially-sintered designs made of irregular powders with a small specific surface of 6,000 m^2/m^3 are viable (powder size of about 500 μm). All these designs have medium air cooling outlet temperature (Obj-Outlet-T° $< 861\ K$). Three architectures can be highlighted:

- The lightest design (**design 1**);
- The most cooling air efficient design (**design 2**);
- A trade-off design (the choice is subjective)(**design 3**);

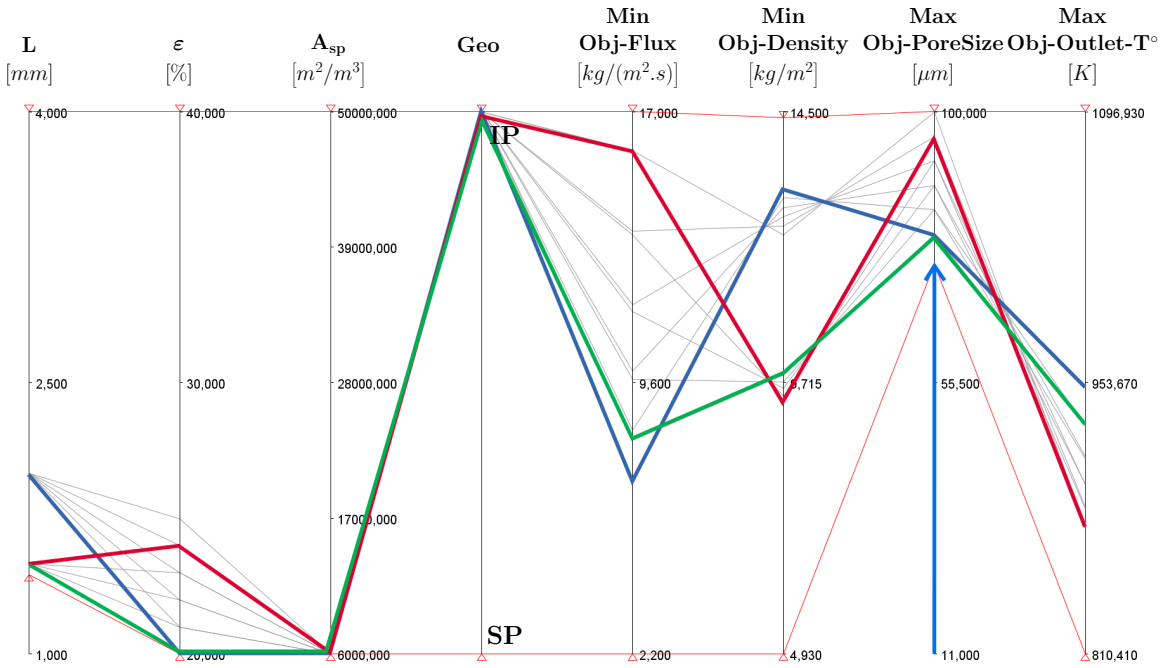

Figure 6.15: Remaining optimal architectures if the pore size has to be larger than 75 μm (cf.blue arrow). Three designs are highlighted: **design 1**: the lightest design, **design 2**: the most cooling air efficient design and **design 3**: the trade-off design.

These three designs are emphasized in the figure 6.15. Their characteristics and their improvements compared to the multi-perforated solution are introduced in the table 6.3 on page 188. The lightest design does not offer real benefits since the cooling air mass flow is only reduced by 6%. On the contrary, **design 2** and **design 3** are extremely interesting from the air efficiency aspect but they lead to an additional load (without taking into account the filtration system mass).

Intermediate filtration system ($d_{pores} > 50\ \mu m$): In a situation where the engine can now have an intermediate filtration system, the minimum acceptable pore size of the porous wall can for instance be reduced to 50 μm. The figure 6.16 shows then the remaining optimal designs having a pore size larger than 50 μm.

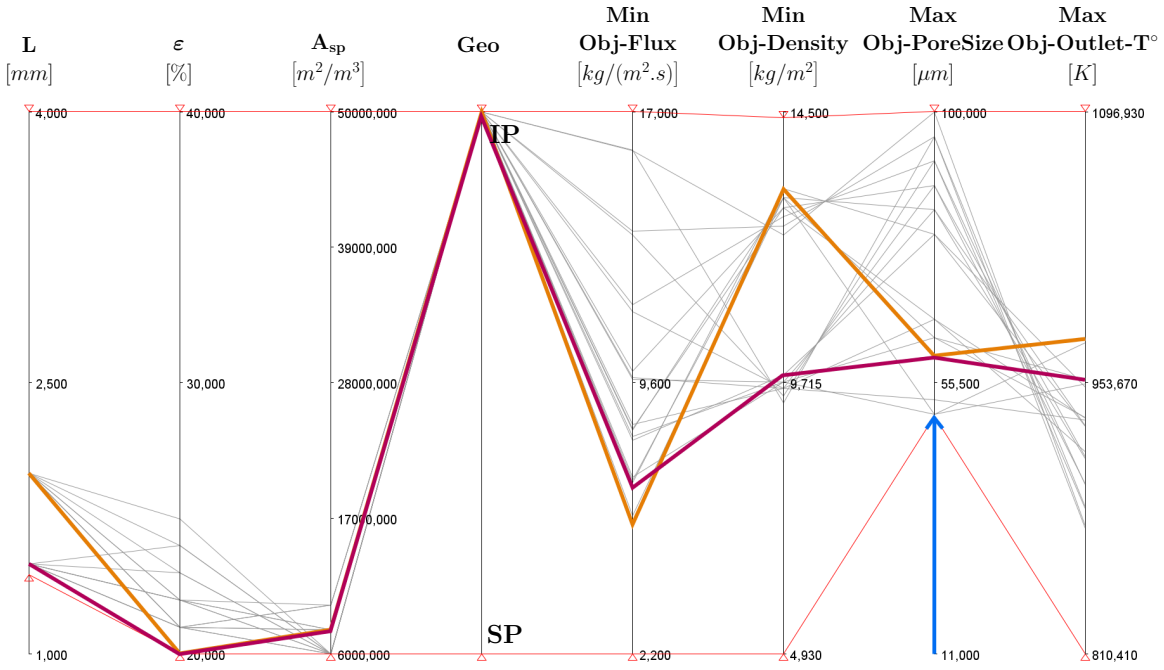

Figure 6.16: Remaining optimal architectures if the pore size has to be larger than 50 μm (cf.blue arrow). Two designs are highlighted: **design 4**: the most cooling air efficient design and **design 5**: the trade-off design.

Relaxing the additional pore size condition to 50 μm gives access to designs with hotter air cooling outlet temperature. The lightest design is the same than with a minimum pore size of 75 μm. A more cooling air efficient design can then be emphasized (**design 4**). A new trade-off design (**design 5**) is also suggested. They are represented in the figure 6.16 and their characteristics are introduced in the table 6.3 on page 188. These two designs

have a slightly larger specific surface area than **design 2** and **design 3**, equal to 8,000 m^2/m^3 (powder size of about 400 μm), . For equivalent weights, they improve the cooling air economy by about 7-8%. The cooling air outlet temperatures are also slightly hotter.

High filtration system ($d_{pores} > 25\ \mu m$): Finally, a situation where a sophisticated upstream filtration system allows a minimum pore size of 25 μm is imagined. The figure 6.17 shows the remaining optimal designs.

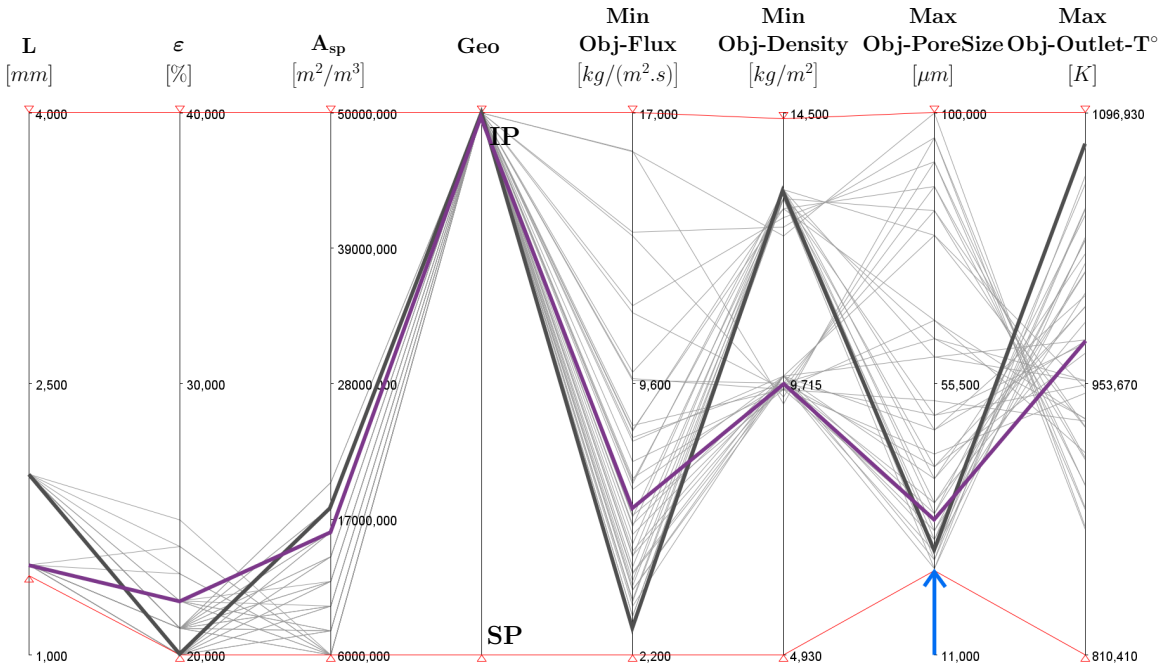

Figure 6.17: Remaining optimal architectures if the pore size has to be larger than 25 μm (cf.blue arrow). Two designs are highlighted: **design 6**: the most cooling air efficient design and **design 7**: the trade-off design.

The relaxation of the pore size has the same impact than previously. The lightest optimal design remains the same. Once again, a more cooling air efficient design (**design 6**) and a new trade-off design (**design 7**) can be highlighted. They are represented in the figure 6.17. Their characteristics are introduced in the table 6.3 on page 188. Both architectures have much larger specific areas, 18,000 and 16,000 m^2/m^3 respectively (powder size of about $170 - 200\ \mu m$). For weights equivalent to the previous highlighted designs, more cooling air can be saved and hotter cooling outlet temperatures are achieved.

Filtration System	All	Low		Medium		High	
Optimum	Obj-Density	Obj-Flux	Trade-off	Obj-Flux	Trade-off	Obj-Flux	Trade-off
Designs	**design 1**	**design 2**	**design 3**	**design 4**	**design 5**	**design 6**	**design 7**
geo	IP	IP	IP	IP	IP	IP	IP
L $[mm]$	1.5	2	1.5	2	1.5	2	1.5
ε [%]	24	20	20	20	20	20	22
A_{sp} $[m^2/m^3]$	6,000	6,000	6,000	8,000	8,000	18,000	16,000
Obj-Flux $[kg/(m^2.s)]$	16 (-6%)	6.9 (-59%)	8.0 (-53%)	5.7 (-66%)	6.7 (-61%)	2.9 (-83%)	6 (-65%)
Obj-Density $[kg/m^2]$	1.4 (-5%)	1.6 (+38%)	1.2 (+3%)	1.6 (+38%)	1.2 (+3%)	1.6 (+38%)	1.2 (+3%)
Obj-PoreSize $[\mu m]$	96	80	80	60	60	27	33
Obj-Outlet-T° $[K]$	877	952	930	977	954	1081	977

Table 6.3: Characteristics of the selected designs with the relative improvements of Obj-Flux and Obj-Density compared to the multi-perforated solution.

Summary: After applying the additional conditions on the mass flow rate, the weight and the liner thickness, the impact of the minimum allowed pore size on the optimal design selection was analyzed. Only designs made of irregular particles were retained for the studied pore size conditions. Without degrading the objective related to the mass, the smaller a pore size is allowed, the more cooling air efficient designs are available. Cooling air saving is achieved because the specific surface area increases and the permeability is then reduced. It also leads to hotter cooling air outlet temperatures.

6.5 Summary

In this chapter, a methodology was introduced to optimize the architecture of partially-sintered metallic materials intended to be used as transpirating liners in aero-engine combustion chambers. Considering the complexity of the involved phenomena (turbulent combustion, radiation,...) and the lack of knowledge regarding the boundary layer states on both sides of the liner, a simple one-dimensional heat transfer model was developed:

- Only the heat transfers in the liner are taken into account thanks to **a thermal non-equilibrium model**;
- The heat and mass transfer equations involve the four investigated effective properties: the effective thermal conductivity of the solid phase λ_{eff}, the volumetric heat transfer coefficient h_v, the permeability coefficient K and the Forchheimer coefficient β;
- The effect of the protective boundary layer is taken into account with a model found in the literature which predicts a heat transfer coefficient h_h, function of the blowing ratio;
- Thermal conditions close to the ones expected in a lean combustion chamber are imposed.

With the help of previously developed relationships predicting the effective properties of partially-sintered materials (chapters 3,4 and 5), the performance of different designs were studied. **Four geometrical variables** were chosen:

- The liner thickness;
- The material porosity;
- The specific surface area of the material;
- The constitutive powder shape (spherical or irregular powders).

To assess the performance of a design, **four objectives** were taken into consideration:

- Minimization of the air cooling mass flow;
- Minimization of the weight;
- Maximization of the pore size to avoid obstruction;
- Maximization of the air cooling outlet temperature to limit carbon monoxyde formation.

Moreover, designs with inner wall temperatures hotter than the maximum allowable operating temperature were automatically rejected.

The set of optimal solutions was analyzed thanks to the "parallel coordinates" visualization technique. After applying additional constraints on the objectives in order to have improvements over the current multi-perforated solution, **partially-sintered materials made of irregular powders turned out to be the most adapted architecture for transpiration cooling**.

To get a sufficiently low cooling air mass flow, a low porosity seems to be required (20-22%). It was also shown that an upstream filtration system is necessary to ensure the integrity of the porous liner. According to the constraint applied on the pore size, more or less cooling air efficient designs can be selected . The minimum allowable pore size constraints the specific surface area and therefore the powder size. Moreover, the lower is the mass flow rate, the hotter is the cooling air temperature. Finally, to obtain an interesting cooling air saving, porous liners heavier than the multi-perforated one are required.

6.6 Criticism and remarks

In addition to the remarks related to the choice of a one-dimensional model, other comments can be made about the optimization.

In the present work, the boundary condition predicting the effect of the protective boundary layer is only a function of the blowing ratio and of the cooling efficiency. However, at equivalent blowing ratio, it is unlikely to obtain the same insulation with materials made of large particles, small particles or even having a smooth surface. More experimental works have to be carried out regarding the impact of the roughness of the transpirating porous materials on the protective boundary layer. Moreover, additional works have also to be done to study the shape of the boundary layer with the associated heat transfer on the suction side.

In the optimization process, no specific mechanical aspect was taken into consideration. However, another limit for the use of porous materials in combustion chambers results from their reduced mechanical properties compared to dense materials. During exceptional events such as blade lost, engine surge, bird ingestion or flame out, the combustion chamber casing must not buckle or rupture (Lefebvre and Ballal, 2010). To be able to validate the mechanical robustness, mechanical testings are essential. Resistance to thermal cycles and high-cycle fatigue has also to be investigated.

The use of a one-dimensional heat transfer model cannot take into account the variation of the efficiency of the boundary layer along the liner. This variation can lead to temperature gradients and therefore to important thermal constraints. Indeed, temperature gradients are responsible for cracks near the holes of multi-perforated walls. A more elaborated model should therefore be able to predict the thermal gradient and potential thermal constraints.

Finally, the optimization was performed for only one engine working point. Different architectures could be more adapted for other engine regimes, which could lead to additional trade-off.

Conclusion and future work

Conclusion

Aim and strategy

The aim of this PhD thesis was to optimize the architecture of partially-sintered metallic materials for a transpiration cooling application in aero-engine combustion chambers. Two kinds of materials were investigated: materials made of spherical powders and materials made of irregular ones. The problematic could be divided into two main parts:

- The first part of the work was focused on the determination of relationships between the architecture of the porous materials and some effective material properties. If the effective thermal conductivity was experimentally investigated, numerical approaches were preferred to study the volumetric heat transfer coefficient, the permeability coefficient and the Forchheimer coefficient. For that purpose, some samples were digitized thanks to X-ray tomography and some materials made of spherical particles were numerically generated.
- The second part of the work was related to the multi-objective optimization of the architecture. A flow and heat transfer model was built in order to assess the performance of partially-sintered designs.

Main results

Geometrical characterization of partially-sintered materials:

The material architectures digitized by X-ray tomography were characterized thanks to image analysis. The porosity as well as the specific surface area, determined with a marching cubes algorithm, were assessed on representative elementary volumes. To have an idea of the size of the particles capable of flowing through the materials, pore sizes were measured using a sphere intrusion algorithm.

Effective thermal conductivity of partially-sintered metallic materials:

- The effective conductivity was experimentally assessed thanks to the flash method and the four-point probes method.

- Measurements carried out at different temperatures showed that the relative conductivity can be considered as constant up to 1300 K.
- The porosity is sufficient to predict the relative conductivity of partially-sintered metallic materials at a given temperature.

Permeability of partially-sintered materials:

- It was shown that the permeability of partially-sintered materials could be assessed thanks to flow simulations on digitized images.
- Almost isotropic properties were computed for each material.
- The numerical result analysis showed that the behavior of the flow could be predicted with an Ergun-like equation using the material porosity and specific surface area.
- However, the parameters h_k and h_b from the Ergun equation have to become functions of the porosity.

Volumetric heat transfer coefficients of partially-sintered materials:

- A numerical method was suggested to assess volumetric heat transfer coefficients in digitized partially-sintered metallic materials.
- A comparative study with empirical laws found in the literature helped to show the accuracy of the method.
- Simulations were performed on digitized partially-sintered material images. The results analysis showed that the volumetric transfer coefficient of each architectural family could be predicted thanks to dimensionless correlations involving the porosity and the specific surface area.

Multi-objective optimization of the architecture for transpiration cooling:

- The needs to reduce the cooling air mass flow, to minimize the weight, to limit carbon monoxide emission as well as to maximize the pore size to avoid blockage issues, while maintaining the wall under a maximum allowable temperature, were taken into consideration in the optimization.
- The thermal performance of a design was assessed thanks to a simplified one dimensional heat transfer model. The effective material parameters were computed with the behavior laws specifically developed in the present work for partially-sintered materials.

- The optimal design analysis shows that the minimum allowable pore size, for example imposed by an upstream filtration system, is critical in the choice of an optimal solution. Materials made of quite large irregular powders ($> 150\ \mu m$), and therefore without so large specific surface areas, would be the most adapted to transpiration cooling. To get improvements compared to the multi-perforated solution, porosities of about 20-22% are recommended but the designs are heavier than the current concept.

Future work

Apply the methodology to other situations

The optimization introduced in the last chapter is only an example. This methodology can easily be implemented to other engine working points for which the optimal designs will certainly be different from those analyzed in the present work. New materials could also be studied and the chosen variables could then change. By taking into consideration other selection criteria, new objectives functions could appear. The methodology has also a vocation to be applied in others situations and in other fields of study: electronic industry (Fedorov and Viskanta, 2000), micro devices (Hetsroni et al., 2006), thermal energy storage systems (Montakhab, 1979), nuclear reactor vessel (D'Hueppe, 2011), etc.

Experimental validation of the selected designs:

The present work highlighted essential geometrical characteristics that partially-sintered design should have to be adapted to transpiration cooling. The next step is to produce some of these designs with superalloy powders. The task is planned to be carried out in the project *MOSART*[1] supported by the *ANR*[2] and the *DGA*[3]. The thermal performance will then have to be validated in a realistic combustion situation. In the project *MOTRICE*[4], some trials are planned on the *EPICTETE* combustion bench at the *ONERA* research center. This bench is able to reproduce the combustion conditions of aeroengines and to

[1]Mise en Oeuvre de Structures Architecturées Refroidies par Transpiration/Implementation of transpiration cooled architectured structures

[2]L'Agence Nationale de la Recherche/The French National Research Agency

[3]Direction Générale de l'armement/French defense procurement agency

[4]Mise en Oeuvre de Traitements Refroidis Innovants pour Chambres de combustion Endurantes (Implementation of innovative cooling treatments for resistant combustion chambers)

monitor the tested walls with an infrared thermography technique.

Development of an accurate heat transfer model:

To predict accurate temperature fields, new wall laws have to be coupled to an internal two- or three-dimensional heat transfer model, as in the work of Bellettre et al. (2000). These laws have to predict realistic heat transfer coefficients on both suction and transpirating sides: the decreases of both the friction factor and the heat transfer coefficient caused by the transpiration have to be captured. The development of new laws may for instance be based on the works of Stevenson (1964) and Simpson (1971). They will also have to take into account the porous wall surface roughness which must certainly interfere with the boundary layers. For that purpose, a modeling work coupled to experimental tests will be carried out at *ONERA* in the context of the project *MOTRICE*. Despite the fact that the efficiency of transpiration cooling was shown several times in the literature, these works will finally be able to say if a transpirated boundary layer can indeed be formed and not be too quickly mixed with the hot main stream at engine conditions.

Study of anisotropic materials:

The present work focused on two families of partially-sintered materials considered as isotropic. However, a similar analysis could now be applied to anisotropic materials. Freeze-casted materials are a good example of potential candidates for transpiration cooling. Figure 6.18 explains the process of freeze-casting.

A slurry is formed with powder and is then subjected to a directional temperature gradient. Ice crystals directionally nucleate and redistribute the suspended particles. Finally, ice is sublimated and the powder is sintered. Figure 6.19a represents freeze-casted alumina and shows that this kind of architecture has orientated pores. If ceramic particles are replaced by metallic ones, the directionality of the solid phase could also lead to large effective thermal conductivity. However, if the process is now well controlled with ceramic powders (Lichtner et al., 2013; Deville et al., 2007), freeze-casting of metallic particles is still challenging. The weight and the size of the metallic powders lead to sedimentation before solidification of the slurry. Oceane Lambert (Lambert, 2017) is currently developing a new elaboration process to freeze-cast metallic particles. Figure 6.19b shows the kind of architecture she is able to generate with stainless steel powders.

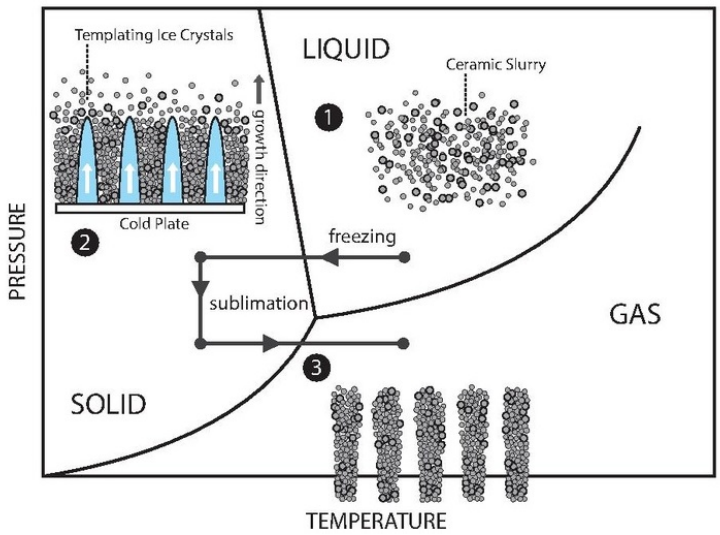

Figure 6.18: Freeze-casting process (Freeze-casting, 2016)

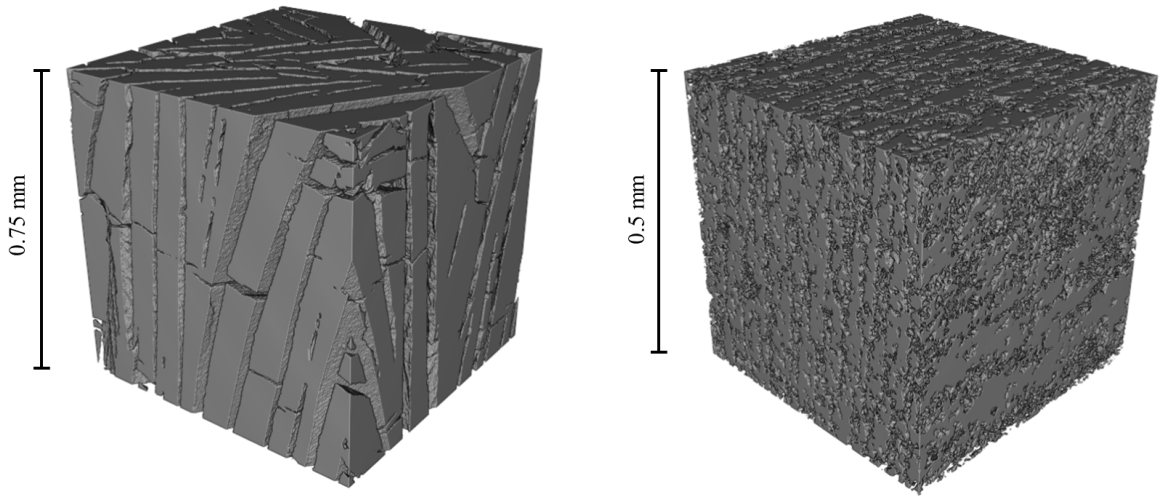

(a) Freeze-casted alumina oxide made at *ONERA*.

(b) Freeze-casted stainless steel powder made by Lambert (2017) at *ONERA*.

Figure 6.19: 3D reconstructed images of freeze-casted materials. X-ray tomography performed at the laboratory *SIMaP*.

Mechanical improvement of transpirating materials:

No mechanical consideration was taken into account in this thesis and the mechanical resistance of the porous materials will obviously have to be characterized. Porous materials are known to have lower mechanical resistance than dense material, this was one of the

reasons limiting the application of porous materials in aero-engine. However, several solutions are today considered to strengthen the porous structure:

- The first one consists in combining the multi-perforated solution with the porous one by sintering the powder directly on a thin multi-perforated wall.
- The second one suggests to create a stiffening structure and to partially-sinter a powder infiltrated in this structure (figure 6.20a).
- The third solution consists in generating simultaneously the stiffening architecture and the porous material by additive manufacturing (figure 6.20b). The partially-sintered parts can be otained by modifying the focus, the power and the scan speed of the beam.
- The last solution involves an improvement of the current multi-perforated solution by taking advantage of additive manufacturing to create more complex channel geometries.

The first two technological paths are currently being studied by Oleskii Liashenko from *SIMaP* and the by the company *Sintertech* in the project *MOSART*. The last two issues are being studied by Océane Lambert (Lambert, 2017) in the project *MOTRICE*. The thermal performance of all these solutions will have to be characterized. First experimental tests on materials made with the last two technological paths were carried out on an aerothermal bench from *ONERA-Toulouse*. They showed promising results.

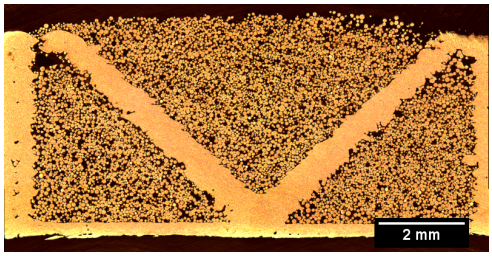

(a) Optical micrograph of partially-sintered powder in a stiffening lattice generated by additive manufacturing. (work of Oleksii Liashenko).

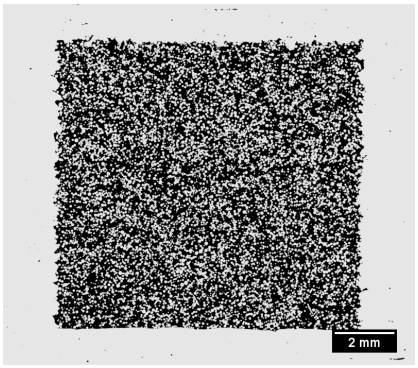

(b) Optical micragh of a porous materials produced by additive manufacturing with its stiffening dense frame. (work of Lambert (2017)).

Figure 6.20: Stiffened Ti-6Al-4V porous materials.

Bibliography

A.B. Abell, K.L. Willis, and D.A. Lange. Mercury intrusion porosimetry and image analysis of cement-based materials. *Journal of colloid and interface science*, 211(1): 39–44, 1999.

M.D. Abràmoff, P.J. Magalhães, and S.J. Ram. Image processing with imagej. *Biophotonics international*, 11(7):36–42, 2004.

E. Achenbach. Heat and flow characteristics of packed beds. *Experimental Thermal and Fluid Science*, 10(1):17–27, 1995.

J.S. Agapiou and M.F. DeVries. An experimental determination of the thermal conductivity of a 304l stainless steel powder metallurgy material. *Journal of Heat Transfer*, 111(2):281–286, 1989.

M.I. Aivazov and I.A. Domashnev. Influence of porosity on the conductivity of hot-pressed titanium-nitride specimens. *Powder Metallurgy and Metal Ceramics*, 7(9):708–710, 1968.

A.A. Alshare, P.J. Strykowski, and T.W. Simon. Modeling of unsteady and steady fluid flow, heat transfer and dispersion in porous media using unit cell scale. *International Journal of Heat and Mass Transfer*, 53(9):2294–2310, 2010.

P. Amatachaya, P. Khantikomol, R. Sangchot, and B. Krittacom. Steady state transpiration cooling system in ni-cr open-cellular porous plate. *World Academy of Science, Engineering and Technology*, 57:475–479, 2011.

A. Amiri and K. Vafai. Analysis of dispersion effects and non-thermal equilibrium, non-darcian, variable porosity incompressible flow through porous media. *International Journal of Heat and Mass Transfer*, 37(6):939–954, 1994.

Y.H. Andoh and B. Lips. Prediction of porous walls thermal protection by effusion or transpiration cooling. an analytical approach. *Applied thermal engineering*, 23(15): 1947–1958, 2003.

G.E. Andrews and A.A. Asere. Transpiration cooling of gas turbine combustion chamber walls. In *1st UK National Heat Transfer Conference, Leeds, I. Chem. E. Symposium Series*, 86, pages 1047–1056, 1984.

A. Angrand. Matériaux poreux et températures élevées. *air & cosmos*, pages 74–78, 2015.

A. Asere. *Gas turbine Combustor wall cooling*. PhD thesis, University of Leeds, 1986.

F.E. Bartell and H.J. Osterhof. The pore size of compressed carbon and silica membranes. *The Journal of Physical Chemistry*, 32(10):1553–1571, 1928.

S. Baxter and T.T. Jones. Physical properties of foamed plastics and their dependence on structure. *Plastics & Polymers*, 40(146):69, 1972.

F.J. Bayley, J.W. Cornforth, and A.B. Turner. Experiments on a transpiration cooled combustion chamber. In *Proc. Instn. Mech. Engnr.*, 1973.

J. Bellettre, F. Bataille, J.-C. Rodet, and A. Lallemand. Thermal behavior of porous plates subjected to air blowing. *Journal of thermophysics and heat transfer*, 14(4): 523–532, 2000.

O. Biceroglu, A.S. Mujumdar, A.R.P. Van Heiningen, and W.J.M. Douglas. Thermal conductivity of sintered metal powders at room temperature. *Letters in Heat and Mass Transfer*, 3(3):183–191, 1976.

J.-P. Bonnet, F. Topin, and L. Tadrist. Flow laws in metal foams: compressibility and pore size effects. *Transport in Porous Media*, 73(2):233–254, 2008.

B.P. Boudreau. The diffusive tortuosity of fine-grained unlithified sediments. *Geochimica et Cosmochimica Acta*, 60(16):3139–3142, 1996.

V. Boulos, V. Fristot, D. Houzet, L. Salvo, and P. Lhuissier. Investigating performance variations of an optimized gpu-ported granulometry algorithm. *Design and Architectures for SIgnal and Image Processing*, pages 1–6, 2012.

D.A.G. Bruggeman. dielectric constant and conductivity of mixtures of isotropic materials. *Ann. Phys.*, 24:636–679, 1935.

P.C. Carman. Fluid flow through granular beds. *Transactions-Institution of Chemical Engineeres*, 15:150–166, 1937.

R.L. Coble. Initial sintering of alumina and hematite. *Journal of the American Ceramic Society*, 41(2):55–62, 1958.

R.S. Colladay and F.S. Stepku. Examination of boundary conditions for heat transfer through a porous wall. Technical report, National Aeronautics and Space Administration, Cleveland, Ohio, United States, 1971.

P.A. Cundall and O.D.L. Strack. A discrete numerical model for granular assemblies. *Geotechnique*, 29(1):47–65, 1979.

E. Dalla, M. Hilpert, and C.T. Miller. Computation of the interfacial area for two-fluid porous medium systems. *Journal of contaminant hydrology*, 56(1):25–48, 2002.

H. Darcy. *Recherches expérimentales relatives au mouvement de l'eau dans les tuyaux*, volume 1. Mallet-Bachelier, 1857.

N.L. De Freitas, J.A.S. Gonçalves, M.D.M. Innocentini, and J.R. Coury. Development of a double-layered ceramic filter for aerosol filtration at high-temperatures: The filter collection efficiency. *Journal of hazardous materials*, 136(3):747–756, 2006.

D. Demange. Mesure de la diffusivité thermique des composites 2d et 3d, des couches minces et des liquides par la méthode flash. *La Revue métallurgie-CIT/Science et Génie Matériaux Mai*, 1999.

S. Deville, E. Saiz, and A.P. Tomsia. Ice-templated porous alumina structures. *Acta Materialia*, 55(6):1965–1974, 2007.

A. D'Hueppe. *Heat transfer modeling at an interface between a porous medium and a free region*. PhD thesis, Châtenay-Malabry, Ecole centrale de Paris, 2011.

Direction Générale de l'Aviation civile. 2013 Rapport Environnement. `www.developpement-durable.gouv.fr/IMG/pdf/DGAC-RApport-environnement-FR2013_cle8b322b.pdf`, 2013.

A.G. Dixon and D.L. Cresswell. Theoretical prediction of effective heat transfer parameters in packed beds. *AIChE Journal*, 25(4):663–676, 1979.

A. Duda, Z. Koza, and M. Matyka. Hydraulic tortuosity in arbitrary porous media flow. *Physical Review E*, 84(3):036319, 2011.

N. Dukhan, R. Picón-Feliciano, and A.R. Álvarez-Hernández. Air flow through compressed and uncompressed aluminum foam: measurements and correlations. *Journal of fluids engineering*, 128(5):1004–1012, 2006.

P. Duwez and J.R. Wheeler. Experimental study of cooling by injection of a fluid through a porous material. *Journal of the Aerospace Sciences*, 15:509–521, 1948.

E. Eckert and J. Livingood. Comparison of effectiveness of convection-, transpiration-, and film-cooling methods with air as coolant. Technical Report 1182, NACA, Lewis Flight Propulsion Laboratory, Cleveland, 1954.

Engine. `https://en.wikipedia.org/wiki/Turbojet#/media/File:Jet_engine.svg`, 2016.

S. Ergun. Fluid flow through packed columns. *Chem. Eng. Prog.*, 48:89–94, 1952.

V.M. Eroshenko and L.A. Yaskin. Heat transfer in forced convection of fluid in porous sintered metals. *Journal of Engineering Physics and Thermophysics*, 30(1):1–8, 1976.

D.J. Essman, R.E. Vogel, J.G. Tomlinson, and A.S. Novick. Tf41/Lamilloy accelerated mission test. *Journal of Aircraft*, 20(1):70–75, 1983.

A.G. Fedorov and R. Viskanta. Three-dimensional conjugate heat transfer in the microchannel heat sink for electronic packaging. *International Journal of Heat and Mass Transfer*, 43(3):399–415, 2000.

P. Forchheimer. Wasserbewegung durch boden. *Z. Ver. Deutsch. Ing*, 45(1782):1788, 1901.

Freeze-casting. `https://en.wikipedia.org/wiki/Freeze-casting`, 2016.

X. Fu, R. Viskanta, and J.P. Gore. Measurement and correlation of volumetric heat transfer coefficients of cellular ceramics. *Experimental Thermal and Fluid Science*, 17: 285–293, 1998.

A.A. Garrouch, L. Ali, and F. Qasem. Using diffusion and electrical measurements to assess tortuosity of porous media. *Industrial & Engineering Chemistry Research*, 40 (20):4363–4369, 2001.

Geodict. The virtual material laboratory geodict. `http://www.geodict.com`, 2014.

R. Gerling, H. Clemens, and F.P. Schimansky. Powder metallurgical processing of intermetallic gamma titanium aluminides. *Advanced Engineering Materials*, 6(1-2):23–38, 2004.

R.M. German. *Powder metallurgy science*. Metal Powder Industries Federation, 1994.

A. Ghassemi and A. Pak. Pore scale study of permeability and tortuosity for flow through particulate media using lattice boltzmann method. *International journal for numerical and analytical methods in geomechanics*, 35(8):886–901, 2011.

L.J. Gibson and M.F. Ashby. *Cellular Solids: Structure and Properties*. Cambridge Solid State Science Series. Cambridge University Press, 1999.

D.E. Glass, A.D. Dilley, and H.N. Kelly. Numerical analysis of convection/transpiration cooling. *Journal of Spacecraft and Rockets*, 38(1):15–20, 2001.

C.J. Gommes, A.-J. Bons, S. Blacher, J.H. Dunsmuir, and A.H. Tsou. Practical methods for measuring the tortuosity of porous materials from binary or gray-tone tomographic reconstructions. *AIChE Journal*, 55(8):2000–2012, 2009.

R.l Goodall, A. Marmottant, L. Salvo, and A. Mortensen. Spherical pore replicated microcellular aluminium: Processing and influence on properties. *Materials Science and Engineering: A*, 465(1):124–135, 2007.

P. Grootenhuis, R.W. Powell, and R.P. Tye. Thermal and electrical conductivity of porous metals made by powder metallurgy methods. *Proceedings of the Physical Society. Section B*, 65(7):502–511, 1952.

C.I. Hammetter, R.G. Rinaldi, and F.W. Zok. Pyramidal lattice structures for high strength and energy absorption. *Journal of Applied Mechanics*, 80(4):1–41, 2013.

John Happel and Howard Brenner. *Low Reynolds number hydrodynamics: with special applications to particulate media*, volume 1. Springer Science & Business Media, 2012.

G. Hetsroni, M. Gurevich, and R. Rozenblit. Sintered porous medium heat sink for cooling of high-power mini-devices. *International Journal of Heat and Fluid Flow*, 27 (2):259–266, 2006.

G.J. Hwang and C.H. Chao. Heat transfer measurement and analysis for sintered porous channels. *Journal of heat transfer*, 116(2):456–464, 1994.

A. Inselberg. The plane with parallel coordinates. *The visual computer*, 1(2):69–91, 1985.

A. Jagota and C.Y. Hui. The effective thermal conductivity of a packing of spheres. *Journal of applied mechanics*, 57(3):789–791, 1990.

B. Jiang, N.Q. Zhao, C.S. Shi, X.W. Du, J.J. Li, and .HC. Man. A novel method for making open cell aluminum foams by powder sintering process. *Materials Letters*, 59 (26):3333–3336, 2005.

P.X. Jiang, M. Li, T.-J. Lu, L. Yu, and Z.-P. Ren. Experimental research on convection heat transfer in sintered porous plate channels. *International Journal of Heat and Mass Transfer*, 47(10):2085–2096, 2004.

K.K. Kar. *Heat and mass transfer characteristics of transpiration cooling*. PhD thesis, Case Western Reserve University, 1981.

M. Kaviany. *Principles of Heat Transfer in Porous Media*. Mechanical Engineering Series. Springer New York, 2012.

J.C.Y. Koh and A. Fortini. Prediction of thermal conductivity and electrical resistivity of porous metallic materials. *International Journal of Heat and Mass Transfer*, 16(11): 2013–2022, 1973.

J.C.Y. Koh, J.L. Dutton, B.A. Benson, et al. Fundamental study of transpiration cooling: final report. Technical report, Boeing Aerospace Company, 1973.

V. Koivu, M. Decain, C. Geindreau, K. Mattila, J.-F. Bloch, and M. Kataja. Transport properties of heterogeneous materials. combining computerised x-ray micro-tomography and direct numerical simulations. *International Journal of Computational Fluid Dynamics*, 23(10):713–721, 2009.

A. Koponen, M. Kataja, and J. Timonen. Tortuous flow in porous media. *Physical Review E*, 54(1):406, 1996.

J. Kozeny. *Über kapillare Leitung des Wassers im Boden:(Aufstieg, Versickerung und Anwendung auf die Bewässerung)*. Hölder-Pichler-Tempsky, 1927.

P. Kumar, J.-M. Hugo, F. Topin, and J. Vicente. Influence of pore and strut shape on open cell metal foam bulk properties. In *Porous media and its applications in science, engineering, and industry: Fourth International Conference*, volume 1453, pages 243–248. AIP Publishing, 2012.

F. Kuwahara, M. Shirota, and A. Nakayama. A numerical study of interfacial convective heat transfer coefficient in two-energy equation model for convection in porous media. *International journal of heat and mass transfer*, 44(6):1153–1159, 2001.

O. Lambert. *PhD thesis in progress*. PhD thesis, Université Grenoble-Alpes, 2017.

O. Lame, D. Bellet, M. Di Michiel, and D. Bouvard. Bulk observation of metal powder sintering by x-ray synchrotron microtomography. *Acta materialia*, 52(4):977–984, 2004.

R. Landauer. The electrical resistance of binary metallic mixtures. *Journal of Applied Physics*, 23(7):779–784, 1952.

R.B. Landis and A.F. Mills. The calculation of turbulent boundary layers with foreign gas injection. *International Journal of Heat and Mass Transfer*, 15(10):1905–1932, 1972.

G. Laschet, J. Sauerhering, O. Reutter, T. Fend, and J. Scheele. Effective permeability and thermal conductivity of open-cell metallic foams via homogenization on a microstructure model. *Computational Materials Science*, 45(3):597–603, 2009.

M.R. L'Ecuyer and R.S. Colladay. Influence of porous-wall thermal effectiveness on turbulent-boundary-layer heat transfer. Technical report, National Aeronautics and Space Administration, Cleveland, Ohio, United States, 1972.

A.H. Lefebvre and D.R. Ballal. *Gas Turbine Combustion: Alternative Fuels and Emissions*. Taylor & Francis Group, 2010.

A.Z. Lichtner, D. Jauffrès, C.L. Martin, and R.K. Bordia. Processing of hierarchical and anisotropic porosity lsm-ysz composites. *Journal of the American Ceramic Society*, 96 (9):2745–2753, 2013.

W.B. Lindquist, S.-M. Lee, D.A. Coker, K.W. Jones, and P. Spanne. Medial axis analysis of void structure in three-dimensional tomographic images of porous media. *Journal of Geophysical Research: Solid Earth*, 101(B4):8297–8310, 1996.

Y.-Q. Liu, P.-X. Jiang, Y.-B. Xiong, and Y.-P. Wang. Experimental and numerical investigation of transpiration cooling for sintered porous flat plates. *Applied Thermal Engineering*, 50(1):997–1007, 2013.

A.L. Loeb. Thermal conductivity: Viii, a theory of thermal conductivity of porous materials. *Journal of the American Ceramic Society*, 37(2):96–99, 1954.

W.E. Lorensen and H.E. Cline. Marching cubes: A high resolution 3d surface construction algorithm. In *ACM siggraph computer graphics*, volume 21, pages 163–169. ACM, 1987.

I.F. Macdonald, M.S. El-Sayed, K. Mow, and F.A.L. Dullien. Flow through porous media-the ergun equation revisited. *Industrial & Engineering Chemistry Fundamentals*, 18(3): 199–208, 1979.

E. Maire, A. Fazekas, L. Salvo, R. Dendievel, S. Youssef, P. Cloetens, and J.M. Letang. X-ray tomography applied to the characterization of cellular materials. related finite

element modeling problems. *Composites Science and Technology*, 63(16):2431–2443, 2003.

C.L. Martin and R.K. Bordia. Influence of adhesion and friction on the geometry of packings of spherical particles. *Physical Review E*, 77(3):031307, 2008.

M. Matyka, A. Khalili, and Z. Koza. Tortuosity-porosity relation in porous media flow. *Physical Review E*, 78(2):026306, 2008.

J.C. Maxwell. *Electricity and magnetism*. A Treatise on Electricity and Magnetism. Clarendon Press, Londres, 1873.

R.E. Meredith and C.W. Tobias. Conductivities in emulsions. *Journal of the Electrochemical Society*, 108(3):286–290, 1961.

B. A. Meyer and D.W. Smith. Flow through porous media: comparison of consolidated and unconsolidated materials. *Industrial & engineering chemistry fundamentals*, 24(3): 360–368, 1985.

H.S. Mickley, R.C. Ross, A.L. Squyers, and W.E. Stewart. Heat, mass, and momentum transfer for flow over a flat plate with blowing or suction. Technical report, Massachusetts Inst. of Tech., 1953.

R.J. Moffat and W.M. Kays. The turbulent boundary layer on a porous plate: Experimental heat transfer with uniform blowing and suction. *International Journal of Heat and Mass Transfer*, 11(10):1547 – 1566, 1968.

A. Montakhab. Convective heat transfer in porous media. *Journal of Heat Transfer*, 101 (3):507–510, 1979.

A. Nakayama, F. Kuwahara, T. Umemoto, and T. Hayashi. Heat and fluid flow within an anisotropic porous medium. *Journal of heat transfer*, 124(4):746–753, 2002.

D.A. Nealy and S.B. Reider. Evaluation of laminated porous wall materials for combustor liner cooling. *Journal for Engineering for Power*, 102(2):268–276, 1980.

D. Nemec and J. Levec. Flow through packed bed reactors: 1. single-phase flow. *Chemical Engineering Science*, 60(24):6947–6957, 2005.

R.K Niven. Physical insight into the ergun and wen & yu equations for fluid flow in packed and fluidised beds. *Chemical Engineering Science*, 57(3):527–534, 2002.

T.D. Papathanasiou, B. Markicevic, and E.D. Dendy. A computational evaluation of the ergun and forchheimer equations for fibrous porous media. *Physics of Fluids (1994-present)*, 13(10):2795–2804, 2001.

F. Parhami and R.M. McMeeking. A network model for initial stage sintering. *Mechanics of materials*, 27(2):111–124, 1998.

W.J. Parker, R.J. Jenkins, C.P. Butler, and G.L. Abbott. Flash method of determining thermal diffusivity, heat capacity, and thermal conductivity. *Journal of applied physics*, 32(9):1679–1684, 1961.

S. Patankar. *Numerical Heat Transfer and Fluid Flow*. Series in computational methods in mechanics and thermal sciences. Taylor & Francis, 1980.

J. Petrasch, F. Meier, H. Friess, and A. Steinfeld. Tomography based determination of permeability, dupuit-forchheimer coefficient, and interfacial heat transfer coefficient in reticulate porous ceramics. *International Journal of Heat and Fluid Flow*, 29(1): 315–326, 2008.

H.M. Quinn. A reconciliation of packed column permeability data: Deconvoluting the ergun papers. *Journal of Materials*, 2014, 2014.

M. Quintard, M. Kaviany, and S. Whitaker. Two-medium treatment of heat transfer in porous media: numerical results for effective properties. *Advances in Water resources*, 20(2):77–94, 1997.

W.D. Rannie. A simplified theory of porous wall cooling. Technical report, JPL California Institute of Technology, Pasadena, USA, 1947.

Lord Rayleigh. On the influence of obstacles arranged in rectangular order upon the properties of a medium. *Philosophical Magazine*, 34(211):481–502, 1892.

O. Reutter, E. Smirnova, J. Sauerhering, S. Angel, T. Fend, and R. Pitz-Paal. Characterization of air flow through sintered metal foams. *Journal of Fluids Engineering*, 130 (5):051201, 2008.

Rolls-Royce Plc. *The jet Engine*. Derby: Rolls-Royce Plc, 1996.

D. Roussel, A. Lichtner, D. Jauffrès, J. Villanova, R.K. Bordia, and C.L. Martin. Strength of hierarchically porous ceramics: Discrete simulations on x-ray nanotomography images. *Scripta Materialia*, 113:250–253, 2016.

M.W. Rubesin. An analytical estimation of the effect of transpiration cooling on the heat-transfer and skin-friction characteristics of a compressible, turbulent boundary layer. Technical report, National Advisory Committee for Aeronautics Ames Aeronautical Lab., Moffett Field, CA, United States, 1954.

L. Salvo, P. Cloetens, E. Maire, S. Zabler, J.J. Blandin, J.-Y. Buffière, W. Ludwig, E. Boller, D. Bellet, and C. Josserond. X-ray micro-tomography an attractive characterisation technique in materials science. *Nuclear instruments and methods in physics research section B: Beam interactions with materials and atoms*, 200:273–286, 2003.

H. Siirtola and K.-J. Räihä. Interacting with parallel coordinates. *Interacting with Computers*, 18(6):1278–1309, 2006.

R.L. Simpson. The effect of a discontinuity in wall blowing on the turbulent incompressible boundary layer. *International Journal of Heat and Mass Transfer*, 14(12):2083–2097, 1971.

R.L. Simpson, R.J. Moffat, and W.M. Kays. The turbulent boundary layer on a porous plate: experimental skin friction with variable injection and suction. *International Journal of Heat and Mass Transfer*, 12(7):771–789, 1969.

Sintertech. Poral: Filtres poreux en métal fritté. `http://sintertech.org/fr/portfolio/poral-filtres-poreux-en-metal-fritte/`, 2016.

R.E. Skochdopole. The thermal conductivity of foamed plastics. *Chem. Eng. Prog*, 57 (10):55–59, 1961.

T.N. Stevenson. Turbulent boundary layers with transpiration. *AIAA Journal*, 2(8): 1500–1502, 1964.

W.C. Sun, J.E. Andrade, and J.W. Rudnicki. Multiscale method for characterization of porous microstructures and their impact on macroscopic effective permeability. *International Journal for Numerical Methods in Engineering*, 88(12):1260–1279, 2011.

P. Suri, R.P. Koseski, and R.M. German. Microstructural evolution of injection molded gas-and water-atomized 316l stainless steel powder during sintering. *Materials Science and Engineering: A*, 402(1):341–348, 2005.

L. Tadrist, M. Miscevic, O. Rahli, and F. Topin. About the use of fibrous materials in compact heat exchangers. *Experimental Thermal and Fluid Science*, 28(2):193–199, 2004.

F. Topin, .J-P. Bonnet, B. Madani, and L. Tadrist. Experimental analysis of multiphase flow in metallic foam: flow laws, heat transfer and convective boiling. *Advanced Engineering Materials*, 8(9):890–899, 2006.

R.K. Traeger. Physical properties of rigid polyurethane foams. *Journal of Cellular Plastics*, 3:405–418, 1967.

R.P. Tye. The thermal and electrical conductivities of porous copper and stainless steel to elevated temperatures. In *ASME PAPER 73-HT-47*, 1973.

R. v.d. Bank, C. Bera, M. Cazalens, and S. Harding. Organisation of european aeronautique ultra-low nox combustion research. In 26^{th} *International congress of the aeronautical sciences*, 2006.

J Von Wolfersdorf. Effect of coolant side heat transfer on transpiration cooling. *Heat and mass transfer*, 41(4):327–337, 2005.

N. Wakao and S. Kagei. *Heat and mass transfer in packed beds*, volume 1. Taylor & Francis, 1982.

N. Wakao and T. Kagei, S.and Funazkri. Effect of fluid dispersion coefficients on particle-to-fluid mass transfer coefficients in packed beds: correlation of nusselt numbers. *Chemical Engineering Science*, 34:325–336, 1978.

A.B. Wassell and J.K. Bhangu. The development and application of improved combustor wall cooling techniques. In *American Society of Mechanical Engineers, Gas Turbine Conference and Products Show, New Orleans, La*, 1980.

S. Whitaker. Forced convection heat transfer correlations for flow in pipes, past flat plates, single cylinders, single spheres, and for flow in packed beds and tube bundles. *AIChE Journal*, 18(2):361–371, 1972.

D.G. Whitten, R.J. Moffat, and W.M. Kays. Heat transfer to a turbulent boundary layer with non uniform blowing and surface temperature. In *4th Inter. heat transfer conf, Versailles*, 1970.

O. Wiener. The theory of mixtures for fields with constant currents. *Akademie der Wissenschaften. Leipsiz Math. Phys. Kl. Abhandlungen*, 32:507, 1912.

M. Wilcox, R. Baldwin, A. Garcia-Hernandez, and K. Brun. Guideline for gas turbine inlet air filtration systems. *Gas Machinery Research Council, Dallas, TX*, 2010.

Xdat. A free parallel coordinates software. `http://www.xdat.org/`, 2016.

S. Yamamoto. Effect of porosity in transpiration cooling system. In 17^th *Int. Symposium on Space Technology and Sciences, Tokyo, Japon*, volume 2, pages 2355–2360, 1990.

S. Youssef, E. Maire, and R. Gaertner. Finite element modelling of the actual structure of cellular materials determined by x-ray tomography. *Acta Materialia*, 53(3):719–730, 2005.

Z. Zeng and R. Grigg. A criterion for non-darcy flow in porous media. *Transport in Porous Media*, 63(1):57–69, 2006.

Appendix A

Discretization of the convection-diffusion equation

For a matter of simplicity, the method to discretize the convection-diffusion equation will be explained for the one dimensional case and with the following generic form:

$$\frac{\partial}{\partial x_i}\left(\rho u\Phi - \Gamma\frac{\partial\Phi}{\partial x_i}\right) = 0 \tag{A.1}$$

where ρ, Γ, u, Φ and x_i are the fluid density, the diffusivity coefficient, the velocity, the variable of interest and the the variable of space respectively.

A.1 The finite volume method

To numerically solve this equation and determine the Φ field, the fluid domain has to be decomposed into small fluid cells. Discrete Φ values are defined at the core of these cells whereas discrete velocity component values are defined at the cell faces. Equation A.1, which is defined for continuous Φ and velocity variables, has therefore to be derived in a discretized form. If the total flux J is defined as:

$$J = F\Phi - \Gamma\frac{d\Phi}{dx} \tag{A.2}$$

where $F = \rho u$ is the mass-flow rate across a face, equation A.1 becomes:

$$\frac{dJ}{dx} = 0 \tag{A.3}$$

The finite volume method consists in integrating equation A.3 over a control volume represented in the 1D case by the hatched cell of the figure A.1.

The integration leads to:

$$J_e - J_w = 0 \tag{A.4}$$

with

$$J_{cf} = (F\Phi)_{cf} - \left(\Gamma\frac{d\Phi}{dx}\right)_{cf} \tag{A.5}$$

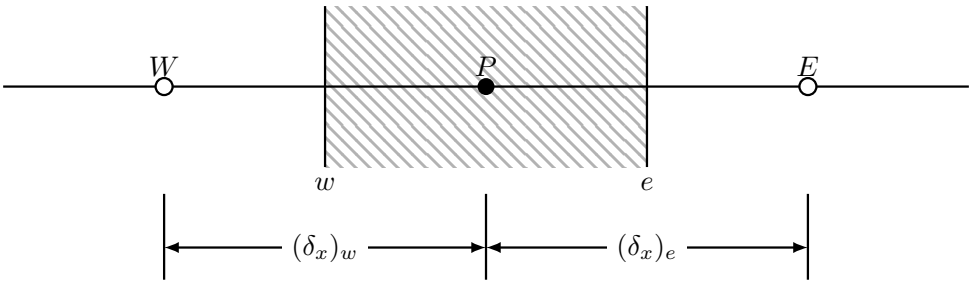

Figure A.1: 1-dimensional control volume (hatched cell) around the point of interest P with its neighboring points.

where the subscripts $_{cf} =_e$ or $_w$ indicates the cell faces. As the values of Φ are stored at the center of the cells, there is a need to use interpolation to express Φ and its derivatives at the cell faces. Different interpolation schemes are introduced in the literature for the specific case of the convection-diffusion problem. As explained by Patankar (1980), their level of complexity leads to different levels of accuracy and stability. Some interpolation schemes will be introduced in the next sections to give the reader a better understanding of the convection-diffusion discretization issues.

A.2 Common discretization schemes

This section aims to introduce the issues relative to the discretization of the conduction-diffusion problem. Different discretization schemes with increasing complexity will be given.

Central differencing scheme: The central differencing scheme is one of the most simplest discretization scheme. It assumes that the profile of the variable Φ can be described by a piecewise linear function as in figure A.2. With this profile, the variable Φ and its derivative at the interface can be simply expressed by:

$$\Phi_w = \frac{\Phi_W + \Phi_P}{2} \text{ and } \Phi_e = \frac{\Phi_E + \Phi_P}{2} \tag{A.6}$$

$$\frac{d\Phi_w}{dx} = \frac{\Phi_P - \Phi_W}{\delta x_w} \text{ and } \frac{d\Phi_e}{dx} = \frac{\Phi_E - \Phi_P}{\delta x_e} \tag{A.7}$$

If all the cells have the same size (δx is constant), and if the diffusion conductance $D = \Gamma/\delta x$ is used, the heat equation is discretized as:

$$a_P\Phi_P = a_W\Phi_W + a_E\Phi_E \tag{A.8}$$

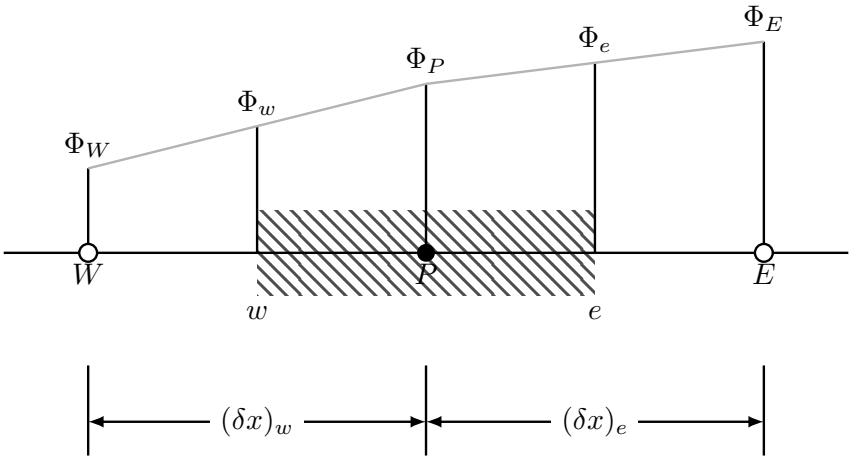

Figure A.2: Piecewise linear profile.

with

a_W	a_E	a_P
$\left(D + \frac{F_w}{2}\right)$	$\left(D - \frac{F_e}{2}\right)$	$a_W + a_E + (F_e - F_w)$

Certainly because of its simplicity, this discretization scheme suffers from severe issues when it is applied to convection-diffusion problems. As it does not take into account the flow direction or the strength of the convection relative to diffusion, instability issues can appear. Indeed, if the cell Peclet number, defined as:

$$Pe_{cf} = \frac{F_{cf}}{D} = \frac{(\rho u)_{cf}\delta x}{\Gamma} \tag{A.9}$$

becomes higher than 2, the coefficients a_E or a_W become negative and lead to oscillation or divergence of the solution.

Upwind differencing scheme: To avoid the transportiveness problem of the central differencing scheme, the upwind differencing scheme suggests that the value of Φ at an interface is equal to that at the grid point on the upwind side of the face. For instance and for the interface $_e$:

$$\Phi_e = \Phi_P \quad \text{if} \quad F_e > 0 \tag{A.10}$$

$$\Phi_e = \Phi_E \quad \text{if} \quad F_e < 0 \tag{A.11}$$

The discretized equation becomes then:

$$a_P\Phi_P = a_W\Phi_W + a_E\Phi_E \tag{A.12}$$

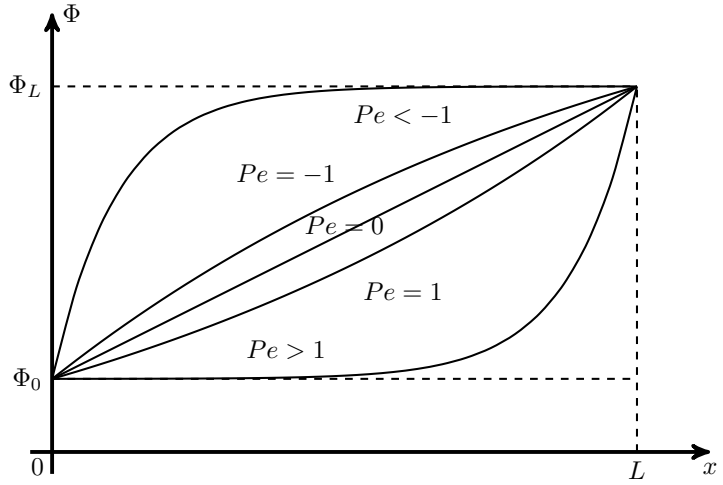

Figure A.3: Variation of Φ in a 1D convection-diffusion problem and for various values of Pe.

with

a_W	a_E	a_P
$D + \max(F_w,0)$	$D - \max(-F_e,0)$	$a_W + a_E + (F_e - F_w)$

Despite its stability and transportiveness, this scheme is not accurate when the flow is not well aligned with the grid. It can then lead to the production of false diffusion.

The exponential scheme: If equation A.1 is used in a 1D case with Γ taken as constant (F being constant by the mass conservation), an exact solution can be found for the domain $0 \leq x \leq L$ when the following Dirichlet boundary conditions are applied:

$$\Phi(x = 0) = \Phi_0 \tag{A.13}$$

$$\Phi(x = L) = \Phi_L \tag{A.14}$$

The exact solution is:

$$\frac{\Phi(x) - \Phi_0}{\Phi_L - \Phi_0} = \frac{\exp(Pe\frac{x}{L}) - 1}{\exp(Pe) - 1} \tag{A.15}$$

with $Pe = \dfrac{FL}{\Gamma}$. It shows that the profile of Φ in a convection-diffusion problem is far from being linear, except for small values of $|Pe|$ where the velocity, and therefore the convection, are low. The profile of Φ for different values of Pe are shown figure A.3. The exact solution A.15 can now be used as a discretization profile between the points P and

E (figure A.1) by replacing Φ_0, Φ_L and L with respectively Φ_P, Φ_E and δx_e. J_e can then be expressed as:

$$J_e = F_e \left(\Phi_P + \frac{\Phi_P - \Phi_E}{\exp(Pe_e) - 1} \right) \tag{A.16}$$

With a similar expression for J_w, the equation A.4 becomes:

$$F_e \left(\Phi_P + \frac{\Phi_P - \Phi_E}{\exp(Pe_e) - 1} \right) - F_w \left(\Phi_W + \frac{\Phi_W - \Phi_P}{\exp(Pe_w) - 1} \right) = 0 \tag{A.17}$$

which ca be written under the following standard form:

$$a_P \Phi_P = a_E \Phi_E + a_W \Phi_W \tag{A.18}$$

with

a_W	a_E	a_P
$\dfrac{F_e}{\exp(Pe_e) - 1}$	$\dfrac{F_w \exp(Pe_w)}{\exp(Pe_w) - 1}$	$a_E + a_W + (F_e - F_w)$

This scheme generates the exact solution for any value of Peclet number and for any number of grid points if it is used in a steady one-dimensional problem. However, as exponentials are time-consuming to compute and as the scheme does not give an exact solution in a 2D or a 3D case, the use of the exponential scheme is not justified. In order to save the physical meaning of the exponential scheme while speeding up the computation of the different coefficients, the power-law scheme was developed.

The power-law scheme: The coefficient a_E from equation A.18 can be introduced under the following dimensionless form:

$$\frac{a_E}{D} = \frac{Pe_e}{\exp(Pe_e) - 1} \tag{A.19}$$

The idea of the power-law scheme is to use a piecewise function to approximate the dimensionless coefficient a_E/D as much as possible without being particularly expensive to compute:

$$\frac{a_E}{D} = \begin{cases} -P_e, & \text{if } Pe_e < -10 \quad \text{(A.20a)} \\ (1 + 0.1Pe_e)^5 - Pe_e, & \text{if } -10 \leq Pe_e < 0 \quad \text{(A.20b)} \\ (1 - 0.1Pe_e)^5, & \text{if } 0 \leq Pe_e \leq 10 \quad \text{(A.20c)} \\ Pe_e, & \text{if } Pe_e > 10 \quad \text{(A.20d)} \end{cases}$$

The discretized equation becomes finally:

$$a_P \Phi_P = a_W \Phi_W + a_E \Phi_E \tag{A.21}$$

with

a_W	a_E	a_P
$D \max\left(0, (1 - 0.1\lvert Pe_w\rvert)^5\right)$ $+ \max(0, F_w)$	$D_e \max\left(0, (1 - 0.1\lvert Pe_e\rvert)^5\right)$ $+ \max(0, -F_e)$	$a_W + a_E + (F_e - F_w)$

Higher order scheme could have also be envisaged. However, the ease of implementation and the satisfying accuracy justify the fact that the power-law scheme was selected to discretize the energy equation in this work.

Résumé

Dans l'optique de refroidir les parois des chambres de combustion aéronautiques le plus efficacement possible, un intérêt particulier est aujourd'hui porté à la technologie de refroidissement par transpiration. L'air de refroidissement s'écoule au travers d'une paroi poreuse dans laquelle une grande quantité de chaleur est échangée par convection. L'éjection de l'air profite ensuite de la distribution des pores pour former une couche limite protectrice relativement homogène.

Les matériaux métalliques obtenus à partir de poudres partiellement frittées sont de bons candidats pour former ces parois poreuses. Ce travail se focalise sur les échanges internes et consiste à développer une méthodologie permettant de dégager les architectures partiellement frittées les plus adaptées à ce type d'application.

L'écoulement et les échanges de chaleur lors du refroidissement par transpiration sont régis par quelques propriétés effectives des matériaux qui sont fonction de l'architecture : la conductivité thermique effective, le coefficient de transfert convectif volumique et les propriétés de perméabilité. A l'aide de travaux expérimentaux ou d'études numériques sur des échantillons numérisés par tomographie aux rayons X, des relations simples entre les propriétés effectives des matériaux partiellement frittés et leurs paramètres architecturaux sont tout d'abord développées. La porosité, la surface spécifique et le type de poudre utilisé sont retenus pour prédire les paramètres effectifs.

Ces relations sont finalement intégrées dans un modèle de transfert de chaleur prédisant la performance d'une solution dans les conditions de fonctionnement du moteur. Une optimisation "multi-objectifs" et une analyse des designs optimaux permettent alors de mettre en valeur quelques architectures montrant un fort potentiel pour des applications de refroidissement par transpiration. Des matériaux peu poreux formés à partir de larges poudres irrégulières semblent assurer le meilleur compromis entre tous les critères pris en compte.
Mot-clés : Refroidissement par transpiration, Matériaux partiellement frittés, Tomographie aux rayons X, Calcul sur images, Optimisation "multi-objectifs"

Abstract

In order to cool aero-engine combustion chambers as efficiently as possible, there is today a special interest given to transpiration cooling technology. The cooling air flows through a porous liner in which a large amount of heat can be exchanged by convection. The air injection could then take benefit of the pore distribution to form a more homogeneous protective boundary layer.

Partially sintered metallic materials are potential candidates to form these porous liners. The present work focuses on internal heat transfers. It aims to develop a methodology capable of highlighting the most adapted partially sintered architectures to this kind of application.

During transpiration cooling, flows and heat transfers are governed by some effective material properties which depends on the porous architecture: the effective solid phase thermal conductivity, the volumetric heat transfer coefficient and the permeability properties. Thanks to experimental works and numerical studies on samples digitized by X-ray tomography, simple relationships are first developed between the effective material properties of partially sintered materials and their architectural parameters. The porosity, the specific surface area and the powder type are selected to predict the effective properties.

These relationships are finally integrated into a heat transfer model predicting the thermal performance of a design at working engine conditions. A multi-objective optimization and an analysis of the optimal designs highlight some architectures as being potentially interesting for transpiration cooling. Materials with a low porosity and made of large irregular powders seem to ensure the best trade-off among the different criteria taken into consideration.
Key-words: Transpiration cooling, Partially-sintered materials, X-ray tomography, 3D image based computing, Multi-objective optimization